

© 2018

Manuel Sebastian Escotet Espinoza

ALL RIGHTS RESERVED

PHENOMENOLOGICAL AND RESIDENCE TIME DISTRIBUTION
MODELS FOR UNIT OPERATIONS IN A CONTINUOUS
PHARMACEUTICAL MANUFACTURING PROCESS

By

MANUEL SEBASTIAN ESCOTET-ESPINOZA

A dissertation submitted to the

School of Graduate Studies

Rutgers, The State University of New Jersey

In partial fulfillment of the requirements

For the degree of

Doctor of Philosophy

Graduate Program in Chemical and Biochemical Engineering

Written under the supervision of

Marianthi G. Ierapetritou and Fernando J. Muzzio

And approved by:

New Brunswick, New Jersey

May 2018

ABSTRACT OF THE DISSERTATION

Phenomenological and Residence Time Distribution Models for Unit Operations in a
Continuous Pharmaceutical Manufacturing Process

By MANUEL SEBASTIAN ESCOTET ESPINOZA

Dissertation Directors

Marianthi G. Ierapetritou and Fernando J. Muzzio

Interest in continuous pharmaceutical manufacturing (CPM) technology is rapidly growing, with all major pharmaceutical companies developing products in their pipelines using this technology. As it has been extensively reported, CPM can deliver enormous advantages including faster product development, less material use, reduced capital cost due to small equipment size, superior process control, optimized performance, and more reliable quality manufacturing. Nevertheless, given the novel and complex nature of the technology, CPM systems require further study compared to traditional batch processes. CPM studies must be carefully designed, optimized, validated, and controlled as holistic system in order to operate robustly, efficiently, and provide the aforementioned advantages. To achieve CPM's advantages in full, it is necessary to develop and implement a framework wherein the processes can be evaluated and studied as integrated systems. In this work, tools established in the process systems engineering (PSE) methodology were implemented to develop models that can aid CPM process design, evaluation, control, and optimization.

The focus of this work included the development and implementation of computationally efficient phenomenological and residence time distribution models for systems in a CPM system.

In the first two chapters of this work, a thorough review of the current implementation of models in the pharmaceutical industry is presented. Within the review, the different types of models currently implemented in the industry are enumerated followed by the challenges of their implementation. Among some of the most difficult challenges for modeling CPM powder-based systems is the ability to determine relationships between critical process inputs and outputs, and the ability capture the impact of material properties on the process. To overcome these challenges a framework for developing predictive phenomenological (i.e., engineering) models that include the effect of material properties on the process was developed.

The third and fourth chapters of this work are devoted to describing the model development framework and provide an example case study of the methodology when it was successfully applied to a tablet compaction process. The successful integration of material property effects into the modeling of the pharmaceutical unit operation led to the development of a material property library that collected a wide array of property measurements for a number of pharmaceutically relevant materials. The material property library, described in the fifth chapter of this work, was used as a tool to determine the impact of material properties on: (1) residence time distribution experiments and (2) the operation of continuous powder feeding units.

Residence time distribution (RTD) methods and models were studied in this work, as their application to characterize CPM systems has become standard. The effect of material properties on RTD methods were evaluated in the sixth chapter to provide recommendations for using the RTD methodology to characterize CPM units. Ultimately, the unit operation characterization and modeling framework presented in this work along with the recommendations offered for RTD experimentation and modeling were applied to the development of a dynamic phenomenological and RTD model for a continuous powder feeding unit. The model, described in the seventh chapter of this work, was used to predict the behavior of the CPM-specific unit over a wide range of material property and process inputs.

ACKNOWLEDGEMENTS

Realizing that the accomplishment of this effort was something I would have never done alone, I would like to gratefully acknowledge the help and support of many people over this amazing journey. First and foremost, I would like to thank my parents Manuel Jose Escotet Rodriguez and Mariajulia Espinoza de Escotet and my two wonderful sisters Celeste del Valle Escotet Espinoza and Valentina de la Guadalupe Escotet Espinoza for their support and encouragement over these past five years of academic development. Without their help and support, this daunting challenge would have never been achieved. Thank you for always setting my bar higher, even when I thought I was not able to reach it. For helping me overcome my thoughts and for pointing me to help when I needed it the most. I would also like to thank and acknowledge the embracing and caring support of my fiancé, Rana Novini, who was there to support my journey and surrounded me with the love and support I needed in my hardest days. Thank you, my dear joon, for giving me the strength to get through this and taking care of me emotionally. You were there in the hardest of times, always with a smile and showing me how to look at the silver linings.

Following my family, I would like to acknowledge the support and teachings from my advisers Dr. Marianthi G. Ierapetritou and Dr. Fernando J. Muzzio. Your guidance and encouragement helped me get through the challenges of research and taught me how to become a better scientist. Even through difficult times, you were always there to lend a hand and help me achieve my academic goals. I would also like to acknowledge and thank my committee members Dr. Dana Barrasso, Dr. Rohit Ramachandran, and Dr. Ravendra Singh. You have been part of my journey and I want to thank you for your continued guidance, suggestions, and feedback. I feel that after having you five as part of my committee I am ready to take on the challenges of the future. I want to also give a special thanks to great mentor and supporter of my work: Dr. Eric Jayjock. Thank you Eric for giving me critical feedback during a pivotal time of my work.

Throughout my time at Rutgers, the comradery and friendship of my colleagues gave me the strength to endure the obstacles of time as a student. Thanks to you: Dr. Sara Moghtadernejad, Dr. Sarang Oka, Dr. Krizia Karry, Dr. Andres Roman Ospino, Dr. Sonia Razavi, Dr. Parham Farzan, Dr. Zilong Wang, Dr. Amanda Rogers, Dr. Heather Emady, Dr. Pallavi Pawar, Dr. Sara Koynov, Dr. Aditya Vanarase, Dr. Pallavi Pawar, Dr. Yifan Wang, Dr. Nihar Sahay, Dr. William Engisch, Dr. Juan Osorio, Dr. Maitraye Sen, Dr. Jin Maeda, Dr. James Scicolone, Dr. Gerardo Callegari, Dr. Sejal Shah, Tianyi Li, Nirupa Metta, Lisa Dias, Abhay Athaley, Thamer Omar, Abhishek Sahay, Wei Meng, Shishir Vadodaria, Charles Foster for being there at conferences, events, and (to some of you) for being great roommates while traveling to conferences. You made the time at Rutgers a memorable time. I hope to not offend anyone I may have missed in this list, but I hope you know that you will always find me as a friend.

I would like to thank Janssen Pharmaceutica for their financial support and their scientific feedback over the course of my PhD work. The work done on this thesis was made better thanks to you and the values your company has for encouraging innovation. Within Janssen, I want to personally thank: Dr. Elisabeth Schaffer, Phillip Cappuyns, Ivo van Assche, and Dr. Bernd van Snick. The challenging presentations gave me the endurance and practice I needed to become a well-rounded scientist.

Finally and most importantly, I would like to thank my grandfather Antonio Espinoza Prieto, the only person with a PhD in my family, for showing me how to be a man of logic and reason. I cherished every second we spent together talking about science, philosophy, and the purpose of education for future generations. To you, my beloved Bibo, I dedicate this work. Although you are not here to read these words, your energy helped me get these words on paper. I know this thesis is not as good as yours, but I think you would have liked glancing it and perhaps even having me translated it for you. Now that I am becoming a doctor, I am going to start telling people as you did: “don’t call me doctor, because I am one.”

TABLE OF CONTENT

Abstracts of the Dissertation	ii
Acknowledgement	iv
Table of Contents	vi
Table of Figures	x
Tables of Tables	xv
1. Introduction	1
1.1. Background & Motivation	1
1.1. Advances in Pharmaceutical Manufacturing.....	3
1.2. Continuous Manufacturing of Pharmaceuticals	4
1.3. Continuous Manufacturing of Pharmaceutical Solid Oral Dosages	6
1.4. Innovation: Process Systems Engineering (PSE)	9
1.5. Background on Models	13
1.6. Types of Models	17
1.6.1. First principle mechanistic	17
1.6.2. Multi-dimensional mechanistic	18
1.6.3. Phenomenological or semi-empirical.....	18
1.6.4. Empirical or data-driven	19
1.6.5. Flowsheet models	20
1.7. Modeling Challenges	21
1.7.1. Computationally Expensive Unit Operations Models.....	21
1.7.2. Modeling Material Property Effects	22
1.7.3. Evaluation of Models & Their Inputs	23
1.7.4. Verification & Application of Models	23
2. Research Objectives	25
2.1. Overall Research Aim.....	25
2.2. Specific Research Aims	25
2.2.1. Aim 1	25
2.2.2. Aim 2	26
2.2.3. Aim 3	27
2.2.4. Aim 4	27
3. Aim 1: Approach for Developing Models Accounting for Material Properties .	28
3.1. Introduction.....	28
3.2. General model development framework.....	29
3.3. Equipment evaluation strategies.....	30
3.3.1. Equipment characterization.....	31
3.3.2. Performance evaluation.....	32
3.4. Modeling approach	32
3.5. Model levels	34
3.6. Model Development Algorithm	36
4. Aim 1: Application of the Methodology for Tablet Press Studies	41
4.1. Introduction.....	42
4.1.1. Effect of material properties on compaction	42
4.2. Materials and Methods.....	44
4.2.1. Materials.....	44
4.2.2. Blend preparation	45

4.2.3.	Material characterization.....	45
4.2.4.	Tablet compaction	46
4.2.5.	Tablet testing methods	46
4.2.6.	Modeling methodology	48
4.2.7.	Software	49
4.3.	Results and Discussion	49
4.3.1.	Blend Characterization and material properties	50
4.3.2.	Tablet tensile strength results	52
4.3.3.	Level 2 model: regression of model coefficients.....	54
4.3.4.	Modeling tensile strength using blend material properties.....	57
4.3.5.	Level 3 model: Application to process development.....	61
4.4.	Conclusions	67
4.5.	Large Tables and Figures	69
5.	Aim 2: Material Property Libraries and their Application in Modeling	72
5.1.	Introduction.....	73
5.1.1.	Rationale for material property libraries	76
5.1.2.	Surrogate materials	78
5.1.3.	Multivariate analysis tools for databases	79
5.2.	Materials and Methods.....	80
5.2.1.	Materials.....	80
5.2.2.	Characterization methods.....	81
5.2.3.	Equipment	81
5.2.4.	Software	82
5.3.	Results and Discussion	82
5.3.1.	Material properties	82
5.3.2.	PCA results.....	83
5.3.3.	Material similarity index using PCA (SIMIN).....	85
5.3.4.	Cluster analysis.....	89
5.3.5.	Measurement correlations	91
5.3.6.	Minimizing number of measurements and tests	93
5.4.	Conclusions	96
5.5.	Large Tables and Figures	99
6.	Aim 3: Performing Residence Time Distribution Experiments and Modeling 107	
6.1.	Introduction.....	107
6.1.1.	RTD application for equipment characterization.....	109
6.1.2.	Important RTD experimental and modeling assumptions.....	110
6.2.	Materials and Methods.....	112
6.2.1.	Materials.....	112
6.2.2.	Equipment	113
6.2.3.	RTD experimental procedure	116
6.3.	Results and Discussion	117
6.3.1.	Feeder-blender characterization at steady state	117
6.3.2.	RTD experiments and concentration profiles.....	118
6.3.3.	Residence time distribution and metrics	121
6.3.4.	RTD comparison using models	126
6.3.5.	Relationship between models and numerical MRT	129
6.3.6.	Effect of material properties on MRT.....	130
6.3.7.	Recommendations for selecting a tracer and performing RTD experiments	132
6.3.8.	Application of RTD model results to process evaluation.....	134
6.4.	Conclusions	142

6.5.	Large Tables and Figures	144
7.	Aim 4: Feeder Characterization and Modeling.....	148
7.1.	Powder feeding.....	148
7.1.1.	Screw feeders	149
7.1.2.	Feeder controls	151
7.1.3.	Feeder refill unit	152
7.2.	Materials and Methods.....	152
7.2.1.	Materials.....	152
7.2.2.	Equipment	152
7.2.3.	Experimental procedure	154
7.2.4.	Software	161
7.3.	Flow Rate Characterization and Modeling.....	162
7.3.1.	Experimental results and visual observations.....	162
7.3.2.	Flow rate characterization	166
7.3.3.	Feed factor profiles	171
7.3.4.	Effect of material properties on feed factor profile.....	182
7.3.5.	Model mean absolute percentage error	192
7.3.6.	Refill case studies	195
7.3.7.	Refill unit characterization	199
7.4.	RTD Characterization	202
7.4.1.	Concentration profiles.....	202
7.4.2.	RTD evaluation and metrics	208
7.5.	Feeder Modeling.....	210
7.5.1.	Mixing and RTD model	210
7.5.2.	Mixing and RTD model calibration	215
7.6.	Integrated Model Implementation	216
7.6.1.	Integrated feeder model in gPROMS Model Builder™.....	216
7.6.2.	Case studies evaluating the model	218
7.7.	Conclusions	221
7.8.	Large Tables and Figures	223
8.	Concluding Remarks	234
8.1.	Conclusions	234
8.2.	Suggestions for Future Work	238
8.2.1.	Application of the methodology to other unit operations.....	238
8.2.2.	Generalization of the feeder model.....	239
9.	Appendices.....	240
9.1.	Appendix A: Material Property Measurements	240
9.1.1.	Bulk and tapped density	240
9.1.2.	Particle size analysis	241
9.1.3.	Powder flow measurements.....	241
9.1.4.	Shear cell test.....	241
9.1.5.	Compressibility test	243
9.1.6.	Permeability test	244
9.1.7.	Dynamic flow test.....	245
9.2.	Appendix B: Statistical Analysis Methods.....	247
9.2.1.	Principal Component Analysis (PCA)	247
9.2.2.	Clustering Analysis.....	249
9.3.	Appendix C: Methodology to Perform RTD Experiments in Solids Unit Operations.	250
9.3.1.	Tracer Properties.....	250

9.3.2. Tracer Addition	253
9.4. Appendix D: RTD Modeling.....	257
9.4.1. Calculation of RTD.....	257
9.4.2. Phenomenological models.....	260
9.5. Appendix E: NIR method development for real time measurements	273
10. References	278

TABLE OF FIGURES

Figure 1. The four major continuous solid dosage form manufacturing routes. (1) Direct compression, (2) dry granulation, (3) wet granulation, and (4) spray drying. 8

Figure 2. Pharmaceutical manufacturing workflow integrating the use of process models. Processes in green are those that can be developed with the use of models. Adapted from [58]..... 12

Figure 3. Simplified schematic of process system engineering’s (PSE’s) model centric approach to evaluate complex systems. 14

Figure 4. Different types of models used within the process modeling structure. Adapted from [50] 16

Figure 5. Description of the relationship between process and material inputs on outputs and the implementation of models 33

Figure 6. Model level categories based on the inputs described by the model..... 35

Figure 7. Model level categories based on the inputs described by the model..... 39

Figure 8. Principal Component Analysis (PCA) results for the material properties listed on Table 4 and Table 5. (A) Score plot of blend’s characterized material properties. (B) Loadings plots for the material properties. 52

Figure 9. Experimental data for tablet tensile strength at varying levels of lubricant concentration (A) Lactose, (B) Avicel PH101, (C) Avicel PH301, and (D) All blends tablet tensile strength with a concentration of 1% magnesium stearate. 53

Figure 10. Experimental data for tablet tensile strength against relative density plotted along the Kuentz and Leuenberger model regressed for (A) Lactose with 0.75% magnesium stearate, (B) Avicel 101 with 0.75% magnesium stearate, (C) Avicel 301 with 0.75% magnesium stearate, and (D) ComPap L (15%) + Avicel 101 with 1% magnesium stearate. 54

Figure 11. Relationship between the regressed values of the Kuentz and Leuenberger equation for all formulations. Standard deviation bars were excluded to minimize clutter in the graph..... 57

Figure 12. Relationship between major material properties and their respective empirical models. (A) Relationship between bulk density and critical relative density. (B) Relationship between maximum tensile strength and permeability..... 58

Figure 13. Prediction of the external validation ternary blender compaction curve using the empirical model to calculate the Kuentz and Leuenberger equation parameters..... 61

Figure 14. Region plots indicating the feasibility region for making tablets based on operational conditions and blend properties. Regions that are not shaded are operationally infeasible, meaning compacts are predicted to not be formed. Tablet thickness is varied at three levels. The breaking force constraint was also varied between 0 and 60 N. For tablets with breaking force higher than 0 N graph (A) varies fill cam depth (mm) and blend permeability (cm²) at a constant bulk density. (B) Varies fill cam depth (mm) and blend density (g/cm³) at a constant blend permeability. For tablets with a breaking force higher than 60 N graph (C) varies fill cam depth (mm) and blend permeability (cm²) at a constant bulk density. (D) Varies fill cam depth (mm) and blend density (g/cm³) at a constant blend permeability. 65

Figure 15. Contour plots showing the application of Equation 11 to determine the effect of operational parameters and material properties on tablet tensile strength. Tablet thickness was varied to three levels. (A) Varying fill cam depth (mm) and blend permeability (cm ²) at a constant bulk density. (B) Varying fill cam depth (mm) and blend density (g/mL) at a constant blend permeability.....	67
Figure 16. Regression results from tablet tensile strength models with respect to the concentration of magnesium stearate. (A) Critical relative density regression results (B) Maximum tensile strength regression results. All error bars represent one standard deviation.	71
Figure 17. Some potential uses for material property databases or libraries.	76
Figure 18. Percent of variability explained per PC and cumulative using the eigenvalues of the PCA results	83
Figure 19. Comparison of results from the SIMIN matrix (Table 16) to the clustering results (Table 10). (A) Materials in group 1, (B) materials in group 2, (C) materials in group 3, (D) materials in group 1 compared to those in groups 2 and 3, (E) materials in group 2 compared to those in groups 1 and 3, (F) materials in group 3 compared to those in groups 1 and 2.....	91
Figure 20. Correlation coefficient (R) map for material property measurements.....	92
Figure 21. Two-dimensional plots for (A) scores and (B) loadings of the first two principal components of the material property database. Three-dimensional plots for (C) scores and (D) loadings of the first three principal components of the material property database. The numbers in square brackets next to the axis labels express the amount of variability in each PC.....	106
Figure 22. Schematic of the equipment experimental set up.....	114
Figure 23. Near Infrared (NIR) sampling interface for RTD experiments.....	116
Figure 24. Concentration v. time for each of the material tracers. Vertical lines represent tracer addition time points.....	119
Figure 25. Residence time distribution probability distribution function graphs for each material	121
Figure 26. Multivariate linear correlation analysis between material properties reported on Table 14 and Table 15 and the tracer mean residence time (MRT). R is the correlation value and p is the statistical significance value	131
Figure 27. Determining the duration of out of specification (OOS) material, using an arbitrary 115% maximum potency contour.	139
Figure 28. Determining the duration of out of specification (OOS) material, using an arbitrary 115% maximum potency contour.	141
Figure 29. Residence time distribution profile metrics comparison. (A) Peclet number and number of tanks. (B) τ_{delay} , AD and $\tau_{delay, tanks}$. (C) $\tau_{dispersion}$ and $\tau_{tanks - in - Series}$. (D) Numerically calculated mean residence time against both the axial dispersion and tanks-in-series model mean residence time values.	146
Figure 30. Case studies varying the P_{max} and $t_{disturbance}$ for 20. (A) $-100\% < P_{max} < 100\%$ and $t_{disturbance} = 10$ seconds. (B) $-100\% < P_{max} < 100\%$ and $t_{disturbance} = 30$ seconds. (C) $0 < t_{disturbance} < 60$ seconds and $P_{max} = +20\%$. (D) $0 < t_{disturbance} < 60$ seconds and $P_{max} = +40\%$	147
Figure 31. Schematic of a screw feeder unit and a refill system.	149

Figure 32. Three different feeder types with their major components symbolized. The feeder hopper (1) is represented inside the red box, the flow aid (2) system is inside the blue box, and the conveying system (3) is shown inside the green box.	150
Figure 33. Equipment experimental set up. (A) Schematic (B) Configuration in the laboratory	155
Figure 34. RTD experiment equipment configuration. (A) Schematic of the unit (B) set up in the laboratory	158
Figure 35. Experimental setup for acquisition of calibration spectra	160
Figure 36. High speed images of powder flow rate for different materials listed in Table 8	164
Figure 37. Feed factor model applied to the profiles for Case C. Regression of feed factor model parameters for profiles from (A) volumetric experiment, (B) gravimetric experiment. Model residuals for the model for (C) volumetric experiment, and (D) gravimetric experiment.	177
Figure 38. Correlation color map indicating level of linear correlation (R) between material properties and regressed feed factor parameters.	183
Figure 39. Parity plots between the RSM Predicted model parameters and the values expected from the regression using experimental data. (A) Feed factor maximum (ff_{max}), (B) feed factor minimum (ff_{min}), (C) transformed feed factor decay ($Ln\beta X2$), and (D) transformed feed factor variability ($LnA1X2$).	191
Figure 40. Comparison of mean absolute percentage error (MAPE) values for the experimental feed factor profile predictions between the level 2 (regressed parameters averaged) and level 3 (i.e., calculated from RSM models) models. MAPE values divided by screw pitch (A) 10mm and (B) 20mm.	194
Figure 41. Results for the feed factor refill experiment at constant fill level intervals. (A) Time series of both feed factor profiles and the feed factor model predictions based on weight (left) and the corresponding feeder weight profile (right). (B) Feed factor profile for weight intervals between each refill. Black line represents the predictions from the feed factor model.	197
Figure 42. Results for the feed factor experiment using cascading refills. (A) Time series of both feed factor profiles and the feed factor model predictions based on weight (left) and the corresponding feeder weight profile (right). (B) Feed factor profile for weight intervals between each refill. Black line represents the predictions from the feed factor model.	198
Figure 43. Results refill unit characterization using a 0.8 L cup volume. (A) Anhydrous calcium di-phosphate, (B) silicified MCC, (C) MCC 2, and (D) magnesium stearate.	200
Figure 44. Top view of the refill unit, looking downwards from the hopper. (A) Arching observed for cellulose, (B) arching observed for acetaminophen (C) view of the hopper unit when empty.	201
Figure 45. RTD experimental results using anhydrous calcium di-phosphate as a base and acetaminophen as the tracer material. Concentration and feeder weight profiles for the experiments with flow rate set point of (A) 2.78 g/s and (B) 5.5 g/s. Mass flow rate and screw speed profiles for the experiments with flow rate set points of (C) 2.78 g/s and (D) 5.5 g/s.	203
Figure 46. RTD experimental results using silicified MCC as the base and acetaminophen as the tracer material. Concentration and feeder weight profiles for the experiments with flow rate set point of (A) 2.78 g/s and (B) 5.5 g/s. Mass flow rate and screw speed profiles for the experiments with flow rate set points of (C) 2.78 g/s and (D) 5.5 g/s.	205

Figure 47. RTD experimental results using acetaminophen as the base and caffeine as the tracer material. Concentration and feeder weight profiles for the experiments with flow rate set point of (A) 2.78 g/s and (B) 5.5 g/s. Mass flow rate and screw speed profiles for the experiments with flow rate set points of (C) 2.78 g/s and (D) 5.5 g/s.....	207
Figure 48. Schematic of proposed mixing model in the feeder unit to simulate the RTD	211
Figure 49. Component models for the feeder model available in gPROMS Model Builder™ v4.2.	217
Figure 50. Examples of the available graphic user interfaces (GUIs) for the feeder model available in gPROMS.	217
Figure 51. Results from the integrated feeder model programmed into gPROMS Model Builder™. (A) Flowsheet of the screw feeder, refill, PID control models. (B) Output results from the screw feeder model. (C) Output results for the refill unit model.	218
Figure 52. Comparison between experimental and simulated results for material properties change experiment. (A) feed factor profile, (B) screw speed profile, (C) flow rate profile, and (D) feeder weight profile. Arrows indicate the instances when MCC 1 was introduced in the system.	220
Figure 53. Visually observed challenges during experimentation: (A) material sticking to sides feeder hopper walls, (B) material sticking to barrel, (C) lumping of material, and (D) bearding at the barrel's outlet	223
Figure 54. Results for volumetric and gravimetric feeding of MCC 4 using a 20mm pitch screw and a 63:1 gearbox ratio. (A) volumetric flow rate profiles, (B) screw speed and feeder weight for volumetric feeding, (C) gravimetric flow rate profile, and (D) screw speed and feeder weight for gravimetric feeding.	224
Figure 55. Results for volumetric and gravimetric feeding of MCC 4 using a 10mm pitch screw and a 63:1 gearbox ratio. (A) volumetric flow rate profiles, (B) screw speed and feeder weight for volumetric feeding, (C) gravimetric flow rate profile, and (D) screw speed and feeder weight for gravimetric feeding.	225
Figure 56. Results for volumetric and gravimetric feeding of Acetaminophen using a 20mm pitch screw and a 63:1 gearbox ratio. (A) volumetric flow rate profiles, (B) screw speed and feeder weight for volumetric feeding, (C) gravimetric flow rate profile, and (D) screw speed and feeder weight for gravimetric feeding.	226
Figure 57. Results for volumetric and gravimetric feeding of Acetaminophen using a 20mm pitch screw and a 445:1 gearbox ratio. (A) volumetric flow rate profiles, (B) screw speed and feeder weight for volumetric feeding, (C) gravimetric flow rate profile, and (D) screw speed and feeder weight for gravimetric feeding.	227
Figure 58. Feed factor profiles for Cases A and B for volumetric and gravimetric feeding. Feed factors calculated from (A) GEA feeder for Case A, (B) GEA feeder for Case B, (C) catch scale for Case A, and (D) catch scale for Case B.	228
Figure 59. Feed factor profiles for Cases C and D for volumetric and gravimetric feeding. Feed factors calculated from (A) GEA feeder for Case C, (B) GEA feeder for Case D, (C) catch scale for Case C, and (D) catch scale for Case D.	229
Figure 60. Feed factor coefficient results from.....	231
Figure 61. RTD PDF curve results for the RTD experiments comparing mixing based on mass flow rate: (A) anhydrous calcium di-phosphate, (B) silicified MCC, and (C) acetaminophen.	

Standardized RTD PDF curves comparing mixing based on mass flow rate: (D) anhydrous calcium di-phosphate, (E) silicified MCC, and (F) acetaminophen.	232
Figure 62. Standardized RTD PDF curve results comparing in hopper mixing between base materials. Flow rate set points of (A) 2.78 g/s and (B) 5.5 g/s.	232
Figure 63. Results of the calibration of the RTD model using the experimental data collected in part 1 of this study. The concentration profiles are separated in based on mass flow rate. For the 10 kg/h: (A) anhydrous calcium di-phosphate, (B) acetaminophen, and (C) silicified MCC. For the 20 kg/h: (D) anhydrous calcium di-phosphate, (E) acetaminophen, and (F) silicified MCC.	233
Figure 64. Development sequence of models from basic to general or “mechanistic” models ...	239
Figure 65. Schematic comparing input and outputs for several methods of introducing tracers for RTD experiments.	254
Figure 66. Schematic representations of the boundary conditions for the axial dispersion model. (A) Open-open boundary condition. (B) Close-close boundary condition.	262
Figure 67. Schematic representation of a tank-in-series system.	265
Figure 68. Comparison between tanks-in-series model and Axial Dispersion model over a broad range of mixing ($1 < n < 25$)	268
Figure 69. Comparison between tanks-in-series model and axial dispersion model for systems with vast mixing ($1 < n < 3.5$).	269
Figure 70. Comparison between the Axial Dispersion and CSTR in series for the maximum value of the Probability Distribution Function.	270
Figure 71. Effect of varying the regression parameters for the Axial Dispersion equation while keeping some constant. (A) Varying Pe while keeping $\tau_{dispersion}$ at 10 seconds. (B) Varying $\tau_{dispersion}$ while keeping Pe at 6.	271
Figure 72. Effect of varying the regression parameters for the tank-in-series equation while keeping some constant. (A) Varying nr while keeping τ_{tank} at 5 seconds. (B) Varying τ_{tank} while keeping nr at 3.	272
Figure 73. Spectral variation between the components of each tracer and the bulk MCC 2.	274
Figure 74. Parity plots for the concentration prediction of tracer in the bulk MCC 2 for all tracers.	275

TABLE OF TABLES

Table 1. Process Systems Engineering (PSE) tools for process development and evaluation in continuous manufacturing of drug substance and products. Adapted from [78]	13
Table 2. Regressed Kuentz and Leuenberger hardness model parameters.....	55
Table 3. Empirical models for Kuentz and Leuenberger hardness model constants	60
Table 4. List of materials used for the tablet compaction and material properties study	69
Table 5. Blends used for the experimental evaluation of compaction and material properties	69
Table 6. Material characterization results. Developed during characterization of this work and adapted from [154].....	70
Table 7. Blend Principal Component Analysis (PCA) result values.....	71
Table 8. List of materials used in experiments and their manufacturers.....	81
Table 9. Material cluster analysis using only 6 measurements from the material property database and from removing all the measurements from the flow energy test.....	96
Table 10. Results of clustering materials into groups based on properties	99
Table 11. Results for the first five principal components of the PCA analysis	100
Table 12. Clustering results for material property measurements. Each set of measurements is divided by their respective test	101
Table 13. Determination coefficients explaining the variability present in the clusters presented in Table 12.....	102
Table 14. Material property measurements for the materials used in this material library analysis.	103
Table 15. Continued material property measurement data table.	104
Table 16. Similarity index results with labeling legend. Pairs with SIMI = 0 have similar material properties based on their scores of the PCA, whereas those with SIMI = 100 have different material properties.....	105
Table 17. SIMIN metric values for the materials selected for the RTD experimentation.....	113
Table 18. Results for mean comparison of pairs using Student T-test for the MRT. Materials that share the same letter have similar statistically noticeable means (p -value < 0.05).....	124
Table 19. Residence time distribution metrics for all tracer experiments.	144
Table 20. Regression results for 14 for each of the RTD PDFs.	144
Table 21. Regression results for 15 for each of the RTD PDFs.	145
Table 22. GEA feeder specifications and capacity metrics. Maximum Servo Motor Speed = 9,000 RPM. Sweeping volume of screws: 10 mm = 2.4 mL/rev; 20 mm = 4.8 mL/rev.....	153
Table 23. GEA feeder experimental conditions evaluated. Feeder flow rates were computed from the drive command set point.....	156
Table 24. Results of NIR calibration model used for RTD experiments	161

Table 25. Number of experiments performed per material and feeder conditions	162
Table 26. Summary of results for regression coefficients of the feed factor model for all materials	180
Table 27. Response surface model (RSM) variables and the reference variables	185
Table 28. Coefficient table for the feed factor maximum (ff_{max}) RSM.....	187
Table 29. Coefficient table for the feed factor minimum (ff_{min}) RSM.....	188
Table 30. Coefficient table for the transformed feed factor decay constant ($Ln\beta X2$) RSM	189
Table 31. Coefficient table for the transformed first coefficient of the feed factor profile cosine Fourier amplitude ($LnA1X2$) RSM.....	190
Table 32. RSM model statistics for Equations 29-33	190
Table 33. Summary of MAPE results comparing the level 2 model with the level 3 model	193
Table 34. Summary of eight sequential refill experiments using a 0.8 L cup and controlled refill time of 3 seconds. Observed refill volume is calculated using the refill mass amount and the conditioned bulk density measurements	200
Table 35. Summary of RTD experimental results	208
Table 36. Results of regressing Equation 26 to feed factor shown in Case C	230
Table 37. ANOVA table for the RSM models shown in Equations 29-33.....	230
Table 38. Results for the RTD model regression.....	233
Table 39. Mathematical descriptors for different tracer addition methods.....	255
Table 40. Summary of tracer addition methods along with the advantages and challenges of each method.....	256
Table 41. Descriptions of distribution functions used to calculate RTD metrics. C_{outt} represents the instantaneous concentration of tracer at the system's outlet as a function of time.....	257
Table 42. Boundary conditions for two axial dispersion systems.....	262
Table 43. Summary of RTD metrics derived from probability distribution function values	271
Table 44. Advantages and challenges of RTD models	272
Table 45. Spectral correlation coefficient between bulk MCC and tracers	276
Table 46. Calibration models of in-line measurements of tracer concentration in RTD experiments.	277

CHAPTER I

1. INTRODUCTION

Acknowledgement of publication status:

Parts of Chapters have been published within a book chapter titled: Process simulation and control for continuous pharmaceutical manufacturing of solid drug products. The chapter was published in September, 2017 in a book titled: Continuous Manufacturing of Pharmaceuticals.

This work was written by the author of this thesis and done in collaboration with:

Ravendra Singh¹ and Marianthi Ierapetritou¹

¹ Engineering Research Center for Structured Organic Particulate Systems (C-SOPS), Department of Chemical and Biochemical Engineering, Rutgers, The State University of New Jersey, Piscataway, NJ 08854, USA.

The writings from the book are properly referenced.

1.1.BACKGROUND & MOTIVATION

Pharmaceuticals is a global business sector focused on the development of performance-based products designed to address the world's healthcare needs. Thanks to advances in this sector, along with medicine and disease eradication, the average world life expectancy has risen from 68 to 74 years in the past 25 years [1]. Global pharmaceutical market sales were at an estimated \$967 billion in 2016, with a steady growth rate of 7% per year over the past decade [2]. The sum base revenue for the top ten pharmaceutical industries, who spearhead most of the research and

development efforts, was valued at \$300 billion in 2008 [3] and global sales exceeded \$1.1 trillion in 2014 [4].

Although the pharmaceutical industry is fundamental in health management and their profits are higher than many other chemical industries, average technological advances across the industry have lagged. Delays, especially in manufacturing technologies, are attributed to the current regulatory framework, high profit margins, time constraints during the drug approval process, and varying physical and chemical properties of drug molecules that affect formulation and process design [5]. However, recent changes in the economic and regulatory environment surrounding the pharmaceutical industry have left the sector facing enormous obstacles.

A decade long flat line in new drug molecule innovation, extended development time due to disease and treatment complexity, relatively inefficient and poorly understood manufacturing practices, increased global competition from manufacturers of generic products (i.e., generic erosion), rising regulatory scrutiny during development, and growing expectations for medical compounds (e.g., fewer side effects, effectiveness, and accessibility) result in decreasing competition-free lifespan of products, increased product risks, and reduced profit margins for major pharmaceutical companies [6-9]. Additionally, companies need to develop new products whose average cost in 2015 per approved molecule range from \$2.3 billion to \$4.9 billion. This paradigm has cut the pharmaceutical sum revenues for the top ten pharma industries in 2014 to \$250 billion; a 16% decrease from 2008 [3]. These technological and regulatory challenges associated with the current pharmaceutical manufacturing standards have pushed industry to invest in more efficient and reliable product manufacturing technologies that help reduce development time, save cost, and improve drug product quality.

In order to aid the modernization of pharmaceutical manufacturing and implementation of new technologies, the Food and Drug Administration (FDA) launched in 2004 an initiative for

enhancing process understanding using the Quality by Design (QbD) methodology and Process Analytical Technology (PAT) tools [10-15]. The major goals of the QbD and PAT initiatives were to push industry to expand and improve their scientific understanding of drug development processes [16-18]. These methodologies, applied for many years in a variety of manufacturing industries including the automotive and specialty chemical, aim at improving product quality and process development. Scientific understanding can be achieved through the development of technologies to perform online measurements of critical material properties, the coordination of processes and equipment, the development and use of process models based on fundamental and experimental knowledge, implementation of process control, and exploration of process design space (i.e., flexibility and feasibility) [19, 20]. With these aims in mind, the pharmaceutical industry has focused on finding new technologies to achieve these goals.

1.1.ADVANCES IN PHARMACEUTICAL MANUFACTURING

Pharmaceutical manufacturing can be divided into two major processes based on their resulting drug commodity: substance or product. Drug substance manufacturing, also known as upstream manufacturing, involves the production of the active pharmaceutical ingredient (API) via chemical synthesis methods. This process is primarily done in liquid systems and the resulting API can be in either liquid or granular (i.e., solid) form [15, 21, 22]. Drug product manufacturing, also known as downstream manufacturing for being performed after the upstream process, takes the API and combines it with other pharmacologically inactive solid materials, known as excipients, to create a dosage form. Drug product manufacturing depends on the drug's delivery method (e.g., tablet, injectable, spray, ointment), but often involves the use of solids (i.e., powders, granular material) handling equipment to create the final product.

Batch processing remains the predominant development route in most of the pharmaceutical industry for both drug substance and product manufacturing. Primarily due to tradition, batch manufacturing has ruled pharmaceutical manufacturing for the past century [23]. Unfortunately, batch manufacturing in pharmaceuticals does not often result in the most efficient manufacturing process given the number of steps and the need to scale up in order to meet demand [24]. Typical pharmaceutical processes are composed of ten or more interacting processing steps, each one affected by several process parameters. This level of interaction makes process development a difficult and daunting task whose solutions are addressed using heuristic methods. Moreover, the constant demand of products for clinical trials, in most cases occurring in parallel with process development, force scientist to study the manufacturing process in an expedited manner [25]. Scale up requires the purchase of larger equipment in order to increase productivity, leading to extended research efforts to maintain performance across equipment and scale. Thus, batch manufacturing processes are often poorly understood, rarely optimized, lack robustness, and are prone to unexpected failure [26-28]. Lastly, risk assessment and failure mode analysis of batch processes is a substantial challenge.

Based on the aforementioned issues with the batch manufacturing paradigm and taking advantage of the QbD and PAT initiatives, the pharmaceutical industry began expanding on a series of technologies. One of the most pronounced technology upgrades is continuous manufacturing of drug products [16, 24, 29-31]. Many of the previously described issues with batch process can be addressed through the implementation of continuous manufacturing processes.

1.2.CONTINUOUS MANUFACTURING OF PHARMACEUTICALS

Continuous drug product manufacturing (CPM) technologies have the potential of addressing issues of process knowledge and robustness by closing the gap between process

development and manufacturing. Since continuous process scale up is done through increases in operation time, throughput, and parallelization of the same continuous train of equipment; process knowledge acquired during development can be directly applied to manufacturing processes [23, 32]. This development strategy minimizes technology transfer to commercial sites, improves risk assessment and failure mode analysis (i.e., equipment is highly studied during development), and reduces the capital cost. Furthermore, continuous manufacturing processes function under “steady state” meaning that product targets are set constant over time by manipulating process variables, raw materials are fed constantly to the process, and products are made and examined as they are produced. In cases when products are detected out of specification by examination methods, they can be diverted from the product stream at any point in the operation and a corrective (i.e., controller) action can be taken to bring product properties to the desired specifications [16, 33]. Therefore, continuous systems with automation and process control result in high quality products.

The advantages are not only limited to the controllability and better process design strategies, they also include the ability to implement processes that were too difficult to be done using batch methods. For example, particle segregation (i.e., a process event that leads to poor quality tablets being manufactured) has been shown to be prominent on batch systems, yet continuous systems have demonstrated the ability to process segregating mixtures without the issues observed in batch [34, 35]. Thus, continuous manufacturing has the potential to decrease the amount of wasted material, improve process performance and robustness, and ensure product quality [36].

The advantages of continuous manufacturing have pushed major pharmaceutical and equipment manufacturing companies to embrace the technology for both legacy and new drug products [37, 38]. As of the writing of this thesis, three major pharmaceutical products have been approved by the FDA to be manufactured using continuous manufacturing [39]. Nonetheless, there

are many challenges with this technology: higher initial cost, extended initial development time, lack of PAT tools available for monitoring continuous processes, and difficulty of implementation for low volume and dosage products [40]. Another notable challenge for continuous manufacturing is dealing with the current state of guidance provided by the regulatory bodies. One example of this issue is the definition of a “batch” of product and raw material traceability, both required by regulatory agencies and pharmaceutical companies alike [31].

1.3. CONTINUOUS MANUFACTURING OF PHARMACEUTICAL SOLID ORAL DOSAGES

Primarily composed of tablets and capsule formulations, solid oral dosages are the most commonly used drug product forms in the market [41, 42]. Multiple routes for drug product manufacturing have been established with the goal of ensuring the production of a quality tablet (or capsule) product. The manufacturing method varies depending on the API compounds and its inherent material properties, yet formulators commonly apply similar routes of manufacturing for solid oral dosages. The four major routes for the production of solid oral dosage forms are: direct compression, dry granulation, wet granulation, and spray drying [43, 44]. The two granulation routes are used in cases where the flow of a particular material in the formulation does not make its processability possible without adjusting some material properties, particularly size. Spray drying is often applied to improve the dissolution properties of the API and control the its material properties along with those of the excipients. All manufacturing routes are currently implemented in batch mode across the pharmaceutical industry, with continuous forms being developed over the last decade [16, 36, 45, 46].

A schematic process flow diagram showing the four major routes of CPM is shown in Figure 1 [40, 47]. The four continuous manufacturing routes begin with the constant feeding of raw

materials into the process by powder feeders. The feeders are typically operated under some form of flow rate control in order to maintain a constant a constant mass ratio of ingredients entering subsequent units. This ratio of ingredients is particularly important for pharmaceutical operations as it dictates the final product's concentration of components. Fed materials may be passed through a delumping unit such as a high shear screen co-mill in order to eliminate large, electrostatic, soft lumps of material that may not lead to good blend uniformity. Co-milled materials are mixed using a continuous blending system wherein materials are mixed in both the axial and radial directions to achieve a uniform composition of ingredients as a function of time. It is important to mention that radial and axial mixing aims at obtaining a homogenous blend of materials and reduce the natural feeder fluctuations by backmixing material over a short period of time; however, the overall concentration of the product is primarily set by the initial feeding ratio. A lubricant, which intends to reduce powder sticking during compression and improve bulk density, may be added at the blending unit operation.

After blending, four different routes of manufacturing can be pursued, all having a diverse set of different unit operations. The simplest of all manufacturing routes is direct compression, wherein the material exiting the blender is directly sent to a tablet press or capsule filling machine to create the final solid product. If the blend flow and/or solubility properties do not allow for good compaction or product properties two granulation routes and a spray drying route may be pursued to improve the powder flow properties by increasing the particle size or the blends porosity. The two granulation methods commonly used include: dry and wet granulation. In dry granulation, blender powder materials are sent to a roller compaction unit, were they are pressed into a higher density ribbon, which is then milled into granules of a desired particle size. Wet granulation is performed in a variety of units, such as twin screw, fluid bed, and high shear granulators. In wet granulation a wetting liquid (i.e., binding agent) composed of typically water and high density

polymer is used to create larger particles via agglomeration. The granulation liquid is then removed at a drying step, which may reduce the granule size to a desired distribution. Optionally, a screen mill can be used to ensure a desired particle size distribution. Lastly, if solubility of the blended material needs to be improved, the ingredients may be homogenized and spray dried using a heated air drying system. The porous and now amorphous form of the API can have improved solubility when compared to the previous form of the material.

The resulting granules obtained from either granulation step or from spray drying are then sent to a tablet press or capsule filling machine to produce tablets or capsules. Tablets made from any of the four processes can be then sent to coater to yield a final coated product.

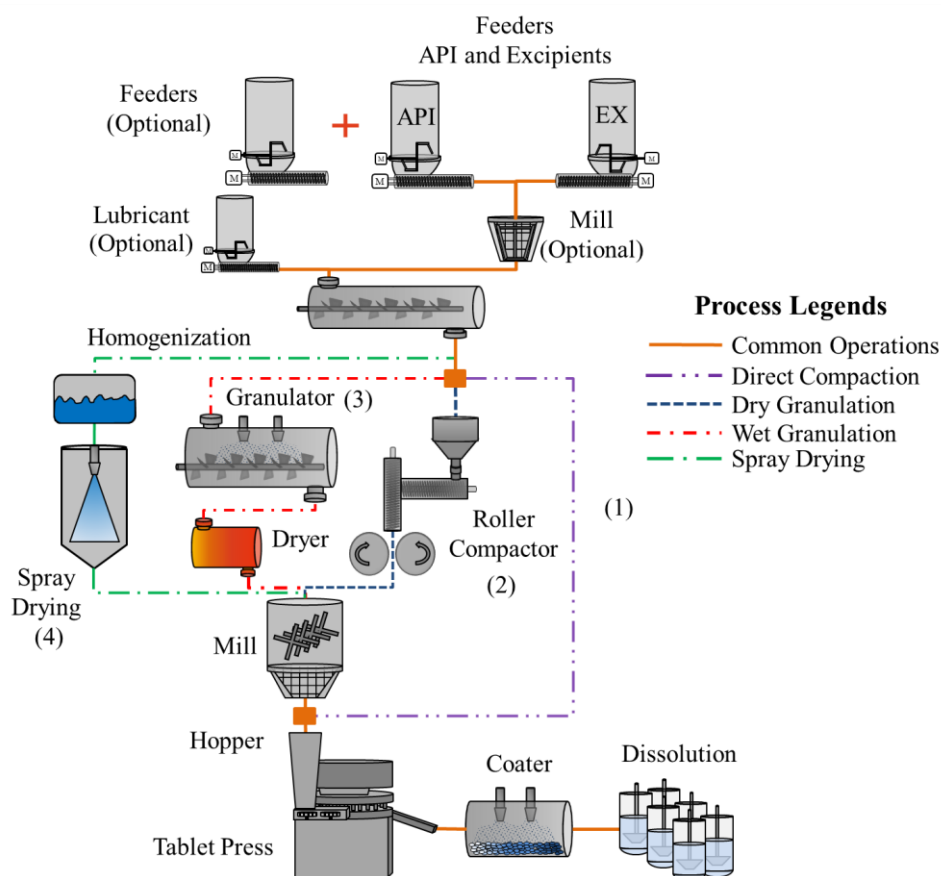


Figure 1. The four major continuous solid dosage form manufacturing routes. (1) Direct compression, (2) dry granulation, (3) wet granulation, and (4) spray drying.

Depending on the implementation of the process, CPM processes for oral solids are assessed based on the quality of the blends and/or tablets produced. Blends are characterized by their uniformity; monitored via spectroscopic and wet chemistry methods. Important tablet quality properties include tablet strength (e.g., hardness, friability), API composition, assay, tablet weight, and composition uniformity (i.e., variability measured as relative standard deviation) and dissolution time.

1.4. INNOVATION: PROCESS SYSTEMS ENGINEERING (PSE)

Given the pharmaceutical industry's continuing modernization and its shifts towards new continuous manufacturing practices, process elements that affect drug substance quality and the techniques used to understand these processes need to be reevaluated. To enable better and seamless process understanding while moving from traditional batch to continuous manufacturing technologies, we must look at previous chemical industries and work towards building the necessary expertise and skills to design and effectively operate continuous manufacturing technology [31, 32, 48]. In designing continuous flow systems, while the analysis and optimization of individual process equipment remain important, the primary objective is to identify and evaluate design elements that pose a potential risk to product quality for the fully integrated system. It is also important to consider the multivariate nature of such systems in process design [49]. Within this context, process systems engineering (PSE) tools have been implemented with the goal of facilitating effective and efficient process design.

PSE is a knowledge-based approach which uses mathematical equations to accurately represent the system's chemistry and physics in order to evaluate complex systems using simulation tools [50]. PSE's special focus involves the application of models along with computer-algorithms to predict, design, analyze, control, optimize, and operate these complex processes. Within this

rigorous (i.e., mathematical) framework, PSE's goal is to provide insight to process development by evaluating integrated manufacturing systems *in silico*.

Rigorous process design and evaluation can greatly improve manufacturing development and optimization of both drug substances and products given the vast amounts of research available from the PSE perspective. Approximate (i.e., heuristic) methods can be supported by having this information at hand, and furthermore can be used to inform future process design strategies for other products. For instance, information developed during the early stages of preclinical and clinical trials (e.g., molecular weight of compounds involved in the process, solubility data, degradation profiles, synthetic routes, boiling and melting points, reaction enthalpies, by-product formation, mixing behavior, powder compressibility) can be used to inform and develop new models, some of which could be used to improve future process development.

Several research teams in both industrial and academic institutions have used PSE methods to evaluate [47, 51-56], design [50, 57, 58], analyze [59-62], control [32, 63-68], and optimize [69-73] pharmaceutical processes. Predictive process models were used to develop and assess control strategies for continuous processes, as well as set the stage for the implementation of control systems in pharmaceutical processes [57, 68, 74-77]. These advanced control strategies can help to ensure consistent product quality. Furthermore, process integration (i.e., the union of multiple processes into a single process flow) and scale up can be performed once several unit operations have been characterized mathematically using models. For integration, the work would simply require carrying over information from one unit to the next, to inform subsequent models about process stream properties. Several units can be adjoined or scheduled one after the next and the process can be simulated and evaluated. Once all the unit interactions are understood, then few experiments with the integrated system can be performed to validate the modeling results. The goal of PSE and the integrated process flow models is not to completely remove experimentation, but

to provide researchers with a smaller set of critical variables that must be evaluated in the process, thus removing the need of running large numbers of experiments. The integrated process simulation can also be very beneficial to evaluate mitigation strategies, process sensor needs, and control algorithms.

Models fit well into the pharmaceutical manufacturing process paradigm by providing a mean to evaluate a process before many process experiments are performed. For example, process companies can start using preliminary and drug discovery data (e.g., solubility, flowability, dissolution) to start building processes, even before their investigative new drug (IND) applications are submitted. This provides a large economic risk reduction for companies, who can test potential process manufacturing routes before incurring in costly process experiments. First pass process design studies can be performed using simulations, small amounts of characterized materials, and libraries of general process models that predict the behavior of the material in the unit. Selecting the equipment and processing conditions from *in silico* experiments based on scientific models can expedite and improve the design of process even before any capital investment is performed. These first pass studies can be used to then speed up the development of a preliminary process, which can then satisfy clinical demand.

Using data acquired from the preliminary process the general model libraries can be further tuned for the process/drug being developed and more rigorous design can be performed. Using the more fine-tuned model, process developers can perform a set of *in silico* experiments that allow them to test scale up scenarios, find process optimums, evaluate process monitoring strategies and develop control architectures for the design. The process model results can then be implemented in a real world plant, which can then be evaluated with respect to the predicted values by the process model. Model information can be used to supplement and help explain the reasoning behind the

current process design and provide great insight behind the process design strategy during the application process.

Figure 2 shows how models fit in the development of a process. In the figure, the light green steps represent locations where the model is informing process development. Step 3, for example, involves the application of a the general process models to determine a first pass process that can be used to satisfy the demand of clinical trials. Steps 5 shows an instance when the models are used to further improve the preliminary process by testing different types of processes, assist with scale up, and help find process optimums. Step 6 shows where models can help select the monitoring strategy for the process and allow for the design of control methods for the process. Ultimately, the model can then be used to provide the supporting information to drug manufacturing applications and can further be used to control manufacturing processes.

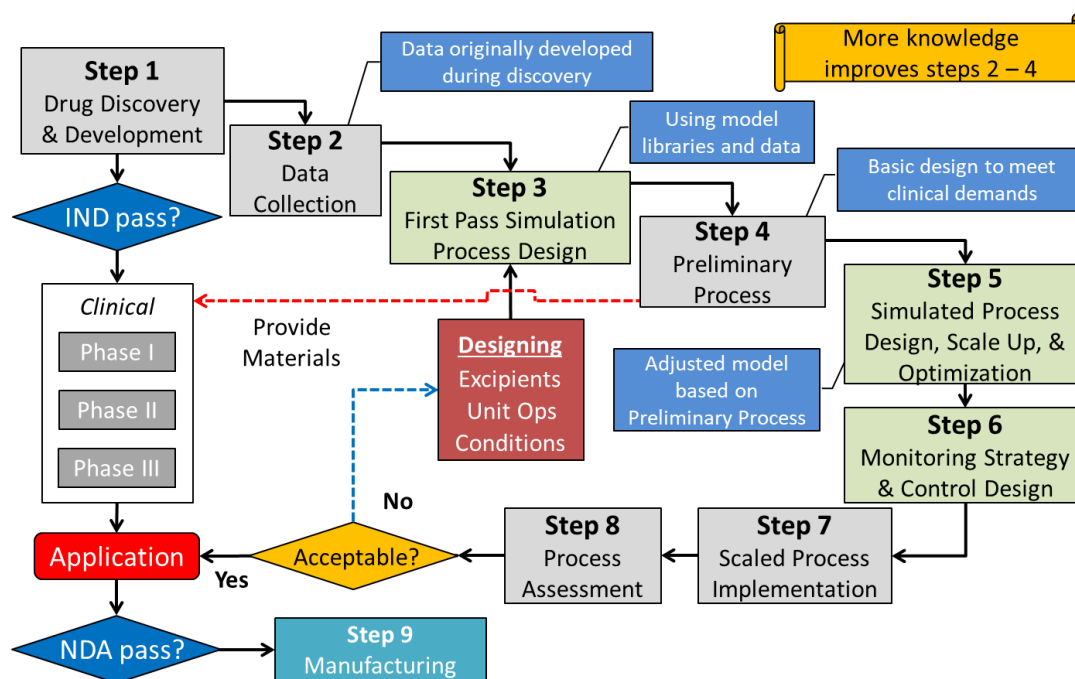


Figure 2. Pharmaceutical manufacturing workflow integrating the use of process models. Processes in green are those that can be developed with the use of models. Adapted from [58]

Repeating this process and developing better models would improve the time of simulation based process design and improves the whole simulation-based development cycle. Regulatory agencies can also greatly benefit from these models as they provide exceptional insight on process development strategies being performed in the industry. Models can serve as tools to compare how different companies are developing processes and what assumptions they are taking (seen from the model assumptions). The process model can also benefit the review process, as it provides a clear algorithmic procedure for process design. From the process models provided by a company, regulatory agencies can further improve the evaluation methods by performing more in silico experiments to test some of the questions that may arise from information request. Process safety evaluation could also be performed to ensure process safety and robustness using the models, which can be evaluated at the regulatory agency or at the company.

Overall, PSE tools and predictive models can facilitate the design of processes where consistent product quality is achieved at every step of manufacturing within the framework of QbD and PAT [58]. Table 1 summarizes the relationship between PSE tools and process development objectives.

Table 1. Process Systems Engineering (PSE) tools for process development and evaluation in continuous manufacturing of drug substance and products. Adapted from [78]

Process Systems Engineering (PSE) Tools	Process Development Objectives
Predictive Models (Mathematical Equations)	Process Understanding and Input-Output Relations (IOR) Building
Flexibility & Feasibility Analysis	Determine Process Parameter Ranges and Control Ranges
Steady State Optimization	Process and Product Design
Dynamic Optimization	Process Improvement and Disturbance Evaluation
Sensitivity Analysis	Risk Assessment and IOR Evaluation
Controller Design	Attainment and Maintenance of Critical Quality Attributes (CQAs)
Flowsheet Modeling	Process Integration and Simulation

1.5. BACKGROUND ON MODELS

One of the major advantages of process modeling includes the ability to store and make available large amounts of process knowledge – accumulated over time and experimentation – in

mathematical equations. The information stored in these equations can be used to by process designers and operations solve several process design and optimization questions. Furthermore, these models can greatly improve future experimental designs, since they can provide insight on which process input-output relationships are important to evaluate. For this reason, PSE and modeling tools are extensively used in the fine chemistry and petrochemical industry to design new process, evaluate current designs, and improve (i.e., optimize) the performance of existing processes. Figure 3 shows a flow diagram of the model-centric approach of PSE. Data acquired from experiments can be analyzed and used to develop or calibrate a model for a specific system. Once a set of models are available, they can be used in an integrated manner to represent the complex system being studied. Insight on the models accuracy can be obtained by performing a verification and validation of the model results. Positive model verification and validation results lead to its use in process evaluation and assessment. Negative verification and validation results lead to revisiting the models original development or need to acquire additional experimental results.

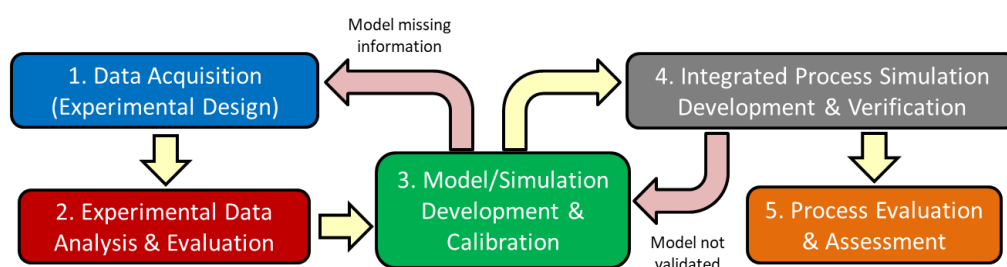


Figure 3. Simplified schematic of process system engineering's (PSE's) model centric approach to evaluate complex systems.

As shown in Figure 3, modeling efforts consist of a set of steps or activities that are not linear in nature. Moving beyond the simplified schematic in Figure 3, modeling efforts are divided into six major activities: (1) determine system characteristics, (2) collect data, (3) analyze data, (4) construct or identify a model, (5) solve or analyze the model, and (6) verify and validate the model.

System characteristic determination is based primarily on empirical knowledge of the system, wherein the relevant input-output relations are considered as important for system performance. Noteworthy is the idea that during this assessment, important system characteristics may not be captured, leading researchers to revisit this instance even after the model has been validated. Data collection and analysis, often performed under the Design of Experiment (DoE) structure, aims at quantitatively measuring the relationships existing between those input-output relationships. Several methods are proposed for performing DoEs and have been extensively reviewed since its inception in the early 20th century [79, 80].

Constructing or identifying the mathematical equations is a fundamental step for process modeling since these models inform the results between process inputs and their output later used for in other PSE tools. These predictive equations (i.e., models) have different forms, which vary on the level of complexity and their incorporation of input and output (i.e., state) variables. For any given process, models can be proposed as set of linear or non-linear equations, written in dimensionless or multidimensional forms encompassing steady state (i.e., time independent) or dynamic (i.e., time dependent) scenarios. Five different models, shown with their relationship in Figure 4, are commonly associated with PSE tools: (1) balance equations, (2) constraint equations, (3) constitutive equations, (4) product models, and (5) product application models. Balance equations ensure that both the physical principles of conservation of mass and energy and conservation of momentum are obeyed throughout the process. Constraint equations, just as their name implies, ensure certain parameters are maintained within certain logical bounds, especially those in balance equations. A frequent example of a constraint equation is the fractional composition of materials in a process stream, which ensures the fractional sum of all the components in the stream is equal one. Constitutive equations involve those sets of equations that describe the chemical and reactive state of the system. Particularly focused on material properties,

constitutive equations need to be evaluated constantly to ensure accurate calculation of both the balance and constrain equations. Product models incorporate the information of product attributes to inform about the product's material properties (e.g., salt solubility, flowability, cohesion). Lastly, product application models are those which aim at predicting product behavior under certain circumstances, like the product dissolution in a specific medium and degradation at given temperature and pressure conditions. Solving these sets of equations requires understanding of several mathematical structures, which depend on the type and number of equations presented in the model. Further review of mathematical methods used to solve various model structures are provided in reviews by Gernaey's [50, 57] and Ierapetritou's [40, 47] groups.

Model verification and validation refer to the modeling steps where model solving methods and accuracy are evaluated, respectively. Within this context, it is important to mention model validation involves the practice of ensuring system models accurately represent previously collected data as well as some new or isolated data sets, not used during model construction and analysis [81-84].

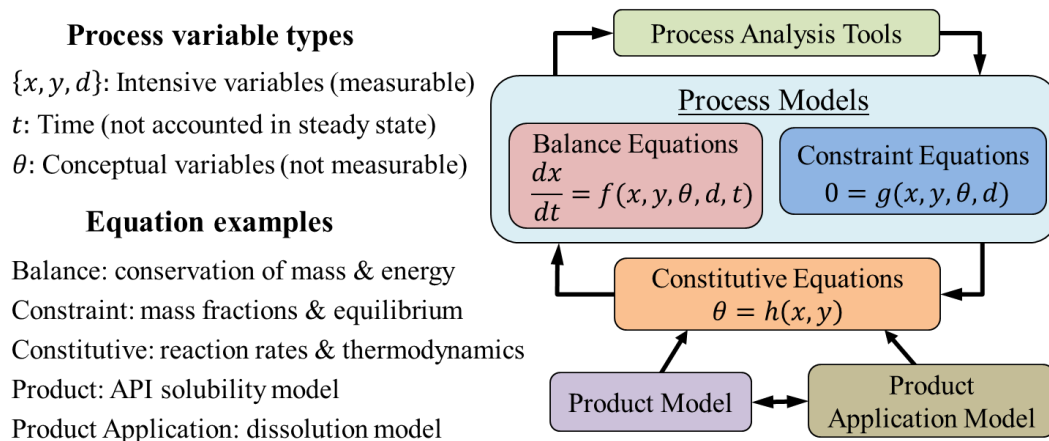


Figure 4. Different types of models used within the process modeling structure. Adapted from [50]

All of these previously described modeling activities must be performed iteratively and constantly, since models require constant revision to ensure their performance still meets the

standards set by users and developers. In some instances, some of these efforts must also be performed in conjunction with experimental efforts to ensure that model development accurately evaluates and accounts for critical process inputs and outputs. Furthermore, model developers need to perform several back and forth instances between model design, validation, and data collection, to properly develop and validate a model. Based on this extensive number of steps and constant need for revision and monitoring, it is clear that modeling as a whole is a labor and time intensive process, yet its benefits in terms of data storing and development outweigh this initial labor cost. Several industries have applied this methodology and encourage it as a mean to improve the value of their labor (i.e., experimental) efforts.

1.6.TYPES OF MODELS

In this section, the major models used in pharmaceutical process modeling are briefly described. Readers interested in learning the different model types in more detail are encouraged to read the reviews by Rogers et al. [40], Escotet-Espinoza et al. [47], and Gernaey et al. [50, 58]. There are four types of models commonly used in the pharmaceutical industry: first principle “mechanistic”, multi-dimensional mechanistic, phenomenological, and empirical or data-driven models.

1.6.1. First principle mechanistic

These models are derived from fundamental equations of motion. Using fundamental physics, these models provide a great detail of the system phenomena by describing material properties in space such as location, momentum, and velocity. Divided into discrete and continuum models, first principles models can be used with solids, liquids, and gas system [16]. First principle models used in the pharmaceutical modeling literature include discrete element models (DEM) [85] and finite element models (FEM) [86]. DEM has been extensively used given its capability for

describing the translation and rotational effects of discrete particles in space. Particles are discretized and equations of motion are written for each individual particle in the system [87]. This degree of discretization generates a large number of equations, which limits and in some cases prohibits the use of DEM to model large number of particle systems with current computing power [88]. Nonetheless, particle and particle-fluid flow has been characterized and studied in great level of detail using DEM for a variety of industries. Confined particle flow is amongst some of the phenomena studied using DEM, which applies to the pharmaceutical industry through operations such as hopper emptying, continuous mixing, powder feeding, conveying, and fluidization [85].

1.6.2. Multi-dimensional mechanistic

Population balance models (PBMs) describe the generation or development of properties in groups (i.e., populations) of entities (i.e., variables) over a set period of time. In the pharmaceutical industry, PBMs are multidimensional models used for the characterization of particle states with respect to internal (e.g., porosity, moisture content) and external (e.g., position) coordinates [89, 90]. Often used in processes where particle size changes occur (e.g., granulation, milling and drying), these models have also been used in a variety of other solid-based processes such as mixing and dissolution [91, 92]. PBMs offer a lower dimensionality model compared to mechanistic models by lumping discrete systems into groups and tracking their average state. Population balance models can also be discretized with respect to the external coordinates in order to resemble the level of discretization achieved with DEM modeling [93]. In these cases the differential terms with respect to the external coordinates are replaced by finite differences. Discretized population balance models can be parameterized and their parameters estimated using experimental or simulated data. PBMs can become computationally expensive if the number internal coordinates increases and the discretization grid of external coordinates is too fine [94]

1.6.3. Phenomenological or semi-empirical

Also known as engineering models because of their frequent application in the field, they are derived from first principle models within which an underlying set of assumptions reduces their complexity. Experimentally obtained parameters are introduced as a means to calibrate the model for a specific combination of material and equipment conditions [95]. These lower dimensionality models involve macroscopic mass, force, and energy balances that provide information about the system's average behavior while maintaining a relationship between model variables and process conditions. They have been used in a variety of pharmaceutical manufacturing problems in order to simplify model complexity [96-102]. Lower dimensionality PBMs also lie within this model category and have been used to characterize the probability density function of a single particle property inside of a unit. One example of low dimensional PBMs is the *residence time distribution* (RTD). Briefly described, RTD is a diagnostic tool that characterizes the time particles spend inside of a unit operation using a tracer material [103, 104]. This type of model has been extensively used in the chemical engineering literature to determine the mixing behavior inside units, and given its important use to characterize continuous equipment will be further investigated in Chapter VI in this work.

1.6.4. Empirical or data-driven

Empirical models, commonly referred to as statistical models, are among the lowest dimensional models and are derived purely by the relationship between inputs and outputs, without much physical explanation behind the correlation. The aim of empirical models is to provide a representation of data collected experimentally or from mechanistic models in a lower dimensional space using input-output correlations [105]. These models include statistical techniques such as black-box modeling approaches, latent variable methods, multilinear regression, response surface modeling, principal component regression, among many others [106-108].

As opposed to any other model type previously described, empirical models are highly

dependent on the data provided for their development. Unlike the aforementioned models, extrapolation using empirical models often leads to erroneous results, since the relationship between the input parameters and the output responses is not defined outside of the data bounds. Nevertheless, since these types of models provide an inexpensive computational relationship they are often preferred for control system design and development [49].

1.6.5. Flowsheet models

In an integrated process, individual pieces of equipment (i.e., unit operations) are connected in series. In such a process, a train of multiple units, one after the next, is connected via piping to sequentially perform powder-to-tablet manufacturing without isolation of intermediates. The output of a preceding unit becomes the input of a subsequent one with material continuously flowing between them. Mathematically, process integration follows the same logic. Individual equipment models, presented previously, are combined by taking the results from a preceding model and using it as the inputs of a subsequent one. The integrated process models are labeled *flowsheet models* as the flow of information between the unit models, resembles the flow of material(s) between unit operations. Therefore, flowsheet models defined as equation-based representations of the series of interconnected unit operations that describe a complete manufacturing process. These types of models have long been used in fluid-based chemical processes for process simulation, design, control and optimization applications [109-111].

Several flowsheet modeling software packages (e.g., ASPEN Plus®, ChemCAD®, gPROMS™) have been effectively demonstrated for predictive modeling and design of fluid-based processes and are already widely used across the chemical and petrochemical industries [112]. However, the development of comparable tools for solids handling processes is challenging due to a lack of available first principles and constitutive models to describe many solids-based processes [30, 113, 114]. Current flowsheet simulation software packages are not capable of modeling first

principle models effectively and require long times to evaluate multidimensional models. If flowsheet models are to be used for optimization, control, and case-scenario evaluation; less complex models need to be developed and implemented for unit operations.

Flowsheet models have long been used in fluid-based chemical processes for process simulation, design, control and optimization applications [109-111]. The recent development of the modeling tools previously presented for solids handling units coupled with the commercial availability of platforms for modeling and simulation of solids-based processes have facilitated the development of flowsheet models in the pharmaceutical industry [113-115]. These models can be implemented in commercially available development environments including gPROMS™ ModelBuilder and Aspen Custom Modeler.

1.7. MODELING CHALLENGES

This work focuses on some of the challenges that continuous pharmaceutical manufacturing modeling faces. More specifically, the development of computationally efficient unit operation models that account for the effect of material properties. These challenges are explained briefly in this section in order to illustrate clearly the research objectives of this work.

1.7.1. Computationally Expensive Unit Operations Models

In spite of the potential benefits of PSE tools in the development of pharmaceutical manufacturing processes, they are severely underutilized [58, 116]. Only recently there have been major efforts to apply methodologies of such as feasibility & flexibility analysis, flowsheet modeling, steady state & dynamic optimization, and sensitivity analysis. These major efforts have been championed after the development and application of models that are computationally feasible and have the ability to model particle systems accurately. First principle models, such as DEM and multidimensional PBM, have been the major focus for development and were extensively used for

design and study of individual unit operations [94, 117-121]. Although they provide a great deal of physical insight into the process and accurately capture dynamical interactions among individual particles, these methods may not be practical or efficient when incorporated with PSE tools.

The most significant drawback of DEM and higher order PBM models involves their high computational cost, which make them difficult to use for applications where multiple or rapid model evaluations are needed. DEM's solution times range from hours to days depending on the number of particles, with computational cost increasing significantly as the number of particles increases. For this reason, DEM simulations often model systems much lower number of particles than in reality, which leads to large approximation of particle flow patterns and interaction. Similarly, PBMs can be difficult and lengthy to solve as the dimensionality of the problem increases. Efforts to reduce the computational expense of PBMs have focused in the implementation of order-reduction techniques [122] and hierarchal solution methods [123, 124]. However, PBM models often require information about distributed parameters like particle velocities within the process geometry, which brings back the need to run DEM simulations to obtain these results [125, 126].

1.7.2. Modeling Material Property Effects

DEM also lacks a clear framework to account for material properties in simulations. Material property parameters that cannot be directly measured for many pharmaceutical compounds, such as friction coefficients and coefficients of restitution for interparticle and particle-geometry interactions, are required as part of the simulation. The parameters need to therefore be estimated using indirect methods [88]. DEM models were characterized using reduced order models (ROMs) to mimic the results from the first principle model. When the ROM is provided with sufficient results, this approach reduces the need to perform DEM simulations for scenarios within the evaluated space. Yet if equipment geometries change and/or there are deviations in the

material properties these ROM are no longer valid and new DEM simulations need to be performed. Insufficient understanding of the interactions between raw material properties, process design factors and operating conditions and their effect on performance presents a challenge in process development and design space determination [116]. These effects are often interactive in nature, so simply visualizing process input and output data may not elucidate the most important process parameters. In order to identify critical process parameters, which may limit the feasible region of operation for the process, it is necessary to quantify the extent to which the various process inputs affect unit operation performance and product quality attributes [13].

1.7.3. Evaluation of Models & Their Inputs

Technical limitations regarding the evaluation and modeling of pharmaceutical systems revolve around the idea that many unidentified variables are affecting output results. Often viewed as inherent process variability these sources of error, mostly associated with material properties and human error, make models less accurate and inefficient. Physical and chemical properties of materials have the potential to influence product quality attributes such as blend and content uniformity, dissolution performance (affecting *in vivo* results), stability, and weight variability [127]. Specifications on physical properties are typically limited to bulk powder properties, which are more straightforward to test, and include bulk and packed density (i.e., compression behavior), particle size distribution, cohesion, and flowability factors [128]. The relationship between bulk properties and product quality is not often well understood, but their ranges corresponding to acceptable product quality can be determined experimentally [30, 116, 127].

1.7.4. Verification & Application of Models

Obstacles in implementation of continuous manufacturing involve the understanding of how unit operations behave holistically. The interconnected effects of units are critical to characterize in order to develop processes that are controllable, effective, and robust. Lower

dimensional models developed to address the challenges of high computational expense can be used to capture these interactions *in silico* through the use of mathematical tools developed in PSE. Sensitivity analysis can be used to quantitatively evaluate the importance of process variables with respect to process performance. Sensitivity metrics can be used to direct experimental efforts towards studies that will improve the estimation of the most important model parameters or will enhance process understanding with respect to key input variables [129, 130]. Lack of sensitivity to certain factors can also be informative. It may either justify reducing the uncertain input space (e.g. by holding these parameters constant in subsequent studies) or suggest additional parameter variations to capture the influence of these factors [130-132].

CHAPTER II

2. RESEARCH OBJECTIVES

2.1. OVERALL RESEARCH AIM

The overall objective of this work is motivated by the challenges provided in the previous chapter, namely the need to develop models that are computationally efficient, incorporate raw material properties, and are applicable to a wide of process conditions. Thus, the main objective of this thesis is to *develop, analyze, and verify predictive phenomenological and residence time distribution (RTD) models that take into account granular material properties for unit operations in a pharmaceutical continuous direct compression (CDC) system*. This objective is attained by completing a set of specific research aims presented in the following subsections.

2.2. SPECIFIC RESEARCH AIMS

2.2.1. Aim 1

Establish a systematic approach to evaluate and integrate material property measurements in a newly or previously developed process model.

Models are an essential component of the new methodology for process design in the pharmaceutical industry. Several efforts target developing higher dimensional, dynamic, complex models for process understanding. Yet, these models are inefficient for process simulation given

their complexity. Other efforts focus on developing steady state data driven models. These models often have little to no relationship to dynamic process inputs (i.e., unit conditions) and require very large datasets to be accurate. The efficient use of dynamic process models for continuous systems requires the development of low dimensional models that are able to dynamically capture process inputs (i.e., critical process parameters and material properties) and relate them to process variables and outputs (i.e., unit conditions and product quality attributes). However, a systematic methodology is often not well provided or summarized in the literature. Further, the use of material properties as predictors is scarce in the literature, given the amount of variability provided in some of the powder measurements

In this aim, the goal was to provide a framework that can be used to develop able to capture both process input conditions and material properties. This approach, was then evaluated and verified with a case study using a powder unit operation. This aim is evaluated over the course of Chapters III and IV in this work.

2.2.2. Aim 2

Evaluate the use of material property libraries for modeling and use them to identify surrogate materials using statistical techniques.

Material properties are known to affect process performance in pharmaceutical operations, yet approaches to establishing the relationship between material properties and process performance are lacking. In this aim, the goal is to establish a relatively small material property library spanning a wide range of material properties and use the information developed in the library for modeling purposes. This aim is provided after the first aim to guide the conversation about the implementation of material properties in phenomenological models. The intent was to first attain the goal of aim 1 before proceeding to developing the material property library in this aim. This aim is covered in Chapter V in this work.

2.2.3. Aim 3

Provide a systematic approach for developing residence time distribution (RTD) models in powder units and determine the impact material properties have on the measurement of the RTD.

Similarly to the development of phenomenological models explaining the relationship between inputs and outputs as a function of material properties, an interest has emerged with regards to the development of residence time distribution (RTD) models in pharmaceutical unit operations. This aim focuses on providing a set of standards for performing RTD experiments as well as evaluate the impact material properties have on the measurement of the RTD. The overall goal of this aim was to provide a framework that future process developers could use to ensure the RTD methods, developed for liquid and gas systems, were upheld for solid systems. This aim is covered in Chapter VI in this work.

2.2.4. Aim 4

Develop a phenomenological and residence time distribution models for twin screw powder feeders accounting for material properties.

Lastly, the goals of aims 1, 2, and 3 are combined into the last aim of this work, wherein a phenomenological and a RTD model are proposed for a unit operation in the continuous direct compression system: a twin screw powder feeder. The experimental characterization, model development, model implementation, and model evaluation are performed in the last aim as an overall application of the methods and techniques proposed in the previous aims. This aim is covered in Chapter VII in this work.

CHAPTER III

3. AIM 1: APPROACH FOR DEVELOPING MODELS ACCOUNTING FOR MATERIAL PROPERTIES

Acknowledgement of publication status:

Full sections of this chapter were published in a scientific article written by the author of this thesis under the title: Modeling the effects of material properties on tablet compaction: a building block for controlling both batch and continuous pharmaceutical manufacturing processes. The article was accepted on March 17th, 2018 in the Journal of Pharmaceutical Innovation. This work was done in collaboration with:

Shishir Vadodaria¹, Ravendra Singh¹, Fernando J. Muzzio¹, Marianthi Ierapetritou¹

¹ Engineering Research Center for Structured Organic Particulate Systems (C-SOPS), Department of Chemical and Biochemical Engineering, Rutgers, The State University of New Jersey, Piscataway, NJ 08854, USA.

Further, sections of this chapter are intended for publication for a journal in conjunction with several sections from Chapter VII of this work.

3.1. INTRODUCTION

The aim of this chapter is to establish a methodology for equipment characterization whose objective is using experimental results to develop models that can be used to predict the unit operation's behavior. This objective can be accomplished by designing experimental evaluations aimed at determining the effect of process and material inputs on the process outputs (i.e.,

responses). These experimental evaluations must be performed as a series of experiments where the effect of process inputs (e.g., screw speed, turret rotational speed, compression force) on process responses is evaluated for single material. After determining the impact of process inputs on the system, then a second level of experimentation varying material inputs must be performed to understand their effect on the output. For example, the initial goal for feeding experiments is to establish the effect of screw speed (i.e., a process input) on flow rate (i.e., a process output). This process input-output experiment can be performed for a set of materials to evaluate the effect of material inputs on the process. If different materials have different process outputs (i.e., responses) at constant process inputs, then the process is found to be dependent of material inputs. In this chapter, a methodology to perform these experiments is presented.

3.2. GENERAL MODEL DEVELOPMENT FRAMEWORK

The general strategy to analyze complex systems from a model development standpoint consists of a series of steps that require both observation and mathematical analysis [84, 103, 133]. First, a problem formulation needs to take place to understand the model objectives and evaluation criteria. Delineating the performance requirements, both computationally and practically, represents a major component in model development. Second, inspection and classification of the system being studied is necessary in order to decompose it into several subsystems, whose interactions and fundamental relationships to process outputs can be determined. Third, interactions between the subsystems need to be formulated as inputs or variables to a set of mathematical equations (i.e., models). In this step it is critical to understand the need of experimental observation in order to find the relationships between variables. Finding relationships between variables in most cases require the incorporation of coefficients, primarily if the model is data driven. Fourth, evaluation and verification of the model as it represents the real process is then needed in order to assert the model fulfill the requirements set out in the first step. Lastly, once the model is developed

it can be applied in accordance with the modeling goals. Continuous evaluation and verification with experimental data throughout its application ensures that the model will remain valid and relevant. This last step in some ways closes the loop for the process, as it requires the model development process to review the objectives and evaluation criteria set out in the first objective [134].

Given the importance of defining the problem, this work focused on defining the different methods for developing knowledge for a unit operation. The equipment evaluation methodology approach used greatly impacts the abovementioned modeling framework by providing more (or less) information than that needed for the process.

3.3. EQUIPMENT EVALUATION STRATEGIES

In previous years, pharmaceutical unit operations research has focused on performing equipment characterization using a formulation based approach. This approach consisted of studying unit operation performance for a specific ingredient (e.g., excipient, lubricant, or API), formulation, or around a desired process condition (e.g., throughput, scale). Although efficient for the early stages of continuous manufacturing, this approach does not provide sufficient information to process developers on instances where the process condition is changed and/or material properties change during the process from the original material used for characterization. These two situations, although uncommon in batch processes (e.g., throughput is set by scale or material properties are not varied during the process) is very frequently occurrent in continuous processes. Therefore, to address these issues a more structured and rigorous approach for equipment characterization based on the input or control variables that accounts for ingredient material properties must be implemented.

For the purpose of this work it is important to make a clear distinction between characterization and performance evaluation. Equipment characterization is, as defined here, the process by which we aim at understanding the unit's fundamental behavior, or in other words how a unit operation behaves for a *wide range* of conditions. This process is tedious and aims at developing a clear understanding of the unit. Performance evaluation is, as defined here, a mean of understanding how the unit performs under a *specific* set of conditions or inputs. This process is shorter but provides a much narrower amount of information. Below we aim at explaining in further detail the differences between these evaluation methods.

3.3.1. Equipment characterization

The process of equipment characterization begins by decomposing the unit based on the individual inputs and outputs affecting process responses. This process requires for the unit inputs to be associated with a particular output and may include not only the equipment process variables, but also the dimensions and sensing equipment used to operate the system. For the case of a screw feeding unit, this process involves the deep understanding of how granular materials move in the hopper with the help of a bridge breaking system as well as the affect such movement has on screw filling and the feed factor. To achieve significant understanding it is critical to evaluate: (1) the hopper dimensions and shape, (2) the flow aid configuration, (3) the sensitivity and accuracy of the load cell where the hopper is placed over, (4) the location of the screws at the bottom of the hopper, and (5) the volumetric displacement and capacity of such screws (i.e., the size and shape of the screws and the motor used to turn such screws). All of these variables help understand how well the material flows out of the system, its feeding capacity, and the accuracy at which this material flow can be measured. In certain instances, equipment dimensions may be relegated to subsequent studies, given that a single unit is studied during initial characterization instances. It is important to

note that the characterization process is not linear in nature, and may require several iterations for different unit operations and equipment vendors.

3.3.2. Performance evaluation

Performance evaluation involves the determination of how unit operations behave under a particular set of experimental conditions. This type of evaluation, focuses on understanding the performance of the equipment given a target range of output variables (e.g., flow rate, tablet weight, tablet hardness). For cases relevant to the pharmaceutical industry, performance evaluation needs to be done at conditions that are similar to the process. For the case of feeder performance, for example, this means that performance evaluations need to be performed on feeders working under gravimetric control with some type of refill. The goal of such experimentation would be to determine flow rate deviations from the desired set point as well as understand its variability over time. If the feeding rate variability for each material is evaluated well, then a blending system can be tailored specifically to add the sufficient back-mixing to the incoming blend to filter out the variability to an almost constant mean value. However, as noted previously, the result would not be to establish a wide range of operation, but rather a narrow observation about the unit's behavior for a particular scenario.

3.4. MODELING APPROACH

Information collected during equipment characterization may be used to develop models relating the inputs and outputs so that predictions can be made from the developed data. Several model types have been described in the literature to develop these input-output correlations. The goal of the correlations is to develop a model that predicts how different process inputs have on process outputs by means of a model. These input-output correlations are hereunto known as the unit operation *process model*. The effect of materials inputs may be introduced to the process model

as a set of categorical inputs or by means of a *material model* capable of relating the effect of material properties to the unit behavior. In conjunction with process models, material models can be used to predict the process outputs (i.e., responses) from the process and material inputs. Material property models can be further used to determine the material property effects and establish a range of control for the materials that can be used for this unit.

Figure 5 shows a schematic of the relationship between the equipment, process inputs, process outputs, material inputs, and process and material models.

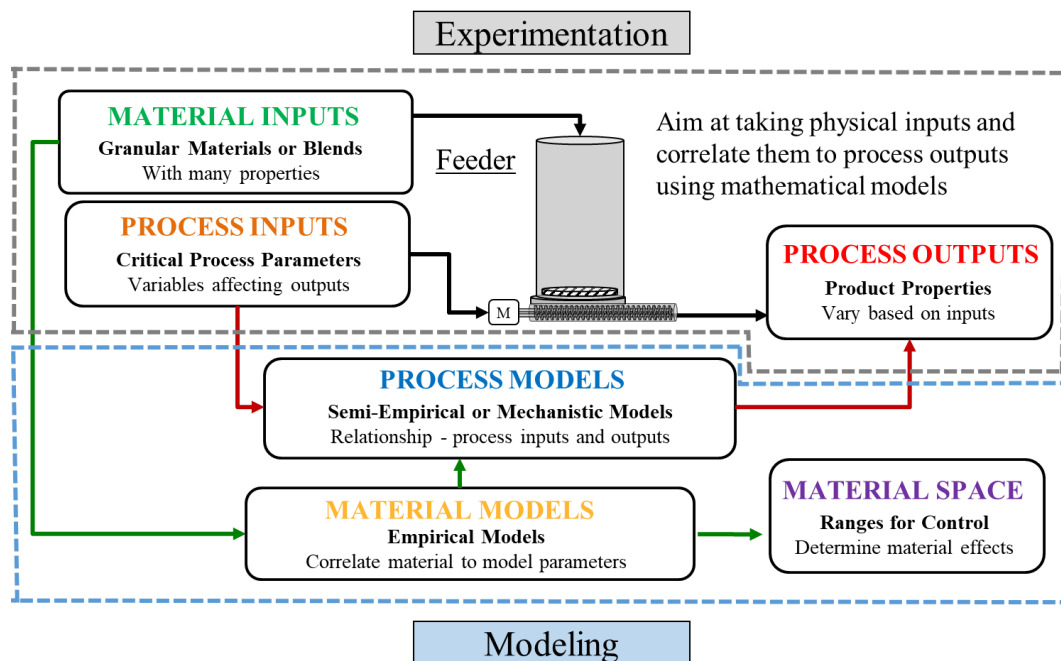


Figure 5. Description of the relationship between process and material inputs on outputs and the implementation of models

As shown in Figure 5, the goal of models is to be able to predict the behavior of the unit and bypass (to an extent) the amount of experimentation needed. Notably, modeling provides a mean to evaluate the operational space for both materials and process inputs. These models may be used to design processes with a desired set of process outputs, effectively accomplishing the goals set out by QbD, wherein the process is designed with the quality of the product in mind.

3.5. MODEL LEVELS

From the distinction between process and material models provided in Figure 5, three different levels of models emerge, each related to the amount of information needed to predict process outputs. In the following points, the different models and their interpretation are described in detail. The nomenclature introduced here is then used on this work to show how the methodology is implemented for the characterization and modeling of tableting and powder feeding equipment.

1. Level 1 models: predict process outputs for set of process inputs (e.g., screw speed, sweeping volume, die fill depth, compression height). These types of models are often developed during the first stages of equipment characterization and focus solely on relating the effect of a single material in a unit operation. Thus, these models assume that all materials behave similarly to one another for a given set of process inputs. Given that this is rarely the case, these types of models are considered to have the least understanding of the unit operation and process.
2. Level 2 models: account for the effect of different materials on the process model. Materials effects to the process model are typically introduced through model parameter calibration, wherein process outputs collected for a particular set of material inputs are used to regress a set of coefficients that would represent the effect of the material in the system. This type of parameter calibration in level 2 models remains categorical, meaning that each material is attributed a set of regressed parameters that would be introduced into the process model. The categorical nature of these models implies the material inputs are consistent from the property perspective, meaning these types of models assume that a material will not change its behavior in the system when the process inputs remain constant. This level of modeling is the most frequently observed for pharmaceutical unit operations given the challenges in establishing material property metrics to characterize materials.

3. Level 3 models: combine the process model with a material model to predict process outputs using quantitative materials descriptors. The material property model is developed to remove the categorical nature of the material inputs in from level 2 by providing a set of quantitative material property measurements (i.e., bulk density, compressibility, particle size) that can be associated to a particular material. The quantitative measurements can be used to develop a correlation between them and the regressed process model parameters from the Level 2. Ultimately, the material model would predict the process model coefficients based on the material property measurements, allowing the model to describe the behavior of not only those materials studied, but of other materials whose properties are known. Given the two model structure of this model level, this type of model is prone to compounding the errors between the first and second models. However, the main advantage is the ability to predict the behavior of a unit based on material properties, rather than assuming the behavior of the unit will be the same when the same name material is used.

Figure 6 shows a graphical representation of the models abovementioned. Notably, the amount of process understanding increases as the model level increases. The prediction of process outputs may also greatly improve with increase model level.

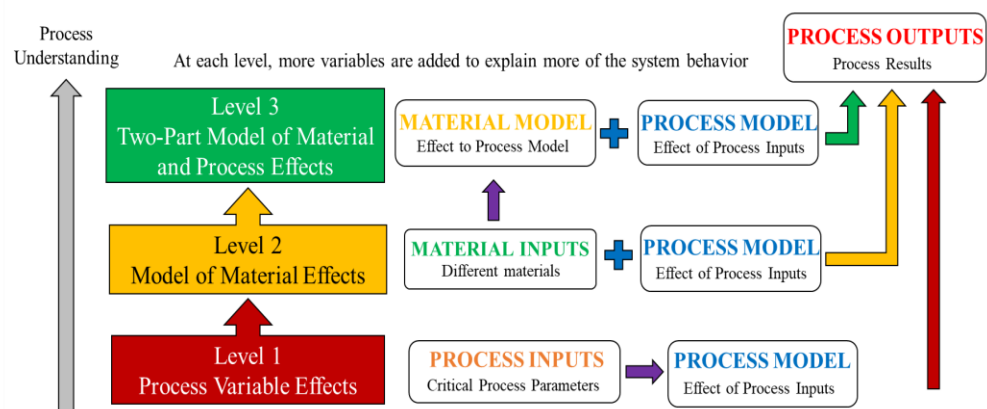


Figure 6. Model level categories based on the inputs described by the model

The model level categories provide a mean to identify the amount of behavior capture in by the current version of the model. For example, if only a level 1 model is provided, it is clear that the effect of material properties on the system is not well understood and that this model only captures the effect of process inputs on the outputs. Thus, when developing complex system models (i.e., flowsheet models) the unit operations represented with level 1 models will be unaffected by changes in material properties, a scenario that must be understood beforehand by the model users. Following on the example, if a unit operation is modeled using a level 2 model, then it is understood that material properties have an observable effect in the system, yet a certain degree of experimentation is needed to capture the effect of these material properties. Model calibration must be performed in order to have these unit operation models represent the system accurately. Lastly, if a unit operation is represented using a level 3 model, then this can be considered to be a model capable of considering changes in material properties and process inputs. Using level 3 models provides the most insight when PSE tools such as flexibility, feasibility, sensitivity analysis, and optimization are used. Nevertheless, these models require the most amount of work to be developed and are highly dependent on the range of material properties used to develop the material models.

3.6. MODEL DEVELOPMENT ALGORITHM

Based on the model classification and level designation, an algorithm to develop level 3 models was established and presented. Based on the general model framework, predictive input/output relationships need to be developed to effectively model the behavior observed from a unit operation. Since several level 1 models have been developed over the years for pharmaceutical equipment, this work focuses on describing the methodology starting from the availability of a level 1 model. Level 2 models are also frequently observed in the pharmaceutical engineering literature, yet they are described here to provide the readers with sufficient background for development

purposes. Most importantly, the means to develop level 3 models is described. To determine these level 3 model relationships, the following approach is proposed:

1. Develop an experimental plan to characterize the effect that changes in the unit operating variables (e.g., fill cam depth, turret speed, screw speed, screw size) have on the unit's responses and on the process outputs (e.g., outgoing tablets, flow rate). This experimental design involves the use of several materials (i.e., raw or material blends) so that the impact their properties (e.g., density, cohesion, flowability, compactability) on the unit's output is captured. The experimental design (i.e., changes in unit operating variables) is essentially repeated multiple times for the different materials.
2. A process model (i.e., level 1), can be developed from first principle mechanics, population balance methods, or from a simple phenomenological observation based on the results from the experimental data. Given the focus on maintaining simplicity for future modeling purposes, it is recommended that a semi-empirical phenomenological model capable of accounting for process variables changes in the experimental protocol is selected. However, regardless of how the model is developed it is important that the model is able to capture: (1) the process inputs evaluated in the experimental plan, (2) the process responses of interest, and (3) the effect of material properties.
3. The level 1 model from step 2 should be written in a way that allows for material property effects to be captured through a set of parameters that can be regressed from experimental data. The regressed parameters, which are obtained from minimizing the sum square error of the model prediction and experimental data at the provided experimental conditions, can be made dependent of any variable except for the variables accounted in the model. Thus, the constant regressed for the unit operation model can be made material-dependent. For each experimental design, for each material, one constant parameter will be assigned,

creating an array between materials and their model constant values. At this stage, the model reaches the second level of model types described in Section 3.5.

4. In conjunction with the experimental plan evaluations, every material tested in the must have its relevant material properties characterized before entering the system. This approach, which must be performed using standard material characterization methods, yields an array of materials and their properties that contextualizes the experimental plan's results to the materials used. Well-maintained material property libraries containing a wide range of properties can be used for this purpose, as they would allow for a record of the material properties and their variability over time.
5. The array of regressed constants and materials from step 3 along with the material property list established in step 4 can be merged into a single matrix, wherein model constants are treated as "material properties" numbers for each of the components. These new "material properties" are clearly associated with the level 1 model, and thus require users to understand the relationship between inputs and outputs expressed in the model. Nevertheless, this expanded matrix, which contains the contextualized results of the model along with the material properties, serves as a useful tool to determine the impact of material properties on the model.
6. From the array developed in step 5, the regressed unit operation model constants and material properties can be used to establish a correlation between the regressed coefficients and the property values. Essentially, the researcher would like to obviate non-numerical (i.e., categorical) information, as they are already accounting for the effect of the material by characterizing the physical behavior. Empirical models (i.e., data driven) would then be used to correlate the model constants to material properties; creating an equation that yields a given model constant value for a set of material properties. Obviously, since numerical

values of physical measurements depend on the units used, the correlations need to be contextualized in terms of units of measurement.

- Combining the material model developed in step 6 with the unit operations level 1 model developed (or selected) in step 2 would then yields a level 3 model, one that predicts unit behavior accounting for material property and unit operating variable inputs.

The approach described above is summarized in Figure 7, along with the respective association to the aforementioned model levels.

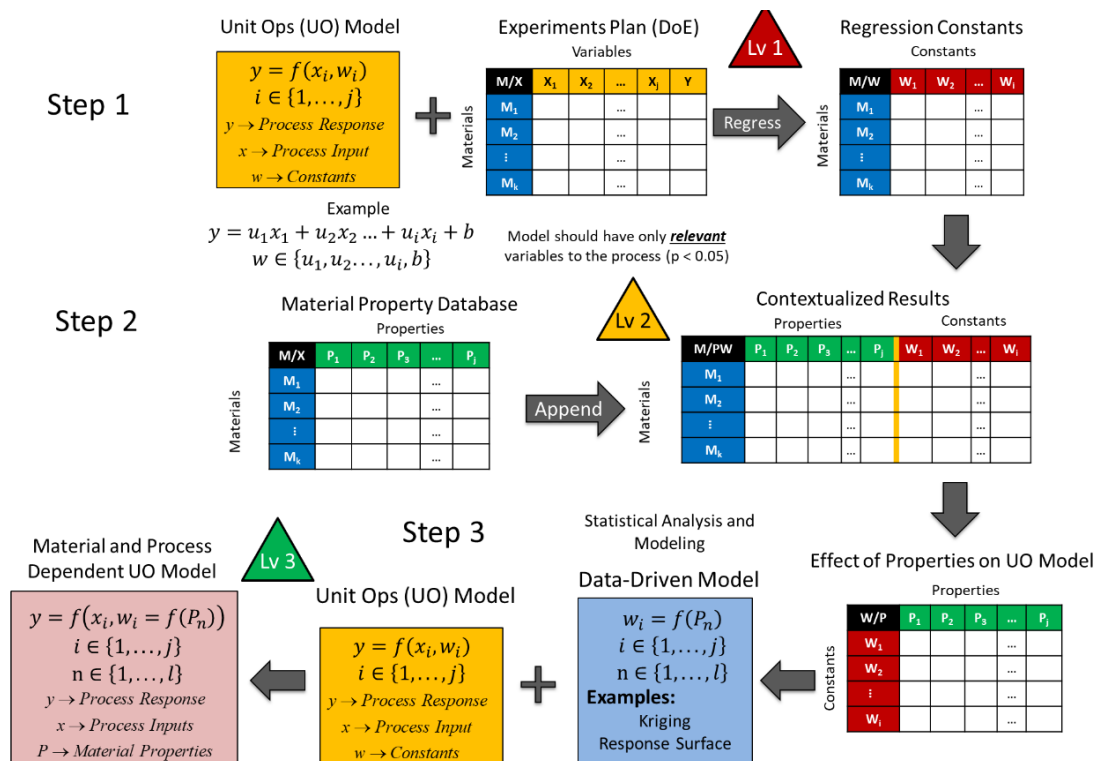


Figure 7. Model level categories based on the inputs described by the model

This methodology, can be performed effectively to any unit operation in the system as it is a derivation of previously established methodologies for model development [16, 135, 136]. The novelty of this algorithm rests on the contextualizing of experiments by collecting the material properties of any component in *conjunction* with the experiment itself. Since granular material

properties typically change irreversibly after a process, the history of the material ought to be captured by characterizing the material as close to the experimentation as possible. This latest snapshot of the physical properties of the material can then be used to develop the models capable of predicting the behavior most accurately. In the future, more detailed material property databases can be used in conjunction with the correlations determined using the proposed methodology to predict unit performance. This two-step model approach can be used to estimate how the performance of a unit varies with respect to material properties.

Following the proposal of this methodology, three unit operations present in the continuous direct compression line were used to apply the methodology. A tablet compression experiment was performed as a case study to prove the methodology's potential. The tablet compression system was selected given the known relationship between process inputs and outputs as well as the effect of material properties on process outputs. This proof-of-concept experiment is described in detail in Chapter IV. Following the proof-of-concept, a material property library was developed using materials used in subsequent equipment characterization experiments. The development and uses of the material property library are described in Chapter V. The unit operations evaluated using the materials characterized in Chapter V included a continuous blending system, covered in Chapter VI, and a powder feeding unit, covered in Chapter VII.

CHAPTER IV

4. AIM 1: APPLICATION OF THE METHODOLOGY FOR TABLET PRESS STUDIES

Acknowledgement of publication status:

Full sections of this chapter were published in a scientific article written by the author of this thesis under the title: Modeling the effects of material properties on tablet compaction: a building block for controlling both batch and continuous pharmaceutical manufacturing processes. The article was accepted on March 17th, 2018 in the Journal of Pharmaceutical Innovation. This work was done in collaboration with:

Shishir Vadodaria¹, Ravendra Singh¹, Fernando J. Muzzio¹, Marianthi Ierapetritou¹

¹ Engineering Research Center for Structured Organic Particulate Systems (C-SOPS), Department of Chemical and Biochemical Engineering, Rutgers, The State University of New Jersey, Piscataway, NJ 08854, USA.

This chapter was also done as part of a collaboration with Shishir Vadodaria, a master student under the supervision of Dr. Ravendra Singh and Dr. Marianthi Ierapetritou. The experimental section of this work was performed as part of Shishir's Master of Science thesis. The experiments and the experimental design were done under the direction of the author of this thesis. Shishir's full thesis can be found via the Rutgers Library Services. Full citation provided below:

Vadodaria, Shishir. "Correlation of compression models to material properties." Masters of Science Thesis. Rutgers, The State University of New Jersey. Department of Chemical and Biochemical Engineering. 2016

4.1. INTRODUCTION

This work is provided as proof-of-concept for the methodology presented in Chapter III. The goal was to aid the development and implementation of phenomenological models in the pharmaceutical process development space by establishing case studies that can be followed by those in the industry. The methodology is applied within the context of tablet compression because of the known effect material properties have on the process as well as the vast literature relating process inputs to outputs.

4.1.1. Effect of material properties on compaction

From previous studies, it was concluded that material properties (e.g. flowability, bulk density) strongly affect process performance (e.g. blending, feeding) [137, 138]. Hence, a thorough understanding of ingredient material property effects in a pharmaceutical formulation is extremely important to aid in process design, scale-up, and optimization [138]. Compaction is the processing step where the tablet structure is created, thus it primarily governs critical quality attributes (CQA's) of a tablet. However, it is well established that the variation in processes previous to the compaction step can drastically affect the tablet's physicochemical properties, such as disintegration [139, 140], dissolution [141, 142], tensile strength [143, 144], and friability [138, 145]. Since some of these properties are often measured using common in-process quality control tests, detailed studies on the connection between blend characteristics and compaction are not often captured. Nevertheless, understanding the relationship between the blend and compaction outcomes could accelerate product and process development, help reduce manufacture of out-of-specification (OOS) batches, and help formulators anticipate process vulnerabilities.

Material properties ranging from the molecular level, due to variation in chemical species or molecular arrangement, to the macroscopic level (e.g., bulk powder cohesion) can influence the

compaction process and final drug product characteristics [138]. For instance, variation in properties of tablets, due to differences in the binding properties of multiple grades of lactose was described by Vromans et al. [146]. On the other hand, the effect of lubricants, which are usually present in relatively small quantities, on tablet properties such as API release and tablets mechanical strength have been extensively documented for over five decades [145, 147]. Effect of the amount and type of magnesium stearate, a commonly used pharmaceutical lubricant, on tablet tensile strength is a well-known occurrence that can be attributed to inefficient inter-particle bonding of the excipients caused due to interference by the lubricant particles [148-151]. Variations in mixture flow properties are known to affect compression parameters such as in-die density, tablet thickness, and compression forces [152, 153].

As the pharmaceutical industry modernizes and shifts towards new continuous manufacturing practices for both legacy and new drug products, process elements that affect product quality and the methods to understand these systems need to be reevaluated. To enable changes from traditional batch to continuous manufacturing technologies the pharmaceutical industry should build the necessary expertise and skills to design and effectively operate the technology [31, 32, 48]. The expertise and skills are obtained through process understanding in terms of the evolution of all critical material properties as a function of its operating parameters and environmental conditions.

While the task of developing predictive models for compaction is quite large due to the number of variables and phenomena involved, this work attempts to make progress by providing a methodology that can be applied in future experimental plans. This work focuses on a narrow number of materials and conditions to implement and demonstrate a methodology for correlating material properties to existing empirical models. This chapter is organized as follows: Section 2 presents modeling and experimental methods used in this research, as well as a description of

materials and characterization methods. Section 3 presents the tablet results from experiments, the regression of empirical model coefficients from data, the empirical models establishing correlations between blend material properties and the regressed coefficients, and the application of such model in product design purposes. Lastly, in section 4 the conclusions and potential avenues of future research are presented.

4.2. MATERIALS AND METHODS

Note: a detailed description of the materials and experimental methods for this work is provided more extensively in Vadodaria's work [154]. The level covered here is provided to establish a framework for the modeling, as it was provided in the journal article written by the author.

Property measurements were collected by Vadodaria, along with the experimental performance of the blending, tablet compression, and breaking. The author of this thesis was focused on the analysis, interpretation, regression, and discussion of the data provided by Vadodaria. Application of the resulting model and any subsequent analysis was performed by the author of this thesis.

4.2.1. Materials

Two grades of microcrystalline cellulose (Avicel[®] PH 101 and Avicel[®] PH 301, FMC BioPolymer, Cork, Ireland), Lactose Monohydrate (Foremost Farms, Wisconsin, USA), and a preprocessed direct compression grade of acetaminophen (ComPap L, Mallinckrodt Inc., Missouri, USA) were used for this work given their availability, deformability during compression, and frequent use in the pharmaceutical industry. These materials were sieved using a 2000 μm mesh to break any large agglomerates that might have formed during storage. Magnesium stearate (MgSt, Mallinckrodt Inc., Missouri, USA) was used as the lubricant. Table 4 provides the names and intrinsic true density information for all materials used in this study. It is important to note that batch-to-batch variability may be observed in future studies if these same materials are used, based on the manufacturers specifications.

INSERT Error! Reference source not found. HERE

4.2.2. Blend preparation

Table 5 describes the details of blended materials involved in this work. Binary blends of the three excipients and lubricant listed in the materials section were prepared to vary the blends' material properties. Magnesium Stearate (MgSt) was varied in concentrations of 0.25, 0.75, 1 and 1.5% to span the range of lubricant concentrations used in industry. There were a total of 12 binary mixtures. A ternary mixture of ComPap L (15%), Avicel® PH 101 (84%), and MgSt (1%) was also prepared.

INSERT Table 5 HERE

Blending was performed in a 7.6-L capacity V-blender (Patterson-Kelley, Pennsylvania, USA) filled to less than 60% of its volume. For binary mixtures, the excipient was loaded first, followed by the lubricant on the top. The blender speed was set at 20 revolutions per minute (RPM) for a period of 2.5 minutes. For the ternary mixture, the API (APAP ComPap L) and excipient (Avicel PH101) were initially blended for a period of 12.5 minutes at 20 RPM, followed by another 2.5 minutes with the lubricant. Note the blending time of lubricant was kept constant to maintain the same level of total strain and lubrication; as strain and lubrication are known to affect tablet tensile strength [155]. Blending was performed in controlled temperatures of 25 – 29°C and at a steady $10 \pm 3\%$ relative humidity.

4.2.3. Material characterization

Material characterization was performed for all thirteen blends to have the appropriate material properties for subsequent modeling efforts. Characterization techniques included both manually measured properties and equipment based measurements. The material characterization techniques used are described in detail in Appendix A (page 240). Material properties collected for

this work included: bulk and tapped density, compressibility, permeability, and particle size distribution.

4.2.4. Tablet compaction

All tablets were manufactured using a PressterTM Compaction Simulator (Measurement Control Corporation, New Jersey, USA) using a standard IPT B tooling. Eight (8) mm flat-face cylindrical tooling was selected for this work. The rate of compaction and pre-compression length were kept constant to simulate a manufacturing rate of 45,000 tablets per hours and 5 mm, respectively. Dwell time was set at 21.6 ms based on the tablet production rate. The compaction profiles and peak compression forces were recorded for each formulation as well as the maximum compression pressure. Four tablets were prepared for each combination of fill depth and tablet thickness, which ranged from 6-10.75 mm and 2.5-3.5 mm, respectively. The detailed distances used for each experiment are provided in the dissertation by Vadodaria [154].

4.2.5. Tablet testing methods

Four tablets ($n = 4$) for each combination of compression parameters (i.e., fill cam depth and tablet thickness) and formulation were selected for weight, thickness, and tensile strength measurements. Weight was controlled during the experiment by measuring the mass of powder placed on the die. The total number of tablets created for modeling purposes for the 13 formulations was 312 (i.e., 24 tablets per formulation). It was known that a larger number of tablets is used for tablet hardness experiments where weight variability was not controlled, given the positive relationship between tablet weight variability and tensile strength variability. However, since weight (and its variability) were controlled, the number of tablets was greatly reduced in this experiment.

All tablets were tested one day after their compaction to allow for complete relaxation. All measurements were performed using a CheckMaster Tablet Tester (Burns Automation LLC, New Hampshire, USA).

4.2.5.1. *Relative density calculation*

Tablet weight and thickness were measured to calculate the tablet's relative density (ρ_r), using Equation 1 [155].

$$\rho_r = \frac{\rho_{tablet}}{\rho_{true}} = \frac{4M_{tablet}}{\pi h_T D^2 \rho_{true}} \quad 1$$

where ρ_{tablet} is the tablet's bulk density and ρ_{true} is the weighted average of the components's true densities. The tablet's bulk density can be computed from their mass (M_{tablet}), height (h_T), and diameter (D) as shown in the far-right form of Equation 1. Notably, the tablet diameter after compression and relaxation did not increase significantly ($< 0.05\text{mm}$) from the in-die diameter. Relaxation appeared to only occur in the vertical direction.

4.2.5.2. *Tensile strength measurement*

Tablets tensile strength was determined using a diametrical compression test, wherein two opposing metal plates compress the tablets until they break. The force required to break the tablets in brittle failure mode is measured and used along with the tablet diameter measurement to compute their tensile strength. The equation to compute tablet tensile strength (H_{tablet}) of a flat-surface cylindrical tablet given by [156] is shown below,

$$H_{tablet} = \frac{2F}{\pi h_T D} \quad 2$$

where F is the breaking force measured in Newtons or Kiloponds. In these calculations, the diameter of tablets was approximated to the nominal die diameter value of 8 mm, given that radial relaxation was minimal.

4.2.6. Modeling methodology

The tablet tensile strength model used in this investigation was proposed by Kuentz and Leuenberger [55, 67, 155, 157, 158]. The Kuentz and Leuenberger equation, rearranged below, describes the tensile strength of a compact (H_{tablet}) as a function of the relative density (ρ_r) and two regressed parameters based on data collected from the tablet strength test: maximum tensile strength (H_{max}) and critical relative density (ρ_c) [100]. This equation, thus, becomes the level 1 model relating the process conditions to an expected process response in the system.

$$H_{tablet} = H_{max}[1 - \text{Exp}(\rho_r - \rho_c + \lambda_h)]$$

Subject to:

3

$$\rho_c < \rho_r < 1$$

The value of maximum tensile strength represents the strength of tablets at a theoretical zero porosity. The critical relative density constant refers to the relative density required to hold the powder with enough shear strength to form a compact [100]. Therefore, it is important to understand that the relative density cannot be lower than the critical relative density. The (λ_h) parameter constrains the relative density values to be greater than the critical relative density by,

$$\lambda_h = \text{Ln}\left(\frac{1 - \rho_r}{1 - \rho_c}\right)$$

4

Both the maximum tensile strength and critical relative density are constant with respect to relative density, yet they are formulation dependent and have to be regressed every time the composition or material is varied. Associating these parameters to measurable material properties

would help predict these coefficients for new formulations and minimize the number of experiments needed to collect data to help regress the constant.

4.2.7. Software

Model parameters were obtained through regression of experimental data. The regression was performed by minimizing the sum-squared error between the experimentally obtained values of tensile strength and the predicted values of from the Kuentz and Luenberger equation. The non-linear regression algorithm provided by Mathematica® Version 11.0 2016 (Wolfram Alpha LLC, Illinois, USA) was used. Similarly, empirical model regression between material properties and regressed model constants was performed using the Mathematica® software and the non-linear regression algorithm provided. Principal Component Analysis on blend material properties was performed using the statistical software Minitab 17® (Mintab Inc., Pennsylvania, USA).

4.3. RESULTS AND DISCUSSION

The main objective of this article is to apply and describe the methodology for correlating material properties to existing empirical models, presented in Figure 7. As an example, this work focused on a case study that consists on predicting the tensile strength of tablets based on their blend material properties. Three filler excipients, one active pharmaceutical ingredient, and one lubricant are used in this work. Twelve binary mixtures of excipients and lubricants are prepared, with the lubricant level varying in four (4) levels. These blends allow for the development of a model that considers material properties and predicted tablet properties. A ternary blend is used to evaluate if the material property methodology can be applied, for a small variation in composition. The thirteen blends are compressed at different levels and their tensile strength was measured. The resulting tensile strength measurements were used to regress the values of phenomenological model constants, which then are correlated with material properties. Once the empirical models are

verified to predict the values for the phenomenological model constants, a case study evaluating the prediction of tensile strength using the material properties is presented.

4.3.1. Blend Characterization and material properties

Table 6 presents the material properties for each of the blends. The results indicate that bulk density, tapped density, and permeability varied significantly between major excipients. However, most of these material properties varied only slightly with the addition of magnesium stearate. Permeability was the only variable significantly affected by the addition of the lubricant. Increasing the lubricant concentration reduced the permeability of the blend, identified by the increased in pressure drop across the powder bed when air was flown through. This result can be explained by the closer packing, resulting in increased contact forces between particles, given the glidant effect of the lubricant material. The addition of the magnesium stearate, a hydrophobic material capable of (1) being squeezed out of the spaces between the two solid excipient surfaces and (2) deform easily when exposed to shear forces, decreases the cohesion and allows the material to pack more densely. As more lubricant was added and sheared during the blending step, the particles formed denser, less permeable matrices that would resist air flow.

INSERT Table 6 HERE

Using the rather highly dimensional material property table (i.e., nine material properties), the data was plotted using principal component analysis (PCA) [159-161] to determine the similarity between blends based on the nine material properties and the number of effective degrees of freedom for the material properties. Blends which are highly similar based on the nine material properties will have close proximity in a PCA score plot, whereas those which more dissimilar will be further apart. Similarly, PCA provides information regarding the material property measurements by means of their proximity in the loadings plot. Collinearity (i.e., relationship) between material property measurements are also assessed using the location of the measurements

in the loadings plot. Properties that are highly collinear are in the same direction in the PCA's loading plot, whereas those that not correlated or collinear are be perpendicular to the measurement.

Table 7 presents the results from the PCA analysis performed. Note Hausner Ratio is not added to the PCA, as the variable represents two of the measurements already accounted in the analysis: bulk and tapped density. From the results, two principal components were selected to plot the results in a 2-Dimensional (2-D) space. The fraction of the variability accounted by these two principal components (i.e., principal components 1 and 2) was 87% of the total variability captured by the materials. The remaining seven principal components accounted for only 13% of the remaining variability, which indicate they contain less variability than the second principal component. Ergo, for the purposes of this work, these remaining seven principal do not contain critical information.

INSERT Table 7 HERE

Principal components 1 and 2 express 69 and 18 percent (%) of the variability in the material property dataset, respectively. The coefficients of principal component 1 (PC1) reflect the majority of contribution in variability is due to bulk density, tapped density, porosity, permeability, and particle size distribution. These properties can be used to express the differences between the components; however, they are largely collinear to one another as they are opposite to one another in PC1. Collinearity in the PC space between the material property variables indicates they should not be used together in the empirical modeling efforts, as the variables would explain the same variability. Principal component 2 (PC2) reflects primarily the effects of the blends' compressibility, and mean particle size. These properties may be used to relate results with properties that are not significantly correlated with those properties accounted in PC1.

The score and loading plots are shown in Figure 8A and B, respectively. Data groups (i.e., cluster) were observed based on each of the blend's major excipient composition. Each excipient binary blend is affected by the concentration of lubricant added as seen by the spread of score values in Figure 8A within each excipient material group, which indicates that lubricant concentration has an effect on one of the measurements in PC1. The lubricant concentration does not appear to have a clear relationship with respect to PC2, as no trend is observed when increasing the concentration mass fraction. The effect of adding the API to the Avicel® PH101 and lubricant mixture has a significant effect in the blend properties, seen by the blend's location away from the Avicel® PH101 group. Addition of API to Avicel® PH101 appears to bring the blend closer towards the behavior of the denser Avicel® PH301, as seen by the shift of the blend towards the Avicel® PH301 group.

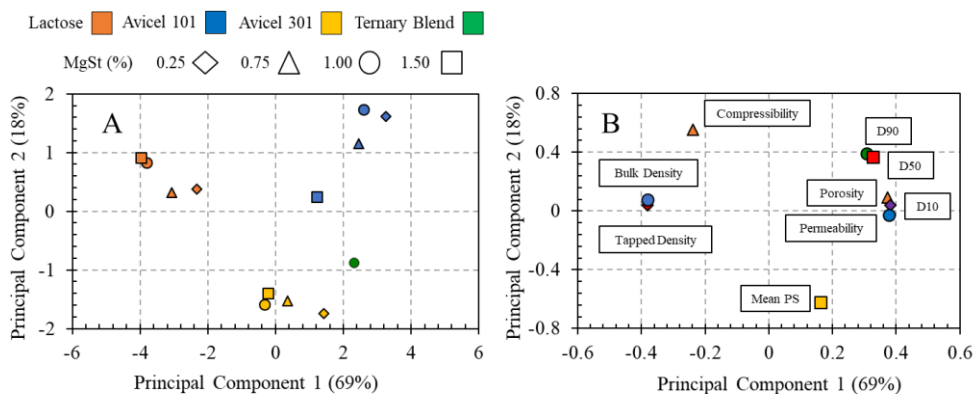


Figure 8. Principal Component Analysis (PCA) results for the material properties listed on Table 4 and Table 5. (A) Score plot of blend's characterized material properties. (B) Loadings plots for the material properties.

As with any modeling strategy, it is critical to determine the range of material properties that lie within the acceptable range. These results establish the material property space where the modeling efforts shown in subsequent sections will perform accurately.

4.3.2. Tablet tensile strength results

Figure 9 shows the results of plotting tablet tensile strength with respect to the tablet relative density for each formulation. Tablet relative density was computed using Equation 1. Figure 9A presents the results for the lactose formulation. As observed, the lubricant addition does not affect substantially the tablet strength between formulations. Nevertheless, there is a small weakening of the tablets at high values of relative density. Figure 9B shows the strength curve values for the Avicel® PH101 formulation. These tablets were found to be the strongest of all three formulations with the strength clearly being affected by the addition of lubricant. As expected, the lowest concentration of magnesium stearate corresponded to the strongest tablets, whereas the highest concentration of lubricant resulted in the weakest ones.

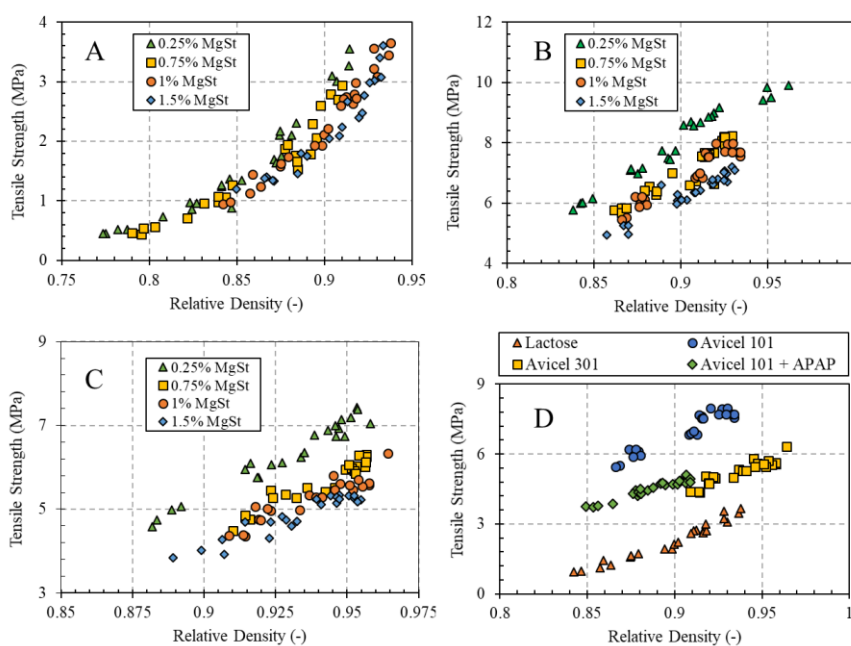


Figure 9. Experimental data for tablet tensile strength at varying levels of lubricant concentration (A) Lactose, (B) Avicel PH101, (C) Avicel PH301, and (D) All blends tablet tensile strength with a concentration of 1% magnesium stearate.

Figure 9C presents the strength curves for the higher density Avicel® PH301 tablets. Again, the negatively correlated effect of magnesium stearate on tablet strength was observed. As the mass fraction of the lubricant increases, the strength of tablets at the same porosity decreases.

The decrease in maximum tensile strength for both Avicel® formulations can be attributed to the reduction of surface area for inter-particle bonding due to coating of excipient particles with lubricant. Figure 9D shows the results for the strength curves of all formulations at a constant 1% magnesium stearate concentration. Adding the API (ComPap L) to Avicel® PH101 decreased the strength of tablets by means of changing the blend's particle structure and potential bonding surfaces. Further, the compaction capacity of the API is lower than that of Avicel® PH101, which in turn lead to a lower bond capacity for the blend. A difference of approximately 5 MPa existed between the strongest and weakest tablets.

4.3.3. Level 2 model: regression of model coefficients

Figure 10 shows the regression results for Equation 3's model parameters and the tablet tensile strength curves from Figure 3. For each formulation, the maximum tensile strength (H_{max}) and the critical relative density (ρ_c) were regressed. All plots appear to accurately represent the relationship between tensile strength and relative density with R^2 values greater than 93% for all blends.

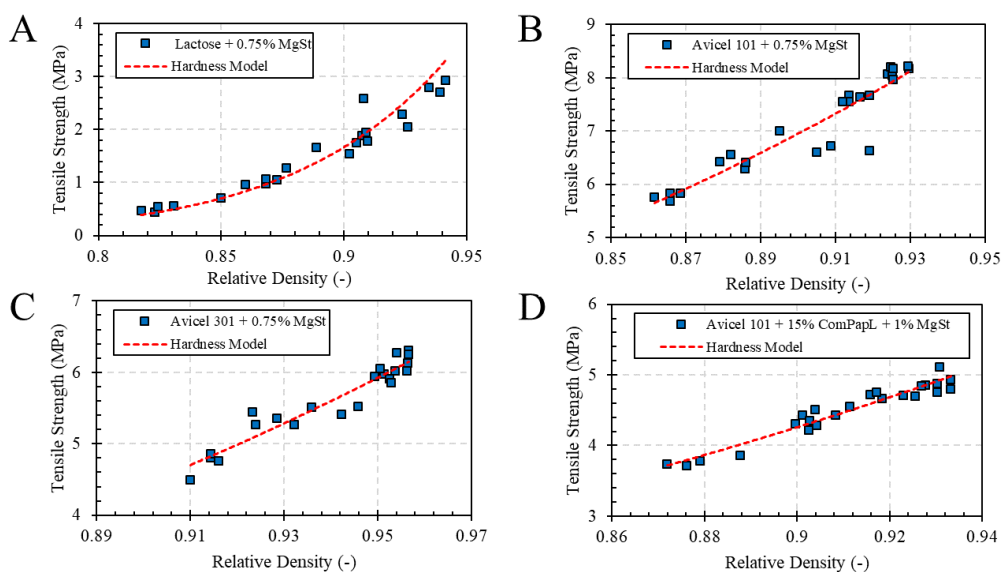


Figure 10. Experimental data for tablet tensile strength against relative density plotted along the Kuentz and Leuenberger model regressed for (A) Lactose with 0.75% magnesium stearate, (B)

Avicel 101 with 0.75% magnesium stearate, (C) Avicel 301 with 0.75% magnesium stearate, and (D) ComPap L (15%) + Avicel 101 with 1% magnesium stearate.

The regressed values of critical relative density and maximum tensile strength along with their regression standard errors are tabulated in Table 2. Regression p-values for each of the variables were less than 0.01, indicating that the values were found to be statistically significant with a high level of confidence. As expected, the values for maximum tensile strength differed between formulations and decreased with the mass fraction of lubricant. Critical relative density differed significantly ($p < 0.05$) between formulations, however, it did not vary significantly ($p > 0.05$) within formulations.

Table 2. Regressed Kuentz and Leuenberger hardness model parameters

Blend	Regressed Parameters*		R ²
	Critical Relative Density	Maximum Hardness (MPa)	
1	0.79 ± 0.01	4.31 ± 0.19	0.951
2	0.80 ± 0.01	3.84 ± 0.17	0.947
3	0.84 ± 0.00	4.37 ± 0.10	0.932
4	0.84 ± 0.01	4.10 ± 0.15	0.964
5	0.58 ± 0.02	11.91 ± 0.20	0.991
6	0.65 ± 0.03	11.02 ± 0.32	0.989
7	0.64 ± 0.03	10.58 ± 0.25	0.982
8	0.62 ± 0.03	9.43 ± 0.22	0.978
9	0.71 ± 0.01	8.99 ± 0.13	0.997
10	0.72 ± 0.02	7.62 ± 0.14	0.942
11	0.69 ± 0.03	7.07 ± 0.16	0.983
12	0.68 ± 0.03	6.61 ± 0.13	0.975
13	0.62 ± 0.02	6.55 ± 0.12	0.970

* The ± values represent the standard error of regression

The effect of magnesium stearate concentration on maximum tensile strength and critical relative density can be observed in Figure 16. Notably, at this stage, once the material parameters have been established for a particular material, the modeling has reached level 2, based on the aforementioned framework. At this point, it is known that most relationships stop within the pharmaceutical modeling literature, particularly for manufacturing processes.

Figure 16A shows the regressed maximum tensile strength with respect to the lubricant mass fraction along with their respective regression errors. For Avicel® PH101 and Avicel® PH301 a decrease in maximum tensile strength with increasing lubricant concentration clearly was observed. A relatively constant maximum tensile strength was observed for the lactose formulation with changing magnesium stearate concentration. The ternary blend had a similar maximum tensile strength to that of the Avicel® PH301 formulation with the same lubricant concentration. Within each group, the Avicel® PH101 tablets were the strongest, followed by Avicel® PH301, the ternary mixture, and lactose tablets. All maximum tensile strength tablets were found to be significantly different ($p < 0.05$), except for the Avicel® PH301 with 1% magnesium stearate and the ternary mixture, which were only near-significant ($p = 0.12$).

INSERT Figure 16 HERE

Figure 16B shows the regressed critical relative density with respect to the lubricant mass fraction along with their respective regression errors. From the graph, there were no significant trends observed between critical relative density and lubricant concentration within each group. Within each formulation, regressed values for critical relative density were found to be statistically similar ($p < 0.05$). These results were expected given that at the strain levels used in this study (just 50 revolutions in a small V-blender) lubricant concentration does not have much of an effect on the material's compactability, which is represented by the critical relative density. Statistical comparison of the critical relative density between formulations are relatively difficult to interpret due to the larger model errors presented by the Avicel® formulations. These large errors can be attributed to the larger extrapolation needed to regress the critical relative density coefficient for the Avicel® formulations. The Avicel® blends stronger tablets at higher relative densities required a much greater extrapolation to the zero tensile strength point, thus the resulting error was much larger than the lactose tablets.

A negative relationship between the maximum tensile strength and the critical relative density was observed. Figure 11 shows this relationship. The result suggests that blends with low critical relative density values (i.e., lower relative density is needed to form a compact) make stronger tablets. An explanation of such phenomena can be attributed to the reduced range of relative densities available to blends with higher critical relative densities. This behavior may not apply to certain materials whose deformation behavior is non-linear; however, tablets with a wider range of relative densities can be compacted further and yield stronger tablets.

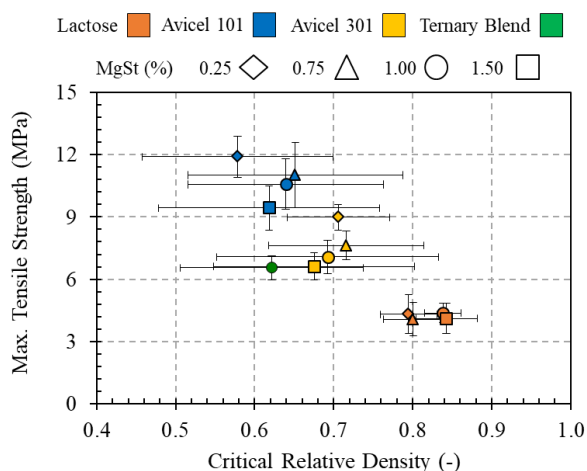


Figure 11. Relationship between the regressed values of the Kuentz and Leuenberger equation for all formulations. Standard deviation bars were excluded to minimize clutter in the graph.

4.3.4. Modeling tensile strength using blend material properties

Regression results were used to establish a matrix of material properties and model regression parameters. Effectively, this matrix combined Table 6 and Table 2. The analysis indicated that a simple linear regression model satisfied the relationship between the two model parameters and two material properties with sufficient accuracy. Figure 12A shows the positive linear relationship between the critical relative density and blend bulk density. The positive relationship between the blend's bulk and critical relative densities can be explained through the positive relationship between powder packing densities in unconfined (i.e., bulk) and confined (i.e.,

consolidated) states. Increases in packing density at an unconfined state indicate the material has a higher packing density in a consolidated state. Thus, since the critical relative density is defined as the density in which the material transitions from a bulk powder to a compact, it is reasonable to see that the density of this confined state is higher than the bulk density.

The positive relationship between the bulk and critical relative densities can also be explained in terms of the material's porosity. Material porosity is a measure that describes the amount of void space in the powder bed. This metric, thus is negatively correlated with critical relative density, meaning that as the material is less porous, its critical relative density is higher. A powder's initial porosity (ξ), calculated as $\xi = 1 - (\rho_{bulk}/\rho_{true})$, indicates that materials with high bulk densities have low initial porosity (i.e., less space void space is available). The decrease in initial porosity suggests that a material (present as a flowing powder at a low porosity) needs to be compressed to an even lower porosity (i.e., a higher critical relative density) in order to form a compact. Thus, for the materials tested here, lactose had the highest critical relative porosity because its bulk density was the highest and it shared similar true densities with respect to the other excipients.

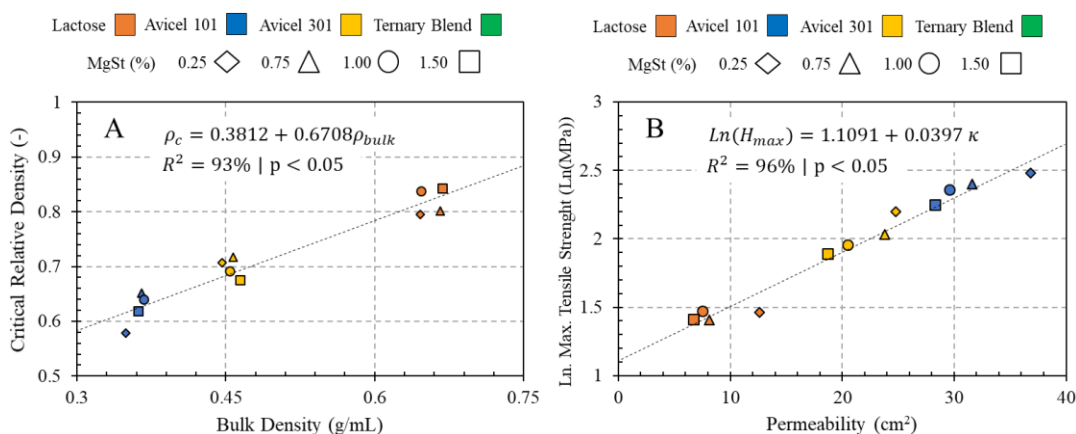


Figure 12. Relationship between major material properties and their respective empirical models. (A) Relationship between bulk density and critical relative density. (B) Relationship between maximum tensile strength and permeability.

Figure 12B shows the positive linear relationship between the permeability and the natural logarithm of the maximum tensile strength coefficient. The relationship between these two properties can be explained given permeability's correlation with particle size and the relationship between particle size and tablet tensile strength. Previous findings have shown that systems with smaller particle sizes (i.e., low permeability) yield lower strength tablets due to the reduced porosity and compactibility of smaller particles [162-164]. Since particle size was shown to be highly correlated with permeability given the loadings plot in Figure 8B, the correlation between these two measurements is in accordance to literature findings. Additionally, more permeable materials are able to evacuate air more quickly from their matrix, which allowed for more bonding surfaces to build between particles. This improved contact between particles increased the compact's tensile strength at a given relative density, which in turn increased the tablet's extrapolated maximum tensile strength.

It is important to note that other correlated measurements with particle size, such as bulk and tapped density as shown in Figure 8B, could alternatively be correlated with the maximum tensile strength measurement. The relationship between the maximum tensile strength and bulk density, based on the correlations described on Figure 8B, shows a negative correlation (i.e., as the first increases, the second decreases). This can also be observed by comparing the results between Figure 12A and Figure 12B, which show that the order of excipient materials reverses based on the property by which the model parameter is plotted against. However, for the purposes of this work since the bulk density was correlated with the critical relative density, the permeability was correlated with the natural logarithm of the maximum tensile strength.

Linear models were regressed for each of the observed relationships, yielding Equations 5 and 6. The coefficients for a_0 , a_1 , b_0 , and b_1 are presented in Table 3. These models provide the material property model needed to reach level 3 modeling. It is important to note these linear models are empirical in nature and may vary for future formulations, particularly for materials with

complex deformation mechanics. Nevertheless, it is important to mention these models are a first step to establishing the correlation between established models and material properties.

$$\ln(H_{max}) = a_0 + a_1\kappa \quad 5$$

$$\rho_c = b_0 + b_1\rho_{bulk} \quad 6$$

The results show that there is good agreement between the material property model and regressed coefficients with an R^2 value above 90%. A p-value less than 0.01 for both linear regressions also indicated the model parameters yielded statistically significant relationships between the regressed model coefficients and the material properties.

Table 3. Empirical models for Kuentz and Leuenberger hardness model constants

Material Property	Constant Value	Units	Model Constants*	
			Log Max Hardness [$\ln(H_{max})$]	Critical Relative Density [ρ_c]
Model Constant	a_0 or b_0		1.109 ± 0.03	0.381 ± 0.01
Permeability (κ)	a_1	$\left(\frac{\ln(MPa)}{cm^2}\right)$	$(3.907 \pm 0.05) \times 10^{-2}$	---
Bulk Density (ρ_{bulk})	b_1	$\left(\frac{g}{cm^3}\right)$	---	0.671 ± 0.02

\pm Value represent the model regression standard error

* Regression p-values for all coefficients were less than 0.01

Using Equations 5 and 6 the values for maximum tensile strength and critical relative density were calculated for the ternary blend (i.e., the external validation sample set). The results for both variables yielded 7.22 MPa and 0.647 for the H_{max} and ρ_c respectively. These results led to a prediction errors 10% and 4.7% between the regressed model parameters, listed in Table 5, and the calculated model parameters using the empirical equation.

Using the predicted model coefficients the tensile strength profiles as a function of relative density was calculated. Figure 13 shows the prediction of the ternary blend's tensile strength as a function of relative density for the ternary blend along with the regressed model and the model whose coefficients were computed using Equations 5 and 6.

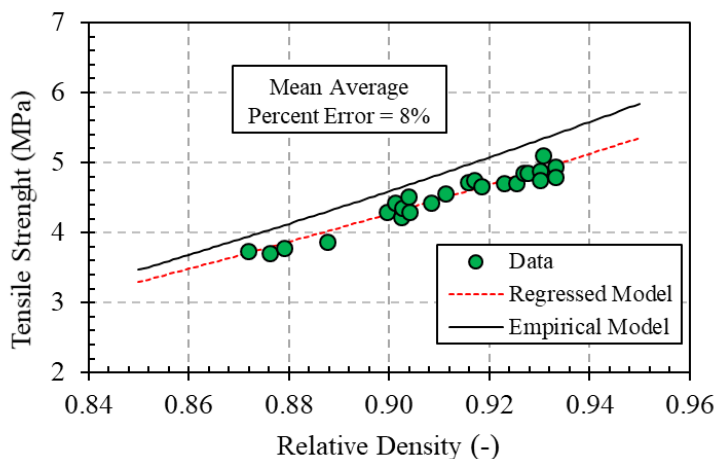


Figure 13. Prediction of the external validation ternary blender compaction curve using the empirical model to calculate the Kuentz and Leuenberger equation parameters.

The calculated mean absolute prediction error over the entire compaction profile was 8%, indicating the model captured the external validation point accurately. It was noted that the curve over-predicted the tensile strength over the whole range of relative densities; such result can be attributed to the slight over-prediction of the maximum tensile strength. Further evaluations of regression models and more materials properties should be incorporated in future empirical models to reduce the model error.

4.3.5. Level 3 model: Application to process development

Combining Equations 3, 4, 5 and 6, the Kuentz and Leunberger equation can be rewritten with respect to material properties, as shown in Equation 7, below.

$$H_{tablet} = \text{Exp}(a_0 + a_1\kappa) \left\{ 1 - \text{Exp} \left[\rho_r - (b_0 + b_1\rho_{bulk}) + \text{Ln} \left(\frac{1 - \rho_r}{1 - b_0 + b_1\rho_{bulk}} \right) \right] \right\} \quad 7$$

With this modification, the Kuentz and Leuenberger equation integrates the effect of material properties, within the characterized range. Application of this equation, however, needs to be within the range of material properties characterized. Extrapolation to values of material properties outside the range may lead to erroneous results. Furthermore, it is important to note that

the range of material properties characterized here is very limited. Future studies need to account for a broader range of material properties and for other materials, which may affect the empirical relationships presented in Equations 5 and 6.

Equation 7 provides an initial relationship, which can be used to predict the tensile strength of a tablet with respect to its material properties and tablet relative density. To further add value to this equation, the relative density value can be substituted by their relationship with critical process parameters. The relative density, as show in Equation 1, is directly related to the mass of tablets, which in turn is related to the volume fixed at the tablet press's fill cam. Equation 8 relates the mass of tablets to the tablet press's fill cam volume using blend bulk density.

$$M_{tablet} = V_{FC}\rho_{bulk}(1 - \varepsilon) = \frac{h_{FC}\pi D^2 \rho_{bulk}(1 - \varepsilon)}{4} \quad 8$$

where V_{FC} is the fill cam volume, and ε is the fractional void space remaining in the fill cam due to incomplete filling. Furthermore, the equation can be related to the height of the fill cam by expanding the volume term, as shown on the far right of Equation 8. Here, h_{FC} is the fill cam depth. Combining Equations 1 and 8, leads to Equation 9, where the relative density of tablets is presented as a function of fill cam depth, tablet height, blend bulk density, blend true density, and efficiency of cam fill.

$$\rho_r = \frac{h_{FC}\rho_{bulk}}{h_T\rho_{true}}(1 - \varepsilon) \quad 9$$

The combination of Equations 7 and 9 leads to Equation 10. In this last equation there are no process or material property dependent constants, meaning that direct measurements of material properties and process parameters can be used to predict tablet tensile strength for a given material property range. The five inputs to this model equation are the blend's permeability, bulk density, and true density, as well as the height of the fill cam and tablet thickness (i.e., height).

$$H_{tablet} = \text{Exp}(a_0 + a_1\kappa) \left\{ 1 - \text{Exp} \left[\frac{h_{FC}\rho_{bulk}}{h_T\rho_{true}}(1 - \varepsilon) - (b_0 + b_1\rho_{bulk}) + \text{Ln} \left(\frac{1 - \frac{h_{FC}\rho_{bulk}}{h_T\rho_{true}}(1 - \varepsilon)}{1 - b_0 + b_1\rho_{bulk}} \right) \right] \right\} \quad 10$$

Equation 10 can be used to establish a parametric space with respect to blend properties and process conditions for tablets. The equation can predict negative values of tensile strength, which would be obviously erroneous and would represent regions were tablets are manufactured outside the given blend properties and blend conditions. Nevertheless, if a constraint is imposed to only use greater than zero values, the results will be valuable.

4.3.5.1. Case 1: Tableting feasible space

Using a constraint that tablet breaking forces needs to be greater than zero, a region were tablet manufacturing would occur under a specific set of parameter conditions was established. Furthermore, a process feasible space of material properties and process parameters was established; one where tablets with a breaking force of 60 Newtons can be manufactured. Breaking force was used given that tablet tensile strength is dependent of the tablet height, a parameter this work wanted to evaluate in the feasibility problem. The feasibility problem is mathematically stated in Problem 11.

$$H_{tablet}\{\rho_{bulk}, \rho_{true}, \kappa, \varepsilon, h_{FC}, h_T\} > \frac{2F}{\pi D h_T}$$

Subject to:

$$\begin{aligned} 0.3 &\leq \rho_{bulk} \leq 0.7 [=] \frac{g}{cm^3} \\ 5 &\leq \kappa \leq 35 [=] \times 10^9 cm^2 \\ 6 &\leq h_{FC} \leq 10 [=] cm \\ h_T &= \{2.8, 3.0, 3.2\} [=] mm \\ \rho_{true} &= 1.5 \frac{g}{cm^3} \\ \varepsilon &= 0 \\ D &= 8 mm \\ F &= \{0, 60\} [=] N \end{aligned} \quad 11$$

Figure 14 shows four region plots where tablet production is feasible in accordance to the problem stated in Equation 11. Regions colored indicate tablets are feasible within the space,

whereas those not colored represent conditions where the feasibility constraint are not met. The blend's true density (ρ_{true}) was held constant at 1.5 g/cm³, tablet diameter was set to 8 mm, and the fractional void value (ϵ) was equal to zero. Figure 14A and Figure 14C show the effect of varying blend permeability, fill cam depth, and tablet height on the predicted tableability at a constant blend bulk density for the two breaking forces. Figure 14A shows changes in blend permeability have no major effect in the tablet's feasible region for breaking forces greater than zero. This result can be explained mathematically by the exponential relationship between permeability and tablet breaking force. Any increase in the permeability would cause an increase in the breaking force, which in turn would fulfill this feasibility problem's constraint of any breaking force being larger than zero. Low values of fill cam depth led to unfeasible regions, and as the tablet height increased, the fill cam depth played a larger role in reducing the size of the region. Increases in tablet height, from 2.8 to 3.2 mm, led to a linear decrease in the feasible region. This reduction in the feasible region is expected since the ability to form a compact is reduced when there is little material to be compacted or when the tablet height is increased at constant total tablet weight. Figure 14C shows permeability influences the tablet feasible region when the breaking force is set to be higher than 60 Newton. This result is in accordance with this work's previous finding, given that it was established that permeability was not related with tableability (i.e., the ability to form a compact) but to tablet strength.

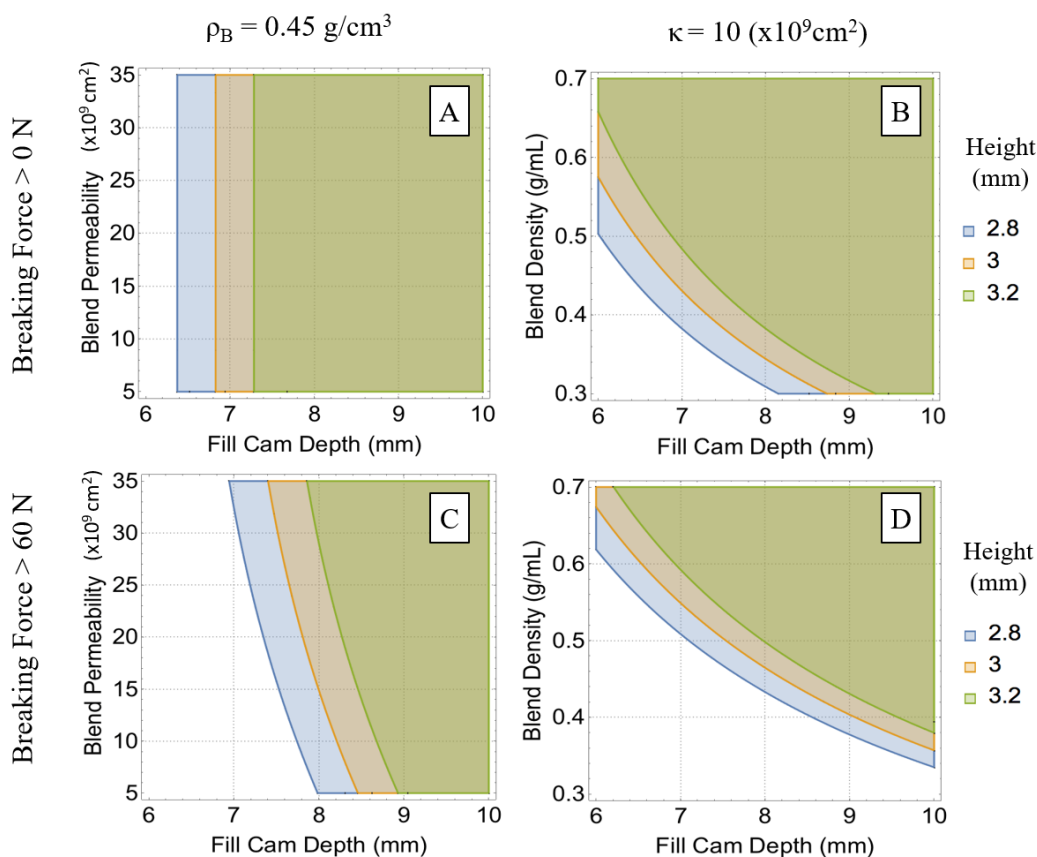


Figure 14. Region plots indicating the feasibility region for making tablets based on operational conditions and blend properties. Regions that are not shaded are operationally infeasible, meaning compacts are predicted to not be formed. Tablet thickness is varied at three levels. The breaking force constraint was also varied between 0 and 60 N. For tablets with breaking force higher than 0 N graph (A) varies fill cam depth (mm) and blend permeability (cm^2) at a constant bulk density. (B) Varies fill cam depth (mm) and blend density (g/cm^3) at a constant blend permeability. For tablets with a breaking force higher than 60 N graph (C) varies fill cam depth (mm) and blend permeability (cm^2) at a constant bulk density. (D) Varies fill cam depth (mm) and blend density (g/cm^3) at a constant blend permeability.

Figure 14B and Figure 14D similarly shows the regime plot for tablet manufacturing, varying the blend density, fill cam depth, and tablet height while maintaining the permeability constant. The results indicate that fill cam depth and blend density have a non-linear effect on the feasible region, which presents infeasibilities at low values of bulk density and low fill cam depth. Once again, increases in tablet height as well as constraints in requiring higher breaking forces reduce the tablet feasible space.

4.3.5.2. Case 2: Tableting design space

Once the feasible space was characterized, this work proceeded to determine the design space of the system by not constraining the breaking force as done in Equation 11. Tablet tensile strength was predicted using Equation 10 and the process and material property ranges presented in the feasibility problem proposed in Equation 11. Figure 15 shows the results in six different contour plots. Figure 15A shows the predicted tensile strength of tablets at constant bulk density ($\rho_{bulk} = 0.45 \text{ g/cm}^3$) and varying levels of tablet thickness and fill cam depth. Blend permeability was held constant in each of the contour plots and varied in intervals of 10 cm^2 . Predicted tablet tensile strength increased with increasing permeability and fill cam depth. This result relates to the previously observed results, as decreases in permeability correlate with the increasing amount of lubricant. As the value for tablet thickness increased, the feasible boundary also decreased and the tablets were weaker. Decreasing the tablet thickness increased the tablet hardness more significantly for the most permeable system, yet it had little impact for the lower permeability system. These results agree with the previously discussed Figure 14. Figure 15B shows the predicted tensile strength of the tablet at a constant permeability ($\kappa = 10 \text{ cm}^2$) and varying tablet thickness and fill cam depth. Bulk density was kept constant at each contour plot and varied in intervals of 0.1 g/cm^3 . Similarly to Figure 15A, the strongest tablets were predicted at the lower right corner of the contour plot, where the tablets fill cam depth was highest and the tablet thickness was lowest. As the tablet thickness increased, there was once again a predicted reduction in the tableting space.

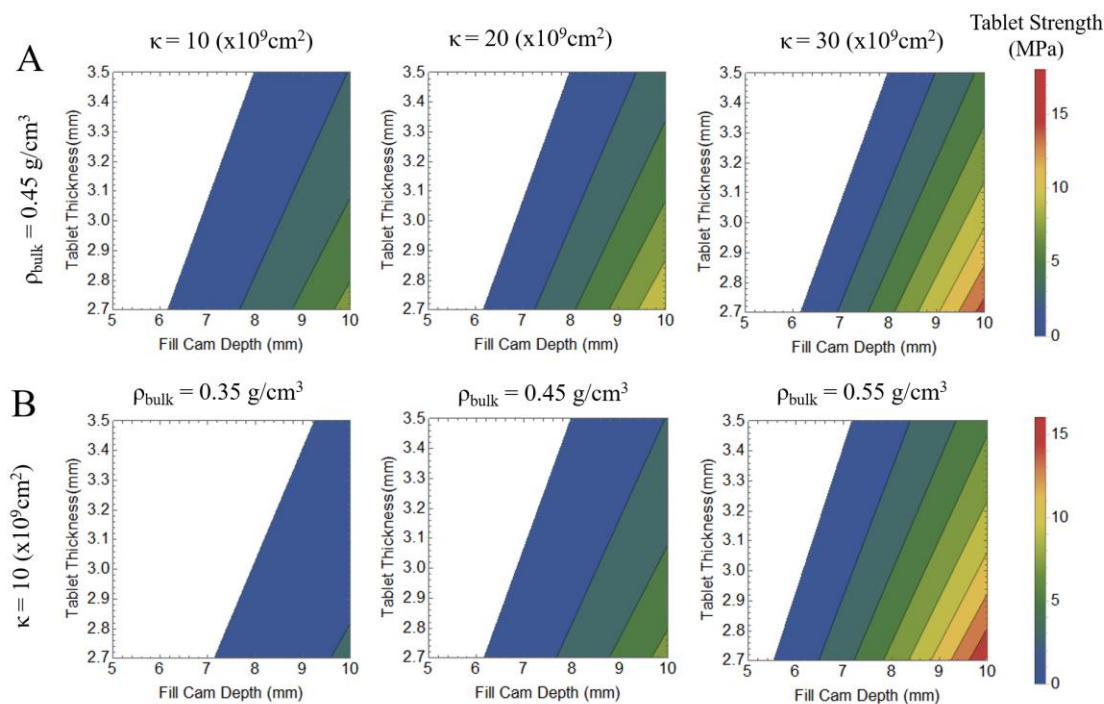


Figure 15. Contour plots showing the application of Equation 11 to determine the effect of operational parameters and material properties on tablet tensile strength. Tablet thickness was varied to three levels. (A) Varying fill cam depth (mm) and blend permeability (cm^2) at a constant bulk density. (B) Varying fill cam depth (mm) and blend density (g/mL) at a constant blend permeability.

It is important to note that all the material property ranges used for these design cases are based on the properties from the original blends. The material property ranges for this experimental design were narrow to provide this as a test of the methodology introduced. Future studies should aim at adding more materials and property measurements to the study and further improving the empirical correlations between material properties and model constants.

4.4. CONCLUSIONS

In this work, a methodology to integrate material properties into existing phenomenological models was presented using a pharmaceutical manufacturing relevant case. Several blends using three commonly used pharmaceutical powders were prepared and

characterized using standard methods. These blends were compressed at various relative densities and the resulting tablets were broken using an axial compression test. Results indicated that, as expected, tablet tensile strength for the case study examined here depends both on material properties and process parameters.

The effect of material properties on tablet tensile strength was studied using a phenomenological model and used to determine model constants. Regressions of phenomenological model coefficient corroborated the empirical relationship between tensile strength and material properties. Results demonstrated that a direct relationship between material properties and phenomenological model coefficients can indeed be determined, greatly accelerating the development of effective models. An empirical model was built subsequently to relate the material properties to the model parameters, effectively preserving the data obtained into a simple model. This empirical model was used to evaluate a compression design space and an operational space, accounting for material properties, and used to determine a “feasible space” for tablet tensile strength.

These results provide a proof-of-concept for the modeling approach described in Chapter III. This approach can aid the process development, especially in design space characterization and robustness analysis. Overall, this work can be used as a template for correlating material properties to phenomenological models of other unit operations involved in continuous pharmaceutical processing.

4.5. LARGE TABLES AND FIGURES

Table 4. List of materials used for the tablet compaction and material properties study

Material	Description	Bulk Density (g/cm ³)	True Density (g/cm ³)	Reference
Lactose	Foremost® NF Lactose Monohydrate	0.64 – 0.68	1.54	[143, 165]
Avicel® PH 101	Microcrystalline Cellulose NF	0.26 – 0.31	1.55	[165, 166]
Avicel® PH 301	Microcrystalline Cellulose NF	0.34 – 0.45	1.55	[165, 166]
Acetaminophen	APAP ComPap L	0.60 – 0.70	1.29	[165]
Magnesium Stearate	Magnesium Stearate, NF	0.15 – 0.18	1.09	[167]

Table 5. Blends used for the experimental evaluation of compaction and material properties

Blend	Main Ingredient	Added Ingredient	Magnesium Stearate
1	Lactose	-	0.25%
2	Lactose	-	0.75%
3	Lactose	-	1%
4	Lactose	-	1.50%
5	Avicel® PH101	-	0.25%
6	Avicel® PH101	-	0.75%
7	Avicel® PH101	-	1%
8	Avicel® PH101	-	1.50%
9	Avicel® PH301	-	0.25%
10	Avicel® PH301	-	0.75%
11	Avicel® PH301	-	1%
12	Avicel® PH301	-	1.50%
13	Avicel® PH101	APAP ComPap L (15%)	1%

Table 6. Material characterization results. Developed during characterization of this work and adapted from [154]

Blend	Bulk Density (g/cm ³)	Tapped Density (g/cm ³)	Hausner Ratio	Permeability at 15kPa (x10 ⁹ cm ²)	Compressibility (% Volume)	Mean (μm)	d ₁₀ (μm)	d ₅₀ (μm)	d ₉₀ (μm)	PS SD* (μm)
1	0.647 ± 0.007	0.883 ± 0.019	1.366	12.62 ± 0.90	14.95 ± 0.54	55.05	11.48	55.69	96.94	31.31
2	0.667 ± 0.000	0.913 ± 0.007	1.370	8.17 ± 0.35	14.91 ± 0.15	53.31	9.57	53.65	96.29	31.90
3	0.646 ± 0.006	0.902 ± 0.000	1.396	7.53 ± 0.51	16.02 ± 0.79	49.31	8.47	49.84	89.33	29.91
4	0.668 ± 0.012	0.915 ± 0.006	1.370	6.76 ± 0.11	16.17 ± 1.21	49.18	7.81	48.90	91.34	31.03
5	0.349 ± 0.003	0.456 ± 0.009	1.307	36.85 ± 1.24	15.19 ± 0.05	71.06	16.29	55.87	106.87	32.78
6	0.366 ± 0.002	0.477 ± 0.002	1.304	31.66 ± 2.28	14.46 ± 0.54	66.24	13.95	51.92	95.72	30.27
7	0.368 ± 0.007	0.479 ± 0.009	1.303	29.62 ± 0.52	14.35 ± 0.36	69.27	12.53	49.04	88.26	28.00
8	0.362 ± 0.001	0.484 ± 0.005	1.339	28.35 ± 2.57	14.14 ± 0.37	56.60	12.13	49.88	94.33	30.38
9	0.446 ± 0.000	0.587 ± 0.007	1.314	24.83 ± 0.60	13.26 ± 0.19	59.01	18.10	66.23	129.63	39.46
10	0.458 ± 0.013	0.592 ± 0.001	1.292	23.81 ± 0.18	13.91 ± 0.16	53.72	17.41	62.61	119.87	37.30
11	0.454 ± 0.007	0.588 ± 0.000	1.297	20.47 ± 0.54	13.93 ± 0.71	49.82	17.47	66.13	123.85	39.21
12	0.465 ± 0.001	0.595 ± 0.004	1.279	18.73 ± 1.18	13.34 ± 0.33	51.94	13.18	55.99	99.34	31.50
13	0.396 ± 0.001	0.514 ± 0.009	1.299	21.88 ± 0.29	12.85 ± 0.31	65.71	16.42	63.22	116.93	36.94

± Value represent one standard deviation

* SD – Standard Deviation

Table 7. Blend Principal Component Analysis (PCA) result values.

		PC1	PC2	PC3	PC4	PC5	PC6	PC7	PC8	PC9
PCA Metrics	Eigenvalue	6.229	1.608	0.6320	0.3315	0.1707	0.0197	0.0065	0.0020	0.0005
	Proportion	69.2%	17.9%	7.0%	3.7%	1.9%	0.2%	0.0%	0.0%	0.0%
	Cumulative	69.2%	87.1%	94.1%	97.8%	99.7%	100.0%	100.0%	100.0%	100.0%
Material Properties	Bulk Density	-0.380	-0.005	-0.386	-0.059	-0.164	-0.088	-0.313	-0.603	-0.455
	Tapped Density	-0.380	-0.041	-0.389	-0.042	-0.132	-0.055	-0.083	-0.039	0.820
	Permeability	0.327	0.076	-0.475	0.679	0.398	0.107	-0.171	-0.016	0.017
	Compressibility	-0.263	-0.530	0.037	-0.246	0.755	0.124	0.020	-0.053	-0.014
	Mean Particle Size	0.183	0.612	-0.347	-0.527	0.351	-0.132	0.228	-0.035	-0.008
	Particle Size d_{10}	0.386	-0.075	-0.061	-0.390	-0.119	0.574	-0.581	0.019	0.088
	Particle Size d_{50}	0.315	-0.418	-0.362	-0.084	-0.266	0.240	0.637	-0.230	-0.024
	Particle Size d_{90}	0.332	-0.397	-0.239	-0.187	-0.073	-0.703	-0.257	0.266	-0.061
Porosity	0.379	-0.002	0.400	0.027	0.119	-0.253	-0.056	-0.712	0.329	

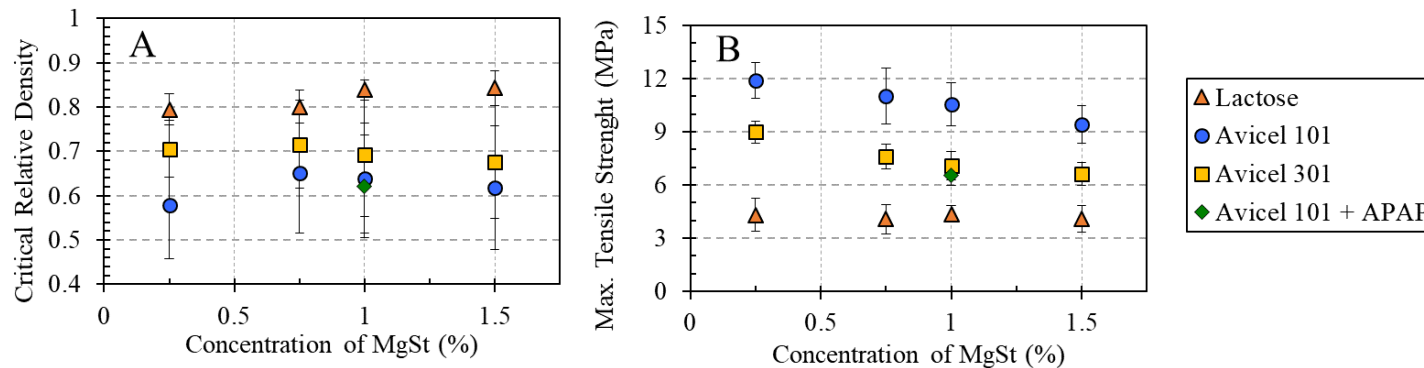


Figure 16. Regression results from tablet tensile strength models with respect to the concentration of magnesium stearate. (A) Critical relative density regression results (B) Maximum tensile strength regression results. All error bars represent one standard deviation.

CHAPTER V

5. AIM 2: MATERIAL PROPERTY LIBRARIES AND THEIR APPLICATION IN MODELING

Acknowledgement of publication status:

Full sections of this chapter were submitted as a scientific article written by the author of this thesis under the title: Using a material property library to find surrogate materials for pharmaceutical process developed. The article was submitted on March 11th, 2018 to Powder Technology Journal. This work was done in collaboration with:

Sara Moghtadernejad¹, Yifan Wang¹, Glinka Pereira¹, Elisabeth Schäfer², Tamas Vigh², Didier Klingeleers², Martin Otava², Marianthi Ierapetritou¹, and Fernando J. Muzzio¹

¹ Engineering Research Center for Structured Organic Particulate Systems (C-SOPS), Department of Chemical and Biochemical Engineering, Rutgers, The State University of New Jersey, Piscataway, NJ 08854, USA.

² Janssen Research & Development. Janssen Pharmaceutical Companies of Johnson & Johnson Beerse, Belgium

Acknowledgement of collaborative work and contributions:

The material property database, as collected and shown in this section of the work, was developed as part of a collaborative effort within the Engineering Research Center for Structured Organic Particulate Systems (ERC-SOPS). The materials, provided by Janssen Pharmaceutica, were analyzed and characterized by a team under the supervision of:

- Dr. Sejal Shah
- Dr. James Scicolone
- Dr. Sara Moghtadernejad

Description of the material property measurement techniques are thus provided in the appendix section of this thesis, in order to focus on the primary aim of this work, which was the application of the measured properties to explore the material space.

5.1. INTRODUCTION

Material properties are critical to the performance, success, and failure of powder-based manufacturing processes, including pharmaceutical solid-dose products. Research in the areas of ceramics [168-171], metallurgy [172-175], catalysts [176-178], food [179-184], and pharmaceuticals [13, 185, 186] have demonstrated that both raw materials properties and material history (i.e., the conditions at which a powder has been exposed) affect the performance and outcomes of subsequent unit operations and the attributes of intermediate materials and final products.

Although the manufacturing process for solid-dose products has been studied for many decades, the link between in-process material properties and product development is still largely empirical. This is partly because powders are intrinsically complex and their behavior is linked not only to chemical composition, but also to particle size distribution, particle morphology, moisture content, and both micro and mesostructure. Another reason why this relationship has not properly established is that it is intrinsically difficult to observe and measure the powder properties when it is flowing or processed. Moreover, while powder behavior and its impact on processing outcomes is a multivariate phenomenon, the use of multivariate methods in pharmaceutical process development has only recently been considered after the PAT and Quality-by-Design (QbD) initiatives of the FDA circa 2003 [13, 14, 65, 187-191].

The effects of critical material attributes on the quality of final products is often examined as part of the QbD-compliant methods to explore a design space. Nevertheless, material property understanding can help addressing the manufacturability of drug products, as discussed in ICH Q8

[192], since manufacturability often involves the interactions between the materials and the manufacturing processes. Some partial empirical examples of interaction between ingredient material properties and their intended applications have emerged over time. For example, viscosity specifications are common in the commercialization of sustained release polymers (e.g., polyethylene oxide, substituted celluloses) and are used by formulators to select grades of such materials for intended release profiles [193-195]. Powder cohesion, a granular material property similar to that of viscosity in fluids, was found to be important at describing process performance for unit operations such as mixing, where the affinity for particles to assemble into agglomerates, impacts the degree of micro-mixing that occurs in a blender, and therefore the resulting blend homogeneity [196-201]. Furthermore, flow properties of cohesive powders are strongly dependent on the state of consolidation, and are dramatically affected by delumping, conveying, and storage. Permeability, or the ability of air to pass through a powder bed, was found to be critical in explaining how powders fill dies in a tablet press [202], related to effects in tablet weight variability [203]. Wettability of blends containing friable hydrophobic ingredients (e.g., magnesium stearate) is strongly sensitive to strain [191, 204-211]. Electric charge storage can be strongly affected by moisture content, which in turn is very strongly affected by blend temperature [212-214]. Other properties such as the propensity of a material to pack under its own weight, the amount of energy required to move a blade through the material, and the segregation tendency of materials can all be important at describing the powder behavior and process performance at different places throughout a continuous manufacturing process [137, 215, 216].

Three of the major hurdles in understanding the effect of material properties on process condition are: (1) variability of raw materials, which is hard to characterize, (2) reduced product/process development timelines, and (3) number of processing steps required to create a drug product. Solid dosage products manufacturing typically involves multiple sequential unit

operations (e.g., delumping, premixing, granulation, drying, milling, lubrication, compaction, coating), wherein each exposes the material to various levels of shear, normal stress, moisture, and temperature. Each of these unit operation steps aims at changing the material's properties (e.g., particle size, acquisition of electrical charge, moisture transfer between ingredients, agglomeration and electrostatic sticking, and other shear dependent phenomena) in order to obtain a desirable outcome that permits the material to be processed into a final product. As a result, the properties of the intermediate materials (e.g., blends, granules, and compacts) throughout a manufacturing process are often dependent on the composition, the raw material properties, and the material's processing history.

Systematic characterization of raw material properties can help anticipate and avoid potential process failures caused by multiple modes such as sticking, agglomeration, poor mixing, and segregation. Moreover, raw material property evaluation and control often is a key element of a robust control strategy. Appropriate specification of material properties can be used to control raw material lot-to-lot variations so that a state of control can be assured.

The work in this chapter seeks to provide a blueprint for building a material property database in an efficient and reliable manner. The goal is to provide a meaningful case study, wherein a representative material property library is developed using a series of measurements, and then use those material property measurements to establish relationships between those materials and process performance. Further, the measured properties are evaluated to group materials based on such measurements. The results are further used to determine which material properties are highly correlated with one another, in an effort to provide a case study for characterizing the level of similarity between measurement in future material property libraries. To achieve these goals, the article is organized as follows. The rest of section 5.1 covers the general rationale and uses of material property databases, the definition of a surrogate material, and the multivariate analysis

methods used in this study. Section 5.2 introduces the materials and property measurement methods used in this work. Section 5.3 is devoted to presentation and discussion of results, whereas section 5.4 presents conclusions of this chapter's work.

5.1.1. Rationale for material property libraries

The compilation of raw and intermediate material properties of granular components to create comprehensive property databases is a critical step in deepening our understanding of how material properties affect process performance. A material property library, besides from complying with documentation, input examination, and operation monitoring guidelines set forth within the Current Good Manufacturing Practices (CGMP) paradigm, may be used for a wide range of uses and applications. Uses of such a material property library include: (1) serving as a repository of information describing effects of material properties on process performance, (2) facilitating the standardization of testing methods and the specification of property value ranges for commercially available ingredients, (3) supporting the identification of equivalent (i.e., interchangeable) materials based on their properties, (4) enabling the identification of surrogate materials for process development based on their properties, and (5) creating mathematical models relating material properties to unit operation performance. Figure 17 graphically summarizes some of the uses and knowledge that can be derived from material property libraries.

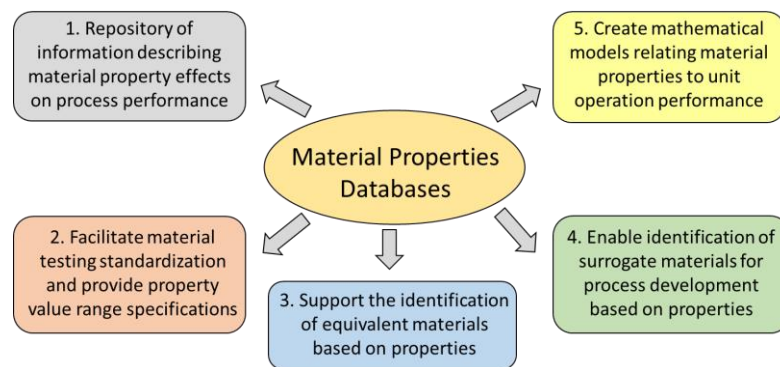


Figure 17. Some potential uses for material property databases or libraries.

Material property libraries used as repositories of information facilitate compliance with cGMP guidelines, which requires the use of material property measurements to evaluate process performance. Gathering and preserving knowledge throughout development and manufacturing stages, as required by FDA guidance documents, enables the scientist to detect trends, and helps evaluate process performance for current and future processes. Given a list of testing methods, process developers can establish a standard framework for characterizing new materials, which serves as a starting point for their development efforts. Further, the measurements collected in the libraries can be used to discern which measurements provide relevant information about a material, as well as determine the concise number of material properties that need to be measured.

A number of commercially available powder characterization methods such as powder rheometers, particle size analyzers, and segregation testers have gained wide acceptance in recent decades. Other examples of current methods and measurements for powder systems include, for example: powder cohesion, bulk and tap density, dilation, permeability, compressibility, shear sensitivity, hydrophobicity, and electrostatics [138]. However, an important missing step is that such methods have not been standardized across equipment or experimental facilities, preventing the creation of reproducible characterization metrics. For example, results obtained using different shear cells cannot be translated [217, 218] and different particle size methods famously give different results [219].

Although results obtained by different powder flow characterization methods may be different, they are often highly collinear, making it possible to collapse the relevant information to a smaller number of degrees of freedom that can be sampled equivalently by different methods [220]. However, since it is not clear *a priori* which testing methods are more accurate or meaningful, at the early stages of library development, all available material property tests should be considered to develop a broad data foundation. After an initial library is developed, the

information gathered can be used to assess which material properties are most relevant to a given process, the relative accuracy of the measurements, and the degree of co-linearity among measurements. This analysis can be performed using several multivariate analysis techniques, some of which will be discussed in this work.

5.1.2. Surrogate materials

Replacement of a material by another with “similar properties” is often desirable in pharmaceutical development. This is the case, for example, when an ingredient must be substituted because it is commercially unavailable (due, for example, to import limitations), undesirable (for example, when magnesium stearate or materials from animal sources needed to be replaced by non-animal material), or when one desires to develop a generic version of a branded formulation. The need to find materials with similar behavior also arises at early stages of pharmaceutical process development, where active pharmaceutical ingredients are scarce, expensive, or unavailable, or when the material to be replaced has high, or unknown, toxicity. Finally, in recent years the rapidly growing interest in continuous manufacturing has highlighted the need to measure the residence time distribution of powders in manufacturing equipment, which requires the use of tracer materials with properties similar to an ingredient or a blend of interest [34, 221]. In all of these situations, one needs to replace the target material with one whose *relevant* properties exhibit a similar behavior. Such a replacement material is hereon referred as a “surrogate” material. The emphasis on “relevant” is critical here as researchers might need different surrogate materials to capture flow, compaction, or dissolution behaviors. However, in any case, the question is the same: *given a material of interest and a finite list of replacement candidates, how do researchers identify a material that will mimic its behavior most closely?* Clearly, the first necessary step is to build a material property database consisting of properties describing or predicting the behavior for which

the researchers want to identify the surrogate. In the following section, this work clarifies how the material database can be explored using multivariate tools to identify a surrogate material.

5.1.3. Multivariate analysis tools for databases

Given the plethora and correlated nature of measurements available to characterize powders it is important evaluate data collection efforts (i.e., population of information onto the database) by means of multivariate methods. Intuitively, one would expect that a larger number of measurements would yield a “better” representation of the system (i.e., powder or blend); however, material, cost, and time constraints often do not allow researchers to measure all the material properties. Moreover, noisy or unreliable measurements may not increase or improve knowledge of the system and perhaps even affect the interpretation of other, more reliable measurements. Thus, the list of material properties to be included in the database must be scrutinized to minimize the number of measurements, measurement noise, and associated expense (e.g., cost of material, time), while maximizing data quality.

The foregoing notwithstanding, the material property database also needs to be broad enough to encompass all the behaviors of interests. Since different measurements are relevant to different process behavior, there is risk in selecting the final list of material properties too early in the process, only to be forced to reverse course at a later date and expand the list again when new process or product challenges emerge. Clearly, such a trade-off will require multiple iterations and accumulation of experience before a final inventory of desirable and appropriate measurements can emerge. Until then, as information is collected, researchers must evaluate the material property library, add data to the library by characterizing new materials and properties, and re-evaluate the library again. This iterative process is important to adapt the library to new material and measurements.

A useful conceptual approach is to maximize the information content of every measurement. Several simple and easily accessible multivariate analysis tools can be used to evaluate material property libraries that are constantly growing in both dimensions and variability [222]. In this work, two widely accepted multivariate methods were applied to the material property library: principal component analysis (PCA) and cluster analysis. Both of these methods are described in further detail in Appendix B (page 247) given that their application in modeling are quite extensive.

5.2. MATERIALS AND METHODS

5.2.1. Materials

This work used a material property library developed at ERC-SOPS that included a set of twenty pharmaceutically-relevant materials. A total of five active ingredients and fifteen excipients composed the material dataset. The names and manufacturers of the materials are provided in Table 8, below. All materials were provided by Janssen Pharmaceutica (i.e., the industrial collaborator of the ERC-SOPS) for a project funded by the company. Note most names of active compounds have been masked for proprietary reasons. Materials were stored under controlled environmental conditions in sealed bags until testing was performed. The temperature and relative humidity of the storage room were kept between the ranges of 20 to 25 °C and 20 to 40%, respectively. Every material was tested within three (3) months of receipt from the industrial collaborator.

Table 8. List of materials used in experiments and their manufacturers

Material	Manufacturer
Acetaminophen	Mallinckrodt, St. Louis, MO
Anhydrous Calcium Di-Phosphate	JRS Pharma JMBH & Co. KG, Rosenberg, Germany
API 1	Janssen Pharmaceutica, Beerse, Belgium
API 2	Janssen Pharmaceutica, Beerse, Belgium
API 3	Janssen Pharmaceutica, Beerse, Belgium
API 4	Janssen Pharmaceutica, Beerse, Belgium
Cellulose	International Fiber Corporation, North Tonawanda, NY
Croscarmellose Sodium	FMC Biopolymer, Philadelphia, PA
Crospovidone	Ashland, Bridgewater, NJ
Lactose 1 & MCC 1	MegglePharma, Wasserburg, Germany
Lactose 2	DFE Pharama, Goch, Germany
Magnesium Stearate	Seidler Chemical, Newark, NJ
MCC 1	FMC Biopolymer, Philadelphia, PA
MCC 2	FMC Biopolymer, Philadelphia, PA
MCC 3	FMC Biopolymer, Philadelphia, PA
MCC 4	FMC Biopolymer, Philadelphia, PA
Silicified MCC	JRS Pharma, Rosenberg, Germany
Starch 1	Everest Starch, Gujarat, India
Starch 2	Venus Starch Suppliers, Tamil Nadu, India
Starch 3	Maruti Chemicals, Ahmedabad, India

API = Active Pharmaceutical Ingredient; MCC = Microcrystalline cellulose.

5.2.2. Characterization methods

To build the material property database, each material used in this study (listed in Table 8) was subject to a standard set of characterization techniques to determine their properties. The characterization techniques are described in Appendix A (page 240) given that measurements they were not performed by the author of this thesis and they have been previously described in detail [217, 218, 223].

5.2.3. Equipment

A single GEA Compact Feeder (GEA Process Engineering, Belgium) feeder fitted with a 20 mm concave screw and a 63:1 servo motor gearbox ratio was used to test the behavior of the material when being fed. The feeding operation was performed under volumetric control at a nominal screw speed of 415 RPM (90% drive command). A high speed DSLR camera (Nikon, New York, USA) was placed at the barrel's exit to photograph the material exiting the unit.

5.2.4. Software

Principal component analysis (PCA) was performed using the algorithm provided in Wolfram Mathematica V11.1 (Wolfram Alpha LLC, Illinois, USA). Within the Mathematica's PCA algorithm mean centering was performed to the variables in order to balance the effect of dimensions on the measurements. A comparative PCA was performed using JMP Pro 13 (SAS, North Carolina, USA). Wolfram Mathematica V11.1 was used to generate graphs and compute the Euclidean distances of materials in the score plot, as well as perform the clustering of materials based on their material properties. A hierarchical categorical clustering method was used, wherein the distances between data points were calculated using the Squared Euclidean Distance method, provided within Mathematica. JMP Pro 13 was used for the development of measurement correlation charts, diagrams, and clustering.

5.3. RESULTS AND DISCUSSION

5.3.1. Material properties

A total of 32 measurements were performed on each of the twenty materials listed in Table 8, as described on the Material and Methods section. This library, developed as part of the ERC-SOPS material library development efforts, solely consisted of the materials listed in Table 8. The characterization work, performed by Dr. Sejal Shah, Dr. Sara Moghtadernejad, and Dr. James Scicolone, is greatly appreciated and acknowledged as part of this work. Table 14 and Table 15 present the averaged results ($n = 3$) of the material property measurements. All material properties measurements had a relative standard deviation below 10%, indicating the measurements were reproducible.

INSERT Table 14 and Table 15 HERE

After the characterization tests were performed and the material properties acquired, the measurements were compiled and transferred to the both Mathematica and JMP software, where the multivariate analysis (the main focus of this work) was performed.

5.3.2. PCA results

The material property results were used to perform a multivariate principal component analysis (PCA), wherein the results were divided into two different matrices: scores and loadings. The scores matrix (20 x 32) contained the linear combination of each of the material properties listed, while the loadings matrix (32 x 20) contained the linear combination of those properties with respect to their original measurements. An eigenvalue matrix containing the vector lengths for each of the 32 principal components (PC) was also reported to determine the variance explained by each PC. The results of the PCA matrices are provided in the supplementary document.

The eigenvalue matrix was used to determine the amount of variability from the original material property list explained by each PC. Eigenvalues were normalized with respect to the sum of all eigenvalues to establish a percent of variability explained. The individual and cumulative amounts of variability explained by the PCs are plotted in Figure 18. The first five principal components explained 55.2, 19.4, 7.3, 7, and 4.7% of the original dataset.

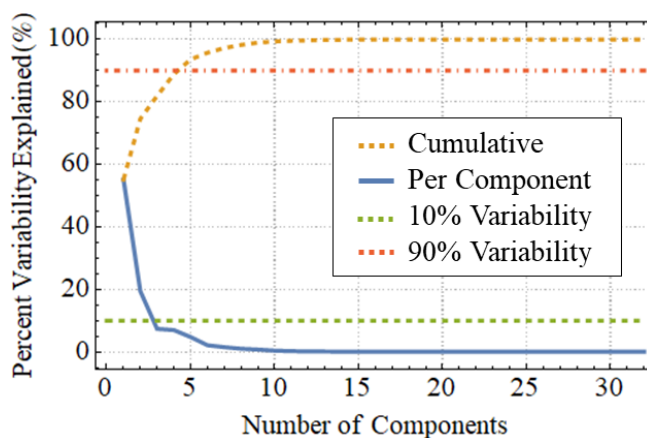


Figure 18. Percent of variability explained per PC and cumulative using the eigenvalues of the PCA results

From the results in Figure 18, this work identified the first three and first five principal components explained 81.9% and 93.6% of the cumulative material property variability in the database, respectively. Using a 90% variability cutoff for explaining sufficient variability of the original dataset, this work identified that the first five (5) PCs could be used to express the 32 measurements (i.e., dimensions) of the 20 different materials, effectively reducing the multidimensional space to a more manageable number of dimensions. These five PCs were used for future analysis of the material property database in subsequent sections. The results for the scores, loadings, and eigenvalues for the first five PCs are listed in Table 11.

INSERT Table 11 HERE

Figure 21A and B shows the two-dimensional (2-D) projections of the scores and loadings plots of the first two principal components of the PCA results, respectively. Figure 21C and D show the three dimensional (3-D) plots of the scores and loadings for the first three principal components, respectively. The numbers in brackets next to the axis labels express the amount of variability in each PC.

INSERT Figure 21 HERE

Figure 21A shows the location of each of the materials from our dataset and their position with respect to the first two principal components, which combined explained 74.6% of the dataset variability. Within the score plot, APIs and other poorly flowing materials such as cellulose and magnesium stearate (i.e., materials G and L, respectively) were observed to group towards the positive end of the first principal component, whereas material with improved flow properties (e.g., MCCs and anhydrous calcium di-phosphate) grouped towards the negative end of the first component. This is an indicator that principal component 1 (PC1) relates to material flowability in a quantitative manner. Figure 21B plots the values for each of the material properties with respect to their first two principal components. The location of these measurements on the loadings plot

indicates the contributions of each original measurements in that PC. For example, from Figure 21B, the results indicate PC1 is composed of the linear combination of all measurements with the highest contributions being from cohesion and d_{10} (i.e., measurements 19 and 29), since they are located at both ends of the PC1 axis. Furthermore, Figure 21B shows that there are two major groups of material properties at opposite ends of the first principal component: permeability and compressibility; both of which were performed at varying degrees of normal compression pressures in the FT4 Powder Rheometer.

The grouping of both measurements at different compression pressures indicates that the results are highly collinear, meaning the measurements are strongly related. However, it is not sufficient to observe PCA results in only 2-D, since 25.4% of the dataset's variability would be left out of the analysis and, as a result, points that appear close to each other in a 2D projection can in fact be quite far apart. Therefore, the third PC was included to verify whether some of the trends observed in the 2-D plots were maintained in 3-D. Notably, in Figure 21C materials were scattered around the eight different quadrants with minimal overlap, indicating that each material was different based on their properties. The third dimension helps to separate the group of crospovidone, starch 1, and starch 3, which fall into the fourth quadrant of Figure 21A. Figure 21D shows that the measurements are not represented in all quadrants, and exhibit a high degree of overlap, especially the aforementioned permeability and compressibility. These measurement similarities will be discussed in the subsequent sections of the article. Such data structure also suggests that additional materials, populating the "empty regions", might be needed in the future to obtain suitably "complete" models.

5.3.3. Material similarity index using PCA (SIMIN)

Determining the differences between materials requires comparing the different material properties and determining if variations in one property are sufficiently large to make them

different. This method is cumbersome when considering more than a few properties, and becomes complicated and potentially misleading as the number measurements increase. Given the results of the PCA analysis, the problem's dimensionality was greatly reduced from 32 measurements to 5 linear combinations of those measurements. The values were normalized to a scale that allows for analysis of several measurements by using one PC value.

From the PCA results a “single number” quantitative metric was developed to determine the degree of similarity of any two materials. The PC score values were transformed to distance values in PC-space using the multidimensional Euclidian distance equation. The Euclidean distance equation was weighted based on the amount of variability explained by each component to properly adjust the distances on each component. The weighted results, given the orthogonal and orthonormal behavior of PCA, would allocate properly the percent variability explained by each PC. The multidimensional weighted Euclidian distance (d) equation between two points p and q is shown in Equation 12, below,

$$d_{p-q} = \sqrt{\sum_{i=1}^m w_i (p_i - q_i)^2} \quad 12$$

where w_i is the percentage variability explained by the PC in dimension i , p_i and q_i are the location of each point in dimension i , and m is the number of dimensions used from the PC. In our case, the number of dimensions is five ($m = 5$). Equation 12 can thus be used to quantitatively measure similarity between two materials by means of their distances. Materials that are close in PC-space (i.e., have small Euclidian distances) are considered to behave similarly based on their material properties, whereas materials that are further apart (i.e., have large Euclidian distances) behave differently based on their properties. Importantly, we re-emphasize that the method should be used for different sets of measurements as they pertain to the specific behavior of interest in order to

identify materials that behave similarly for the specific behavior of interest (i.e., flow, mixing, compression, dissolution, etc.).

Using the results presented in Table 11 and the five PC dimensions, the weighted Euclidean distance between all of the materials was calculated, creating a matrix of distances between components. Each material had different minimum (d_{p-min}) and maximum (d_{p-max}) distances in PC-space. To compare the distances between a material p and any other material (X), a metric that would base the analysis with respect to pairs of distances was developed. To maintain a 0 – 100% scale comparison metric, each distance was normalized with respect to the individual minimum and maximum distances. The resulting value was defined as the similarity index (SIMIN), shown in Equation 13.

$$SIMIN = 100 \left(\frac{d_{p-x} - d_{p-min}}{d_{p-max} - d_{p-min}} \right) \quad 13$$

Table 16 presents the results for the similarity index (SIMIN) between all materials used in this study. As shown in Table 16 the SIMIN metric matrix is not symmetrical given that distances between materials vary depending on the minimum and maximum distances of the materials. The denominator for each material varies depending on how far or close that material is to its nearest or furthest neighbor. A symmetrical SIMIN matrix can be developed if the minimum and maximum values are used to re-scale the values for each material. Thus, rows U and V in Table 16 show the minimum and maximum distances for the material listed on the column, as calculated using Equation 12.

INSERT Table 16 HERE

The results from the SIMIN metric readily show that each material is associated with materials possessing similar and dissimilar properties. For example, material A (i.e., acetaminophen) is in close proximity to materials E and C (i.e., APIs 3 and 1) and far away from

materials B and J (i.e., Anhydrous calcium di-phosphate and Lactose 1 & MCC 1). This relationship appears to be in agreement with expected findings: both of the APIs that are in close proximity were selected qualitatively because they had flow properties “similar” to acetaminophen. Likewise, the results of materials that are far apart were in agreement with the expected values as these materials were qualitatively selected to have very different flow properties.

From a development standpoint, this result indicates that an experimenter could use acetaminophen as a surrogate material for performing equipment and process characterization in processes where APIs 1 and/or 3 are used. This also means that API’s 1 and 3 could be used interchangeably to characterize a process dominated by flow properties (i.e., flow in a hopper, gravimetric feeder, blending, and tracers in a RTD study). On the other hand, this results shows that materials such as anhydrous calcium di-phosphate and lactose 1 & MCC 1 may not be used to replace acetaminophen during process development and/or equipment characterization. Importantly, if the “similar” material is required to study a different behavior, one that is potentially independent of flow properties (e.g., for example, wettability) a different set of materials properties is likely to be needed in the original database.

From the SIMIN values, it is also possible to observe how materials of the same group fall close to each other based on their chemical composition. The starches (i.e., materials R, S and T on Table 16) have all SIMIN values less than 40%, which indicate their materials properties are relatively similar to each other. Furthermore, both well-flowing excipients with lactose as a main ingredient (i.e., materials J and K) also appear to have similar flow properties, with SIMIN values less than 5%. Importantly, although the material property database used here is quite small, it suggests that the methodology could be very useful; from the knowledge obtained by the SIMIN metric, manufacturers may be able to determine whether an excipient can be used as a surrogate

for another while maintaining the chemical composition of the formulation, for example when replacing one grade or commercial supplier of microcrystalline cellulose.

It is important to note that the SIMIN metric depends on the measurements (i.e., test) available on the material property database. However, given the normalization of the distance based on the materials minimum and maximum distances, the results of the SIMIN are robust with respect of the order that materials have on the matrix. On page 93, the robustness of material order is tested using clustered groups of materials.

5.3.4. Cluster analysis

Following the calculation of the SIMIN metric, JMP's hierarchical cluster analysis was used to analyze the material property database and establish groups of materials with similar properties. The clustering method evaluated distance using the Squared Euclidean Distance metric to utilize all available material properties (i.e., 32 measurements). The distance grouping algorithm to cluster materials was based on their proximity in Euclidian space. It is important to emphasize that the clustering method did not use the aforementioned PCA scores and values, but rather the full set of material properties and their standardized distances.

The number of cluster groups to allocate materials for the analysis was set to three (3) groups. The results for the cluster analysis are listed in Table 10, where the materials in Table 8 are listed as a function of the three groups based on their material properties.

INSERT Table 10 HERE

Acetaminophen, API 1, API 3, cellulose, and magnesium stearate belong to group 1. Based on this result and previous experience with these ingredients, this group lists materials with poorly flowing materials with high tendency to stick to surfaces. Group 2 is composed by API 2, API 4, croscarmellose sodium, crospovidone, MCC 1, MCC 4, MCC 3, and the 3 starches. From this

cluster result, this group represents materials with slightly better flow properties than group 1 (i.e., more granular flow) and do not tend to stick to surfaces. Lastly, group 3 is composed by the better flowing materials: anhydrous calcium di-phosphate, lactose 1 & MCC 1, lactose 2, MCC 2, and silicified MCC. These materials resemble each other on their ability to flow well and have no tendency for sticking to surfaces.

Figure 19 compares the clustering results of Table 10 with those of the SIMIN. Notably, the SIMIN values for the materials within each of the designated groups in Table 10 were between 0 and 50, particularly for the materials in groups 1 and 3. This result indicates that these materials had a similar flow behavior based on both the SIMIN and clustering methods. Group 2's results ranged between 0 and 72, indicating that some materials had relatively more dissimilar materials than those grouped in groups 1 and 3. This last result is reasonable given that this group encompassed the largest set of materials and, therefore, should include the largest set of material properties. Further, the materials clustered in each group appear to be largely similar to one another, which is the main objective of the clustering method. For these reasons, it is believed that both the results from the SIMIN metric and the clustering method agree with each other.

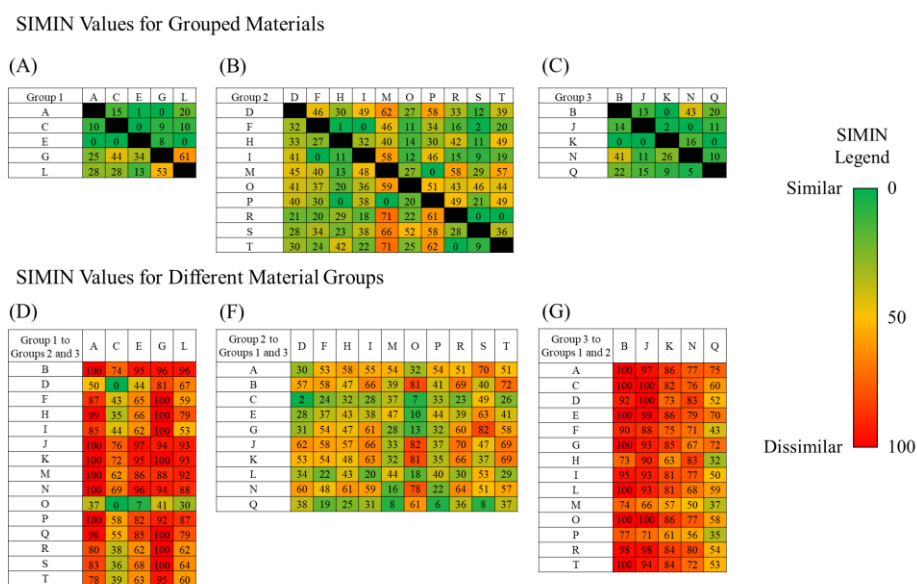


Figure 19. Comparison of results from the SIMIN matrix (Table 16) to the clustering results (Table 10). (A) Materials in group 1, (B) materials in group 2, (C) materials in group 3, (D) materials in group 1 compared to those in groups 2 and 3, (E) materials in group 2 compared to those in groups 1 and 3, (F) materials in group 3 compared to those in groups 1 and 2.

Figure 19 also shows the results of comparing the SIMIN values of grouped materials against those materials not belonging to that group (i.e., comparing groups of materials from those in Table 10). As expected, the results from comparing groups 1 and 3 against their two other groups (i.e., groups 2 and 3 and groups 1 and 2, respectively) indicate that the materials in these groups are highly dissimilar. SIMIN values regularly reached 100 in these two comparisons, which indicated that materials were the furthest with respect to each material. Markedly, within the results of Figure 19D, the results show that material C (i.e. MCC 3) had similar behavior to materials O and D (i.e., API 2 and MCC 3). This result indicates that the clustering method had to balance out the similarities between material C and these two materials, over the dissimilarities with the remaining materials. The SIMIN matrix, thus provides a method to remove this grouping and establish quantitative similarities between the materials based on their properties.

5.3.5. Measurement correlations

After observing the overlap in material properties measurements on the loading plot (Figure 21B), we examined the level of correlation between measurements using the linear correlation coefficient (R) metric. Each of the 32 material property measurements were plotted against each other and a linear fit was performed. The resulting linear correlation coefficient (R) metric was computed for each of the bivariate plots and the results are shown as a correlation map in Figure 20. The colors in the correlation map indicate the level of linear correlation, measured using the correlation coefficient (R), between the different measurements. Measurements that share red or blue colors are highly correlated (i.e., $R > 80\%$ or $R < -80\%$), while measurements sharing green, yellow, or teal colors show little to no correlation ($-30\% < R < 30\%$). Notably, the results of

the correlation map are symmetrical given that the map projects the same measurement list in both axes.

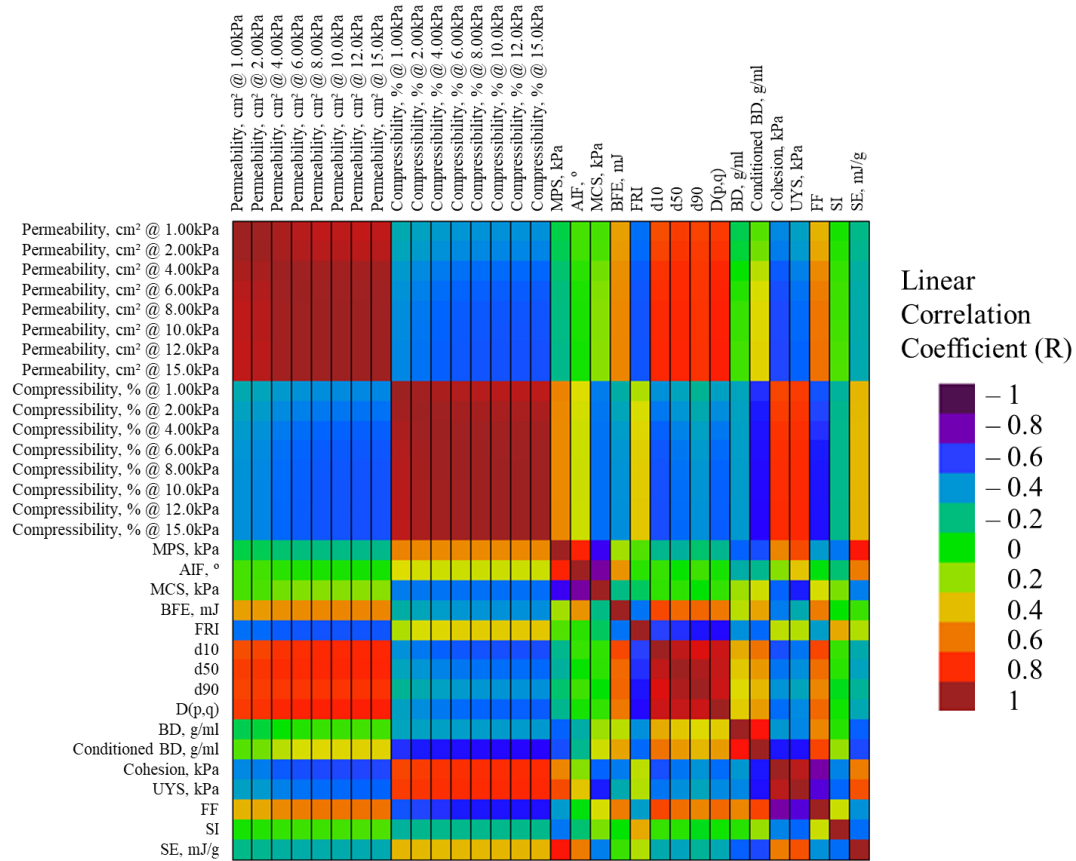


Figure 20. Correlation coefficient (R) map for material property measurements.

As observed in the correlation map, the permeability measurements at varying normal compression stresses were highly correlated ($R > 80\%$) among one another. Similarly, the compressibility measurements showed a high degree of correlation at different normal stresses ($R > 80\%$). Furthermore, the anti-correlation between the permeability and compressibility measurements was observed by the negative correlation coefficient. Different values of particle size showed a high degree of correlation, which was expected from previously reported findings [219, 224, 225].

Several measurements exhibited no relationship between each other, indicated by a linear correlation coefficient close to zero ($R \sim 0$). Examples of measurements that were not related include bulk density (BD) and permeability, stability index (SI) and particle size, and the angle of internal friction and cohesion. This last finding was consistent with previously reported results, wherein cohesion was not correlated with the angle of internal friction [218, 226, 227]. These non-related measurements could be used in future modeling efforts as a mean to explain the variability observed in the data and correlate it to material properties. Furthermore, once additional materials are included to the database, the correlation map can help identify which measurements may be eliminated based on their relationship with other measurements and which help capture the most material property variability.

5.3.6. Minimizing number of measurements and tests

Once the groups of materials were determined based on their properties, similar metrics and techniques were used to establish groups of measurements. The aim was to evaluate if certain material properties remained similar enough to others so they may be removed totally or partially from future material characterization methods. It is important to note that this work is not proposing to remove any material property measurement at this point, particularly since the material characterization community is still in the early stages of building detailed material property databases. However, in the future, the techniques presented here can be used to quantitatively provide a rationale, and eventually a rigorous method, for selecting a specific set of standardized material property measurements.

Using the clustering method available in JMP, the clustering of material property measurements shown in Table 14 and Table 15 was performed. The results of the clustering indicate that a total of six clusters can be formed from the measurements correlations. This result is in line with the results observed in Figure 20, where several groups of highly correlated material properties

were observed along the diagonal of the correlation plot. These clusters were identified from a cluster coefficient calculated using the correlation matrices for all calculations. The results for the cluster coefficient and their association with both the test and measurement are shown in Table 12, below.

INSERT Table 12 HERE

Several material property tests were allocated to their own clusters, namely: permeability, compressibility, particle size, and bulk density measurements. This outcome indicates that these measurements are highly correlated with each other. Therefore, these test are shown to produce results that can be estimated with only one of the measurements. The shear cell and flow energy tests populated non-intersectional clusters, indicating that the measurements in these tests contain independent information from each other.

The results from clustering material property measurements were compared with the correlation coefficient values presented in the map in Figure 20. A comparison of the measurement's squared linear correlation coefficient (R^2) was performed for materials in each cluster listed in Table 12. Subsequently, the nearest closest material property measurement's R^2 was obtained to determine the level of linear correlation shared by the cluster with respect to the closest measurement. The results of the clustering and correlation coefficient comparison are listed in Table 13. As expected, measurements within each of the six different clusters had a high correlation ($R^2 > 70\%$) with each other, except for basic flow energy and the flow rate index measurement in cluster 4 and the bulk density measurement in cluster 5. The reason for these measurements having slightly lower correlations within each cluster may have been due to the high variability of these measurements, which ranged from 8 to 10% in relative standard deviation. The correlation coefficient between measurements from neighboring clusters was at least 15% lower

than those of the materials within their cluster, indicating the allocation into that cluster was representative.

INSERT Table 13 HERE

Based on the results provided in Tables 3 and 4, the number of measurements were reduced by selecting one measurement *ad hoc* from each cluster groupings in Table 13. The material clustering based on their properties was then repeated in order to obtain a table similar to that shown in Table 10. The goal of this exercise was to determine the effect of having fewer material property *measurements* on the clustering. The six material property measurements selected were: permeability at 15kPa, compressibility at 15kPa, angle of internal friction (AIF), d50, cohesion, and specific energy (SE).

The results from the cluster analysis of materials using the reduced number of measurements is shown in Table 9. Three materials changed their locations from the groups listed in Table 10: API 1, magnesium stearate, and MCC 3. Although the number of materials that shifted columns was not large, the shift of both API 1 and magnesium stearate to the group 2 column did not satisfy the flowability associations made during the characterization procedure.

Since in some cases multiple measurements are associated with a single test, reducing the number of measurements would not always be an effective way of using the information available in the library to reduce the number of tests. For instance, the particle size analysis test yields the results for the d_{10} , d_{50} and d_{90} from a single evaluation, meaning that selecting one of the measurements (e.g., d_{50}) implies that the researcher possesses the measurements for the other particle size distribution values. Thus, it is not always reasonable to discard tests if clustering analysis wants to be performed, since in some cases the measurements are already available from the testing. In other words, from the point of view of using all of the information provided from the database, we find it better to exclude a full test rather than particular measurement from a test. For

this reason, the basic flow energy test was excluded from the database and the material clustering analysis was repeated.

Table 9. Material cluster analysis using only 6 measurements from the material property database and from removing all the measurements from the flow energy test

Material	6 Measurements			Minus Flow Energy Test		
	Groups			Groups		
	1	2	3	1	2	3
Acetaminophen	X			X		
Anhydrous Calcium Di-Phosphate			X			X
API 1		C		X		
API 2		X			X	
API 3	X			X		
API 4		X			X	
Cellulose	X			X		
Croscarmellose Sodium		X			X	
Crospovidone		X			X	
Lactose 1 & MCC 1			X			X
Lactose 2			X			X
Magnesium Stearate		C		X		
MCC 1		X				C
MCC 2			X			X
MCC 3	C				X	
MCC 4		X			X	
Silicified MCC			X			X
Starch 1		X			X	
Starch 2		X			X	
Starch 3		X			X	

* C = represents the materials that changed groups in comparison with Table 10

From these results, it was shown that removing a single measurement may not be the correct approach to reduce the number of variables, but rather reducing the number of tests being performed. Future analysis of material property library should include all material properties and periodically remove measurement that are highly collinear in order to avoid overpopulating libraries with less-than-significant measurements.

5.4. CONCLUSIONS

Material properties libraries are a critical component to begin establishing relationships between materials from a process development standpoint. Libraries can aid researchers and

scientist broadly during development: from selecting surrogate materials to reducing the amount of material needed during for characterization. In this work, a relatively small material property library was built as part of the collaboration with researchers at the ERC-SOPS using six different tests and twenty materials. A total of thirty-two different measurements were taken for each material, amounting to a library of 640 data points. Principal component analysis (PCA) was performed to reduce the number of dimensions and standardize the measurements into principal components.

After establishing a material properties library and performing PCA, this work used the information to establish quantitative metrics to analyze the data and establish a methodology to relate materials based on their properties. A material similarity index (SIMIN) was established using the score results from the PCA. This quantitative metric provided a mean to compare materials using a level of “similarity” between materials based on their weighted Euclidian distances in PC-space. The work proceeded to implement clustering algorithms available in statistical software to determine, using the quantitative metric of Squared Euclidian Distances, groups of materials based on their material properties. The results from the grouping analysis were evaluated by comparing the groups of materials with the behavior the materials exhibited while being fed using a continuous twin screw powder feeder. Lastly, using the results from the correlation coefficient map and similar clustering methods to those used in the previous section, groups of material property measurement methods were identified. Using the grouping of measurements, this work demonstrated methods to reduce the number of measurements for future material property testing.

PCA and clustering were found to be powerful methods for extracting information, identifying which materials are similar to each other, and which measurements contain co-linear or orthogonal information. More importantly, these methods provide a rigorous basis for selecting materials with similar properties, which is essential to our ability to select surrogates materials,

replace ingredients, and select appropriate tracers for residence time distribution studies. Much more importantly, the authors believe that all necessary building blocks are in place for the pharmaceutical development community to launch a sustained effort seeking to create a comprehensive material property database of excipients and commercially available APIs. Such database, supported by standardized testing methods and enabling the creation of predictive process models, would pave the way for true science-based product and process development and regulation.

5.5. LARGE TABLES AND FIGURES

Table 10. Results of clustering materials into groups based on properties

Material	Groups		
	1	2	3
Acetaminophen	X		
Anhydrous Calcium Di-Phosphate			X
API 1	X		
API 2		X	
API 3	X		
API 4		X	
Cellulose	X		
Croscarmellose Sodium		X	
Crospovidone		X	
Lactose 1 & MCC 1			X
Lactose 2			X
Magnesium Stearate	X		
MCC 1		X	
MCC 2			X
MCC 3		X	
MCC 4		X	
Silicified MCC			X
Starch 1		X	
Starch 2		X	
Starch 3		X	

Table 11. Results for the first five principal components of the PCA analysis

Principal Component Analysis		Principal Component					
		1	2	3	4	5	
Eigenvalues		17.65	6.22	2.36	2.23	1.51	
Scores	Acetaminophen	6.28	2.89	1.16	2.36	0.24	
	Anhydrous Calcium Di-Phosphate	-7.24	1.30	-1.82	1.60	1.31	
	API 1	3.51	0.38	-0.21	1.15	-0.22	
	API 2	1.20	-0.07	-0.89	3.04	-0.76	
	API 3	5.97	0.86	0.17	0.43	1.21	
	API 4	0.31	-2.54	-0.03	-1.21	0.20	
	Cellulose	4.81	6.11	-1.50	-0.97	-1.79	
	Croscarmellose Na	-0.33	-1.16	-2.98	-0.92	1.24	
	Crospovidone	0.90	-3.37	0.05	-1.45	0.25	
	Lactose 1 & MCC 1	-7.14	2.13	1.44	-0.11	-0.18	
	Lactose 2	-5.98	1.29	0.19	1.31	0.97	
	Magnesium Stearate	4.76	-1.29	3.27	-0.24	2.83	
	MCC 1	-1.45	1.74	-0.48	-1.87	0.39	
	MCC 2	-4.27	2.08	3.26	-1.29	-1.45	
	MCC 3	3.75	-0.37	-1.57	-1.99	0.08	
	MCC 4	-1.17	0.78	-0.65	-1.90	0.31	
	Silicified MCC	-4.06	-0.62	0.52	-0.28	-0.16	
	Starch 1	1.20	-3.57	-0.05	0.57	-1.63	
Starch 2	-2.30	-3.31	-0.76	1.78	-0.44		
Starch 3	1.25	-3.26	0.88	-0.02	-2.41		
Loadings	BD, g/ml	-0.39	-0.37	-0.24	0.75	-0.03	
	CBD, g/ml	-0.67	-0.37	-0.30	0.51	0.06	
	Compressibility (%)	1 kPa	0.77	0.51	0.17	0.28	0.07
		2 kPa	0.81	0.47	0.19	0.26	0.09
		4 kPa	0.84	0.44	0.19	0.24	0.09
		6 kPa	0.85	0.42	0.19	0.22	0.09
		8 kPa	0.86	0.41	0.19	0.21	0.08
		10 kPa	0.86	0.41	0.19	0.21	0.08
		12 kPa	0.86	0.41	0.19	0.20	0.09
	15 kPa	0.87	0.40	0.19	0.19	0.08	
	Permeability (x 10 ⁹ cm ²)	1 kPa	-0.75	0.57	0.25	-0.21	-0.03
		2 kPa	-0.77	0.55	0.23	-0.19	-0.02
		4 kPa	-0.82	0.50	0.21	-0.14	0.00
		6 kPa	-0.84	0.47	0.20	-0.12	0.00
		8 kPa	-0.86	0.46	0.18	-0.10	0.00
		10 kPa	-0.86	0.45	0.18	-0.10	0.01
		12 kPa	-0.87	0.44	0.18	-0.09	0.01
	15 kPa	-0.87	0.44	0.18	-0.10	0.01	
	Cohesion, kPa	0.82	0.32	0.00	0.03	-0.30	
	UYS, kPa	0.79	0.46	-0.13	-0.02	-0.23	
	MPS, kPa	0.51	0.62	-0.49	-0.27	0.00	
	FF	-0.78	-0.07	-0.17	0.24	0.29	
	AIF, °	0.18	0.60	-0.63	-0.21	0.36	
MCS, kPa	-0.39	-0.55	0.47	-0.02	-0.29		
BF _E , mJ	-0.58	0.38	-0.57	0.07	0.23		
SI	-0.21	-0.34	0.31	-0.05	0.80		
FRI	0.56	-0.28	0.16	-0.37	0.54		
SE, mJ/g	0.51	0.40	-0.48	-0.40	-0.16		
d ₁₀	-0.84	0.35	-0.15	0.30	0.06		
d ₅₀	-0.81	0.40	-0.02	0.31	0.00		
d ₉₀	-0.74	0.49	-0.05	0.31	-0.04		
D(3,2)	-0.82	0.41	-0.03	0.27	-0.04		

Table 12. Clustering results for material property measurements. Each set of measurements is divided by their respective test

Test	Measurement	Cluster Coefficients					
		1	2	3	4	5	6
Permeability, cm ²	at 1 kPa	35%	-	-	-	-	-
	at 2 kPa	35%	-	-	-	-	-
	at 4 kPa	36%	-	-	-	-	-
	at 6 kPa	36%	-	-	-	-	-
	at 8 kPa	35%	-	-	-	-	-
	at 10 kPa	35%	-	-	-	-	-
	at 12 kPa	35%	-	-	-	-	-
	at 15 kPa	35%	-	-	-	-	-
Compressibility, %	at 1 kPa	-	35%	-	-	-	-
	at 2 kPa	-	35%	-	-	-	-
	at 4 kPa	-	35%	-	-	-	-
	at 6 kPa	-	35%	-	-	-	-
	at 8 kPa	-	35%	-	-	-	-
	at 10 kPa	-	35%	-	-	-	-
	at 12 kPa	-	35%	-	-	-	-
	at 15 kPa	-	35%	-	-	-	-
Shear Cell	AIF, °	-	-	60%	-	-	-
	MCS, kPa	-	-	-57%	-	-	-
	MPS, kPa	-	-	57%	-	-	-
	Cohesion, kPa	-	-	-	-	-46%	-
	UYS, kPa	-	-	-	-	-46%	-
	FF	-	-	-	-	46%	-
Particle Size, microns	d ₁₀	-	-	-	-44%	-	-
	d ₅₀	-	-	-	-44%	-	-
	d ₉₀	-	-	-	-44%	-	-
	D(3,2)	-	-	-	-44%	-	-
Density, g/mL	Bulk	-	-	-	-	38%	-
	Conditioned bulk	-	-	-	-	46%	-
Flow Energy	FRI	-	-	-	33%	-	-
	BEF, mJ	-	-	-	-34%	-	-
	SI	-	-	-	-	-	71%
	SE, mJ/g	-	-	-	-	-	-71%

Table 13. Determination coefficients explaining the variability present in the clusters presented in Table 12

Cluster	Members	R ² with Own Cluster	R ² with Next Closest
1	Permeability, cm ² @ 1 kPa	97%	55%
	Permeability, cm ² @ 2 kPa	98%	58%
	Permeability, cm ² @ 4 kPa	100%	63%
	Permeability, cm ² @ 6 kPa	100%	65%
	Permeability, cm ² @ 8 kPa	99%	66%
	Permeability, cm ² @ 10 kPa	100%	66%
	Permeability, cm ² @ 12 kPa	99%	67%
	Permeability, cm ² @ 15 kPa	99%	67%
2	Compressibility, % @ 1 kPa	97%	49%
	Compressibility, % @ 2 kPa	99%	53%
	Compressibility, % @ 4 kPa	100%	56%
	Compressibility, % @ 6 kPa	100%	58%
	Compressibility, % @ 8 kPa	100%	59%
	Compressibility, % @ 10 kPa	100%	59%
	Compressibility, % @ 12 kPa	100%	60%
	Compressibility, % @ 15 kPa	99%	60%
3	MPS, kPa	82%	60%
	AIF, °	92%	20%
	MCS, kPa	82%	23%
4	d ₁₀	95%	62%
	d ₅₀	94%	65%
	d ₉₀	94%	60%
	D(3,2)	93%	68%
	BFE, mJ	56%	29%
	FRI	53%	28%
5	BD, g/ml	54%	16%
	CBD, g/ml	80%	42%
	Cohesion, kPa	80%	62%
	UYS, kPa	79%	64%
	FF	81%	44%
6	SI	74%	12%
	SE, mJ/g	74%	47%

Table 14. Material property measurements for the materials used in this material library analysis.

Material	BD, g/ml	CBD, g/ml	Compressibility (%)								Permeability (x 10 ⁹ cm ²)							
			1 kPa	2 kPa	4 kPa	6 kPa	8 kPa	10 kPa	12 kPa	15 kPa	1 kPa	2 kPa	4 kPa	6 kPa	8 kPa	10 kPa	12 kPa	15 kPa
Acetaminophen	0.48	0.31	28.8	35.5	41.7	44.7	47.0	48.4	49.7	51.2	24.3	20.1	14.5	12.1	10.4	9.1	8.4	7.4
Anhydrous Calcium Di-Phosphate	0.76	0.74	2.3	2.7	3.2	3.7	4.0	4.2	4.4	4.7	142.2	140.7	137.7	134.3	134.7	133.6	133.1	130.3
API 1	0.61	0.39	15.4	20.5	25.4	28.4	30.4	31.9	33.0	34.4	29.8	23.0	16.8	13.8	12.0	10.8	9.8	8.7
API 2	0.69	0.54	13.7	16.8	19.5	21.0	22.0	22.7	23.2	23.9	5.7	5.4	5.0	4.8	4.7	4.6	4.6	4.5
API 3	0.47	0.37	18.0	25.0	31.2	35.2	37.6	39.6	41.1	42.8	2.1	1.9	1.6	1.4	1.3	1.2	1.1	1.0
API 4	0.45	0.34	3.4	5.1	7.4	9.3	10.5	11.5	12.3	13.4	29.8	27.2	23.6	21.4	19.8	18.7	17.8	16.7
Cellulose	0.23	0.15	23.7	28.6	33.5	36.5	38.6	40.3	41.7	43.3	88.7	77.4	66.8	60.2	56.6	52.7	49.7	46.5
Croscarmellose Sodium	0.55	0.52	5.2	6.7	8.3	9.5	10.1	10.6	11.0	11.5	31.7	30.5	29.1	28.3	27.8	27.4	27.1	26.6
Crospovidone	0.42	0.39	5.2	7.0	8.8	10.3	11.1	11.7	12.2	12.8	11.2	10.6	9.7	9.3	8.9	8.7	8.5	8.3
Lactose 1 & MCC 1	0.55	0.53	3.0	3.7	4.4	5.1	5.5	5.8	6.1	6.4	199.2	194.1	184.7	178.6	174.3	171.2	170.9	165.8
Lactose 2	0.69	0.64	5.0	6.6	7.9	8.8	9.3	9.8	10.1	10.5	154.8	151.2	144.3	141.5	138.3	136.5	135.3	132.9
Magnesium Stearate	0.33	0.26	18.7	24.9	30.2	33.1	35.1	36.7	37.9	39.4	14.8	9.3	9.5	7.7	4.5	3.7	4.2	3.6
MCC 1	0.38	0.33	8.1	10.3	12.6	13.9	14.8	15.5	16.1	16.8	128.2	116.8	106.4	100.9	97.4	95.7	93.2	89.7
MCC 2	0.38	0.34	7.1	8.9	10.7	11.8	12.5	13.1	13.6	14.2	213.9	196.4	175.7	167.0	159.5	156.7	153.5	150.0
MCC 3	0.41	0.33	8.1	11.7	15.6	18.0	19.5	20.7	21.6	22.7	12.8	11.3	9.3	8.4	7.8	7.4	7.1	6.8
MCC 4	0.56	0.44	6.1	8.0	10.1	11.6	12.5	13.2	13.7	14.4	100.5	92.9	85.6	82.1	78.5	77.1	75.2	73.4
Silicified MCC	0.48	0.48	3.4	4.3	5.3	6.1	6.6	7.0	7.4	7.9	111.4	106.7	101.8	98.6	96.4	94.9	93.9	91.6
Starch 1	0.65	0.58	3.5	6.5	10.5	12.7	14.1	14.9	15.6	16.5	6.8	6.0	4.7	4.1	3.7	3.5	3.3	3.2
Starch 2	0.83	0.74	5.5	6.2	6.9	7.7	8.0	8.3	8.6	8.9	0.0	0.0	35.8	50.1	54.4	50.4	52.8	46.5
Starch 3	0.54	0.43	6.6	9.1	11.7	13.5	14.6	15.4	16.0	16.8	8.8	8.2	7.5	7.0	6.7	6.5	6.3	6.1

Table 15. Continued material property measurement data table.

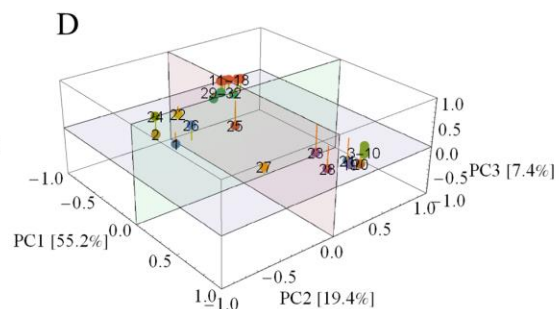
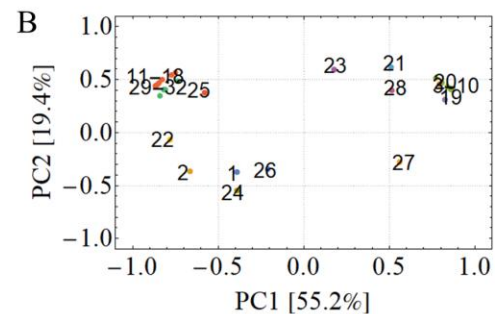
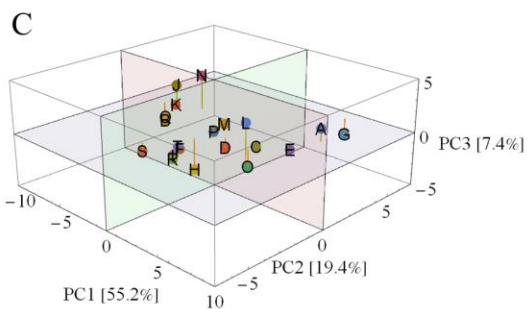
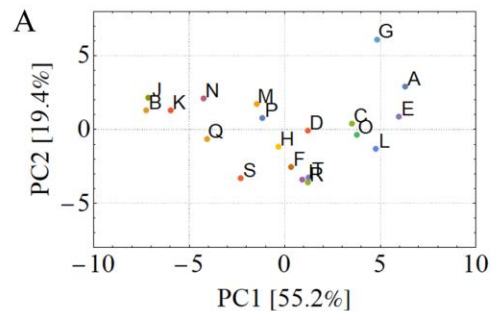
Material	Cohesion, kPa	UYS, kPa	MPS, kPa	FF	AIF, °	MCS, kPa	BEF, mJ	SI	FRI	SE, mJ/g	d10	d50	d90	D(p,q)
Acetaminophen	1.12	4.18	11.96	2.87	33.4	2.26	98.4	0.97	1.54	6.20	10.4	40.2	88.7	22.5
Anhydrous Calcium Di-Phosphate	0.00	0.38	9.60	27.45	34.5	2.68	483.5	1.14	1.34	5.32	62.7	167.0	229.5	75.5
API 1	0.71	2.71	11.31	4.18	34.7	2.36	87.9	0.89	1.80	5.83	8.8	37.7	92.3	20.7
API 2	1.01	3.30	9.65	2.93	27.1	2.37	164.3	1.04	1.12	5.19	34.0	111.5	184.0	67.3
API 3	1.17	4.54	12.24	2.70	35.7	2.03	53.5	1.18	2.39	7.63	3.9	13.9	28.3	8.5
API 4	0.43	1.45	9.19	6.39	28.7	2.71	54.1	1.13	2.40	5.58	16.9	44.7	80.7	30.1
Cellulose	1.29	5.95	17.84	3.01	43.1	2.24	205.9	0.62	1.41	14.00	22.3	55.8	116.0	42.3
Croscarmellose Sodium	0.24	1.08	13.64	12.64	42.0	2.49	327.2	1.16	1.62	7.60	19.0	35.1	71.5	29.3
Crospovidone	0.27	0.89	9.15	10.42	27.2	3.07	56.1	1.09	2.70	6.58	8.5	22.4	49.1	17.1
Lactose 1 & MCC 1	0.18	0.60	8.92	15.49	28.7	2.93	171.1	1.13	1.11	3.93	50.1	146.5	208.0	91.4
Lactose 2	0.09	0.32	8.83	28.03	31.8	2.64	233.3	1.16	1.11	3.87	48.8	118.0	180.5	85.0
Magnesium Stearate	0.56	1.76	9.45	5.65	24.8	3.14	12.9	1.45	3.73	4.71	4.1	12.2	31.7	8.6
MCC 1	0.38	1.53	12.09	7.96	37.9	2.53	276.6	1.06	1.64	8.04	20.9	57.9	112.0	40.4
MCC 2	0.58	1.69	8.63	5.11	21.4	3.24	110.7	1.04	1.16	3.92	28.1	97.0	145.0	56.0
MCC 3	1.22	4.75	12.68	2.67	35.7	2.09	82.6	1.05	3.07	10.79	7.9	21.8	45.7	15.3
MCC 4	0.50	1.97	11.49	5.89	36.4	2.43	254.5	1.12	1.46	6.86	19.3	56.7	104.0	37.6
Silicified MCC	0.13	0.43	9.03	22.75	28.2	3.08	154.5	1.08	1.14	3.85	26.8	95.7	144.0	54.3
Starch 1	0.71	2.12	8.73	4.13	22.6	2.94	48.2	0.92	1.38	3.07	8.6	15.1	21.8	13.5
Starch 2	0.13	0.39	8.38	22.58	23.9	3.38	169.9	1.03	1.25	5.07	25.5	49.3	78.9	41.3
Starch 3	0.74	1.95	8.58	4.41	15.6	3.81	44.1	0.97	1.38	7.72	9.3	31.3	69.8	19.0

Table 16. Similarity index results with labeling legend. Pairs with SIMI = 0 have similar material properties based on their scores of the PCA, whereas those with SIMI = 100 have different material properties.

	A	B	C	D	E	F	G	H	I	J	K	L	M	N	O	P	Q	R	S	T
A		100	15	50	1	87	0	99	85	100	100	20	100	100	37	100	98	80	83	78
B	100		100	92	100	90	100	73	95	13	0	100	74	43	100	77	20	98	38	100
C	10	74		0	0	43	9	35	44	76	72	10	62	69	0	58	55	38	36	39
D	30	57	2		28	46	31	30	49	62	53	34	62	60	27	58	38	33	12	39
E	0	95	0	44		65	8	66	62	97	95	0	86	96	7	82	85	62	68	63
F	53	58	24	32	37		54	1	0	58	54	22	46	48	11	34	19	16	2	20
G	25	96	44	81	34	100		100	100	94	100	61	88	94	41	92	100	100	100	95
H	58	47	32	33	43	27	47		32	57	48	43	40	61	14	30	25	42	11	49
I	55	66	28	41	38	0	61	11		66	63	20	58	59	12	46	31	15	9	19
J	97	14	100	100	99	88	93	90	93		2	93	66	0	100	71	11	98	47	94
K	86	0	82	73	86	75	85	63	81	0		81	57	16	86	61	0	84	26	84
L	28	96	28	67	13	59	53	79	53	93	93		92	88	30	87	79	62	64	60
M	54	39	37	45	47	40	28	13	48	33	32	44		16	27	0	8	58	29	57
N	77	41	76	83	79	71	67	83	77	11	26	68	50		77	56	10	80	45	72
O	32	81	7	41	10	37	13	20	36	82	81	18	59	78		51	61	43	46	44
P	54	41	33	40	44	30	32	0	38	37	35	40	0	22	20		6	49	21	49
Q	75	22	60	52	70	43	72	32	50	15	9	59	37	5	58	35		54	1	53
R	51	69	23	21	39	20	60	29	18	70	66	30	71	64	22	61	36		0	0
S	70	40	49	28	63	34	82	23	38	47	37	53	66	51	52	58	8	28		36
T	51	72	26	30	41	24	58	42	22	69	69	29	71	57	25	62	37	0	9	
U	3.14	2.41	3.00	3.14	3.00	1.06	5.90	3.42	1.06	2.64	2.41	4.33	1.02	3.81	3.52	1.02	3.35	1.39	3.96	1.39
V	14.0	14.0	11.0	9.5	13.4	10.1	13.6	9.5	10.6	13.7	12.5	13.5	9.0	11.5	11.7	9.0	11.5	10.5	12.2	10.8

Material Legend	
A	Acetaminophen
B	Calcium Di-Phosphate
C	API 1
D	API 2
E	API 3
F	API 4
G	Cellulose
H	Croscarmellose Sodium
I	Crospovidone
J	Lactose 1 & MCC 1
K	Lactose 2
L	Magnesium Stearate
M	MCC 1
N	MCC 2
O	MCC 3
P	MCC 4
Q	Silicified MCC
R	Starch 1
S	Starch 2
T	Starch 3
U	Minimum Distance
V	Maximum Distance

Material Legend	
A	Acetaminophen
B	Calcium Di-Phosphate
C	API 1
D	API 2
E	API 3
F	API 4
G	Cellulose
H	Croscarmellose Na
I	Crospovidone
J	Lactose 1 & MCC 1
K	Lactose 2
L	Magnesium Stearate
M	MCC 1
N	MCC 2
O	MCC 3
P	MCC 4
Q	Silicified MCC
R	Starch 1
S	Starch 2
T	Starch 3



Measurement Legend	
BD, g/ml	1
CBD, g/ml	2
1 kPa	3
2 kPa	4
4 kPa	5
6 kPa	6
8 kPa	7
10 kPa	8
12 kPa	9
15 kPa	10
1 kPa	11
2 kPa	12
4 kPa	13
6 kPa	14
8 kPa	15
10 kPa	16
12 kPa	17
15 kPa	18
Cohesion, kPa	19
UYS, kPa	20
MPS, kPa	21
FF	22
AIF, °	23
MCS, kPa	24
BFE, mJ	25
SI	26
FRI	27
SE, mJ/g	28
d10	29
d50	30
d90	31
D(p,q)	32

Figure 21. Two-dimensional plots for (A) scores and (B) loadings of the first two principal components of the material property database. Three-dimensional plots for (C) scores and (D) loadings of the first three principal components of the material property database. The numbers in square brackets next to the axis labels express the amount of variability in each PC.

CHAPTER VI

6. AIM 3: PERFORMING RESIDENCE TIME

DISTRIBUTION EXPERIMENTS AND MODELING

Acknowledgement of publication status:

The work contained in this chapter will be submitted for publication after the scheduled defense date on April 5th, 2018 to a journal yet to be determined. This work was written by the author of this thesis and was done in collaboration with:

Sara Moghtadernejad¹, Sarang Oka¹, Yifan Wang¹, Andres Roman-Ospino¹, Elisabeth Schäfer², Philippe Cappuyns², Ivo Van Assche², Mauricio Futran², Marianthi Ierapetritou¹, Fernando Muzzio¹

¹ Engineering Research Center for Structured Organic Particulate Systems (C-SOPS), Department of Chemical and Biochemical Engineering, Rutgers, The State University of New Jersey, Piscataway, NJ 08854, USA.

² Janssen Research & Development. Janssen Pharmaceutical Companies of Johnson & Johnson Beerse, Belgium

6.1. INTRODUCTION

The residence time distribution (RTD) methodology was introduced in 1953 by Danckwerts as a mean to describe non-ideal liquid mixing in chemical reactors [104]. This seminal concept, for which Danckwerts has been directly cited over 2,500 times, brought upon an extensive discussion regarding reactor behavior and paved the way to a subfield of chemical engineering science: reactor mixing. Within the reactor mixing literature RTD methods have been discussed in

more than 5,000 research articles and in excess of 50,000 articles RTD techniques are used to evaluate flow systems [228, 229].

Briefly described, RTD is a diagnostic tool that characterizes the distribution of time a material spends (i.e., *resides*) inside of a unit operation. This technique, which in the case of blending systems aims at describing temporal mixing (i.e., mixing occurring as a function of time inside of the unit), is performed by introducing a traceable material (hereon referred to as the *tracer*) at a known position of a unit operation and then tracking the location of the tracer material until it exits the system. The goal is not to provide information regarding the spatial mixing (i.e., the blend's homogeneity), but to describe the tracers residence time in the system. Differences in the mean and distribution of that residence time for various conditions can be used to determine the completeness of mixing inside of a system. Based on the data collected from RTD analysis, mixing patterns can also be characterized as ideal or non-ideal and mixing models having similar dynamics to the system can be developed, as described extensively in the chemical reaction engineering literature [230, 231].

In recent years, a growing number of industrial and academic research groups have examined the dynamics of continuous pharmaceutical equipment using established chemical engineering methods. Among the most used methods for characterizing equipment, the residence time distribution (RTD) has emerged as a major tool used as part of the development and control strategies [65]. Although RTD is not a novel concept in the engineering toolbox [103, 104, 228], its use to examine powder-based pharmaceutical processes is less common than for other similar solids or liquid processes. Yet, as the pharmaceutical industry begins to use this methodology more frequently, it is important to remember that it must be implemented carefully, in particular regarding the choice of tracers, to ensure compliance with the method's underlying assumptions.

In this chapter, specific focus is placed on investigating the effect of tracer material properties on RTD measurements for a continuous blending system using a single base material.

RTD measurements obtained for various tracers with different material properties were compared to determine how those properties affect the resulting RTD curves. This work further evaluates the differences between the measured RTDs as a function of their distribution metrics. The results were used to provide guidelines for selecting tracers that best describe the bulk powder transport inside of the blender and its blending behavior.

6.1.1. RTD application for equipment characterization

The RTD methodology has been extensively used in liquid systems to determine the hydrodynamics and mixing behavior in many chemical processes units. Examples of units include fixed and fluidized bed reactors, two-phase stirred tanks, heat exchangers, distillation and absorption columns, chromatography columns, and trickle bed reactors [228, 231, 232]. Besides being used in reactor and heat exchanger systems, RTD studies have been implemented to an extensive number of systems and fields including those in microfluidics [233, 234], hydrology [235], and pharmacokinetics and pharmacodynamics [236]. Noticeably, all these aforementioned fields relate to both liquid and/or gas systems, wherein the continuum assumption is reasonably well kept, and the mathematics for residence time distribution are straightforwardly applied.

Until recently, RTDs were rarely used to characterize the mixing behavior of solid processes [102, 237-239]. Several publications have recently emerged regarding the application of residence time distribution concepts in solids systems such as, batch and continuous mixing systems [240], rotary calciners [241-243], fluidized beds [216, 244-246], entrained flow gasifiers [247, 248], and biomass pretreatment reactors [249]. In pharmaceutical research, with the implementation and growing interest in continuous solid oral dose manufacturing, RTDs have been extensively used to characterize powder-based continuous processes in the manufacture solid oral dose products. In a series of publications, Gao et al. used RTD methods to characterize the blender performance [101], describe the dampening of feeder disturbances [250], and establish a parametric

space for blending based on a particular formulation [251]. Portillo et al. used RTD methods to characterize horizontal and inclined blenders and propose a mathematical model for the mixing occurring inside of the unit [196, 197, 252, 253]. Similarly, Berthiaux et al. used RTD methods to develop mathematical models explaining the mixing and powder movement inside of the blender, which included the mass accumulation in the system [254-258]. Most recently, Galbraith et al. proposed a mixing model for a inclined blender based on the results from an RTD experiment and implemented the model to evaluate the dissipation of upstream feeder disturbances on the material properties [259].

Mixing dynamics in feed frames have also been characterized using RTDs [260-265]. Most recently, work by Van Snick et al. focused on characterizing the RTD of continuous manufacturing lines for direct compression to establish performance metrics [198, 266]. Most notably, RTDs have been used to develop traceability algorithms to trace lots of raw materials in continuous processes [34, 47], develop feed-forward control strategies [267], and establish out of specification (OOS) ranges based on disturbance levels [34, 268, 269]. The use of RTD models for process controls has additional importance in situations where sensing-based PAT models cannot be used, for example, in situations where the API concentration is below spectroscopic detection limits. Despite the challenge of studying multiphase particle system, powder behavior in continuous dry granulators [268, 269] and wet granulators [270-272] have also been characterized using RTDs.

6.1.2. Important RTD experimental and modeling assumptions

When considering the application of RTD methods for equipment characterization, it is important to revisit the primary assumptions from which both experimental and mathematical understanding can be derived. The major assumptions and requirements provided by Danckwerts [104] and Nauman [228, 229] for the application of RTD as a characterization tool are listed below. They include that:

1. The system being studied is continuous (or semi-continuous) based on the addition and removal of components through streams with constant or intermittent flow.
2. The continuous (or semi-continuous) incoming and outgoing system flows have reached steady and equal values, indicating the system is now invariant throughout time or repeatable periods of time; these two conditions are known as *steady (or pseudo-steady) state*.
3. The inlet and outlet streams have unidirectional flows, so that once material and tracer enter the system it stays within the unit until it exits, never to return.
4. The addition of tracer materials does not affect the system's overall flow and the tracer is evenly distributed along the entire system's cross-section. Although observer effects are expected when studying any system, this last assumption aims at reminding experimenters to minimize this error.

These assumptions were critical in the development of RTD as a concept alongside with the mathematics that made it an important diagnostic tool for characterizing process equipment. In recent years, with the advent of numerical methods and other simulations tools (e.g., computational fluid dynamics, discrete element methods), several researchers were able to perform RTD experiments and/or simulations without closely following assumptions 1 and 2; effectively developing a field of unsteady state (i.e., dynamic) RTDs [229]. However, for experimental purposes, it is critical to follow the aforementioned assumptions to establish a clear and consistent methodology for evaluating and performing RTD experiments.

Note: given the general knowledge of RTD methods, the general introduction of the RTD material in this chapter is provided in Appendix C (page 250, section 9.3) and Appendix D (page 257, section 9.4). Within Appendix C, tracer properties and addition methods are covered. In Appendix D, RTD calculation methods, different phenomenological models, and assumptions are covered. Both of these appendices contain information needed to understand the results of this chapter, but in order to minimize the amount of background, the content was placed as background.

6.2. MATERIALS AND METHODS

6.2.1. Materials

Based on the clustering results shown in Table 10 and with the objective of minimizing the number of tests and materials needed for this experiment, a subset of materials from Table 8 was selected to reduce the number of on-line measurement calibration methods needed for the RTD experiments. A material from group 3 was selected as the base because it would represent more reliably the well-flowing behavior often observed in formulations being sent through mixing systems.

Lactose 1 and MCC 1 and silicified MCC were not selected given that these materials are mixtures of two commonly used ingredients, a fact that could make the detectability with other tracer materials difficult to calibrate and assess. Based on this exclusion, anhydrous-calcium diphosphate, lactose 2, and MCC 2 remained as the potential base materials. Taking into account material feedability (i.e., ability to feed material), previous experience, and material availability, MCC 2 was selected as the base material.

Following the selection of the base, materials that would serve as tracers were selected. The aim of this work is to test whether tracer material properties affected the system's RTD. With this in mind, a total of seven tracers, ranging widely in both flow and bulk properties, were investigated. From Table 10 two materials from group 1, four materials from group 2, and one material from group 3 were chosen as tracers.

From group 1, acetaminophen and API 3 were selected as tracers. API 1, cellulose, and magnesium stearate were not selected as tracers because of the materials' toxicity risk, NIR similarity with the base material, and stickiness to equipment surfaces. Selected group 2 materials

included starch 1, API 4, crospovidone, and croscarmellose sodium. The remaining MCCs and starches in group 2 were not used because of their chemical similarity with respect to the base material. Lastly, from group 3 anhydrous calcium di-phosphate was chosen given its distinct chemical differences with the bulk, which eased the development of an online sampling method.

Table 17 lists the values of the SIMIN matrix for the materials selected for this study. Notably, only anhydrous calcium di-diphosphate had a value of less than 50% for the SIMIN value for the base MCC 2. After MCC 2, the material with the most similarity based on the metric was starch 1. Interestingly, starch 1 was the only material that did not have a SIMIN value with another material over 70%. This indicates that starch 1 was the material with the most similar from all of those selected for this study.

Table 17. SIMIN metric values for the materials selected for the RTD experimentation

	A	B	E	F	H	I	N	R
A		100	0	53	58	55	77	51
B			95	58	47	66	41	69
E				37	43	38	79	39
F					27	0	71	20
H						11	83	29
I							77	18
N								64
R								

Material Legend	
A	Acetaminophen
B	Calcium Di-Phosphate
E	API 3
F	API 4
H	Croscarmellose Sodium
I	Crospovidone
N	MCC 2
R	Starch 1

The relatively wide range of SIMIN values being used here to characterize the RTD as a function of material properties provides a reasonable mean of evaluating the effect of the material properties on the method.

6.2.2. Equipment

Four processing and online testing units were used for the experiment: a continuous powder feeder, a horizontal paddle blender, a near infrared (NIR) acquisition instrument, and a vibratory feeder. The equipment configuration is shown schematically in Figure 22. Additional information on the equipment and their configuration for the experimental procedure is provided below.

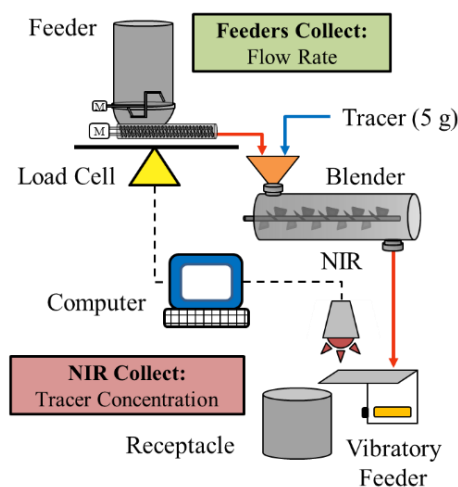


Figure 22. Schematic of the equipment experimental set up.

6.2.2.1. Feeder

A single K-Tron K-CL-SFS KT20 (Coperion K-Tron Pitman Inc., Sewell, NJ) feeder fitted with a coarse concave screw configuration and a C type motor was used to maintain a steady flow of base powder into the continuous mixing system. Based on the vendor specifications this feeder had a maximum nominal screw speed of 154 revolutions per minute (RPM) and a volumetric displacement capacity ranging between 0.3 and 200 L/hour. The feeding operation was performed under gravimetric control using the built-in controllers systems under the “normal” control settings. A transition hopper with a wide aperture was placed at the feeder’s screw outlet (i.e., blender’s inlet) to channel the flow of powder to the subsequent mixer. The transition hopper was the point at which tracer was added into the system.

6.2.2.2. Blender

A modified Gericke GCM 250 mixer (Gericke USA, Somerset NJ) was used as the blending system. The modification to the original unit includes a specially fitted glass top casing that allows for visualization of powder movement along the blender’s length. The unit was fitted with a forwards-alternating-forwards blade configuration, wherein the first and last one-third (1/3)

blade sections were placed in a transport position (i.e., forward pushing) and the middle one-third section had an alternating sequence of forward-backward pushing blades. This blade configuration was selected based on previous experience [221, 273] and remained fixed throughout the experimental design.

6.2.2.1. *Near infrared interface*

Acknowledgement of collaborative work and contributions:

The chemometric section of this work was developed as part of a collaborative effort within the Engineering Research Center for Structured Organic Particulate Systems (ERC-SOPS). Development, calibration, and implementation of NIR chemometric methods were performed by Dr. Andres Roman-Ospino. Dr. Roman-Ospino worked in collaboration with the author of this thesis, who provided Dr. Roman-Ospino with the list of materials, target concentrations, and conditions needed to develop the chemometric models. The author of this thesis is very grateful to the work done by Dr. Roman-Ospino developing the chemometric methods.

The vibratory feeder from a sample divider PT 100 (Retsch, Haan Germany) was used at the blender exit as the interface between the NIR instrument and powder samples. A FT-NIR Matrix (Bruker Optics Billerica, MA, USA) was used for spectral acquisition. The fiber optics probe with NIR source and collection fiber was adapted to the vibratory feeder for diffuse reflectance measurements. OPUS 7.0 from Bruker was used to control the NIR instrument and to construct the calibration models. The interface between the sample and the NIR instrument is a critical part for any in-line method development. The NIR interface is responsible of delivering the sample to the instrument in a way that allows representativeness, minimizing the modification of physical properties in the sample and giving all the points in the sample the same probability to be analyzed [274].

Figure 23 shows the NIR interface used here, which was included a vibratory feeder that conveys the powder at the blender's exit in front of the probe for diffuse reflectance spectral acquisition. The proposed interface allows representativeness via 1-dimensional sampling [275].

As a consequence, the powder blend moves continuously without interruption or confinement that affects the flowability. The NIR interface was used both for calibration and for the actual RTD experiments to avoid method transfer issues such as off-line models vs. in-line acquisition. Calibration blends were prepared using a Laboratory Resodyn Accoustic mixer (LabRAM) by using 60g's for two minutes for a mass of 100g of base-tracer. This configuration ensures the minimization of agglomerates in cohesive materials and is a suitable system to create standards for PLS methods [199, 276]

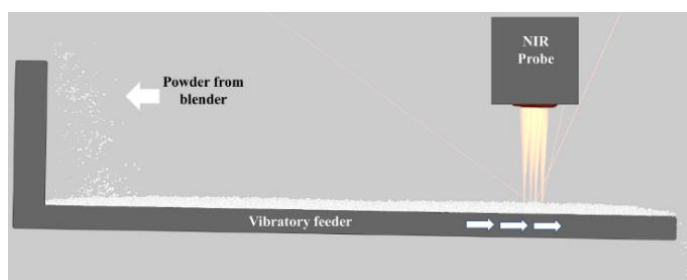


Figure 23. Near Infrared (NIR) sampling interface for RTD experiments

Each calibration blend was transferred to the vibratory feeder interface for NIR spectral acquisition. The vibration frequency was adjusted to obtain a constant flow of blend in front of the NIR probe. Sixty (60) spectra for each concentration (0 – 9% w/w) were acquired to construct the seven calibration models. Forty (40) additional spectra were acquired using the same in-line approach and stored for further testing of the models.

6.2.3. RTD experimental procedure

The procedure to perform the RTD experiments was developed giving special consideration to the assumptions and requirements. First, the blender was allowed to reach steady state by running the system until no changes were observed in the outlet flow rate. Second, a mass of tracer sufficiently large to be within the detectable ranges of the online chemometric models was measured. Since the online chemometric models were built using a 0 – 9% w/w tracer concentration calibration set, it was decided to introduce a tracer mass equivalent to 4.5% of the blender's steady

state mass hold up. With this relatively small percentage of tracer mass, it would be reasonable to assume that the tracer would be detectable by the chemometric methods but would not drastically change the properties of our bulk material inside the blender. Third, a series of three pulses for each tracer were introduced in a sequential manner, allowing for the system to completely wash out the tracer of each pulse before introducing a subsequent one. The focus during pulse addition was on delivering the entire tracer amount in a single instance (i.e., less than 1 second). Addition of the tracer to the system was confirmed visually by noting the tracer entered the process stream. Complete washout of the pulse was ensured before adding a new pulse by observing a zero value on the on-line concentration predictions for at least forty-five (45) seconds. Lastly, after the three pulses were performed for each ingredient, the feeder-blender system was stopped and the blender was vacuumed to prevent any effects of residual tracer on subsequent tests. This four step process was repeated for all tracers.

6.3. RESULTS AND DISCUSSION

Acknowledgement of collaborative work and contributions:

As disclosed previously, the NIR method development and calibration efforts were performed by Dr. Roman-Ospino, a collaborator of this work. As an acknowledgement of the outside contribution and because the results are critical for the discussion of this work, Dr. Roman-Ospino's work was placed in Appendix E of this thesis (page 273, section 9.5).

6.3.1. Feeder-blender characterization at steady state

To ensure that all relevant information for the feeder-blender system was collected, the system's feeding and blender mass hold up were characterized before performing the tracer experiments. A detailed description of this procedure is presented in a recent publication from the Muzzio group [46]. Fifteen (15) kilograms of base MCC 2 were added to the K-Tron feeder, after which the recommended startup sequence was performed. The startup sequence included screw filling and feed factor calibration, during which no major feeding issues were observed. The

feeder's feed factor at maximum fill was estimated as 32.5 kg/h, which indicated – based on controllable feeding ranges – that the maximum recommended flow rate was 26 kg/h, or 80% of the feed factor value. The mass of MCC 2 remaining in the feeder was recorded for subsequent blender mass hold up calculations.

After the feed factor calibration, the blender was powered on and set to a blade speed of 100 revolutions per minute (RPM). Once the blender reached the desired blade speed, the feeder flow was initiated and set to 10 kg/h. Throughout the entire experiment, the mass flow rate was closely monitored to ensure there were no major flow rate deviations. The resulting flow rate oscillated around the set point with a relative standard deviation (RSD) of 2.6%.

Powder exiting the blender was collected in a receptacle as shown in Figure 22. The system was allowed to continue for four minutes, which provided sufficient time for the system to reach a steady state (i.e., no changes in the system as a function of time). After four minutes, both the feeder and blender were simultaneously stopped. The mass remaining in the feeder and collected in the receptacle at the blender's outlet was noted. Using the measurements for starting feeder mass ($M_{feeder,start}$), end feeder mass after four minutes ($M_{feeder,end}$), and mass collected in the receptacle ($M_{receptacle}$) the mass hold up inside of the blender was calculated by subtracting the latter two values from the starting feeder mass (i.e., $M_{blender} = M_{feeder,start} - M_{feeder,end} - M_{receptacle}$). This process was repeated three times ($n = 3$), yielding an average mass hold up of 140.1 ± 2.0 g.

The system's space-time ($\tau_{space\ time}$) was then computed using the results from the mass hold up characterization and average feeder flow rate. The result yielded a $\tau_{space\ time}$ of 50.5 ± 0.7 seconds. This result was used as the mean residence time of our bulk MCC 2, since no major dead spaces inside of the system were observed.

6.3.2. RTD experiments and concentration profiles

The RTD experiments were performed using the procedure described in section (2.4). Figure 24 shows the concentration versus time plots for the 21 tracer experiments performed. The instance of tracer addition is denoted in Figure 24 by dashed vertical lines. Each tracer was added after the previous tracer had completely cleared the blender. The concentration of each tracer was measured in weight percent (i.e., % w/w) using the NIR methods. Tracer concentrations ranged from 0 to 6.88% w/w, depending on the tracer. The introduction of each pulse was carefully monitored throughout the experiment. The entire pulse was introduced quickly and evenly into the blender. As shown in Figure 24, the tracer curves were highly reproducible, indicating that our procedure was sufficiently accurate.

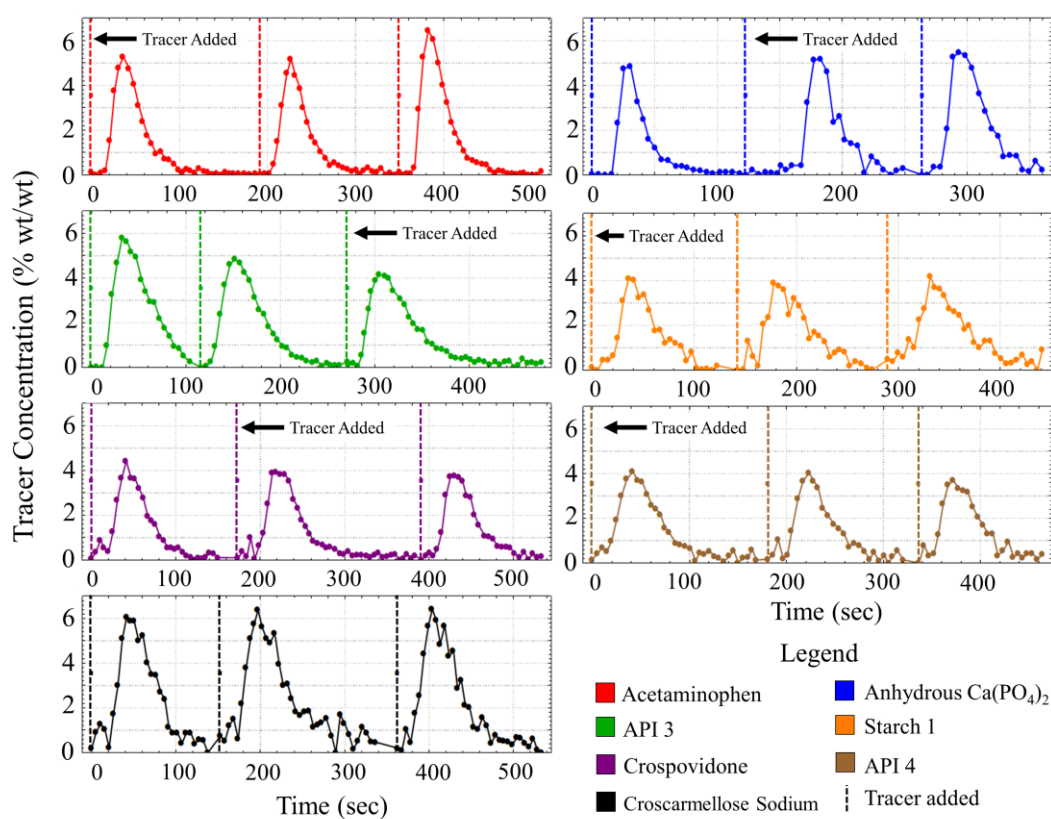


Figure 24. Concentration v. time for each of the material tracers. Vertical lines represent tracer addition time points.

Figure 24 shows that several tracer materials had more noise in their measurement based on the fluctuation of points on the distribution. Acetaminophen, anhydrous calcium di-phosphate,

crospovidone, API 3, and API 4 showed relatively smooth distribution curves. On the other hand, starch 1 and croscarmellose sodium showed more variation between the distribution points. These differences in noise may be attributed to: (1) poor mixing of material along the length of the unit or (2) the chemometric model used to determine the tracer's concentration. Both of these hurdles relate to the tracer selection standards based on their properties: (1) represents the system well by not segregating and (2) it is easily detectable in the process stream.

Poor micro-mixing of the tracer in the bulk leads to pockets of well mixed tracer and bulk, which may cause oscillations of the concentration measurement as a function of time. The amplitude of these variations are important since they may affect the overall interpretation of the system's RTD. Noisy chemometric calibrations can also lead to a similarly noisy output of the RTD, which is why it is especially important to develop chemometric models minimizing such variability. Minimizing the chemometric model's variability is also critical when using RTD models for control purposes as they may be used to establish confidence intervals for both NIR and the RTD measurements. For the two tracers with the highest variation, the chemometric models had the highest RMSE variation due to similarities in the spectral bands. This increased noise on the measurement results in a higher amplitude of variation, which in turn may negatively affect the RTD calculations. To minimize these fluctuations, several new methods have been implemented in recent work regarding the optimization of chemometric methods [277, 278].

After reviewing the profiles provided in Figure 24 and ensuring there were no overlap between pulse experiments, the curves were spliced at the tracer introduction time points for further analysis. The resulting data were treated by shifting the time axis to the re-zeroed position for each of the three curves, making all data curves initiate at time equal to zero. These curves were then used to compute the residence time distribution's probability distribution function, discussed in the following section.

6.3.3. Residence time distribution and metrics

The RTD's probability distribution function (PDF) was computed using the tracer results from Figure 24 and the equation in Table 41. The concentration plots provided in Figure 24 were thus transformed to a standard scale (i.e., the $E(t)$ distribution) for which a more clear comparison between the tracers can be made. Figure 25 shows the PDF for the three pulse experiments for each material selected. The variability between each pulse addition for a given tracer was relatively small, which confirmed the tracer pulsing procedure was reproducible.

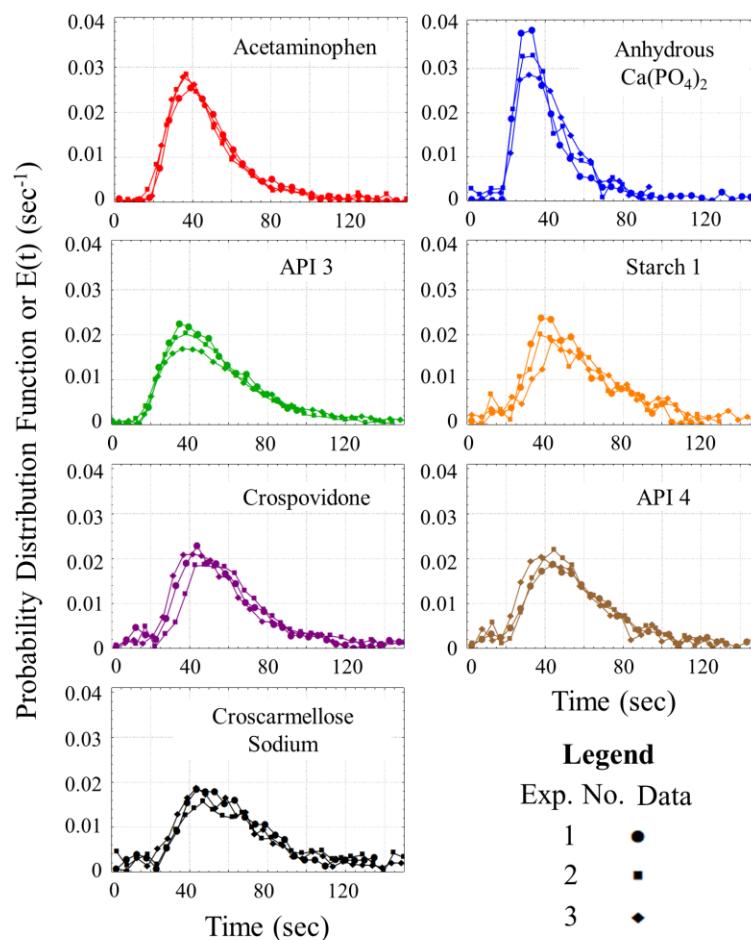


Figure 25. Residence time distribution probability distribution function graphs for each material

Given the standardization of the tracer concentration measurement, Figure 25 shows there are clear differences between the maximum values for the distributions for each of the tracers.

Anhydrous calcium di-phosphate had the highest maximum (i.e., peak) tracer PDF value (between 0.029 and 0.038 sec⁻¹), while croscarmellose sodium had the lowest maximum PDF value (between 0.017 and 0.020 sec⁻¹)

All tracer curves shown in Figure 25 presented two major features: (1) a delay time between time zero (i.e., tracer insertion time) and the first major increase in the PDF value and (2) a degree of right skewness, characterized by a front ended distribution and a long tail towards the higher time points. The first feature was associated with the minimum time needed for powders to traverse the blender's length of before reaching the outlet. This time is characteristic of powder systems and was in accordance with previously studied blending systems [65, 196, 259, 279].

Using the PDF values, the RTD metric values were calculated using the equations listed in Table 43. The resulting mean residence time (MRT), mean centered variance (MCV), and skewness for each of the experiments' RTDs are presented in Table 19. The MRT, MCV, and skewness for all tracers averaged 54.3 ± 8.3 seconds, 21%, and 11%, respectively. Between all tracers, the MRT ranged from 41.6 to 64.7 seconds, which yields a time window where the space-time calculated for the bulk MCC 2 can be found. These results were in agreement with previous work performed on this system, wherein a similar material to our MCC 2 was used as a the bulk [279]. The MCV and skewness ranged from 18 to 24% and 3 to 29%, respectively. All curves had positive values for skewness, as seen from the results of Table 19, which indicates that all distributions shared right skewness.

INSERT Table 19 HERE

The relative standard deviation (RSD) for the MRT measurements within each material did not exceed 15%, confirming that the triplicate tracer experiments offered a reproducible result with respect to the MRT. API 3 and crospovidone had the largest RSD in their RTD, equal to 14% and 12%, respectively.

MCV values were relatively similar between all materials, as seen by their average results. Nevertheless, it is important to note that these variance measurements provide a larger error than the MRT values, as they require to repeat the numerical integration of the original concentration data twice. Moreover, the MCV metric is based on the estimation of the RTD as a normal distribution, making the measure less reliable for other distributions. Thus, these values must be compared with each other using variance testing techniques, which are discussed in the subsequent section. Similarly, the results for skewness yield an even larger potential for error, and thus are solely used to provide a quantitative confirmation that the distributions share some right skewness. The positive skewness indicates that these distributions are not normal, making measures of moments about the mean difficult to interpret without a more rigorous statistical approach.

3.6 Comparison of RTD metrics

The effect of different materials on the MRT were evaluated using a One-Way ANOVA test. MCV and skewness were not included as part of this analysis given that these metrics do not follow a normally distributed set of errors, and thus make the application of ANOVA not a correct approach. The ANOVA tested the null hypothesis (H_0) that all of the means for the MRTs were statistically different based on the material used as tracer. The ANOVA estimated, based on the results provided in Table 19, there were statistically noticeable differences between the means of the MRT ($p = 0.002$) for the samples studied. The results indicate that the observed within-group variability in MRT values is small enough that statistical significance can be demonstrated even when just three experiments per group are performed.

The differences in MRT indicate that tracer materials take different times to traverse the blender, which reveals that materials with different properties travel at different speeds inside of the unit. This result hints at the possibility of differential mobility in convective systems, particularly those whose length may provide sufficiently different residence times between materials. In batch systems, differential mobility can cause extensive segregation.

To further evaluate the relationship between the statistically dissimilar means of the MRT, a pairwise means comparison was performed using Student's T-test for pairs of MRTs using an alpha of 5%. The results of this analysis, which indicate the statistical similarity between two pairs and automatically clusters them into groups based on those similarities, are shown in Table 18. The space-time of MCC 2 was included in this comparison to determine if the tracer MRT's were similar to those of the bulk and thus provide a picture of the base material using RTD. The results of the pairs comparison indicate there are four groups of statistically noticeable MRTs, where within each group the MRT means are found to be statistically similar (i.e., not significantly different) from each other.

Table 18. Results for mean comparison of pairs using Student T-test for the MRT. Materials that share the same letter have similar statistically noticeable means (p -value < 0.05)

Material	Material Property Group	MRT Group				Mean
		A	B	C	D	
Acetaminophen	1	*	*			49.2
API 3	1		*		*	54.5
API 4	2		*		*	54.1
Croscarmellose Sodium	2			*		64.7
Crospovidone	2			*	*	59.5
Starch 1	2		*	*	*	57.1
Anhydrous Calcium Di-Phosphate	3	*				41.2
MCC 2 ^a	3		*			50.5

^a MCC 2 value represents the bulk material's space-time, not the MRT

The results in Table 18 indicate that six out of the seven tracers had statistically similar MRTs with two or more tracers. The bulk MCC 2 had statistically observable similarities with four tracer MRTs. The only tracer to have only one statistically similar MRT with another tracer was anhydrous calcium di-phosphate, whose MRT was similar to acetaminophen's as shown in group A.

With the exception the materials in group A, the remaining tracer materials are grouped with materials that have relatively similar properties, as shown in the grouping from Table 10. Both of the tracers belonging to group 1 were found to have statistically similar MRTs, as shown by

group B. Interestingly, the two group 1 materials were also found to have statistically similar MRTs to starch 1 and API 4. Table 14 and Table 15 showed that the four materials in group B exhibited similar flow function coefficients, ranging from 2 to 6.5. Tracers from Table 10's group 2 were all similar with one another, with the exception of croscarmellose sodium, which is only shown to have statistical similarity with crospovidone and starch 1 in group C. Thus, the results indicate tracer materials with similar flow properties (e.g., permeability, flow function coefficient) provide statistically similar MRTs.

The similarity between tracer MRTs and the base material was compared using the space-time result from the feeder-blender characterization. The goal was to determine which tracer material would yield similar time values to those calculated using the space-time measurement. Remarkably, MCC 2's space-time did not share statistical similarity with the MRT of anhydrous calcium di-phosphate, which in accordance to the clustering results had the closest flow behavior to the base (i.e., both materials were in group 3). This result may be attributed to the fact that, although both materials are grouped in Table 10, their properties are widely different. For instance, the flow function coefficient difference between anhydrous calcium di-phosphate and MCC 2 is almost a five-fold (5x) difference. This vast difference may lead to significant variations in MRT and therefore show that not all materials that fall within the same property groups may be used. To further examine this hypothesis it was observed that MCC 2's space-time shared statistical similarity with the MRT of tracer materials listed in group B on Table 18. All of these materials share the same range of flow function coefficient and cohesion values, which led to the conclusion that this property was important to match the residence time of a material in the system.

Starch 1 had the most statistical similarities with other tracers' MRTs as well as the bulk MCC 2, as shown by belonging to three of the four groups shown in Table 18 (i.e., groups B, C, and D). This result indicates the starch 1 may be used as a tracer to obtain similar MRTs to the other five tracers as it shares statistical significance with the other tracer materials and describes

the space-time behavior of the base most similarly. Starch 1 had a range of SIMIN values ranging between 15 and 70%, which indicated that the material was relatively similar to all of the other tracers. Starch 1 shared property commonalities between all the five tracers it had similar MRTs, particularly with regards to permeability, flow function coefficient, and particle size. On the other hand, bulk density, a common property between starch 1 and anhydrous calcium di-phosphate, did not appear to be a good predictor of similarity between the MRTs. Given that previous findings had established a correlation between the properties, this result was investigated more thoroughly using a multivariate test in the following section.

6.3.4. RTD comparison using models

6.3.4.1. Axial dispersion (AD)

To accurately represent the blending system, Equation 61 was transformed to consider: (1) time in units of seconds and (2) the delay time exhibited by all PDFs. Since the data is provided in units of seconds, the normalized time variable θ was transformed to the original time variable. To account for the time delay, a time-shift convolution integral of a plug flow system's equation was performed on Equation 61. The plug flow system's equation is represented by a unit step, as discussed in the introduction. Equation 14 shows the result of these transformations to 61, wherein the time delay ($\tau_{delay,AD}$) is considered.

$$E(t) = \frac{u(t - \tau_{delay,AD})}{\tau_{dispersion}} \sqrt{\frac{Pe \tau_{dispersion}}{4\pi (t - \tau_{delay,AD})}} \text{Exp} \left[-\frac{Pe \left(1 - \frac{(t - \tau_{delay,AD})}{\tau_{dispersion}}\right)^2}{\frac{4(t - \tau_{delay,AD})}{\tau_{dispersion}}} \right] \quad 14$$

Using Equation 14 and the PDF values for each of the tracer experiment, the regression of Pe , $\tau_{dispersion}$, and $\tau_{delay,AD}$ was performed. The obtained RTD curves had a coefficient of determination (R^2) value above 95%, a MAPE value under 15%, and all variables showed statistical significance using an alpha value of 5% (i.e., p-value < 0.05).

Table 20 shows the regressed coefficient results of 14. The results show an average Pe for tracers' systems of 5.61 ± 1.58 , an average $\tau_{delay,AD}$ of 12.8 ± 5.9 seconds, and a $\tau_{dispersion}$ of 32.6 ± 8.4 seconds. Within each of the tracer materials the relative standard deviation of Pe ranged between 11 and 44%, wherein acetaminophen had the lower and croscarmellose sodium the larger value. The larger variance in Pe for croscarmellose can be attributed to slight differences in the distributions width. This slight variability in the distributions' width may appear to be insignificant, yet it is one of the critical aspects to be capture while using the model dependent method of comparing RTD curves. Notably, the values of Pe were between the pre-established ranges, which confirmed that the open vessel boundary condition was a suitable model.

INSERT Table 20 HERE

The delay time ($\tau_{delay,AD}$) RSDs within each tracer ranged between 16 and 71%, indicating this parameter was the one with the higher variability compared to the other three regressed constants. The reasoning behind this high variability can be attributed to the relatively high noise in the concentration profiles at the beginning of each pulse experiment. Starch and API B had the largest RSD values for the delay time, calculated at 70.6 and 64.6%, respectively. We can see from Figure 25, that starch 1 had two off trend points due to noise at the beginning of experiment 3 that forced the curve to regress a shorter delay time. The potential for off trend values to significantly affect the regressed coefficients is one of the major drawbacks of this methodology. To mitigate the effect of off-trend values, it is important to closely monitor the statistical significance of all the regression terms while performing the regression. The residence time due to axial dispersion ($\tau_{dispersion}$) resulted in the lowest within-tracer RSD values, ranging between 5 and 30%. This indicates that $\tau_{dispersion}$ was the most reproducible value for all experiments. Anhydrous calcium di-phosphate had the lowest $\tau_{dispersion}$, followed by acetaminophen.

6.3.4.2. Tank-in-series

Similarly to the axial dispersion equation system, in order to accurately represent the delay time observed in the data, the tank-in-series equation shown in Equation 66 was transformed to include the convective transport time ($\tau_{delay,CSTR}$). Equation 15 shows the transformed tank-in-series in real time units.

$$E(t) = \frac{u(t - \tau_{delay,tanks})}{\tau_{tank}} \frac{Exp \left[-\frac{t - \tau_{delay,tanks}}{\tau_{tank}} \right] \left(\frac{t - \tau_{delay,tanks}}{\tau_{tank}} \right)^{n_r - 1}}{(n_r - 1)!} \quad 15$$

Using Equation 15, n_r , τ_{tank} , and $\tau_{delay,tanks}$ were regressed from the experimental data. The τ_{tank} variable was presented as the average residence time in all tanks ($\tau_{tanks-in-Series}$) to more easily compare with previously calculated results. Similar to the axial dispersion model, all regression curves had a coefficient of determination (R^2) value above 95%, a MAPE value under 13%, and the all variables showed statistical significance using an alpha value of 5% (i.e., p-value < 0.05).

Table 21 shows the regression results for the tank-in-series equation. The level of dispersion in the system was shown to be relatively high for this system, given that the average number of tanks (n_r) for all blends was 2.17 ± 0.36 . This relative low number of tanks also indicates that the material travels as a bulk along the unit's length and progressively is back mixed with the incoming material. The average residence time in all tanks ($\tau_{tanks-in-Series}$) for all materials was 35.57 ± 8.6 seconds, which resulted in an average residence time per tank (τ_{tank}) of 16.52 ± 4.06 seconds. The $\tau_{delay,tanks}$ resulted in an average value of 20.91 ± 3.78 seconds. Notably, the RSD for the number of tanks and the residence time in all tanks were relatively small, ranging between 4 and 17%. This low RSD from the regression indicates this model has robust regression values that account for the system's variability. The RSD for the delay time within materials was also relatively small, ranging from 2 to 26%. Croscarmellose sodium was the material with the highest

RSD, which can be attributed once again to the distribution's width and high variability in the starting pulse times.

INSERT Table 21 HERE

6.3.5. Relationship between models and numerical MRT

The regressed results between the RTD models and the numerically calculated mean residence times were compared. Figure 29A shows the relationship between the Peclet number (Pe) and the number of tanks (n_r) for each of the regressed values. There was a positive relationship between the two values, as expected given the model formulations. Most Pe values are between the $y = 2x$ and $y = 2x + 1$, which indicate the values of Pe were twice those of the number of tanks. This result is in agreement with the findings from [103] who proposed the relationship between the Pe and n_r by equating the variance between the two models shown in 69. This relationship was used by Wang et al. [62] to correlate the results from number of tanks to the Peclet number. Figure 29B shows the relationship between $\tau_{delay,AD}$ and $\tau_{delay,tanks}$.

Remarkably, the $\tau_{delay,AD}$ was consistently lower than $\tau_{delay,tanks}$. This result, can be explained by the open vessel boundary conditions of the axial dispersion model, wherein a pulse system introduced instantaneously at the systems $z = 0$ position is allowed to disperse in both the negative and positive axial position. The effect of having dispersion in both directions, allows for the distribution to have smoother tails at both ends, and thus in order to allow for a minimal value of the sum of squared errors during regression, it must move the starting delay time to an earlier point. An example of this case can be observed by the starch 1 value at the lower right corner of Figure 29B. As noted previously, the starting values for the concentration plot for starch are noisy, therefore it leads to a solution for the regression that is relatively infeasible for this system. Nevertheless, a linear correlation between most of the points was observed, wherein values were just shifted towards the right of the graph. A potential solution to the differences between the two

values includes using the closed boundary system solution, to avoid dispersion to occur at the systems inlet.

INSERT Figure 29 HERE

Figure 29C shows the correlation between $\tau_{dispersion}$ and $\tau_{tanks-in-series}$. There was a relatively high degree of correlation between the two sets of values ($R^2 = 78\%$), which indicated both models resulted in similar residence time values. The material with the highest differences between the two parameters was croscarmellose sodium, which appeared to have distinct differences that were attributed to the introduction of the tracer pulse. Lastly, Figure 29D shows the parity plot between the numerically integrated mean residence time and the regressed mean residence time by the two models. The mean residence time from the regressed models were calculated by adding the delay time to the related mixing residence time (i.e., $\tau_{MRT-CSTR} = \tau_{delay,tanks} + \tau_{tanks-in-series}$ and $\tau_{MRT-AD} = \tau_{delay,AD} + \tau_{dispersion}$). The results show a strong linear correlation between the regressed mean residence times, wherein the correlation coefficient R^2 for the tanks-in-series and axial dispersion models were 92% and 90%, respectively. Notably, the axial dispersion mean residence time was consistently lower than the integrated value; a result that can be attributed to the shorter time delay ($\tau_{delay,AD}$).

6.3.6. Effect of material properties on MRT

After comparing the MRT results between materials and establishing that different materials showed statistically different MRTs, it was noted that developing a level 2 model for RTD and a subsequent level 3 model would be difficult because both the material properties of the tracer and the bulk appear to affect the measurement. Thus, the analysis primarily focused on establishing the effect of material properties on the measurement of the MRT.

A multivariate linear correlation analysis was performed to relate the material properties measurements from Table 14 and Table 15 with the tracer residence time results. The multivariate

analysis determined the level of correlation between the material property measurements and the MRT, as well as the level of statistical significance of the correlation using the p-value. Figure 26 shows the results of the correlation analysis between all of the measured material properties and the MRT results.

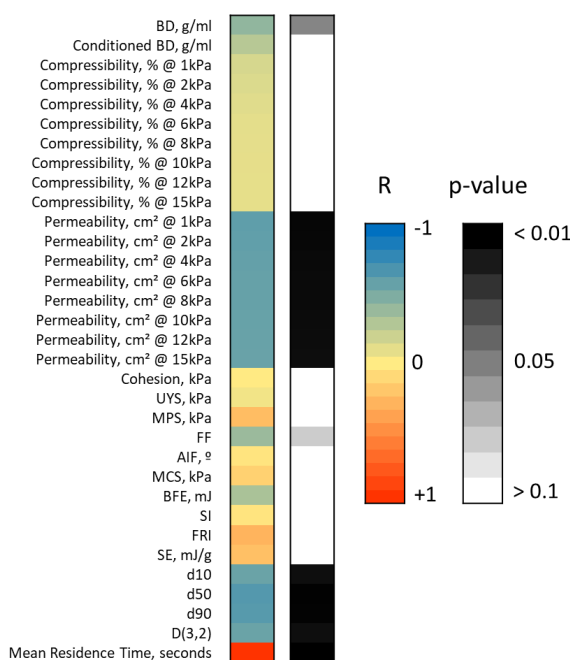


Figure 26. Multivariate linear correlation analysis between material properties reported on Table 14 and Table 15 and the tracer mean residence time (MRT). R is the correlation value and p is the statistical significance value

Figure 26 shows the correlation value (R) between each material property and the MRT. The results indicate that both permeability and particle size measurements had a strong negative ($R < -0.5$) correlation with the MRT, while other material properties had weaker correlations ranging from -0.5 to 0.5 . Particle size d_{90} and d_{50} had the largest correlation values of -0.66 and -0.67 , respectively. More importantly, the correlations between permeability and particle size appear to show significance, with p values less than 1% (i.e., $p\text{-value} < 0.01$).

Two material properties had results that indicated both had a correlation with the MRT: bulk density and flow function coefficient (FF). Bulk density had a moderate correlation value (R

= - 0.43) with a level of statistical significance $p = 0.052$, and FF had a relatively low correlation value ($R = - 0.39$) with a p -value = 0.080. Thus, these two material properties appear to have an impact on the MRT given that, with the work performed, there is not sufficient proof that the properties do not have an impact on the MRT.

The correlation between the permeability, particle size, bulk density, and flow function coefficient properties measurements with respect to MRT indicate that these material properties have a negative impact on the RTD metric, meaning they decrease the value of the MRT as the material property value increases. This result is in agreement with the hypothesis that materials with larger particle sizes travel at faster velocities (i.e., take less time to travel a particular distance) than smaller particle counterparts. Further, the result also indicates that materials with higher bulk density and better flowing behavior have travel faster through the unit given that they do not provide a high resistance to flow.

Using these findings, some recommendations for selecting powder tracer materials for performing accurate RTD experiments are provided in the subsequent section.

6.3.7. Recommendations for selecting a tracer and performing RTD experiments

Based on the established tracer criteria and this work's experimental results, indicate some guidelines to perform RTD experiments and select the most appropriate tracers materials to (1) capture the mixing behavior of a tracer material inside of the system and (2) represent most similarly the space-time behavior of the base material in the system. To achieve these two goals it is important to recognize that both tracer-blend and tracer-ingredient material property similarities are relevant, especially those regarding flow properties. Assuming that researchers using these recommendations will already have selected a base material (or a blend), the following recommendations focus solely on tracer selection:

1. Select a tracer material that has a distinctly observable chemical or physical property (e.g., spectral band on NIR, color) in comparison to the base blend but whose permeability, flow function coefficient, bulk density, and particle size resembles that of the bulk blend.
2. For pulse experiments, introduce a mass of tracer material that does not exceed over 5% of the blender's mass hold up at steady state. This recommendation is paramount to avoid changing the flow properties of the system.
3. Select the point of tracer introduction (i.e., port) with a clear line of sight to the process' powder stream. This recommendation is given to ensure that the tracer is introduced instantaneously and entirely. This is critically important to accurately represent the system and prevent tracer material from collecting in the port area.
4. Develop an online method to characterize the outgoing tracer concentration in real time. This method would ensure that tracer does not stay behind in the system before introducing subsequent pulses, and allows for experimental monitoring while pulses are performed.
5. Perform the tracer addition experiment in (at least) triplicate to ensure that no variability is introduced by means of the tracer insertion. For pulse experiments, avoid changing methods (e.g., size of pulse, countdown) during the experiment.
6. Capture and understand the variability (i.e., noise, error) introduced by the sensing system (i.e., measurement). Select materials whose chemical composition, although different from the base, do not yield a noisy concentration signal.
7. Determine the base material's space-time and compare it statistically with respect to the RTD tracer results. This result will provide additional value when considering the RTD given by the tracer.

8. Have a single feeder unit in operation while performing the RTD characterization. Monitor closely the feeder flow rate to ensure that no additional disturbance is being provided to the system.

It is important to mention that if the goal of performing an RTD experiment is to determine the dissipation of a particular disturbance caused by a specific ingredient (e.g., an API lump) in a specific unit (e.g., a multifeeder, multiblender system), it is highly recommend to prioritize the use of the ingredients and units in question rather than the recommendations provided here.

6.3.8. Application of RTD model results to process evaluation

RTD data and models can be used to translate input signals into outputs using the convolution algorithm. This section is focused on the application of RTD data and models to perform discrete and continuous convolution, respectively.

6.3.8.1. Convolution

Convolution is a mathematical technique that effectively maps an input signal over a signal filter by means of integration to yield an output signal. In mathematical terms, convolution is the solution for the multiplication of Laplace transforms. This technique is used for digital signal analysis and solving complex sets of ordinary differential equations, therefore it is heavily used within the electrical and computer science community to understand electrical current patterns [280, 281].

Convolution can be performed using both continuous functions or discrete data. Continuous convolution aims at yielding a new function from the multiplication of two functions. To perform this multiplication of the two functions, continuous convolution requires that every value on the two functions is defined over the entire finite interval of time (t). Thus, continuous convolution cannot be applied to a moving time data (i.e., inputs which acquires new data points

over time). Continuous convolution has been applied to a variety of systems, including pharmacokinetic systems [282-284]. Mathematically, the continuous convolution of two functions time-dependent functions $f(t)$ and $g(t)$ can be represented using the standard notation shown in Equation 16

$$h(t) = (f * g)(t) = \int_0^t f(\alpha)g(t - \alpha)d\alpha \quad 16$$

Discrete convolution is the mapping of an input data sequence over a discrete time system, yielding an output sequence. A discrete time system effectively can be described as an impulse response of the system. The discrete convolution is rather similar to the continuous form. Nonetheless, one of the main advantages of the discrete convolution form is the capability of evaluating streams of data that change over time. The discrete convolution of an input sequence over a discrete time system yielding an output sequence is shown in Equation 17.

$$y(n) = x(n) * h(n) = \sum_{m=-\infty}^{\infty} x(m)h(n - m) \quad 17$$

Both of these convolution equations can be used with RTD data and equations. For example, the continuous convolution can be used to study the effect of a time function input on the system's output. The time function inputs can be represented using trigonometric functions (e.g., sine and cosine), step changes, and series of pulse inputs. This process can be performed during development stages to study the effect of different non-random inputs on the system's output. On the other hand, the discrete convolution method can be used for instances where data is being transferred into the system as a function of time, such as a concentration stream given by feeding data or a random input over time. The system would be able to predict the outlet concentration of the material in time using discrete RTD results. In the pharmaceutical field, papers using discrete convolutions can be found in the field of physiology and pharmacokinetics [285]. In this work, the

results from the RTDs will be applied to determine concentration outputs using both discrete and continuous convolution algorithms.

6.3.8.2. Continuous convolution

To perform a continuous convolution example and demonstrate its potential uses, the tanks-in-series models was used because of its mathematical simplicity. Nevertheless, it is important to mention that either model could be used to perform the convolution calculation. The goal of the convolution method is to take an incoming input signal and apply a fixed signal filter. In this case, the incoming signal is an arbitrary input weight fraction (i.e., concentration) of material entering the system, which varies as a function of time ($C_{in}(t)$). The output signal is the weight fraction of materials coming out the blender, also a function of time ($C_{out-blender}(t)$). The relationship between these two variables, which has been introduced by several authors [240], is shown in Equation 18

$$C_{out-blender}(t) = (C_{in} * E_{tank-in-Series})(t)$$

$$C_{out-blender}(t) = \int_0^t C_{in}(\alpha) E_{tank-in-Series}(t - \alpha) d\alpha \quad 18$$

Once the relationships between the inlet and outlet concentrations are established using the convolution integral, the work proceeded to select a simple input concentration function that would be easy to integrate with the tank-in-series PDF. The inlet concentration profile considered was a simple step up and step down (i.e., variable step) with a maximum disturbance value of (P_{max}), which begins at $t = 0$ and ends at $t = t_{disturbance}$. The equation for this input concentration is shown in 19.

$$C_{in}(t) = P_{in}(t) = 100 + P_{max}(u(t) - u(t - t_{disturbance})) \quad 19$$

Using Equation 15, 18, and 19, continuous convolution was performed to yield Equation 20. Notably, this resulting function contained both the complete and incomplete forms of the Gamma function, which is described using the capital Greek letter Γ .

$$P_{out-blender}(t) = 100 + \frac{P_{max}}{(n-1)! \tau_{tank}^{n_r}} [R(\tau_{delay,tank}) - R(\tau_{delay,tank} + t_{disturbance})]$$

where,

$$R(x) = u(t-x)(t-x)^{n_r} \left(\frac{t-x}{\tau_{tank}} \right)^{-n_r} \left(\Gamma(n_r) - \Gamma\left(n_r, \frac{t-x}{\tau_{tank}}\right) \right) \quad 20$$

$$\Gamma(n_r) = \int_0^{\infty} t^{n_r-1} \text{Exp}[-t] dt$$

$$\Gamma\left(n_r, \frac{t-x}{\tau_{tank}}\right) = \int_{\frac{t-x}{\tau_{tank}}}^{\infty} t^{n_r-1} \text{Exp}[-t] dt$$

Equation 20 represents the resulting API claimed label potency out of a blender whose mixing has been modeled using the tank-in-series model with a variable step input. Using Equation 20, several case studies were developed, wherein the size of the maximum potency deviation (P_{max}) and duration of the disturbance ($t_{disturbance}$) were varied. Figure 30 shows the results from the case studies. The n_r , $\tau_{delay,tanks}$, and τ_{tank} used for these case studies were: $n_r = 2.17$, $\tau_{delay,tank} = 20.91$ seconds, and $\tau_{tank} = 16.52$ seconds. It should be noticed that the values for these RTD model parameters vary with material properties, which indicate that different tracers may have an impact on the results from the subsequent analysis.

INSERT Figure 30 HERE

Figure 30A and B show the cases where the maximum potency disturbance (P_{max}) was in the positive and negative direction (i.e., -100 to 100%) at two different disturbance durations ($t_{disturbance}$): 10 and 30 seconds, respectively. The resulting potency would indicate whether the outgoing material was over or under potent based on the deviation from 100%. Each contour

represents the outgoing concentration of material over the operating time (t). Both Figure 30A and B show a gap of time between 0 and 20 seconds, which represents the effect of the delay time on the output concentration. Both Figure 30A and B show that after a given period time, the process will return to its original 100% potency value. However, this time is not after the end of the disturbance, indicating that there is dispersion and delay of the disturbance. The delay and mixing time would be critical to capture to track more accurately the disturbance and take a corrective measure (e.g., deviate material). Furthermore, as seen from the increase in size for both the $85\% < P(t)$ and $P(t) > 115\%$ contours between Figure 30A and B, increasing the duration of the disturbance increased the time the process was producing either under or over potent material. This result is expected, given that increasing the disturbance would lead to burden that the blender may not be able to dissipate. Notably, Figure 30A and B show similarity with the funnel plots discussed by Garcia-Munoz et al. [51] as well as Tian et al. [286], who developed these plots taking a numerical approach with data collected from experiments. However, it is important to note that Garcia-Munoz et al. [51] did not add a variable allowing for variations in the disturbance duration, which is considered in this work.

Figure 30C and D show the effect of varying the $t_{disturbance}$ with for two different values of P_{max} : +20 and +40%, respectively. The disturbance time was varied between 0 and 60 seconds. Varying the P_{max} as the disturbance duration is increased, increases the area of material whose label claim potency is over the arbitrary 115% upper specification contour. This result is in agreement with the fact that as the disturbances in the process occur for longer time, more material will be affected and in a more extensive manner. The results from Figure 30C and D can be used to determine the relationship between disturbance time and amount of time material is out of specification (OOS).

Figure 27 shows an example of how to determine the window of OOS material using the results from Figure 30D. In this example, three (3) arbitrary disturbance durations were chosen: 10,

30, and 50 seconds. Using the 115% as the upper specification bound, three horizontal lines across the entire operation time window were drawn to inspect whether the disturbance would cross the upper specification. The disturbance with a duration of 10 sec did not cross at any instance the 115% upper specification, which indicated that the blender may be able handle the disturbance and yield product that is within the established bounds. However, as observed from the 30 and 50 sec lines, both cross into the 115% upper specification contour. The amount of time the material is OOS can be measured by taking the difference of the intersections between the horizontal and 115% contour lines. Figure 27 shows the OOS time window for a 30 second disturbance (OOS_{30s}) is smaller than the 50 sec long disturbance (OOS_{50s}).

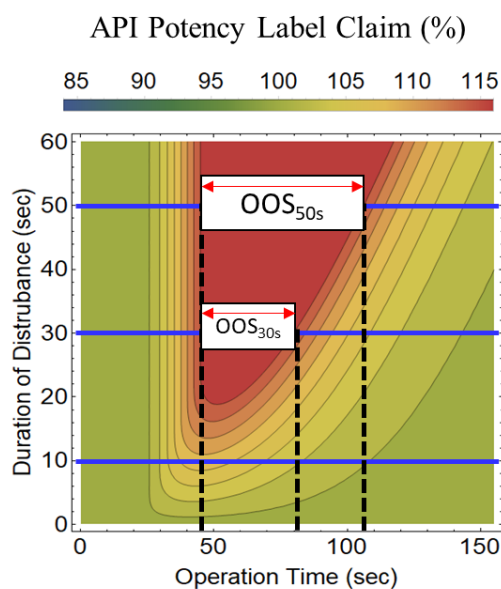


Figure 27. Determining the duration of out of specification (OOS) material, using an arbitrary 115% maximum potency contour.

These OOS windows can be used to design control methods to divert this material, if so desired. One of the main advantages of having the analytical solution to the outlet concentration includes the capability of deriving an equation for the OOS window. The potential to find the intersecting points between the disturbance duration and the upper specification (whichever the product manufacturer wishes it to be) can be determined by solving the non-linear problem wherein

the user specifies the potency and obtains the operation times corresponding to that potency value. Given the complexity of this highly non-linear solution, the authors leave this problem for future research.

6.3.8.3. *Discrete convolution*

Discrete convolution and RTD information (including experimental data) allows for mapping an input signal to an arbitrary filter without having an analytical solution for the filter [251]. As previously mentioned, this method is extensively used in signal analysis and electrical circuit design and may be applicable for cases when blending systems present mixing patterns that are not easily describable using the RTD models discussed. In this work an example case is provided on how to compute the discrete convolution along with the results using two RTD curves from the pulse experiments for different materials and a random input concentration that will serve as the base signal.

The case study used the resulting RTD curves for experiments 1 and 2 of the croscarmellose sodium and anhydrous calcium di-phosphate pulses, respectively. Each pulse experiment had 36 and 29 data points, respectively. The two RTD PDF curves are shown in Figure 28A along with their inherent acquisition error. Following the selection of the RTD distribution curve, a random input potency signal was generated spanning 650 seconds in 1 second intervals using a normal distribution with a mean of 99.6% and a standard deviation of 23.7%. The resulting relative standard deviation (RSD) for the system was estimated at 23.8%. This random inlet distribution is shown in Figure 28B. The 650×2 input signal was multiplied with the 36×2 and 29×2 RTD PDF curve arrays, generating two matrices of 650×36 and 650×29 dimensions. The varying sampling times of the RTD were accounted for by multiplying the $E(t)$ value by the time difference. Subsequently, the diagonal sum of the two resulting matrices was performed to yield the outgoing potency curves as a function of time in Figure 28B.

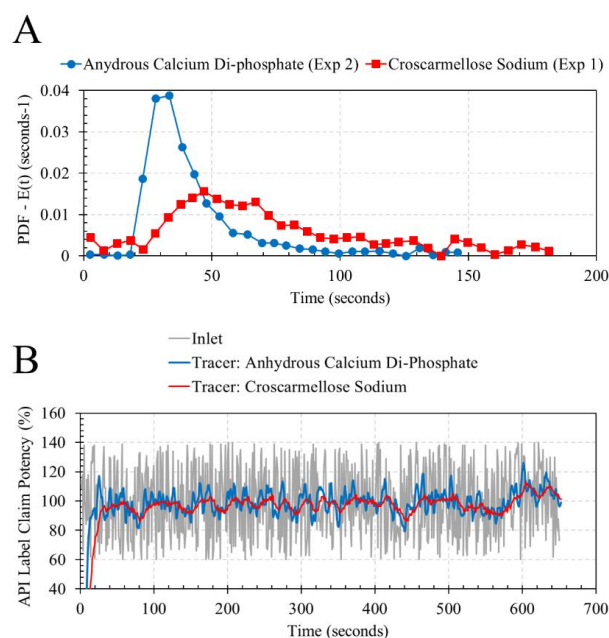


Figure 28. Determining the duration of out of specification (OOS) material, using an arbitrary 115% maximum potency contour.

The outlet potency differences between the two RTD curves appear to be significant, which agrees with the aforementioned discussion about RTD and material properties. The resulting moving concentration relative standard deviations (RSD) for the inlet concentration input using the croscarmellose sodium and anhydrous calcium di-phosphate RTD curves were 4.6% and 7.7%, respectively. Given this reduction in the RSD, the croscarmellose sodium RTD results would have predicted a lower variation in the outlet potency (i.e., better blend homogeneity) compared to when anhydrous calcium diphosphate was used as tracer. This result is significant from the point of view of comparing collecting the initial RTD data, particularly when performing using the data to inform future models. Particularly, it is important to select the right tracer to perform the characterization of the blending system and provide ample room for material property effects when developing regimes of operation.

The major advantage of the discrete convolution method is its capability to compute the outlet concentration of a moving set of data, meaning a data whose input is not provided by an

explicit equation. One of the major downsides, however, is being unable to develop region plots as it has been done with the analytical solution to determine OOS metrics. Iteratively evaluating discrete convolution results for varying input systems may be a solution to this downside.

6.4. CONCLUSIONS

This work emphasized the assumptions and fundamentals of the residence time distribution (RTD) methodology with a particular interest of solid systems. The underlying assumptions for tracer addition with respect to their mathematical representation were discussed, along with the two most commonly used RTD models for describing continuous powder blending systems – the convection-dispersion model and the tank in series model.

For this experimental evaluation seven materials with a wide range of properties were selected as tracers and a single material as our base material. The experimental results led to two major conclusions: (1) materials with significantly different material properties have dissimilar mean residence times inside the systems and (2) materials do not travel at the same speed inside of continuous blending systems. Using the experimental results each of the parameters for the presented RTD models were regressed to assess the impact of material properties. The effect of material properties on the RTD was discussed using the model parameters. Differences in the parameters were shown to be significant for one material in particular: anhydrous calcium-diphosphate.

The analysis revealed that the material properties of the tracer had a statistically observable impact on the RTD model parameters for the axial dispersion and tanks-in-series models for the range of properties examined in this study, further emphasizing the need to select a tracer that faithfully tracks the movement of the material of interest. These observations were also used to identify a set of recommendations on how to select materials that would help characterize the mixing inside of a system taking into account material properties.

This work further showed how RTD models and continuous convolution can be used to determine the operational regions of the blending system. Furthermore, using this model, process developers may be able to determine the impact of disturbance duration and size on the outgoing material as well as establish the duration of out of specification material using the convolution integral. A case study particularly using discrete convolution showed that results from two RTD experiments using different tracers would have led to different predictions of blending performance. These results point to a need for further evaluation to take place to determine the full impact of material properties on the RTD inside of the blending system.

6.5. LARGE TABLES AND FIGURES

Table 19. Residence time distribution metrics for all tracer experiments.

Tracer Material	Mean Residence Time - MRT (seconds)					Mean Centered Variance (MCV)				Skewness		
	Experiment No.			Avg.	SD	Experiment No.			Avg.	Experiment No.		
	1	2	3			1	2	3		1	2	3
Acetaminophen	51	48.9	47.8	49.2	1.6	20%	24%	18%	21%	14%	20%	11%
Anhydrous Calcium Di-Phosphate	42.5	39.3	41.6	41.2	1.7	26%	16%	12%	18%	29%	4%	4%
Croscarmellose Sodium	59.6	71	63.4	64.7	5.8	18%	30%	24%	24%	5%	13%	13%
Crospovidone	54.9	67.8	55.8	59.5	7.2	19%	27%	18%	21%	8%	22%	7%
Starch 1	53.1	56.6	61.6	57.1	4.3	15%	19%	22%	18%	3%	5%	7%
API 3	48	52.2	63.2	54.5	7.8	13%	20%	34%	23%	3%	9%	27%
API 4	58.1	53.1	51.1	54.1	3.6	26%	18%	21%	21%	17%	6%	8%

Avg. = Average; SD = Standard deviation (n = 3)

Table 20. Regression results for 14 for each of the RTD PDFs.

Tracer Material	Peclet Number (Pe)					Delay Time (sec) - $\tau_{delay,AD}$					Residence Time AD (sec) - $\tau_{dispersion}$				
	Experiment No.			Avg.	St. Dev	Experiment No.			Avg.	St. Dev	Experiment No.			Avg.	St. Dev
	1	2	3			1	2	3			1	2	3		
Acetaminophen	6.36	7.75	6.47	6.86	0.77	12.5	8.8	12.4	11.3	2.1	29.0	30.4	26.9	28.8	1.7
Anhydrous Calcium Di-Phosphate	3.38	5.35	5.18	4.64	1.09	18.7	13.8	14.4	15.6	2.7	13.7	20.2	22.2	18.7	4.4
Croscarmellose Sodium	6.24	2.78	3.53	4.18	1.82	14.2	19.5	19.1	17.6	2.9	40.0	35.8	31.4	35.7	4.3
Crospovidone	5.70	3.89	4.16	4.58	0.98	16.5	24.5	18.2	19.7	4.2	32.6	30.2	28.0	30.3	2.3
Starch 1	5.22	4.71	8.20	6.04	1.89	16.4	14.1	2.1	10.9	7.7	29.5	34.4	52.2	38.7	11.9
API 3	6.87	7.40	4.32	6.20	1.65	7.4	3.4	8.5	6.4	2.7	35.3	39.6	36.3	37.1	2.3
API 4	8.17	6.03	6.27	6.82	1.17	3.1	13.6	8.0	8.2	5.3	46.0	34.3	35.8	38.7	6.4

Table 21. Regression results for 15 for each of the RTD PDFs.

Tracer Material	Number of tanks in series (n_r)					Delay Time (sec) – ($\tau_{delay,tanks}$)					Residence Time in Tanks (sec) – ($\tau_{tanks-in-series}$)				
	Experiment No.			Avg.	St. Dev.	Experiment No.			Avg.	St. Dev.	Experiment No.			Avg.	St. Dev.
	1	2	3			1	2	3			1	2	3		
Acetaminophen	2.31	2.47	2.30	2.36	0.09	20.4	18.3	20.0	19.6	1.1	29.8	28.7	27.5	28.6	1.1
Anhydrous Calcium Di-Phosphate	1.40	1.66	1.87	1.65	0.24	22.7	21.5	21.0	21.7	0.9	17.8	21.1	24.1	21.0	3.2
Croscarmellose Sodium	2.42	1.86	2.57	2.28	0.37	14.2	24.1	22.9	20.4	5.4	42.0	52.3	44.7	46.3	5.4
Crospovidone	2.37	2.70	1.89	2.32	0.40	23.9	24.6	24.6	24.4	0.4	35.4	40.9	33.9	36.7	3.7
Starch 1	1.81	2.07	1.90	1.93	0.13	26.0	21.6	26.2	24.6	2.6	31.6	40.1	44.0	38.6	6.4
API 3	2.50	2.77	2.04	2.44	0.37	16.6	13.1	15.9	15.2	1.8	35.9	39.7	43.9	39.8	4.0
API 4	2.45	2.06	2.13	2.22	0.20	18.3	24.2	19.0	20.5	3.2	42.4	35.2	36.2	37.9	3.9

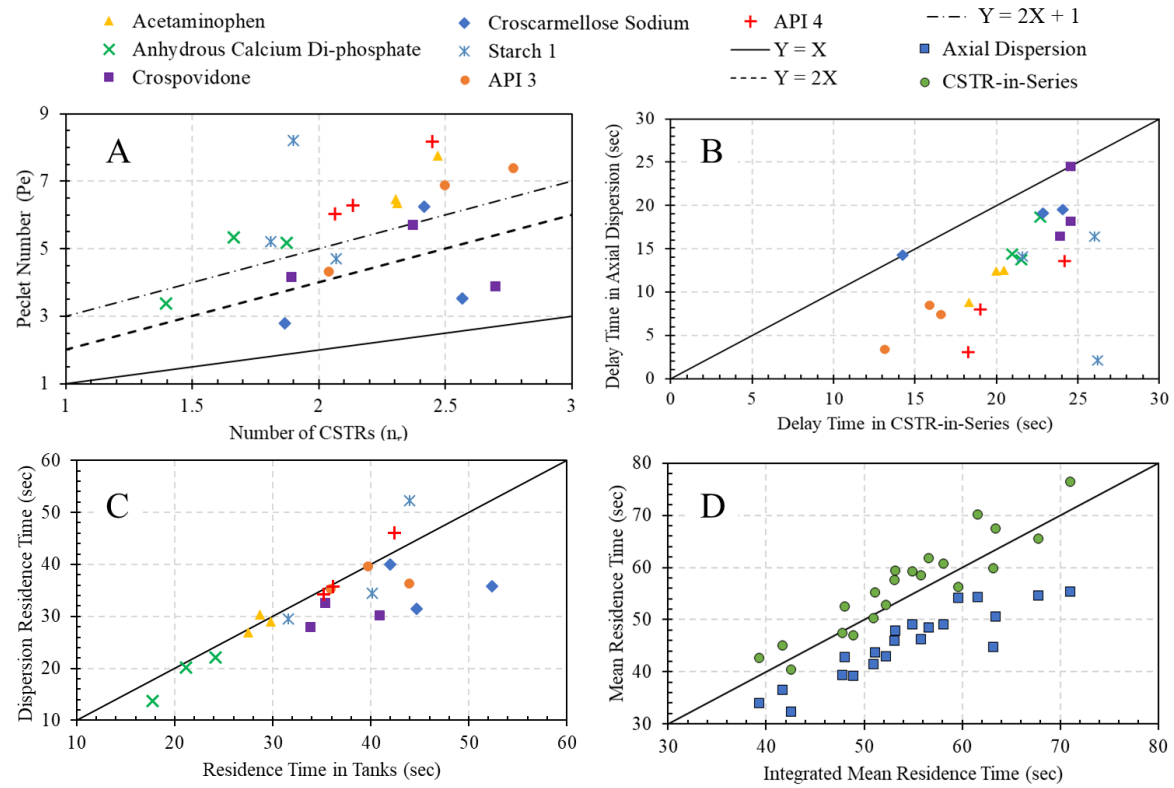


Figure 29. Residence time distribution profile metrics comparison. (A) Peclét number and number of tanks. (B) $\tau_{delay,AD}$ and $\tau_{delay,tanks}$. (C) $\tau_{dispersion}$ and $\tau_{tanks-in-series}$. (D) Numerically calculated mean residence time against both the axial dispersion and tanks-in-series model mean residence time values.

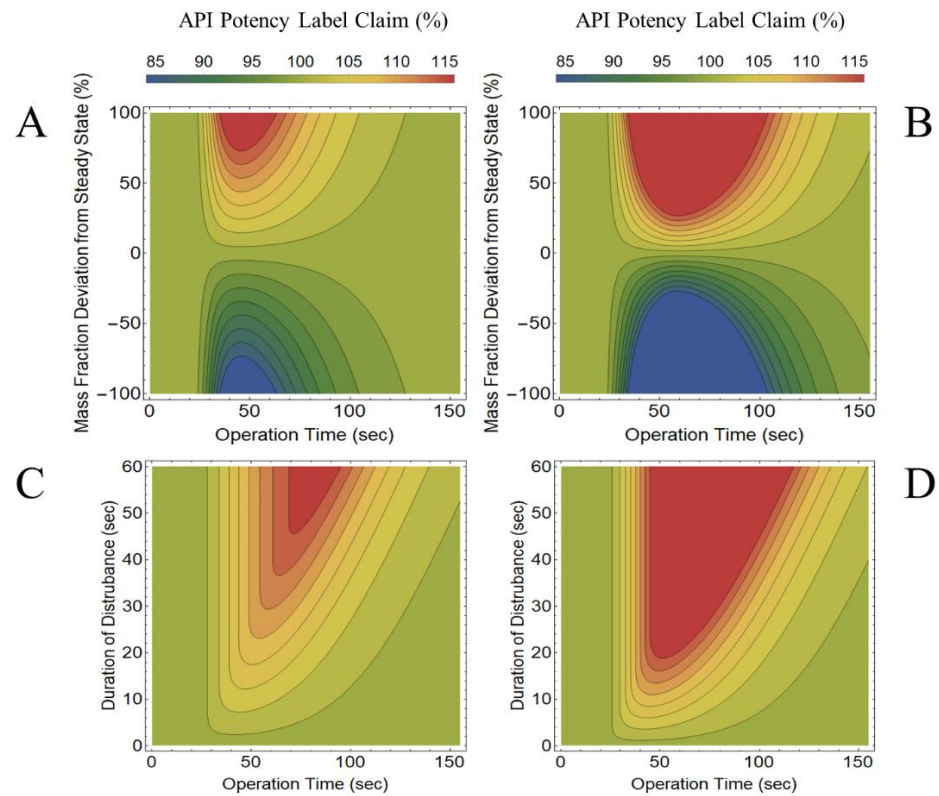


Figure 30. Case studies varying the P_{max} and $t_{disturbance}$ for 20. (A) $-100\% < P_{max} < 100\%$ and $t_{disturbance} = 10$ seconds. (B) $-100\% < P_{max} < 100\%$ and $t_{disturbance} = 30$ seconds. (C) $0 < t_{disturbance} < 60$ seconds and $P_{max} = +20\%$. (D) $0 < t_{disturbance} < 60$ seconds and $P_{max} = +40\%$.

CHAPTER VII

7. AIM 4: FEEDER CHARACTERIZATION AND MODELING

7.1. POWDER FEEDING

As seen in Figure 1, feeders are one of the three most commonly observed unit operations in continuous manufacturing (CPM) processes. From a process development standpoint, powder feeding is the first and most important step in continuous pharmaceutical processes since it sets up the process mass balance, steady state, and has the greatest impact on the concentration of the final product. In a steady state scenario, the materials at any location of the process have the same or very similar *average* concentration (i.e., mass fraction) from the ratio at which they were fed. Thus, accurate feeding of *all* ingredients in a CPM process ensures that a desired blend and content uniformity is attained. Poor feeding performance or large deviations in feeding can seldomly (if at all) be corrected by subsequent unit operations and may lead to process failure. For this reason, developing accurate models and controls are paramount for their implementation in CPM processes.

Figure 31 shows a schematic of the units included under the category of powder feeding unit operations. Feeding units are composed of a screw feeder, a refill unit, and a weight

measurement system, also known as a load cell. In the following subsections, each of the components are described in further detail.

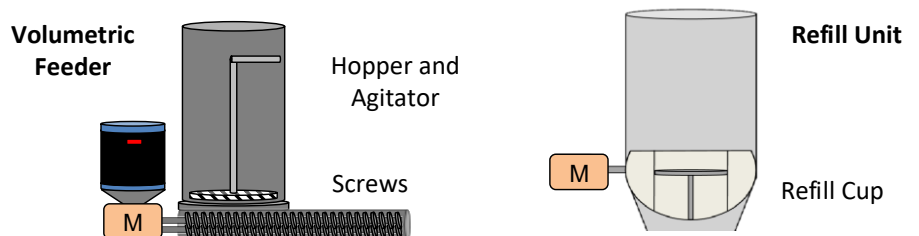


Figure 31. Schematic of a screw feeder unit and a refill system.

7.1.1. Screw feeders

Screw feeders are among the most frequently used feeding systems for pharmaceutical ingredients given their ability to provide the most accuracy for feeding processes, even when low flow rates are required as is sometimes the case for APIs and lubricants [287, 288]. Screw feeders typically consist of a single feeder hopper, one or multiple bridge breaking systems, and a single or twin configuration of conveying screws from which material is dispensed out of the unit [289, 290]. Materials are placed inside of the feeder hopper, whose dimensions and shapes vary depending on the material being dispensed. Bridge breaking systems aimed at ensure a consistent and smooth flow of material from the feeder hopper to the screws are available in most commercially available screw feeders. Bridge breakers are be located inside or outside of the feeder hopper depending on their type and mode of action. Examples of bridge breakers include: vertically or horizontally rotating paddles, jack-hammers, and vibratory or ultrasound systems. The screw conveying system, composed of a single or a twin set of screws, is located at the bottom of the feeding unit, under the feeder hopper and the bridge breaking system.

Figure 32 shows a schematic of some commercially available feeders and points to each of the components described.

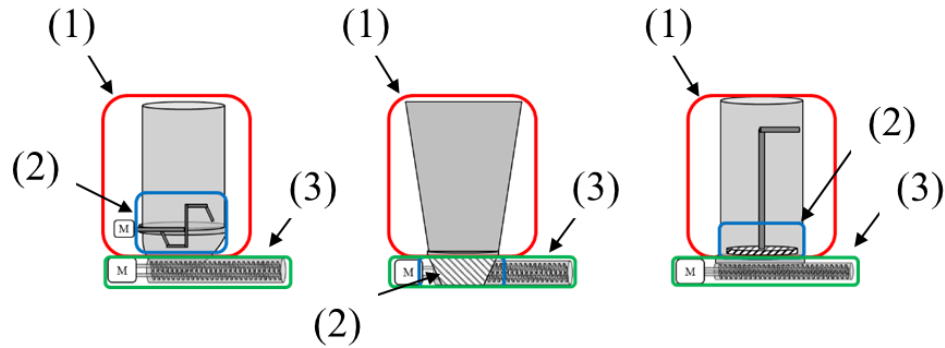


Figure 32. Three different feeder types with their major components symbolized. The feeder hopper (1) is represented inside the red box, the flow aid (2) system is inside the blue box, and the conveying system (3) is shown inside the green box.

To dispense materials out of the feeder, the single or twin screw configuration is rotated to a given angular speed (ω) to displace volume of material per unit time ($\dot{V}_{displacement}$). The volume displaced per screw revolution is known as the screw sweeping volume (V_{screw}) and is calculated from the annular dimensions of the screw. When the volumetric displacement ($\dot{V}_{displacement}$) is considered for a material with a given density value (ρ), the material's mass flow rate (\dot{m}) can be calculated using the conversation equation $\dot{m} = \rho \dot{V}_{displacement}$. However, it is important to note that powder feeding operations typically do not have a constant value of material density given the compressible nature of granular materials. Furthermore, the fill efficiency (ϵ) of material in the V_{screw} is highly dependent on the ability of the material to go from the feeder hopper into the screws at the bottom of the unit [289, 291, 292]. Thus, powder feeding operations often refer the material density at the screws (ρ_{screws}) by defining it as $\rho_{screws} \approx \rho \epsilon$. However, since the density at the screws cannot be measured inside of the unit, a feed factor (ff) value, defined in Equation 21, is used to denote the mass of material being dispensed per screw revolution.

$$ff \approx \rho_{screws} V_{screw} [=] \frac{mass}{revolution} \quad 21$$

The feed factor, unlike the density at the screws, can be measured by using screw speed and mass flow rate measurements with the relationship shown in Equation 22. Thus, this metric

provides a simple metric that lumps the behaviors of screw filling efficiency, screw sweeping volume, and other screw feeding phenomena.

$$\dot{m} = \omega ff \quad 22$$

Other definitions of the feed factor have been provided by equipment vendors, but for this work the feed factor is defined as the amount of material being dispensed per unit revolution [46].

7.1.2. Feeder controls

Based on the current state of screw feeder technologies, feeders can be operated under two control modes: volumetric and gravimetric control. Under volumetric control, the volumetric displacement of the feeder is varied by means of controlling the angular speed of the screws. Volumetric mode is often referred to as open-loop control and it is recommended for operation where the density of the material is not significantly changed or when a precise mass flow rate of material is not required. Under gravimetric control, screw feeders must be operated while monitoring the rate of weight loss from the system. This mode of operation, often referred to as Loss-in-Weight (LIW) feeding, is performed in a closed-loop where a controller changes the screw speed to achieve a desired rate of weight loss. Flow rate is computed as a moving average of the negative time derivative of mass measured by the weight measuring device, commonly referred to as a load cell. Gravimetrically controlled operations ensure flow rate accuracy by maintaining a tight control over the screw speed of the system and constantly monitoring the flow rate out of the system.

It is important to note that while the feeder is being refilled, gravimetric controls cannot be implemented given that the rate of weight loss is being obscured by the mass being delivered by the refill system. Thus, during refill operations, gravimetrically control feeders are momentarily controlled volumetrically. This unsupervised feeding of material during refill often leads to a deviation from the flow rate set point and has been characterized by Engisch et al. [287, 293, 294].

7.1.3. Feeder refill unit

Feeders need to be refilled in order to maintain a constant flow rate entering the process. Since the size of feeder hoppers are often constrained by the maximum weight capacity of the load cell, screw feeders are often equipped with refill systems that will dispense a given mass of material and prevent the feeder from running empty. Given the importance of refill units in feeding operations, these units need to be characterized and modeled in order to have full understanding of this system. One of the major differences between feeders and refill units is the controllability of material dispensing, particularly on whether or not the material flow rate is controlled. Refill unit mass flow rates are often controlled and are constrained by a refill time that aims at minimizing disturbances of gravimetrically controlled screw feeders. Thus, most refill units deliver lump sums of materials in a fast manner, in order to avoid disturbing the feeder system for extended time periods.

7.2. MATERIALS AND METHODS

7.2.1. Materials

A set of the nineteen pharmaceutically-relevant materials shown in Table 8. Lactose 1 & MCC 1 was excluded from the experimentation given that no material was available to perform sufficient feeder characterizations.

7.2.2. Equipment

7.2.2.1. *Feeder and catch scale*

A twin screw GEA Compact Feeder (GEA, Belgium) was used as the feeding unit for this work. The unit, which comes equipped with a load cell and a servo motor was placed on a countertop so that external vibrations or disturbances were minimized. The maximum load and

weight measurement error of the load cell was provided by the equipment manufacturer as 5 kg and ± 1.5 mg, respectively. The working volume capacity of the feeder was obtained from the manufacturer as 2.1 L. Two screw sizes were used in this study: 10mm and 20mm pitch concave screws, each having a sweeping volume of 2.4 and 4.8 ml/revolution, respectively. Three gearbox ratios were used in this study: 63:1, 235:1, and 445:1. Each gearbox ratio provided a maximum screw speed, which in turn varied the maximum volumetric displacement and range of operational screw speeds. A list of the maximum screw speeds and the respective volumetric displacements is provided in Table 22. The feeder unit was operated in both volumetric and gravimetric settings and was controlled using the provided software by GEA. A K-Tron Load Cell (Coperion K-Tron Pitman Inc., Sewell, NJ) from a K-Tron K-CL-SFS KT20 was used as part of the external measurement unit (i.e., catch scale) to characterize the flow rate dispensed out from the unit. The load cell's weight measurement maximum load range and error were provided by the equipment manufacturer as 12 kg and ± 3.6 mg, respectively. The load cells was connected to the computer used to control the GEA feeder.

Table 22. GEA feeder specifications and capacity metrics. Maximum Servo Motor Speed = 9,000 RPM. Sweeping volume of screws: 10 mm = 2.4 mL/rev; 20 mm = 4.8 mL/rev

Gearbox Ratio	Screw RPM/Servo Motor RPM (x 1000)	Maximum screw speed (RPM)	Max. Volumetric Displacement (L/h)	
			10 mm	20 mm
445:1	7.1	65.3	9.40	18.81
235:1	13.7	123.7	17.82	35.63
63:1	51.3	461.5	66.46	132.92

The maximum screw speed was used to compute the drive command (DrCmd) as $DrCmd = \omega / \omega_{max}$. Drive command is used to establish the minimum and maximum ranges of operation. The recommended DrCmd ranges for feeding operations under gravimetric control is between 20 and 80%, given that at this range the controls are capable of providing the best performance [46, 294].

7.2.2.2. Refill system

A GEA Refilling Unit (GEA, Belgium) was fitted with a 0.8 L refilling cup and used to automatically refill the unit during the continuous feeding experiments. The unit is controlled from the computer from which the GEA feeder is controlled and dispenses a fix volume of powder from a hopper unit by rotating a globe around its axis 180 degrees. The speed and duration of a refill can be controlled, based on user specifications; for the purpose of this work, the refill time was set constant to 3 seconds.

7.2.2.3. *Near infrared interface*

A FT-NIR Matrix (Bruker Optics Billerica, MA, USA) was used for spectral acquisition. The fiber optics probe with NIR source and collection fiber was adapted to the vibratory feeder for diffuse reflectance measurements. OPUS 7.0 from Bruker was used to control the NIR instrument and to construct the calibration models. The interface between the sample and the NIR instrument is a critical part for any in-line method development. The NIR interface is responsible of delivering the sample to the instrument in a way that allows representativeness, minimizing the modification of physical properties in the sample and giving all the points in the sample the same probability to be analyzed [274]. An in-house conveyer belt system with controllable speed was used as the interface between the NIR instrument and powder samples.

The proposed interface allows representativeness via 1-dimensional sampling [275]. As a consequence, the powder blend moves continuously without interruption or confinement that affects the flowability. The NIR interface was used both for calibration and for the actual RTD experiments to avoid method transfer issues such as off-line models vs. in-line acquisition.

7.2.3. Experimental procedure

Two sets of experiments were performed for this study: flow rate characterization and residence time distribution experiments. The flow rate characterization aimed at understanding the

flow rate variability from the feeder due to different materials, while the residence time distribution aimed at characterizing the amount of back mixing occurring in the feeder hopper. Below, information on the experimental design and data collection methods is provided.

7.2.3.1. Flow rate characterization

Figure 33 shows the set up for the feeder-catch scale configuration used to characterize the flow rate out of the feeder. Figure 33A shows the schematic of the equipment configuration, wherein the feeder is shown to dispense material to a receptacle atop the K-Tron catch scale. The GEA feeder's controls are shown to be directed by the computer, which is also connected to the K-Tron catch scale. In Figure 33A, the refill unit is also depicted on top of the feeder unit. Figure 33B shows an image of the unit's arrangement in the laboratory.

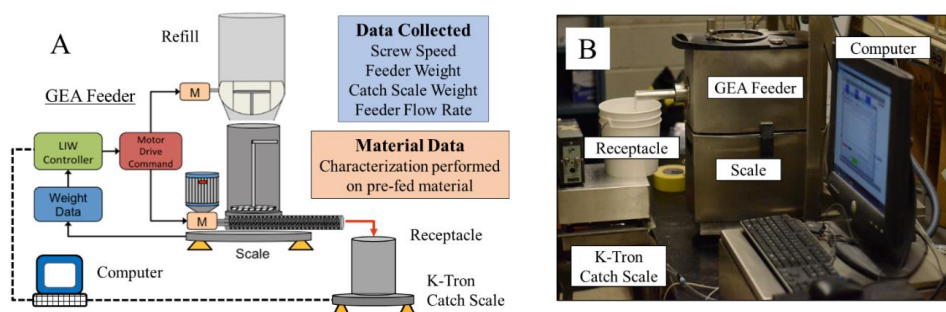


Figure 33. Equipment experimental set up. (A) Schematic (B) Configuration in the laboratory

Flow rate out of the GEA compact feeder was characterized under two control modes, two screw sizes, and two gearbox ratios. Volumetric and gravimetric control feeding was characterized using the 10 and 20mm screws and the 63:1 and 445:1 gearbox ratios. Data collected from the feeding operation included the feeder's screw speed, weight, refill condition, and calculated flow rate, as well as the K-Tron catch scale's weight and calculated flow rate.

Given that the objective of this study was not to characterize the unit under a formulation-based set of flow rates but rather to explore the unit's feeding capability over a wide range of screw speeds, the flow rates were selected based on drive command ranges for experiments using a

particular gearbox. Table 23 presents a list of drive command set points used for experiments. Notably, the experiments were divided into high, medium, low, and lowest capacity based on the gearbox and screw pitch configuration. Given time constraints, most experiments were performed for high capacity conditions. Selected materials were chosen to perform the lowest capacity experiments, as the time it required to perform a full drawdown of the feeder was in the order of 8 to 10 hours.

Table 23. GEA feeder experimental conditions evaluated. Feeder flow rates were computed from the drive command set point.

Condition	Gearbox Ratio	Screw Pitch (mm)	Control	Drive Command Set Point (%)*
High	63:1	20	Volumetric	20
				90
			Gravimetric	10
				45
Medium	63:1	10	Volumetric	80
				20
			Gravimetric	90
				35
Low	445:1	20	Volumetric	70
				90
			Gravimetric	50
				70
Lowest	445:1	10	Volumetric	90
				90
			Gravimetric	50
				50

*Drive command set point for gravimetric cases are based on the feed factor calculated during calibration. The calibrated feed factor (g/rev) was used to estimate the flow rate set point needed to attain the drive command set point using $\dot{m}_{set\ point} = ff_{initial} \omega_{max} DrCmd_{set\ point}$

For the volumetric experiments, the screw speed set point was selected as the percentage of the maximum screw speed provided by the servo motor and the gearbox ratio. Table 23 shows that for the high and medium capacity experiments (i.e., those with the 63:1 gearbox), 20 and 90% DrCmd were selected as the two conditions for feeding at this level. For the low and lowest feeding conditions, given time constraints, the volumetric feeding conditions was kept at 90% DrCmd. Gravimetric experiments were performed immediately after volumetric experiments for each material. Before the gravimetric runs, the feeder's feed factor calibration sequence was performed for a period of one minute to obtain an initial feed factor. The calibration feed factor was used to

predict the flow rate set point ($\dot{m}_{set\ point}$) that would yield a desired starting screw speed, in order to have all material gravimetric test begin at similar screw speeds. Given that in gravimetric mode the flow rate is the target control variable, the screw speed changed over time for these experiments. Thus, the gravimetric feeding test for all materials had different flow rates, ranging from 1 to 75 kg/h for the 63:1 gearbox ratio and 0.01 to 5 kg/h for the 445:1 gearbox ratio.

For each of the flow rate experiments, the feeder hopper began filled (i.e., 100% fill) and was completely emptied by feeding all of the powder out of the hopper through the screws. This was performed to characterize the full feeding range of the feeder from full to empty. Both the starting and remaining mass of material at the end of the feeding operation were recorded to ensure that these values were available for analysis.

7.2.3.2. *Refill unit characterization*

Tests were performed on the refill unit to determine the variability in amount of material being dispensed per refill cycle. Nine materials were selected from those listed in Table 8. The materials used to characterize the refill unit were: acetaminophen, API 4, anhydrous calcium diphosphate, cellulose, magnesium stearate, MCC 1, MCC 4, and silicified MCC. A total of 6.5 L of material were added to the refill unit's hopper to test a total of eight refill actions. The K-Tron catch scale and receptacle were placed at the outlet of the refill unit to capture the weight increase due to the refill action in real time. A total amount of material added and a flow rate curve was obtained for each refill action.

7.2.3.3. *RTD experimental procedure*

The RTD and mixing of material inside of the feeder hopper was evaluated using the GEA feeder, the GEA refill unit, a conveyer belt system, the K-Tron catch scale, and a near infrared (NIR) spectral acquisition unit. Figure 34 shows the configuration of the system used to perform

the feeder experiments. Figure 34A shows the schematic arrangement of the units, wherein the refill unit is shown on top of the feeder, which dispenses the material into a funnel that channels the material to a conveyor belt that transports the samples the NIR spectrometer with minimal mixing. Figure 34B shows the arrangement of the unit in the laboratory.

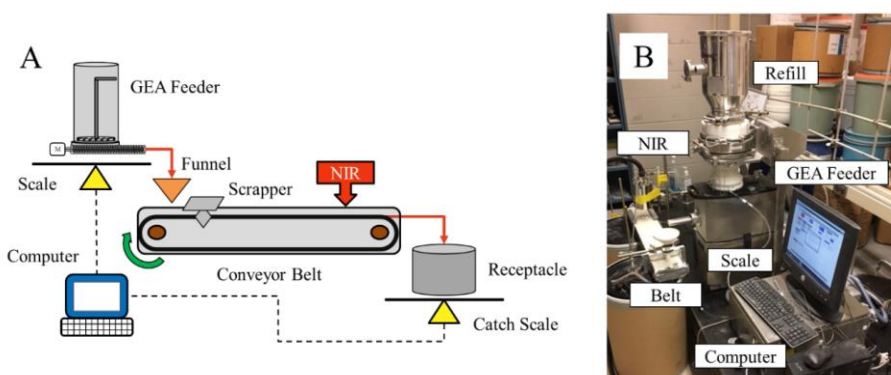


Figure 34. RTD experiment equipment configuration. (A) Schematic of the unit (B) set up in the laboratory

Six impulse RTD experiments were performed using three materials at two different flow rate set points: 10 and 20 kg/h (i.e., 2.78 and 5.5 g/s – Note: these two units will be interchanged regularly). The base materials used for the RTD experiments included: anhydrous calcium di-phosphate, silicified MCC, and acetaminophen. The tracer material was acetaminophen for the first two base materials and milled caffeine was used as the tracer when acetaminophen was the based.

To ensure that the flow rates would be attained for all three materials, the GEA feeder unit was configured with the 63:1 gearbox ratio and the 20mm pitch concave screws. The refill unit cup volume remained constant at 0.8 L per refill. Two kilograms (2 kg) of tracer blends were mixed in a batch V-blender to a 93:7 base to tracer ratio for 20 minutes at a speed of 12 RPM to ensure blend homogeneity. The ratio of base to tracer material was chosen to ensure there would be minimal impact to the flow properties of the material inside the feeder hopper.

The RTD experiment was performed as a refill impulse, meaning the tracer was added as part of a full size refill being performed while the feeder was in operation. For each of the four

materials tested, the feeder feed factor was calibrated and refilled with base material (i.e., material without tracer) to 100% fill level. The refill unit was then connected to the feeder and 0.8 L of tracer blend material (i.e., one refill equivalent) was added to the refill unit. A refill set point of 60% fill level was set for the GEA feeder, meaning that once the feeder reached a level of 1.2 L the refill unit would be automatically activated to dispense a mass of 0.8 L of material. The feeder was then set to the experimental mass flow rate and started. During the first few seconds of operation, the conveyer belt's speed was adjusted to ensure the material did not accumulate on the belt and that the material being dispensed was not intermixing. Accumulation rates on the conveyer belt were monitored using the catch scale flow rate measurements. The flow rate coming into the catch scale system was matched to that calculated from the GEA feeder to ensure that no mass was being accumulated in the belt once the system had reached a steady state. Immediately after the refill of tracer material occurred, the refill unit's hopper was quickly and carefully vacuumed to ensure that no tracer residue remained from the previous refill. The refill unit's hopper was then filled with 1.6 L of base material as the washout of the tracer in the system. The feeder was then allowed to completely dispense all of the material, totaling 4.4 L of material fed. Once an RTD experiment was performed, all pieces of equipment were thoroughly vacuumed to avoid cross-contamination. This process was repeated for all six RTD experiments.

7.2.3.4. *NIR method development*

Acknowledgement of collaborative work and contributions:

The chemometric section of this work was developed as part of a collaborative effort within the Engineering Research Center for Structured Organic Particulate Systems (ERC-SOPS). Development, calibration, and implementation of NIR chemometric methods were performed by Dr. Andres Roman-Ospino. Dr. Roman-Ospino worked in collaboration with the author of this thesis, who provided Dr. Roman-Ospino with the list of materials, target concentrations, and conditions needed to develop the chemometric models. The author of this thesis is very grateful to the work done by Dr. Roman-Ospino developing the chemometric methods.

Figure 35 shows the experimental setup for acquisition of calibration spectra. A K-tron MT 12 feeder was used to dispense each calibration blend in gravimetric mode on a vibratory feeder. The second feeder, makes the powder flowing in front of the NIR probe before it is collected in a bucket. The vibratory feeder allows adjusting the flow of powder. Another important feature is that the stainless-steel surface does not interfere with the spectral acquisition. This setup corresponds to a similar sample speed as the one used for RTD measurements. The NIR instrument is a Matrix F FT NIR from Bruker (Billerica, MA USA). For each material to analyze, a projection to latent structures (PLS) calibration model was constructed including variation in composition established from 0-9% w/w of tracer relative to the bulk material to study.

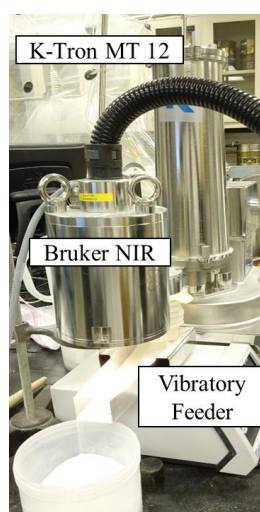


Figure 35. Experimental setup for acquisition of calibration spectra

The blending of standards constituted by tracer-bulk material was performed using a Laboratory Resodyn Acoustic mixer (LabRAM) (60g's for two minutes for a mass of 100g of base-tracer) [199, 276].

Each calibration blend was transferred to the gravimetric feeder to discharge on the vibratory interface for NIR spectral acquisition Figure 35. One hundred spectra were collected for each calibration blend (0, 3, 6 and 9 %w/w) for a total of four hundred calibration/test (60 for calibration and 40 for test) spectra for each material. OPUS 7.5 from Bruker (Billerica, MA USA)

for data acquisition, construction of PLS model and for real time measurements. Three spectral range, five data pretreatments and up to four latent variables were evaluated by using test samples. Calibration models for each case were selected based on the lowest RMSEP values. Table 24 shows the calibration models implemented for RTD measurements.

Table 24. Results of NIR calibration model used for RTD experiments

Base material	Tracer	Spectral Range (cm ⁻¹)	Pre-treatment	LV	RMSEP	R ²
Silicified MCC	Acetaminophen	6102-5448	1 st Der (17) + SNV	2	0.057	97.85
Anhydrous Calcium Di-Phosphate	Acetaminophen	9401-4248	1 st Der (17)	2	0.107	96.07
Acetaminophen	Caffeine	5450-4248	1 st Der (17)	2	0.067	97.06

7.2.4. Software

All GEA feeding data was acquired using the provided software by the equipment's vendor. K-Tron catch scale data was acquired using the K-Tron Sampler software. Both data formats were compatible with Excel® 2016 (Microsoft Corporation, Washington, USA) were the data was imported and pretreated. Data pre-treatment included data time-matching and standardizing the sensor measurement units to SI. RTD concentration results from the NIR acquisition software were imported to Excel in order to be evaluated. Plotting, analysis of raw data, and model regressions were performed using Wolfram Alpha Mathematica V11.1 (Wolfram Alpha LLC, Illinois, USA). Model regressions were performed using the non-linear model fit algorithm provided within Mathematica. Results from model regression were analyzed and compared using the statistical software JMP Pro 13 (SAS, North Carolina, USA). The full feeder model implementation and evaluation was performed in gPROMS Model Builder™ v4.2 (Process Systems Enterprise, London, UK). Model implementation was performed using gPROMS Model Builder™ v4.2 given the ease to connect the different models developed using the flowsheeting capability.

7.3. FLOW RATE CHARACTERIZATION AND MODELING

7.3.1. Experimental results and visual observations

A total of 237 feeder experiments were completed for flow rate characterization at varying flow conditions using the materials listed in Table 8. Table 25 shows the number of experiments performed for each material along with the respective equipment configurations. The data collected for each experiment included: feeder weight (i.e., mass of powder remaining in the feeder), feeder screw speed, feeder calculated flow rate, catch scale weight, and catch scale calculated flow rate. The feeder data was plotted as a function of time for all experiments to observe trends that could be used to describe the behavior of the feeder when feeding different materials.

Table 25. Number of experiments performed per material and feeder conditions

Gearbox Ratio Screw Pitch (mm)		No. of Experiments				From			Observations during feeding
		63:1		445:1		Groups			
		10	20	10	20	1	2	3	
Materials	Acetaminophen	4	7	1	4	X			(1) (2) (3)
	Anhydrous Calcium Di-Phosphate	4	2	-	4			X	
	API 1	4	5	-	-	X			(3)
	API 2	2	4	-	4		X		(3)
	API 3	5	5	3	4	X			(1) (2) (3) (4) (5)
	API 4	4	4	-	2		X		(1) (2) (4) (5)
	Cellulose	3	7	-	2	X			(2) (4) (5)
	Croscarmellose Sodium	5	4	3	4		X		
	Crospovidone	5	5	-	4		X		(2)
	Lactose 2	4	3	-	-			X	
	Magnesium Stearate	4	4	3	2	X			(1) (3)
	MCC 1	5	4	-	4		X		
	MCC 2	5	4	-	4			X	
	MCC 3	4	5	-	4		X		(2) (4)
	MCC 4	6	6	-	4		X		
	Silicified MCC	4	3	-	4			X	
	Starch 1	2	4	-	4		X		(3)
	Starch 2	4	4	3	4		X		
	Starch 3	5	3	3	1		X		

Feeding observations: (1) sticking to the walls of the feeder, (2) sticking to the outgoing barrel, (3) flow in soft lumps, (4) bearding, and (5) inconsistent flow.

Several other observations regarding material feeding challenges during the experiments were also noted. These challenges included: (1) sticking to the walls of the feeder, (2) sticking to

the outgoing barrel, (3) flow in soft lumps, (4) bearding at the barrel's outlet, and (5) inconsistency in flow. Notes of which materials presented these challenges are provided in Table 25. Figure 53 shows images of the first four challenges observed.

INSERT Figure 53 HERE

Figure 53A shows the tendency for highly sticky materials to adhere to the walls of the hopper. Although the GEA feeder unit comes equipped with a bridge breaking impeller (shown in the figure) to allow for material to smoothly enter the screws, sticky materials will adhere to the walls of the hopper and effectively avoid the shearing effect of the impeller. In some cases, this sticking seen to occur in part by the shearing of the impeller, which mechanically carve a bridge for the material. Figure 53B shows the effect of material sticking to the outer walls of the barrel due to triboelectric charging of the material. As the material is dispensed from the screws it acquires an electric charge that makes the material stick to the barrel as it exits. This effect was especially seen for smaller particles. Bearding, shown in Figure 53D, is a variant of this triboelectric charging, wherein the materials form electrostatic clumps that are released periodically as their weight overcomes the electric forces. Bearding is of particular interest for feeding operations as it can greatly affect flow rate controls by suddenly losing a relatively large mass of material, which would be translated as a deviation in the flow rate [287, 294, 295].

High speed images were collected throughout the experiment to capture the behavior of the material exiting the feeder. Figure 36 shows the images take for the 19 different materials dispensing material at a 200 RPM constant screw speed using a 20mm screw pitch. The result indicated that materials such as API 1, API 2, API 3, magnesium stearate, and starch tended to exit the unit in large lumps or *slices* of powder that broke upon contact with the receptacle over the catch scale. Although the observed lumps appeared to break upon contact, their size and frequency pose a question regarding the need for delumping operations between feeders and subsequent unit

operations. Large lumps that are not sufficiently broken may hinder the outcomes of blend and content uniformity, particularly for low concentration materials such as APIs and lubricant. On the other hand, materials such as anhydrous calcium di-phosphate, lactose, MCC 1, MCC 2, and silicified MCC tended to flow more freely and did not tend to form lumps.

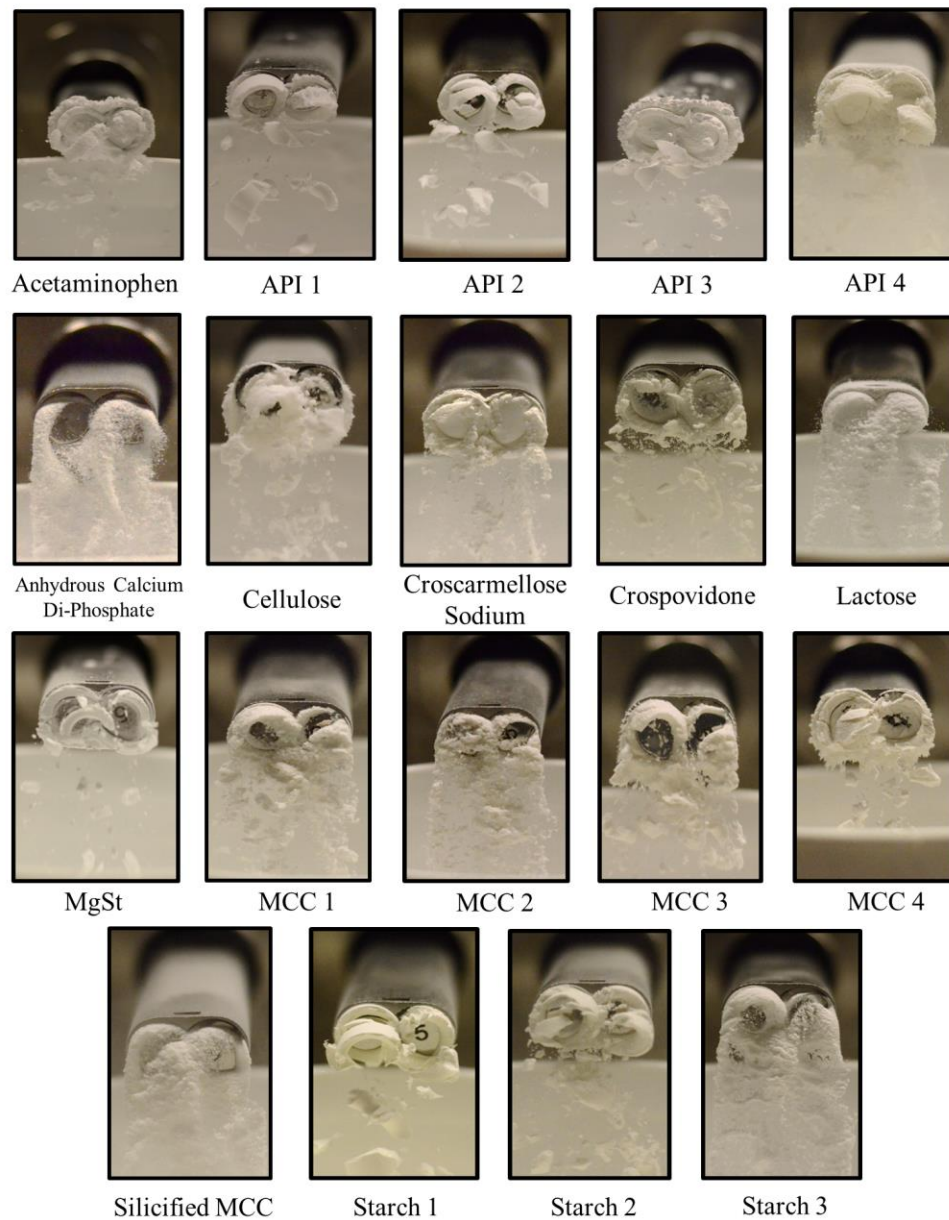


Figure 36. High speed images of powder flow rate for different materials listed in Table 8

Both the cluster analysis results provided alongside the feeding observations in Table 25 and Figure 36 show that *all* materials with properties belonging to group 1 displayed at least one challenge during their feeding. For example, API 3 had all of the challenges observed during the feeding trials, and the material is listed in group 1. Furthermore, cellulose and acetaminophen also displayed several observations and were allocated to group 1 in the clustering based on material properties. The results indicate that materials within group 1 (and thus materials that have similar material properties to those in the group) will present the most feeding challenges.

Materials in group 3 were did not appear to have observable issues during the performed feeding trials in this study. The result show that materials with properties similar to those belonging to group 3 are suitable for feeding operations and will not lead to major challenges during operation. Nevertheless, it is important to not discard the potential of other issues arising for these materials and/or that the visual observations may eventually occur during operation for these materials.

Group 2 materials were found to behave like a combination of materials in group 1 and group 3, meaning that several materials presented some feeding challenges while others did not display major observations. This result can be explained by the intermediate nature of the materials properties for materials in this group. For example, API 4, material with relatively similar behavior to those in group 1 had several major observations, seen for materials in group 1. However, materials like starch 3 and MCC 4 did not display these behaviors, given their tendency to behave more closely to materials in group 3 rather than group 1. Given this result, materials in these group present themselves in a gray area, wherein they have properties that may affect feeding performance. One of the possible ways to establish a more clear set of materials and behaviors associated with them, is to increase the number of groups in the hierarchical clustering. For this work, since the number of materials studied was relatively small, this approach was not pursued, given that subdividing the groups may lead to over classification problems. The approach for increasing the number of clusters is suggested when the number of materials in one group exceeds

the number of groups used for the hierarchical clustering (i.e., number of materials per group should exceed the number of groups).

Notably, all APIs displayed some challenges during feeding trials. This result is indicative that material properties of the studied APIs should try to mimic more closely those of excipients. Although this is often a difficult and tedious task, the advantages to the process performance may greatly increase. Moreover, APIs whose current properties do not allow for implementation of CPM process may require minor modifications to their manufacturing in order to greatly vary their flowability. Several techniques such as silication, co-precipitation of APIs with glidant materials, and larger particle sizing may aid in the improvement of flow, as shown by Capece et al. [165, 296] and Dave et al. [297-299].

The results on this section further confirm the intrinsic relationship between material properties and the ability to feed the material through a feeding unit.

7.3.2. Flow rate characterization

For all volumetric (i.e., open loop) experiments, it was noted that the flow rate decreased as a function of time, while for gravimetrically controlled (i.e., close loop) experiments the screw speed increased over time. This relationship was found to be correlated with the mass inside of the feeder (i.e., feeder weight) given that the mass decreased linearly as a function of time. For the sake of brevity, four cases involving eight experiments are discussed to illustrate the behaviors that were observed in the flow rate characterization experiments performed.

7.3.2.1. Case A: high flow rate capacity of MCC 4

Figure 54 shows the volumetric and gravimetrically controlled time profiles for flow rate, mass of material in the feeder, and screw speed for MCC 4 using the 63:1 gearbox ratio and 20mm screw pitch size.

INSERT Figure 54 HERE

Figure 54A shows the flow rate profile for the volumetrically controlled experiment from both the catch scale and the feeder data. The catch scale flow rate appears to have less noise than the feeder flow rate, which can be attributed to the fact that the catch scale load cell is not sensing the powder movement inside of the feeder hopper as well as the intrinsic noise provided by the screws and impeller movement. Nevertheless, the flow rate means are consistent with one another, indicating that a filter for the feeder noise could be applied to remove the effect of the equipment parts on the flow rate. From Figure 54A's time profile, both flow rates are seen to start at around 12 g/s and remains relatively constant until the time reaches 65 seconds, when both flow rates start decreasing steadily until they reach 11 g/s. At around 87 seconds the flow rate sharply decreases as the feeder empties. Figure 54B shows the trends of both the screw speed, which was held constant at 415 RPM, and the mass inside of the feeder. Markedly, the slight deviation in the flow rate seen in Figure 54A is not seen as pronounced in the weight profile, which indicates that it is necessary to observe the first derivative of the weight profile to observe the changes in flow rate.

The trend seen in Figure 54A indicates that to maintain a steady flow, the feeder would require gravimetrically controlled flow rate. Figure 54C shows the gravimetrically controlled results, which show the flow rate setpoint of 10.7 g/s being matched over the entire feeding profile. It was noted that towards the end of the operation, the flow rate profile of the feeder began to increase in noise, which indicated that the gravimetric controls had to perform screw speed adjustments faster than for earlier time points in order to correct the flow rate deviation observed in Figure 54A. Figure 54D shows that the screw speed increased around the $t = 60$ mark, which corresponded with the changes in flow rate observed from the volumetric experiments.

7.3.2.2. Case B: medium flow rate capacity of MCC 4

Figure 55 shows the volumetric and gravimetrically controlled time profiles for the flow rate, mass of material in the feeder, and screw speed for MCC 4 using the 63:1 gearbox ratio and 10mm screw pitch size. Similarly to experiment A, the Figure 55A shows the flow rate profile of the volumetric experiment as a function of time. The flow rate for this experiment, which maintained the screw speed at 415 RPM, as shown in Figure 55B, shows how the flow rate remained relatively constant at 6 g/s over the first 125 seconds of operation and thereafter the flow rate decreased until it reached a flow rate around 5 g/s. Notably, the flow rate noise observed in the feeder profile was heteroscedastic in nature, meaning it did not remain constant over the course of the operation. This change in the noise appears to be related to the filling efficiency of the smaller pitch screws when the feeder is reaching a lower mass in the hopper. Thus, the behavior indicates that screw filling is affected towards lower fill levels more significantly for the smaller screw pitches.

INSERT Figure 55 HERE

The decrease in flow under volumetric performance, once again, indicated that in order to maintain a constant flow rate, the system required to be operated under gravimetric or close loop control. The results of the gravimetrically controlled flow rate are shown in Figure 55C. The results indicate that the feeder was able to maintain the flow rate relatively constant over the whole feeder emptying process around the set point of 5.5 g/s. Screw speed was adjusted over the course of the operation as seen in Figure 55D from 390 RPM to over 410 RPM to maintain the flow rate.

Markedly, flow rate was almost reduced by half during in this experiment when compared to experiment A as a result of varying the screw pitch from 20mm to 10mm. The result, thus, indicate that the flow rate and volumetric displacement relationship discussed holds for this type of powder feeding operation with screw fill efficiency and bulk density playing a significant role.

7.3.2.3. Case C: high flow rate capacity of Acetaminophen

Acetaminophen was chosen as a case material because of its vast use in feeding evaluations in the CPM powder feeding literature [67, 74, 76, 300]. Figure 56 shows the flow rate, screw speed, and weight time profiles of this API using the 63:1 gearbox ratio fitted with the 20mm pitch screw. Figure 56A shows the flow rate profile did not remain as relatively constant as the previous two experimental cases, which was attributed to the poorer flow properties of the acetaminophen when compared to the better flowing MCC 4 excipient. The flow rate under volumetric controls, shown in Figure 56A, is seen to start at around 6 g/s and increase slightly over the next 70 seconds, followed a sharp linear decrease from 6 g/s to 2 g/s. Figure 56B shows the screw pitch remained constant over the whole operation at a value of 415 RPM. It is important to note that the weight profile showed a relative small curvature past the $t = 70$ seconds, which agrees with the decrease in the flow rate observed in Figure 56A.

INSERT Figure 56 HERE

The gravimetric flow rate profile, shown in Figure 56C, shows the flow rate of the API remained relatively constant over the first 100 seconds of operation, but then proceeded to decrease until the feeder was emptied at the end of the operation. Decrease in the flow rate after the first 100 seconds was explained by looking at the screw speed changes, shown in Figure 56D. The screw speed appears to vary over a range of speeds between 340 and 420 RPM and increase to maintain the flow rate setpoint of 6.2 g/s. After the first 90 seconds, the screw speed appears to increase rapidly to try and maintain the flow rate setpoint, however, at around 95 seconds the screw speed reached the unit's operation maximum value of 495 RPM. Given that that the screw speed was not able to exceed the operational maximum, the flow rate was seen to decrease as the volumetric capacity was capped.

The gravimetric feeding results indicated that certain maximum capacity limits are obtained not only from the initial ability of the feeder to reach the desired flow rate, but must be

obtained by studying the feeder's flow rate over the entire range of fill levels. This is was a critically important result, as it provides a mean to understand that feeder performance should be evaluated solely after characterization is performed to avoid confounding the unit's limitations with the intrinsic powder flow behavior.

7.3.2.4. Case D: low flow rate capacity of Acetaminophen

Figure 57 presents the results for two flow rate capacity experiments using acetaminophen in the GEA feeder fitted with the 20mm screw and the 445:1 gearbox ratio. Figure 57A shows the flow rate as a function of time at a constant speed of 58 RPM, as shown in Figure 57B. The API's flow rate during the first stages of the operation appears to decrease during the first 100 seconds of feeding, increase during the following 100 and repeat this cycle over the next 200 seconds. This result was attributed to the inability of the powder bed to move downwards on the hopper due to surface friction with the sides of the unit. The oscillatory behavior was only reserved to cohesive materials, which tended to stick to the vessel's walls. Sticking to the walls is a inhibiting behavior that may avert the unit from operating normally and even prevent flow (as seen with API 3 during the visual characterization). Nevertheless, once material reached a lower level inside of the hopper, the internal impeller was able to effectively move the powder towards the feeder screws. This behavior was observed after the 400 second time mark, where the flow rate steadily decreases, similarly as Case C.

INSERT Figure 57 HERE

The feeder weight for the volumetric case, shown in Figure 57B, clearly shows the different flow rate results over the constant screw speed. Figure 57C shows the gravimetrically controlled flow rate, which remained relatively constant around the 1.1 g/s set point over the whole operation for both the calculated GEA feeder and catch scale flow rates. This is a good indication that the variations in the material were well controlled by the LIW system and deviations such as the ones

observed in the gravimetric case can be overcome by appropriately tuned control methods. Figure 57D shows the increase in screw speed as a function of time, demonstrating the effect of controls over the screw speed. Notably, the screw speed almost reached the operation maximum for this gearbox configuration, hinting that the feeder was barely capable of maintaining the flow rate over the whole operational window.

7.3.3. Feed factor profiles

7.3.3.1. *Characterization from data*

The observed changes in flow rate as function of time for volumetric experiments and the increases in screw speed over time for gravimetric experiments, indicated a decrease in the amount of material dispensed per unit revolution (i.e., the feed factor) as a function of time. This behavior was previously noted in recent publications by Wang et al. [62], Van Snick et al. [198, 301], and work done by Engisch et al. [287, 293, 294]. The feed factor was simply calculated by dividing the instantaneously observed flow rate by the respective screw speed. This result, in grams per revolution, serves as an indicator of how much material is being dispensed per screw revolution.

The results from the case studies shown in the previous four sections, could be described using the feed factor plotted as a function of the amount of material remaining in the feeder. This curve, hereunto described as the feed factor profile, serves as a mean to describe the amount of material being dispensed per unit revolution at a given fill level of the unit, making the metric independent of time. From a characterization perspective, this result would yield a valuable profile that can be used to relate the observed feeder flow rate behavior at given process conditions with material properties. Once feed factor curves are developed for varying feeder conditions (e.g., screw speed, gearbox ratio) then the curves can be compared between materials in order to evaluate the effect of different materials. Thus, it was paramount to evaluate the feed factor curves for this

work for the 237 performed feeder experiments and establish some relationships that were useful to develop a mathematical model for feeders.

For instance, using the results from Cases A and B, Figure 58 shows a comparison of the feed factor curves for MCC 4. Figure 58A and Figure 58C show the feed factor results for Case A, wherein the system was fitted with a 20mm pitch screw, for the results collected from the GEA feeder and the catch scale, respectively. Both figures show the results for the gravimetric and volumetric experiments. Although the flow rates did not match exactly for Case A's results, both pairs of feed factor curves for each of the data collection systems appear to overlap very well. The feed factor for MCC 4 for this case was seen to range between 1.2 and 1.9 g/rev with the most decrease occurring at the lower feeder weights. As expected, given that the flow rate from the GEA feeder was seen to be noisier due to the internal powder movement and the rotation of the screw, the feed factor profiles appear to vary in a greater amount than those for the catch scale, which was not prone to this variation. Nevertheless, both pairs of curves seem to match well even though they were performed under two different sets of controls. This result, thus indicates that the feed factor profile can be used to characterize and compare feeder experiments even when the flow rates are not matched exactly, since the amount of material per screw revolution depends on the equipment configuration.

INSERT Figure 58 HERE

Figure 58B and Figure 58D show the results of the subsequent Case B, wherein the feeder was fitted with a 10mm pitch screw, for both the data collected from the GEA feeder and the catch scale. Once again, the pairs of feed factor profiles results appear to match very well, as seen in both Figure 58A and Figure 58C. Markedly, the feed factor values for the case ranged between 0.1 and 1 g/rev. The 20mm and 10mm screw pitches indicate that the reduction in sweeping volume on the screw led to a halving of the feed factor for MCC 4 at the same conditions. This result was in

accordance with expected results, given that halving the volumetric displacement of the screws per revolution would lead to a proportional decrease in the amount of material being displaced by the screws.

Results for Cases C and D are shown in Figure 59. The feed factor curves for Case C are shown in Figure 59A and Figure 59C. The feed factor for this case is shown to range between 0 and 1.2 g/rev for both the volumetric and gravimetric cases. Moreover, the feed factor is shown to decrease as a function of the feeder weight, indicating that the maximum capacity of the feeder (i.e., the maximum flow rate that can be achieved by the unit) decreases over the fill level of the unit. The outcome of the feed factor decrease, thus indicate the unit's flow rate will vary if the screw speed is held constant or the screw speed will increase to maintain a given flow rate.

INSERT Figure 59 HERE

Figure 59B and Figure 59D show the changes in feed factor for Case D. Given the longer duration of the feeding experiment and the fact that the sampling frequency remained the same for all experiments, the number of observations (i.e., data points) was shown to be much larger than for the higher flow rate counterparts. It was observed that for the lower feeding experiments, the amount of noise in the measurement was larger than for higher flow rate experiments.

As it was discussed in the volumetric case, there was a change in feed factor as a function of feeder weight the led to a decrease in the amount of material being dispenses per revolution. This result can be clearly seen in Figure 59D, where the volumetric feed factor curve calculated from the catch scale data deviates from that of the gravimetric control at the higher feeder weights. This result, previously attributed to poor powder movement inside of the hopper, still showed that between the feeder weights of 600 and 700 grams, the volumetric feed factor profile closely matched the gravimetric one. Thus, the feed factor profile for the volumetric case provided a mean

to understand that the deviations observed in the flow rate were not part of a larger trend, but rather a situational occurrence in the experiment.

It was noted that for all the feeder experiments the feed factor profiles showed some form of an asymptotically rising profile which could be best described by a first order model with respect to feeder weight. This behavior for the feed factor profile can be explained by the relationship between hopper flow and the filling of the screws as the hopper empties. The screws are filled as a function of both the apparent bulk density of the material and the flow rate of material from the hopper. Therefore, given the cylindrical nature of the GEA feeder hopper and the relationship between hopper flow rates, this result appears to be in agreement with asymptotically increasing hopper stresses known to affect the flow rate of material at the outlet of the hopper. Using the first order relationship between feeder weight and feed factor, an empirical model was proposed.

7.3.3.2. *Feed factor model*

Given the observed behavior of the feed factor profiles with respect to feeder weight, in this work a focus was placed in attempting to capture the behavior using a pseudo-first order equation. It is important to mention that several equipment manufacturers, such as K-Tron and GEA, currently collect the feed factor data as the feeder is dispensing to have a growing array from which a prediction can be made during operation. However, since the interest of this work is to establish a model that can be used to predict and model the feed factor profile, the data that was collected during feeder experiment must be used to develop the model. Thus, the following section aims at providing a semi-empirical model that can be tuned for different materials and can be used to predict the feed factor profiles *in silico*. Other model forms, capturing a more mechanistic behavior inside of the hopper and screw configuration, are highly encouraged, but will remain outside of the scope for this work.

The main objective of this work's feeder factor models is to determine the effect of changes in the apparent feed factor ($ff_{apparent}$) inside of the hopper so that an accurate flow rate can be computed at a given screw speed (i.e., volumetric displacement). Thus, the feed factor model along with the volumetric displacement model provides the level 1 models for the powder feeder system.

Given the results provided by the analysis of the data provided in Figure 58 and Figure 59, the apparent flow rate appears to change in a pseudo first order relationship with feeder weight. This relationship resembles previous findings for compression and density changes [40]. Heckel established an exponential relationship between densification of a materials and increases in pressure.

$$\rho_{apparent}(P) = \rho_{true} - (\rho_{true} - \rho_{bulk})Exp[-kP] \quad 23$$

where $\rho_{apparent}$ is the apparent material density after compression, ρ_{true} is the true or skeletal density of the material, ρ_{bulk} the material's bulk density, P is the pressure exerted on the material, and k is the material specific constant relating compression pressure to changes in apparent density. Given the similarities between the model and the behavior observed in the feeder, this model was used as a *framework* to characterize the changes in density (and thus the feed factor) inside of the feeder units. The model variables were varied in order to more accurately represent the system. The new model would need to evaluate the densification at moderate pressures given that this would be driven by changes in weight. Therefore, the vertical pressure shown in Heckel's equation is assumed to be the pressure exerted by the feeder weight (P_{weight}). This assumption, was also used by Johansson for the modeling cylindrical silos [302]. The resulting equation, which includes the feeder weight (W), cross-sectional area of the feeder (A_{feeder}) is shown in Equations 24 and 25.

$$P_{weight}(W) = \frac{Wg}{A_{feeder}} \quad 24$$

$$\rho_{feeding}(W) = \rho_{max} - (\rho_{max} - \rho_{min})Exp\left[-K \frac{Wg}{A_{feeder}}\right] \quad 25$$

where g is the gravitational constant, $\rho_{feeding}$ is the perceived density at the inlet of the screw, ρ_{max} is the density at which the perceived density does not to change when more material is added to the feeder, ρ_{min} the minimum density seen when the feeder is near empty (i.e., $W \rightarrow 0$), and K is the modified pressure decay constant. Given the established relationship in Equation 21 between the ρ and ff , Equation 25 can be re-written by multiplying both sides of the equation by the screw flight volume to yield Equation 26. This model, hereunto is referred to as the feed factor model.

$$ff_{apparent}(W) = ff_{max} - (ff_{max} - ff_{min})Exp\left[-K\frac{Wg}{A_{feeder}}\right] \quad 26$$

In the feed factor model, the values of the ff_{max} and ff_{min} represent the extrapolated values when the feed factor profiles approach infinity and zero, respectively. Thus, the values of ff_{max} , ff_{min} , and K must be regressed from experimental data, which allows for a calibration of the model based different materials. This ability to adapt (i.e., calibrate) the model to material properties allows for implementation of the model using the methodology presented in Chapter III.

It is important to note that in further references to this model, the constant parameters inside of the exponential are lumped into a single variable β so that $\beta = Kg/A_{feeder}$. The units of β are then in the form of $mass^{-1}$, which represent the changes in feed factor as a function of mass remaining in the feeder.

7.3.3.3. Calibration of feed factor model

Using Equation 26, regression of the ff_{max} , ff_{min} , β were performed using the feed factor profiles from the flow rate characterization experiments. This procedure, when repeated for a variety of materials, would then take the level 1 feed factor model to level 2, as the effect of materials would be considered for this model. Figure 37 shows the results for the regression of the feed factor model coefficients for the example provided in Case C in this work.

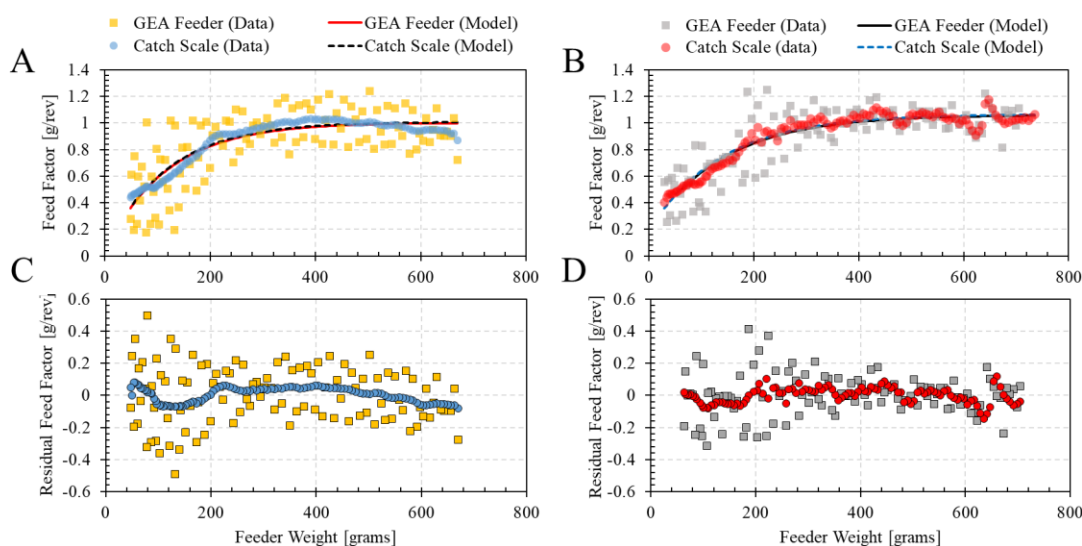


Figure 37. Feed factor model applied to the profiles for Case C. Regression of feed factor model parameters for profiles from (A) volumetric experiment, (B) gravimetric experiment. Model residuals for the model for (C) volumetric experiment, and (D) gravimetric experiment.

Figure 37A and Figure 37B show the regression of the feed factor model coefficients using the feed factor profile data from the volumetric and gravimetric feeder experiments, respectively. Four sets of three model coefficients are regressed for this data. The results for these coefficients are presented in Table 36.

INSERT Table 36 HERE

Coefficients of determination (R^2) greater than 70% and a statistical significance value (p -value < 0.05) were obtained for the model and each of the coefficients in these regressions, indicating that model and the coefficients accurately represented the data. The results for the ff_{max} were very close to one another, which indicated that the result was consistent for this material and the experiments studied. However, the results for the ff_{min} and β were shown to have some variation for this material in these two experiments. This can be explained through the definition of the two model variables from Equation 26. The ff_{min} represents the extrapolated value of the feed factor when the amount of material in the feeder approaches zero (i.e., $W \rightarrow 0$). Thus, since this value is not an observed parameter, a larger degree of error is expected for this model

parameter. Consequently, since the rate of decay of the exponential is dependent on the gradient set by $\Delta ff = (ff_{max} - ff_{min})$, the values of β are also subject to higher variability when compared those from the ff_{max} .

Since the noise provided in the feed factor profile was considered to be an intrinsic property of the material, the model errors (i.e., residuals) were calculated and plotted in Figure 37C and Figure 37D. The model error for these feed factor profiles appear to have a mean centered at 0 g/rev and a standard deviation ranging between 0.048 and 0.178 for all the experiments. It was noted that the standard deviation for the residuals for the GEA feeder was larger than that of the catch scale, which was attributed to the higher noise observed by the load cell on the GEA feeder. Markedly, the average of the residuals was close to zero, which indicated that the model and in combination with the regression parameters were able to capture the average behavior of the feed factor profiles.

Given that there was interest in capturing the amplitude of the feed factor profile noise for future modeling purposes, a truncated cosine Fourier series, shown in Equation 27, was used to capture the feed factor variability due to noise (ff_{var}). Three terms ($j = 3$) were used for the truncated Fourier series. To minimize the number of variables regressed for the Fourier series, the trigonometric coefficient (i.e., frequency dependent) values (B_j) were all set to 1 and the cosine phase shift (P_j) values were set to 100, 150, and 200 grams for each of the terms, respectively. This parameter selection was done based on an approximation of the mean after all the coefficients were regressed.

$$ff_{var} = \sum_{j=1}^3 A_j \text{Cos}(B_j W - P_j) \quad 27$$

The feed factor variability (ff_{var}) was added to the feed factor model as shown in Equation 28. Alternatively, a random number generator could be added to the deterministic prediction of the

feed factor from Equation 26, yet for future implementation purposes the Fourier series provided a feasible solution.

$$ff(W) = ff_{max} - (ff_{max} - ff_{min})Exp[-\beta W] + \sum_{j=1}^3 A_j \text{Cos}(W - P_j) \quad 28$$

Similarly to the procedure followed to acquire the results in Figure 37, the feed factor profile analysis and regression of the ff_{max} , ff_{min} , β , A_1 , A_2 , and A_3 were performed for the 237 experimental results from the flow rate characterization experiments. Given the similarity of the regressed model coefficients from the GEA feeder or catch scale profile data, only the coefficients obtained from catch scale data were used for further analysis. The reasoning behind only capturing the catch scale data rested on the fact that these values offered the least noisy of all the measurements, which also provided a better dataset for regression. Furthermore, if future researchers were interested in capturing the noise of the feeder, the results from the experiment indicated that scaling the catch scale amplitudes by a factor of 3 to 5 would yield similar results to those obtained from the GEA feeder.

Results for the 237 sets of six regressed feed factor model parameters ($n = 1,422$ parameters) were separated based on the individual materials and averaged for each material. Further, the results from the regressed ff_{max} , ff_{min} , and cosine Fourier amplitude values (A_1 , A_2 , and A_3) coefficients for the feeder were separated based on the screw pitch and averaged within each of the materials given the known relationship between the feed factor and screw flight volume (i.e., screw pitch). Since the results for the β since they are attributed to the behavior of the material in the hopper, they were only averaged within the materials. Table 26 shows the results for the regressed coefficients, excluding the last two amplitude values A_2 , and A_3 . These values were highly correlated to the A_1 as shown in the following section relating the material property measurements to the regressed variables. Markedly, for all feed factor model regressions the R^2

was above 70% and coefficient results were only used if they showed statistical significance (i.e., p -value < 0.05).

Table 26. Summary of results for regression coefficients of the feed factor model for all materials

Material	Screw Pitch (mm)	ff_{max} (g/rev)		ff_{min} (g/rev)		A_1 (g/rev)		β (1/kg)	
		Mean	St. Dev	Mean	St. Dev	Mean	A_1/ff_{max}	Mean	St. Dev
Acetaminophen	10	1.03	0.2	0.16	0.08	0.08	8%	5.78	1.29
	20	1.22	0.26	0.32	0.28	0.1	8%		
Calcium Di-Phosphate	10	0.87	0.09	0.78	0.13	0.02	2%	1.72	0.43
	20	2.5	0.03	2.15	0.24	0.02	1%		
API 1	10	1.24	0.08	0.61	0.04	0.05	4%	4.85	0.84
	20	2.08	0.11	1.19	0.08	0.02	1%		
API 2	10	1.54	0.21	1.27	0.08	0.08	5%	2.49	0.89
	20	2.93	0.14	2.17	0.28	0.05	2%		
API 3	10	1.0	0.07	0.48	0.09	0.04	4%	5.31	1.34
	20	1.42	0.3	0.14	0.19	0.08	6%		
API 4	10	0.34	0.05	0.15	0.06	0.02	5%	5.7	2.89
	20	1.34	0.34	0.71	0.25	0.07	5%		
Cellulose	10	0.32	0.04	0.26	0.03	0.01	3%	15.46	4.25
	20	0.72	0.12	0.51	0.16	0.1	14%		
Croscarmellose Sodium	10	1.3	0.07	0.95	0.08	0.02	2%	6.16	0.96
	20	2.47	0.14	1.99	0.13	0.03	1%		
Crospovidone	10	0.32	0.01	0.35	0.00	0.01	4%	6.8	1.98
	20	1.35	0.04	0.96	0.23	0.06	4%		
Lactose 2	10	0.72	0.02	0.52	0.12	0.04	5%	7.44	0.74
	20	2.07	0.01	1.82	0.01	0.01	1%		
Magnesium Stearate	10	0.44	0.02	0.22	0.05	0.03	7%	17.76	8.28
	20	0.81	0.01	0.51	0.08	0.05	6%		
MCC 1	10	0.69	0.02	0.47	0.03	0.01	2%	9.01	4.34
	20	1.35	0.06	1.17	0.13	0.01	1%		
MCC 2	10	0.55	0.05	0.36	0.1	0.02	3%	10.82	4.27
	20	1.24	0.04	1.08	0.14	0.02	1%		
MCC 3	10	0.59	0.02	0.01	0.01	0.05	9%	9.66	4.24
	20	1.39	0.03	0.77	0.64	0.07	5%		
MCC 4	10	0.82	0.03	0.65	0.05	0.03	4%	7.51	3.05
	20	1.68	0.06	1.48	0.08	0.03	2%		
Silicified MCC	10	0.79	0.06	0.63	0.16	0.04	5%	4.98	2.35
	20	1.88	0.08	1.68	0.17	0.05	3%		
Starch 1	10	1.07	0.33	0.24	0.01	0.12	11%	6.53	0.46
	20	2.69	0.19	1.33	0.29	0.09	3%		
Starch 2	10	1.1	0.28	0.92	0.11	0.04	4%	10.88	6.87
	20	2.09	0.04	1.57	0.41	0.02	1%		
Starch 3	10	1.71	0.23	1.27	0.11	0.03	2%	2.61	1.23
	20	3.27	0.18	2.85	0.3	0.03	1%		

St. Dev = standard deviation. The number of samples in the standard deviation was the number of experiments performed for that particular material

Table 26's results are also shown graphically in Figure 60. The results indicate there are significant differences in the coefficients for different materials. Feed factor maximum values ranged for the materials ranged between 0.32 and 1.71 g/rev and 0.72 and 3.27 g/rev for the 10 and

20mm pitch screws, respectively. Notably, these two ranges show that the feed factor increased almost two-fold when the size of the screw was doubled. The minimum feed factor ranges were consistently lower than the maximum feed factor, ranging between 0 and 1.27 g/rev for the 10 mm and 0.14 and 2.85 g/rev for the 20mm screw pitches.

INSERT Figure 60 HERE

Figure 60A and Figure 60B show the relative differences between material maximum and minimum feed factors at different screw pitch sizes. The material with the largest maximum feed factor was recorded as starch 3, with a value of 3.27 ± 0.18 g/rev. The second and third largest feed factor was noted for API 2 and starch 1, respectively. Using starch 3's feed factor and the maximum screw speed of the GEA feeder ($\omega = 461.5$ RPM), the maximum flow rate capacity for the unit using our material dataset was estimated at 90.5 kg/hr.

The first Fourier series amplitude coefficient (A_1) results for the materials, as shown in Figure 60C, ranged between 0.01 and 0.12 g/rev for the 10mm and 0.01 and 0.14 g/rev for the 20mm screw pitch. At first look, indicated that a larger degree of noise was observed for the 20mm screw pitch system; however, proportionally, the amount of noise observed on the feed factor curve profiles for the 10mm screw pitch experiments was higher given that the feed factor ranges were smaller for the smaller screw size. To compare the amplitudes over a similar scale, the A_1 values in Table 26 were divided by the averaged ff_{max} , resulting in value that would indicate at the amount of variability observed in the feed factor as a function of the maximum feed factor. The results showed that more variability in the feed factor curves was observed for the smaller screw pitch for 17 of the 19 materials studied. This observation was in agreement with previous findings regarding the difficulty for materials to fill smaller pitch screws. Cellulose and API 3 appeared to deviate from the variability trend; a result that was explained by the intrinsic difficulties in powder feeding visually observed for these two materials. Cellulose had a tendency to flow so poorly, that

in several occasions when the screw speed was above the maximum for the 445:1 gearbox ratio (i.e., $\omega > 100 \text{ RPM}$) the screws would jam and even become dislodged from the bayonet fitting. The resistance to flow provided by the cellulose provided an excellent case study for materials that ought to be dispensed using a small screw size at lower feed rates in order to avoid jamming. API 3 had a high tendency to stick to the walls of the hopper, particularly when the material was sheared at high rotational speeds by the impeller inside of the hopper.

Lastly, the results from the feed factor decay constant (β), shown in Figure 60D, showed that the studied materials had a wide range of values for this coefficient. The values for β ranged between 1.72 and 17.7 kg^{-1} . Notably, magnesium stearate and cellulose had the highest β values, which indicated that materials with relatively poorer flow properties had a faster decrease in the rate of feed factor values. Materials with better flow, such as anhydrous calcium di-phosphate and API 2 had the smallest values of β . This result can be explained by resistance of the material to flow inside of the hopper, a property that would then diminish the feed factor significantly by not delivering material to the screws.

7.3.4. Effect of material properties on feed factor profile

7.3.4.1. *Correlations between regressed parameters and material properties*

Correlations between the material properties and the regressed feed factor model parameters was first evaluated using a multivariate plot representing the level of linear correlation (i.e., the correlation coefficient) between the properties and the parameters. Figure 38 shows the multivariate chart for set of selected material properties and the feed factor model parameters. Notably, several material property measurements, such as compressibility and permeability at different compression pressures were shown to have a high degree of correlation, as described in Chapter V; therefore, only the 15kPa results for these material property measurements were selected for the correlation analysis.

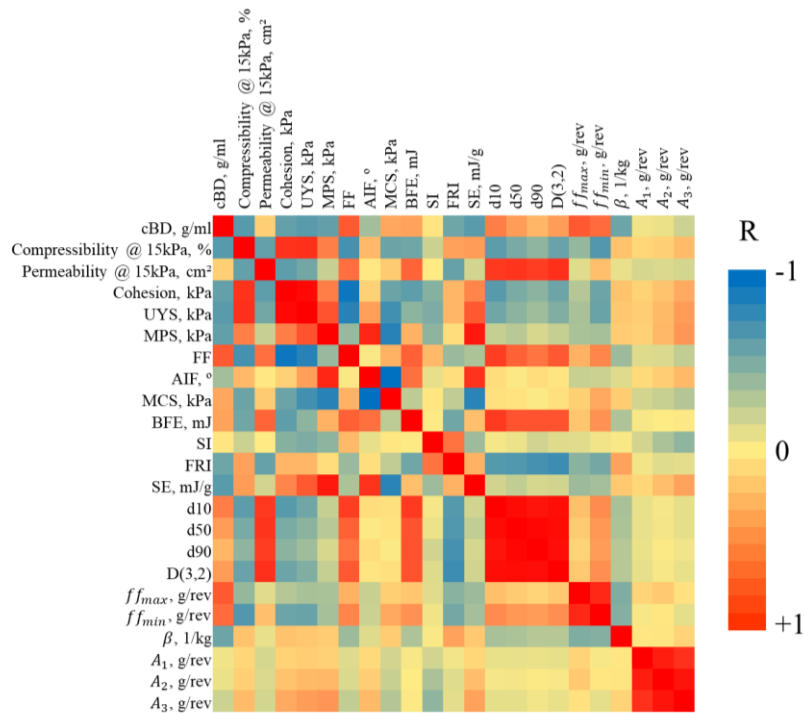


Figure 38. Correlation color map indicating level of linear correlation (R) between material properties and regressed feed factor parameters.

The results from Figure 38 show that both ff_{max} and ff_{min} had the highest correlation with conditioned bulk density (CBD). This result was expected given the correlation between the volumetric displacement from the screws sweeping volume and material density. Nevertheless, the level of correlation (R) between the bulk density and the ff_{max} and ff_{min} was 0.63 and 0.56, respectively; indicating that other properties were needed to explain the behavior of the material in the system. Notably, for both the ff_{max} and ff_{min} the second largest linear correlation coefficient was with compressibility at 15 kPa. The linear correlation coefficients between compressibility and ff_{max} and ff_{min} were -0.34 and -0.56, respectively. The negative correlation between the compressibility and the feed factor indicated that as the material was more compressible, the feed factor coefficients would be reduced. This result can be explained by the inability of compressible materials flow as well as less compressible materials. This result is further corroborated by the work from Van Snick et al. [198, 301] who found that compressible materials also have a tendency

to coat the screws of the feeder, leading to a lower sweeping volume ultimately affecting the feed factor. Both feed factor metrics were found to be highly correlated with each other with a level of linear correlation of $R = 0.84$. This result indicates that both measurements share some level of proportionality, which is in line with the expected behavior.

Figure 38 shows β has negative linear correlations with respect to conditioned bulk density ($R = -0.47$) and flow function coefficient ($R = -0.31$). This result indicates that materials with higher bulk densities and better flow properties have lower values of the decay rate, meaning their feed factor decreases more slowly than less dense and more poorly flowing counterparts. This behavior agrees with the previously made observation, wherein materials with poorly flowing properties such as magnesium stearate and cellulose had a faster and larger rate of change in the feed factor compared to better flowing materials such as anhydrous calcium di-phosphate and silicified MCC.

The three cosine Fourier series amplitudes were found to have a moderate level of correlation with shear cell test measurements such as cohesion, MPS and UYS. This result is in agreement with the notion that increased materials cohesion leads to highly variable filling efficiency in the screws, which in turn affects the feed factor variability [303]. Relationships between cohesion and fill efficiency have been noted for tablet weight variability in the tablet press [203], allowing for this relationship to hold similarity with the filling efficiency in the screws. Lastly, the results from Figure 38 further indicated that A_1 , A_2 , and A_3 values were highly correlated with each other, with correlation coefficient between A_1 and A_2 of $R = 0.88$ and between A_1 and A_3 of $R = 0.84$. These results led to the use of A_1 as the only variable being modeled as a function of material properties. Linear regression models between the first coefficient and the remaining two coefficients indicated that $A_2 = 0.41A_1$ and $A_3 = 0.38A_1$, regressions that were obtained with coefficients of determination (R^2) greater than 60%.

7.3.4.2. *Material property models predicting regressed parameters*

After investigating the correlations between material properties and feed factor model parameters (i.e., development of the level 2 model), a set of response surface models (RSMs) were proposed to correlate material properties to the regressed feed factor model parameters. These RSM would serve as the connection between the material property measurements and the categorical material property variables that results from the level 2 model.

The RSMs were developed using the highest correlated material properties, shown in Figure 38, for each of the regressed parameters and performing a regression using the material properties as inputs. RSM variables were removed from the model sequentially until all of the variables displayed a level of significance of less than 5% (i.e., $p\text{-value} < 0.05$). This sequential removal of variables was performed in order to avoid having parameters which impact in the model would be minimal.

RSMs relating material properties were developed for ff_{max} , ff_{min} , β and the cosine Fourier amplitude values (A_1 , A_2 , and A_3). From the analysis, several variables were found to be repeated in all models. These material properties, listed in Table 27, were therefore found to have an impact on the feeder performance based on the analysis performed. Notably, all of the materials appeared to have some correlation in the multivariate color map, indicating the approach of previewing the variables provided successful insight for the subsequent data-driven modeling. Furthermore, screw pitch was found to be a critically important variable, particularly for the feed factor parameters. This was in agreement with expected results, given the relationship between feed factor and sweeping volume.

Table 27. Response surface model (RSM) variables and the reference variables

Variable	Re-coded Variable	Reference Value	Units
Screw Pitch	X_1	15.79	mm
Conditioned Bulk Density (CBD)	X_2	0.45	g ml ⁻¹
Compressibility (CPS)	X_3	21.63	%
Permeability	X_4	44.55	x10 ⁹ cm ²
Cohesion (kPa)	X_5	0.606	kPa
Flow Function Coefficient (FF)	X_6	8.48	-
Angle of Internal Friction (AIF)	X_7	31.13	Degrees (°)

Each of the material properties was recoded using the letter variable X , which would be used to describe the RSM models. Reference values representing the average of the property for the full material property sample set are also reported in Table 27. The reference values are used in conjunction with Equation 29 to represent the standardized effect of the material property on the RSM model prediction.

$$\overline{\Delta X}_y = X_y - \overline{X}_y \quad 29$$

where \overline{X}_y is the reference value for variable y , X_y is the material property value for variable y and $\overline{\Delta X}_y$ is the standardized material property effect value observed in all of the subsequent RSM models. The reference values provide a reference for the ranges of material properties that were used in this study.

Equation 30 provides the relationship between ff_{max} , screw pitch size, and four material properties listed in Table 27. The model included single and interaction terms of screw pitch size, conditioned bulk density, compressibility, permeability, and cohesion. These four material properties are known to correlated with the flowability of material and further describe the amount of material able to occupy a particular volume. Interaction effects were found to occur between all material properties for this model, indicating that more complex physics related the behavior of these properties to the maximum feed factor.

$$ff_{max} = a_0 + \sum_{i=1}^5 a_i X_i + \sum_{j=1}^4 a_{j+5} \overline{\Delta X}_1 \overline{\Delta X}_j + \sum_{l=2}^5 a_{l+8} \overline{\Delta X}_2 \overline{\Delta X}_l + \sum_{k=3}^5 a_{k+11} (\overline{\Delta X}_k)^2 + a_{17} \overline{\Delta X}_4 \overline{\Delta X}_5 \quad 30$$

The values of the 18 regression coefficients a_x for this model are provided in Table 28

Table 28. Coefficient table for the feed factor maximum (ff_{max}) RSM

Coefficient (a_x)	Estimate (x 1000)	Standard Error (x 1000)	Units
0	-3071.7	219.8	g rev ⁻¹
1	89.7	2.6	g (rev mm) ⁻¹
2	5699.0	280.2	ml rev ⁻¹
3	19.0	3.9	g (rev %) ⁻¹
4	7.0	1.2	g (rev cm ²) ⁻¹
5	385.0	139.9	g (rev kPa) ⁻¹
6	0.0	0.0	ml (rev mm ²) ⁻¹
7	137.1	19.8	ml (rev mm) ⁻¹
8	-1.7	0.3	g (rev % mm) ⁻¹
9	-0.2	0.1	g (rev cm ² mm) ⁻¹
10	-8938.9	939.2	ml ² (rev g) ⁻¹
11	-51.1	26.8	ml (rev %) ⁻¹
12	13.9	5.5	ml (rev cm ²) ⁻¹
13	2451.8	865.8	ml (rev kPa) ⁻¹
14	-0.7	0.1	g (rev % ²) ⁻¹
15	0.0	0.0	g (rev cm ⁴) ⁻¹
16	1669.3	255.4	g (rev kPa ²) ⁻¹
17	25.6	3.3	g (rev kPa cm ²) ⁻¹

All coefficients have a p-value < 0.05 and the overall model has a p-value < 0.0

Similarly to Equation 30, Equation 31 shows the RSM correlation between material properties and the ff_{min} . In this relationship, only three material properties and the screw pitch were found to have statistically significant values (i.e., p-value > 0.05). During the regression, the coefficients (b) for the cohesion variable displayed a high error, which indicated that the material property did not provide much additional information to the model. This increase in error may be due to the intrinsic error of the ff_{min} values, which as previously discussed tend to have a higher regression error since the parameter is extrapolated from data. Given this increase in error for the cohesion variable parameters, the ff_{min} model was reduced to a total of 11 terms, including the intercept. Like the ff_{max} the remaining material properties (i.e., bulk density, compressibility, and permeability) were found to have some physical correlation with the defined feed factor parameter.

$$ff_{min} = b_0 + b_1X_1 + b_2X_2 + b_3X_4 + \sum_{j=1}^2 b_{j+3} \overline{\Delta X_2} \overline{\Delta X_j} + \sum_{k=1}^4 b_{k+5} \overline{\Delta X_3} \overline{\Delta X_k} + b_{10} (\overline{\Delta X_4})^2 \quad 31$$

The values of the 11 regression coefficients b_x for this model are provided in Table 29

Table 29. Coefficient table for the feed factor minimum (f_{fmin}) RSM

Coefficient (b_x)	Estimate (x 1000)	Standard Error (x 1000)	Units
0	-1285.08	118.75	g rev^{-1}
1	68.38	4.26	g (rev mm)^{-1}
2	2948.93	189.10	ml rev^{-1}
3	5.56	0.75	$\text{g (rev cm}^2\text{)}^{-1}$
4	90.43	32.38	ml (rev mm)^{-1}
5	-10258.10	1456.85	$\text{ml}^2 \text{(rev g)}^{-1}$
6	-2.08	0.36	$\text{g (rev \% mm)}^{-1}$
7	-145.88	26.90	ml (rev \%)^{-1}
8	-0.49	0.21	$\text{g (rev \%}^2\text{)}^{-1}$
9	0.42	0.10	$\text{g (rev \% cm}^2\text{)}^{-1}$
10	-0.04	0.01	$\text{g (rev cm}^4\text{)}^{-1}$

All coefficients have a p-value < 0.05 and the overall model has a p-value < 0.01

The feed factor decay (β) was found to correlations with several material properties, including conditioned bulk density, permeability, flow function coefficient (FF), and angle of internal friction (AIF). The RSM for β , shown in Equation 32, shows that a variable transformation had to be performed to yield the highest determination coefficient for this model. The β values for each of the materials was divided by the conditioned bulk density and the natural logarithm was taken in order to shift the distribution of values to a more normal distribution. The results for the transformed values of β – now $\text{Ln} \left[\frac{\beta}{X_2} \right]$ – were then used as the RSM response variables. Notably, AIF was found to have an exponential correlation with the feed factor decay variable, a result that resembles the relationship observed by Johansson for stresses and pressures observed in cylindrical silos [217, 304]. This result, indicates that is correlated with the amount of pressure the material is exerting at the screw entrance and further confirms the original assumption made by the model relating feeder weight to pressure at the screw inlet.

$$\text{Ln} \left[\frac{\beta}{X_2} \right] = c_0 + \sum_{i=1}^4 c_i X_{i+3} + \sum_{j=4}^7 c_{j+1} \overline{\Delta X_4} \overline{\Delta X_j} + \sum_{k=6}^7 c_{k+3} \overline{\Delta X_5} \overline{\Delta X_j} + c_{11} \overline{\Delta X_6} \overline{\Delta X_7} \quad 32$$

The values of the 11 regression coefficients c_x for this model are provided in Table 30

Table 30. Coefficient table for the transformed feed factor decay constant ($\ln \left[\frac{\beta}{X_2} \right]$) RSM

Coefficient (c_x)	Estimate (x 1000)	Standard Error (x 1000)	Ln(Units)
0	-7159.20	1037.66	mL g ⁻²
1	-12.63	3.11	mL (g ² cm ²) ⁻¹
2	6535.67	831.08	mL (g ² kPa) ⁻¹
3	633.11	75.84	mL g ⁻²
4	85.25	9.37	mL (g ² °) ⁻¹
5	0.30	0.08	mL (g ² cm ⁴) ⁻¹
6	-30.93	13.23	mL (g ² cm ² kPa) ⁻¹
7	-1.10	0.39	mL (g ² cm ²) ⁻¹
8	1.43	0.32	mL (g ² ° cm ²) ⁻¹
9	1134.50	119.97	mL (g ² kPa) ⁻¹
10	437.47	64.73	mL (g ² ° kPa) ⁻¹
11	17.70	3.99	mL (g ² °) ⁻¹

All coefficients have a p-value < 0.05 and the overall model has a p-value < 0.01

Lastly, the effect of material properties on the observed amplitude of the feed factor profile noise was established in Equation 33. Untransformed amplitude values had some of the least significant relationships with material properties. Given the relationship between the strong relationship between feed factor and density, the A_1 were transformed similarly to the β . A_1 values were divided by conditioned bulk density and the natural logarithm of that ratio was calculated. After the transformation, a third order factorial correlation with respect cohesion and single order with respect to screw pitch were to accurately represent the system. Markedly, the statistical significance of the first order cohesion term was above the statistical significance limit, yet based on the relationship with the other higher order terms, the authors found the current model suitable and retained the model variable.

$$\ln \left[\frac{A_1}{X_2} \right] = h_0 + h_1 X_1 + h_2 X_5 + \sum_{i=2}^3 h_{i+1} (\overline{\Delta X_5})^i \quad 33$$

The values of the 4 regression coefficients h_x for this model are provided in Table 31

Table 31. Coefficient table for the transformed first coefficient of the feed factor profile cosine Fourier amplitude ($\ln \left[\frac{A_1}{X_2} \right]$) RSM

Coefficient (h_x)	Estimate (x 1000)	Standard Error (x 1000)	Ln (Units)
0*	-1815.82	233.06	ml rev ⁻¹
1*	24.29	8.77	ml (rev mm) ⁻¹
2**	-803.37	323.51	ml (rev kPa) ⁻¹
3**	-291.78	334.35	ml (rev kPa) ⁻¹
4*	5769.16	1095.26	ml (rev kPa) ⁻¹

* Coefficients have a p-value < 0.05. **Coefficients with p-value > 0.05, but associate with another effect.

Table 32 provides a summary of the statistics for the abovementioned RSM models with respect to their coefficient of determination, root mean square error, and mean response. The mean responses between ff_{max} and ff_{min} show that the models are in line with the expected results of the maximum value being larger than the minimum. The results also show the coefficient of determination (R^2) for the first three feed factor model parameters anticipate an accurate prediction of the regressed parameters based on material properties. The model for A_1 showed the model may not provide as accurate a prediction to the amplitude values, yet for the purpose of this work the authors found the model sufficient.

Table 32. RSM model statistics for Equations 29-33

Variable	ff_{max}	ff_{min}	$\ln \left[\frac{\beta}{X_2} \right]$ Model	$\ln \left[\frac{A_1}{X_2} \right]$ Model
R^2	94%	88%	81%	54%
Root Mean Square Error	0.19	0.32	0.53	0.66
Mean of Response	1.39 g/rev	0.95 g/rev	2.66 ml/g ²	-1.86 Ln(mL/rev)

The ANOVA results for each of the models is provided in Table 37. Most importantly, all models showed a level of statistical significance of $p < 0.001$, which indicated that all of the RSM models established a correlation between the selected properties and the regressed feed factor model parameters.

INSERT Table 37 HERE

Figure 39 shows the parity plots comparing the expected values of the feed factor model parameters (i.e., those regressed from the data) and those calculated from the RSM models. Figure

39A shows the results between the RSM calculated (i.e., predicted from model) and regressed ff_{max} values. The black line in the figure represents the $x = y$ line, meaning the point where there are no differences between the predicted and regressed values. The red dashed lines represent the individual 95% confidence interval (CI) for the predictions. As seen in Figure 39A, the results show the RSM accurately predicting the values of ff_{max} for the whole range of materials. Figure 39B presents the results for the ff_{min} parity plot. As seen by the lower correlation coefficient, the predictions of the ff_{min} appear to be slightly worse than the ff_{max} . This difference, as previously discussed, is attributed to the larger error observed in the regressed parameter. Nevertheless, it is important to note that a large number of data are closely grouped along the $x = y$ line, indicating that the model predicts the value accurately for a vast number of trails.

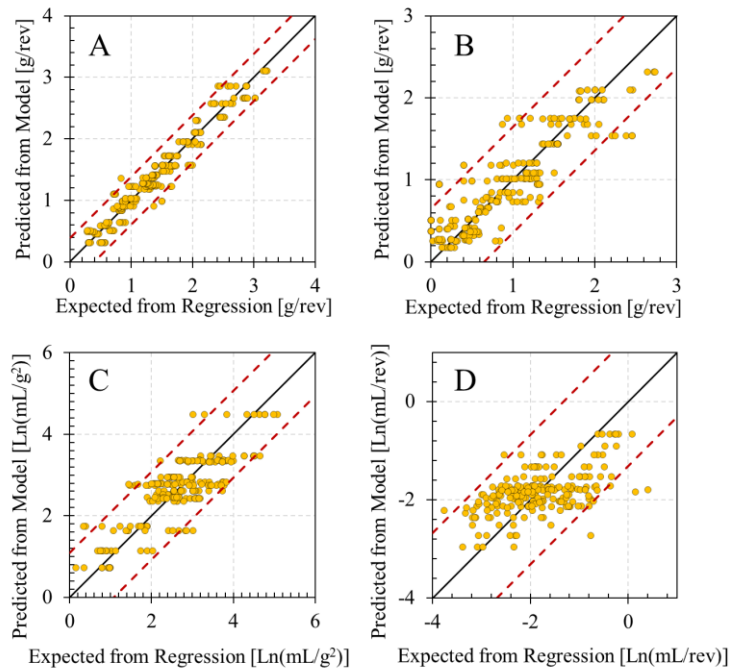


Figure 39. Parity plots between the RSM Predicted model parameters and the values expected from the regression using experimental data. (A) Feed factor maximum (ff_{max}), (B) feed factor minimum (ff_{min}), (C) transformed feed factor decay ($Ln \left[\frac{\beta}{X_2} \right]$), and (D) transformed feed factor variability ($Ln \left[\frac{A_1}{X_2} \right]$)

The parity plot for the transformed feed factor decay variable (Figure 39C) show a relatively good agreement between the predicted values from the RSM and the regressed coefficients. This result indicates the variable transformation successfully aided in obtaining a good regression fit for the β values. Notably, several results appeared to have variability in the horizontal direction, which indicated the RSM model was not representing some intrinsic variability seen by the expected results. Based on this finding, it is encouraged that further material property measurements and variables are included in subsequent material property model to account for this observed variability. Similarly to Figure 39C the results from Figure 39D show that certain variability in the observed A_1 was not captured by the current model, indicating that future variables and material properties ought to be considered.

7.3.5. Model mean absolute percentage error

Using the RSM models presented in Equations 29 through 33, the relationship established between A_1 and the remaining two amplitude coefficients, and the feed factor model (Equation 28), a level 3 model was compiled for the feeder. The feed factor model had as inputs the parameters estimated from the RSM models, which in turn had as input the property measurements of the materials. Using this level 3 model, a comparison of the feed factor profiles obtained experimentally was performed using the MAPE metric shown in Equation 34.

$$MAPE = \frac{100}{r} \sum_{i=1}^r \left| \frac{y_i - \hat{y}_i}{y_i} \right| \quad 34$$

where r is the number of observations in the feed factor profile, y_i is the experimental value of feed factor at a given feeder weight value i , and \hat{y}_i is the predicted value of the feed factor at that given weight. The MAPE results for the feed factor profiles predicted using the level 3 model were compared with those from the averaged feed factor model coefficient in

(effectively, the level 2 model). For the level 3 model, the material property measurements for the variables listed in Table 27. Response surface model (RSM) variables and the reference variables and the screw pitch were the only inputs to the model. For the level 2 model, the feeder's experimental screw pitch configuration and material being tested were the only input parameters.

The average results for each of the feed factor model coefficient in

were used to calculate the feed factor profiles of the 237 feeder experiments. The results of the MAPE model are shown in Table 33.

Table 33. Summary of MAPE results comparing the level 2 model with the level 3 model

Material	Screw Pitch (mm)	MAPE Values (%)			
		Regressed Parameters Averaged (Level 2)		Calculated from RSM Models (Level 3)	
		Mean	St. Dev	Mean	St. Dev
Acetaminophen	10	19.7	13.1	18.7	11.6
	20	23.2	7.6	20.2	9.0
Calcium Di-Phosphate	10	11.3	6.4	21.8	3.0
	20	3.4	1.2	11.6	0.7
API 1	10	4.7	2.4	7.4	1.7
	20	4.3	2.1	8.8	4.0
API 2	10	3.9	1.3	8.8	1.5
	20	3.4	1.9	13.4	3.8
API 3	10	6.8	2.7	8.1	3.7
	20	23.6	11.7	22.9	18.8
API 4	10	11.4	4.1	42.2	6.8
	20	18.8	12.0	18.9	16.8
Cellulose	10	13.1	7.1	36.2	7.8
	20	19.5	7.0	25.1	13.6
Croscarmellose Sodium	10	3.5	2.0	7.7	0.2
	20	5.1	1.8	7.4	2.1
Crospovidone	10	11.2	2.0	41.3	7.3
	20	5.0	3.0	10.2	2.7
Lactose 2	10	5.1	0.8	32.1	2.0
	20	1.6	1.8	9.8	0.9
Magnesium Stearate	10	6.8	2.0	16.5	3.8
	20	6.6	6.0	11.1	3.7
MCC 1	10	3.8	2.3	33.9	6.0
	20	3.8	2.0	8.7	2.4
MCC 2	10	9.4	3.4	14.0	2.3
	20	3.1	1.4	6.1	0.6
MCC 3	10	6.7	3.8	7.7	3.0
	20	4.6	1.1	5.6	1.0
MCC 4	10	3.0	0.7	8.0	0.4
	20	3.2	1.3	5.4	0.3
Silicified MCC	10	9.1	6.8	15.4	4.7
	20	6.6	6.6	8.7	4.7
Starch 1	10	28.6	12.8	37.5	19.0
	20	6.9	2.6	10.3	4.7
Starch 2	10	14.7	6.9	9.7	2.1
	20	2.5	1.7	5.0	1.5
Starch 3	10	12.2	4.7	18.1	9.2
	20	7.0	4.5	12.3	6.1

Table 33 results indicate the average MAPE coefficients ranged between 1.6 and 28.6% for the level 2 modeling strategy and between 5.0 and 42.2% for the level 3 model. The increase in the MAPE values between the level 2 and 3 modes was expected, given that the error and variability from the RSM models would compile and appear as part of the overall result. Nevertheless, it is important to note that the MAPE results for the level 3 model varied with respect to those from level 2 by more than 10% only in 5 instances. The five instances where the level 3 model significantly exceeded that of the level 2 involved the 10mm screw pitch for materials whose particular flow properties were difficult to capture in several instances. Figure 40 shows the MAPE results for each material to compare the results between models and with respect to screw pitch length.

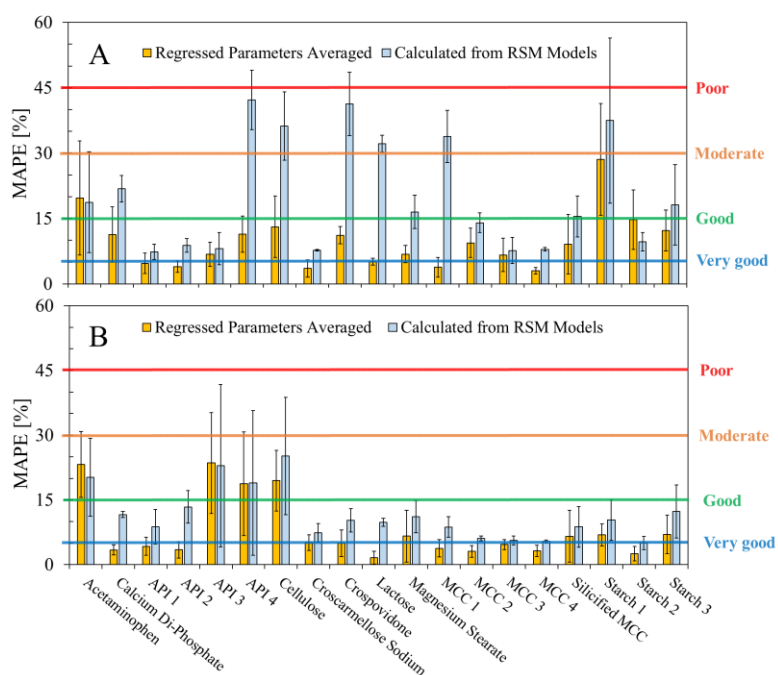


Figure 40. Comparison of mean absolute percentage error (MAPE) values for the experimental feed factor profile predictions between the level 2 (regressed parameters averaged) and level 3 (i.e., calculated from RSM models) models. MAPE values divided by screw pitch (A) 10mm and (B) 20mm.

Using a heuristic standard to evaluate the level of prediction, wherein MAPE values less than 5% are considered very good predictions, between 5 and 15% good, 15 and 30% moderate, 30

and 45% poor, and above 45% very poor, Figure 40 shows that 9 of the 19 cases for the 10mm pitch were between very good and good for both the level 2 and level 3 models. In several instances, such as for anhydrous calcium di-phosphate, lactose, and starch 3, the RSM model errors appear to increase the MAPE enough to reach the moderate range for the level 3 model. Most notably, the MAPE predictions appear to increase dramatically when the level 3 model is used to predict the feed factor profiles for API 4, cellulose, crospovidone, lactose, and MCC 1. This large increase in MAPE is attributed to relatively amount of data for the materials tested, particularly at low flow rates and with the 10mm screw. The reduced number of data for these materials lead to a underrepresentation during the RSM predictions, which led to a higher level of error for these materials. Starch 1 appeared to have a high MAPE for both the level 2 and level 3 models, indicating that the material presented issues for feeding. This was attributed to the high compressibility and cohesion of starch 1, which made the flow into the smaller screws much more difficult and erratic than with the larger screw length.

MAPE results for the 20mm screw pitch, for which many more experiments were performed, resulted in very similar values between the level 2 and level 3 models. A total of 15 out of the 19 materials were seen to have MAPE values within the very good and good range both models. Notably, materials that were seen to present feeding challenges had MAPE values within the moderate range for this screw pitch length. This result hints at the possibility that the model behavior applies to well flowing materials in the feeder hopper.

7.3.6. Refill case studies

To evaluate the reproducibility of the feed factor curve as a function of feeder weight, sequential refill experiments were performed for selected materials. The experiments were divided into two sets: constant feeder fill level refilling and cascade refilling. The former consisted in

refilling the feeder between two constant levels of filling (e.g., between 50 and 100% fill level), while the latter performed refills at various levels of fill.

In the following subsections, the results for the refilling experiments using MCC 4 with a 63:1 gearbox and a 20mm pitch screw are shown. For these experiments, a total of three refills are performed under gravimetric control for a flow rate set point of 2.78 g/s. A time based feed factor profile is shown for both the GEA feeder and catch scale feed factor profile. The predictions of the feed factor model for the material are provided using the results from

. Furthermore, the feed factor data is spliced as a function of the refill intervals to evaluate the prediction of the feed factor model with respect to the predictions of the feed factor curve as a function of feeder weight.

7.3.6.1. Case 1: Constant refill level

Figure 41 shows the results of the multiple refill experiment at a constant fill level interval. The interval for fill level was set between 40 and 90%, meaning the refill unit would refill when the hopper was filled to 40% up to the higher fill value. The average flow rate throughout operation remained relatively constant, with an average and standard deviation of 2.80 ± 0.15 g/s (i.e., RSD of 5.35%). Feed factor was monitored for both the GEA feeder and the catch scale results. Figure 41A shows the time series of both feed factors along with the recorded feeder weight. The feed factors remained relatively constant until the time reached 500 seconds, when the profile began to decay.

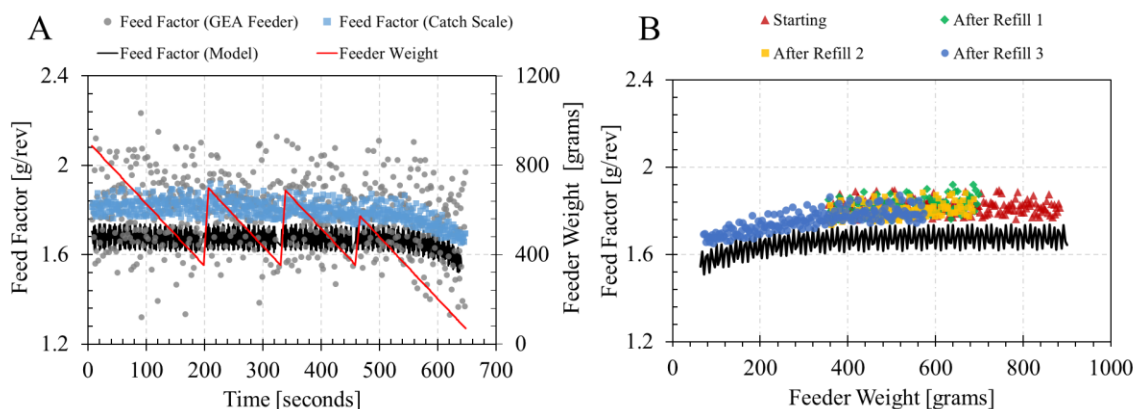


Figure 41. Results for the feed factor refill experiment at constant fill level intervals. (A) Time series of both feed factor profiles and the feed factor model predictions based on weight (left) and the corresponding feeder weight profile (right). (B) Feed factor profile for weight intervals between each refill. Black line represents the predictions from the feed factor model.

Figure 41B shows the catch scale feed factor profile separated based on the refill intervals. The starting feed factor profile was that achieved before the feeder was refilled, and ranged between 870 and 480 grams. Two sections for the subsequent two refills between 40 and 90% are shown in Figure 41B. It was seen that both of these feed factor profiles, ranging between 480 and 700 grams had very similar feed factor values, which corroborated the reproducibility of the feed factor curve. Ultimately, a small refill was performed before the feeder was depleted, showing the feed factor decreased as previously observed. The feed factor profiles shown in Figure 41B had a MAPE with respect to the modeled feed factor profile of 7.2%, indicating that the model accurately represented this system over the whole weight range.

The observed offset between the feed factor model predictions and the experimental results, although relatively small, is attributed to the slight variability between material properties as the material enters the system. Since the material is being dropped into the unit, this added shear and flow alters the material properties slightly from those of the powder when characterized (i.e., when the material conditions were static). A potential solution to improve the prediction from the model

can be to introduce an expected variability in the material property measurements in order to develop “feed factor prediction bands” that can account for potential variability in properties.

7.3.6.2. Case 2: Cascading refill

Similarly to the constant fill level study, Figure 42 shows the results of the multiple refill experiment but at varying fill levels. The objective was to have some overlap in the feed factor profiles in between refills and capture the full feed factor curve. The interval for fill level were set between 40 and 90%, followed by 25 to 75%, and ultimately 12.5 and 62.5%. The average flow rate throughout operation was less accurate than the previous case study, given that the controls were not able to quickly adapt to the rapidly changing refill profile. The average flow rate was 2.67 g/s with a standard deviation of 0.85 g/s (i.e., RSD of 31.8%). The increase variability in the flow rate occurred solely during the refill, as the feeder controls were blind during operation and there was no collected feed factor values.

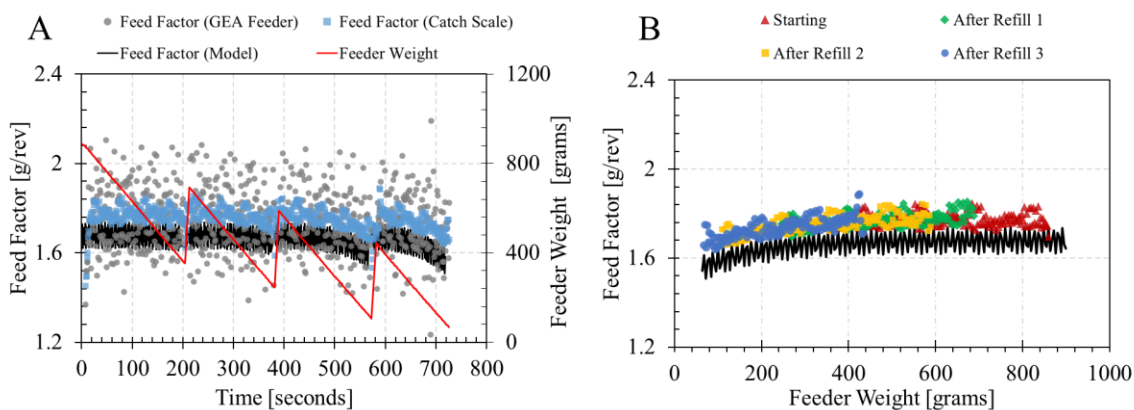


Figure 42. Results for the feed factor experiment using cascading refills. (A) Time series of both feed factor profiles and the feed factor model predictions based on weight (left) and the corresponding feeder weight profile (right). (B) Feed factor profile for weight intervals between each refill. Black line represents the predictions from the feed factor model.

Again, feed factor was monitored for both the GEA feeder and the catch scale results.

Figure 42A shows the time series of both feed factors along with the recorded feeder weight.

Similarly to the constant refill case, the feed factors remained relatively constant until the

time reached 500 seconds, when the profile began to decay. Figure 42B shows the spliced feed factor profile in between the refill intervals. As expected, the feed factor profiles after each refill appear to overlap less than in the previous case, particularly for the feed factors after the first and second refills. The feed factor profile once again appears to follow the trends observed during the flow rate characterization experiments without refill, supporting the established correlation between feed factor and feeder weight. The prediction of the feed factor curve shown in Figure 42B showed a MAPE of 5.5%, which is in line with the results presented in Table 33 for MCC 4.

The results from this section, thus, indicate that the feed factor model is able to be used evaluate the differences in feeding performance between materials and establish their maximum flow rates. In the subsequent part of this article, the feed factor model is related mathematically with the material property measurements for each of the materials used using empirical models. The resulting models would then allow researchers to implement these results using materials with known property values.

7.3.7. Refill unit characterization

Before performing the GEA feeder's RTD experiments, it was critical to evaluate the performance of the refill unit to establish the effectiveness and accuracy of refills being performed. The refilling procedure, described in the methods sections, was performed for the materials listed within the procedure. Figure 43 shows the flow rate results for the eight refills performed using (A) anhydrous calcium di-phosphate, (B) silicified MCC, (C) MCC 2 and (D) magnesium stearate. The flow rate of each material appeared to be have a triangular profile, with peaks ranging from 160 to 50 g/s. Flow rate values from the refills varied between materials, but within each of the materials they were very consistent, as shown by the reproducible profile shapes and maximum flow rates for the materials in Figure 43. The average refill time (i.e., when mass flow rate was greater than zero) noted for these four sets of refill experiments calculated as 10.7 ± 1.3 seconds.

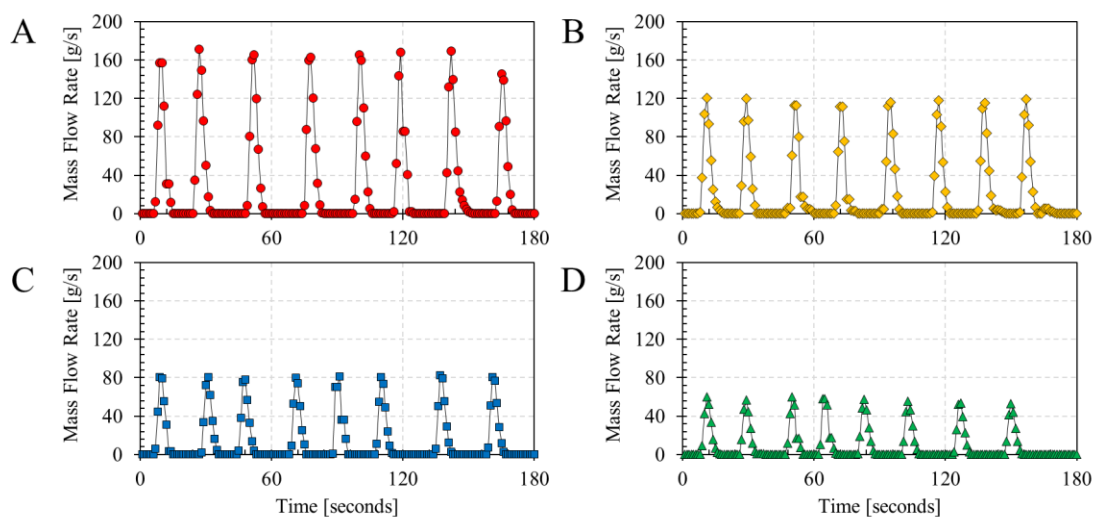


Figure 43. Results refill unit characterization using a 0.8 L cup volume. (A) Anhydrous calcium diphosphate, (B) silicified MCC, (C) MCC 2, and (D) magnesium stearate.

Similar plots were evaluated for the remaining materials, namely MCC 1, MCC 4, API 4, cellulose and acetaminophen. The results indicated that, similarly to the materials shown in Figure 43, MCC1 and MCC 4 had reproducible refill flow rates, similar refill times, and consistent refill masses. However, API 4, cellulose, and acetaminophen had highly variable refills due to arching occurring in the hopper as material was dispense by the refills. Table 34 lists the results for the average mass dispensed by the 0.8 L refill cup for the 8 sequential refills performed for the nine materials. Notably, most material refills were seen to be slightly higher than the cup volume, based on their conditioned bulk density. This result can be attributed to the rotating motion of the refill unit, which allows for some extra material to enter the unit as the cup is rotation 180 degrees.

Table 34. Summary of eight sequential refill experiments using a 0.8 L cup and controlled refill time of 3 seconds. Observed refill volume is calculated using the refill mass amount and the conditioned bulk density measurements

Material	Refill Mass (grams)	Observed Refill Volume (L)	RSD
Acetaminophen *	232.9 ± 42.0	0.75 ± 0.14	18%
Anhydrous calcium di-phosphate	626.3 ± 31.0	0.85 ± 0.04	5%
API 4 *	289.0 ± 29.9	0.85 ± 0.09	10%
Cellulose *	99.4 ± 66.2	0.66 ± 0.44	67%
Magnesium stearate	213.0 ± 8.0	0.82 ± 0.03	4%
MCC 1	298.9 ± 23.7	0.91 ± 0.07	8%
MCC 2	305.1 ± 6.8	0.90 ± 0.02	2%
MCC 4	382.0 ± 4.8	0.87 ± 0.01	1%
Silicified MCC	452.5 ± 4.3	0.94 ± 0.01	1%

* Material was observed to arch inside of the hopper, leading to *empty* refill actions – cup was not filled even though material was present in the refill hopper. Number after the ± represents the standard deviation of the measurement.

The significantly larger RSDs for acetaminophen and cellulose were of particular interest given that these materials in several instances would not dispense any material due to the level of arching occurring inside of the refill unit's hopper. Figure 44A shows the formation of a significant arch for cellulose and Figure 44B shows the accumulation of acetaminophen on the angled section of the refill hopper. Figure 44C is shown to have a comparison of the refill hopper when empty.



Figure 44. Top view of the refill unit, looking downwards from the hopper. (A) Arching observed for cellulose, (B) arching observed for acetaminophen (C) view of the hopper unit when empty.

For future experiments, this result was considered when choosing the amount of material placed in the refill unit's hopper. To ensure that material would flow, the arches for any subsequent experiments were broken by introducing a small rod and stirring the material in the refill hopper. Moreover, the amount of material placed in the refill hopper was kept below 2L, which ensured that minimal arching would be formed at the higher levels of the hopper.

7.4. RTD CHARACTERIZATION

7.4.1. Concentration profiles

Six RTD experiments were performed in accordance to the methods described. Three materials were used as a base for the experiment and the RTD was performed at two different flow rates. In the following subsections, the results for each RTD experiment is discussed for each material. Feeder weight, input concentration of tracer, outlet concentration of tracer, feeder flow rate, and screw speed were tracked as a function of time for the whole experiment to ensure that (1) the flow rate of the system did not significantly vary and (2) to establish a clear time when the impulse of tracer blend was added by determining the refill time. It was important to monitor the flow rate outgoing from the feeder, given the known relationship between flow rate and residence time. The experiments were performed under gravimetric control to ensure that the flow rate was not varying as a function of feeder weight.

The abovementioned, although collected as a function of time, are plotted in the next subsection as a function of the amount of material dispensed by the feeder (i.e., material fed or totalized mass of material fed) in order to account for the differences in flow rate between the two experiments performed for each material. Expressing the results using the mass of material fed allows for a 1:1 comparison between the two flow rate experiments, since the volume (and thus mass) of material being dispensed remained the same between experiments.

7.4.1.1. Anhydrous calcium di-phosphate with Acetaminophen tracer

Anhydrous calcium di-phosphate represented the material with the largest bulk density, which led to a total mass of material being dispensed of around 3,000 g. Given this mass amount, the total run time for the RTD experiments were 539.6 and 1,079.5 seconds for the higher and lower flow rate set points, respectively. Figure 45 shows the results for the monitored variables for the two

RTD experiments. Figure 45A and Figure 45C show double y-axis (i.e., bivariate) plots for the 2.78 g/s experiment, while Figure 45B and Figure 45D shows the same plots for the 5.5 g/s experiments.

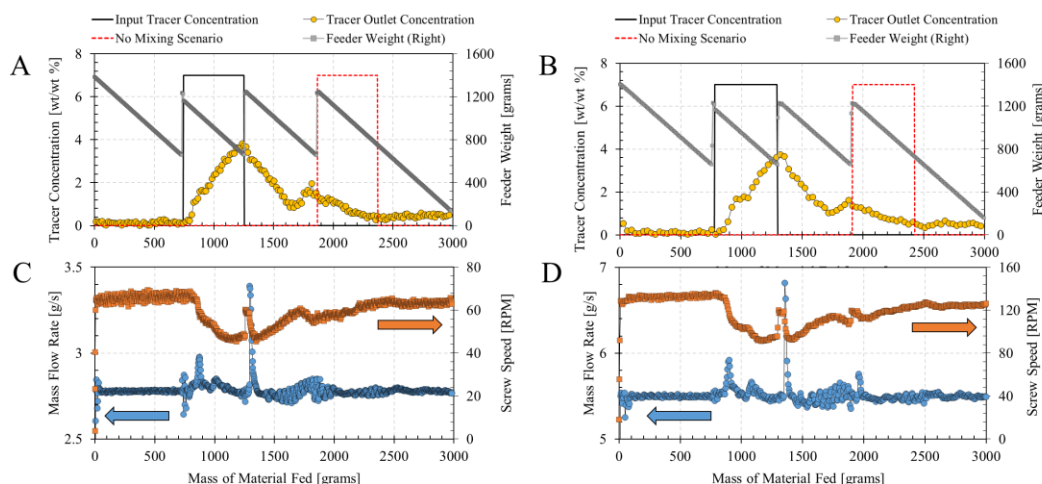


Figure 45. RTD experimental results using anhydrous calcium di-phosphate as a base and acetaminophen as the tracer material. Concentration and feeder weight profiles for the experiments with flow rate set point of (A) 2.78 g/s and (B) 5.5 g/s. Mass flow rate and screw speed profiles for the experiments with flow rate set points of (C) 2.78 g/s and (D) 5.5 g/s.

Figure 45A and Figure 45B show the expected concentration profiles for the tracer as it entered the system (black line) and if it left the system without any mixing occurring in the system (red dashed line). The profile shown by the *no mixing scenario* would indicate the material inside of the feeder hopper did not back-mix with the material that was inside of the unit from a previous refill. Notably, the results from the measured outlet concentration profiles (yellow circles) showed that for both experiments, the lines did not follow the *no mixing scenario* profile and indicated there was some back-mixing occurring inside of the GEA feeder hopper.

Figure 45C shows the impact of adding the tracer material on the flow rate and screw speed of the system. After the tracer blend was added in the first refill (mass of material fed = 714 grams), the mass flow rate profile showed notable disturbances, which included a maximum flow rate deviation of 0.19 g/s (i.e., the flow rate reached a nominal value of 2.97 g/s). These deviations were attributed to the varying feed factor due to the difference in material properties between the tracer

blend and the base material. Markedly, immediately after the tracer was added in the first refill, an asymptotically decreasing profile in the screw speed was observed, indicating that a different material (one with a higher apparent feed factor) was being progressively dispensed out of the feeder. After the second refill was performed with just base anhydrous calcium di-phosphate, the screw speed began to steadily increase as the tracer concentration was washed out of the system, until it reached a similar screw speed range as the starting condition. A large deviation in the flow rate was noted after the second refill and was attributed to the fast changes occurring in the feed factor of the material inside of the GEA feeder hopper. After the observed deviation in flow rate following the second refill, the mass flow rate variability appeared to decrease as the amount of tracer was washed out of the system, which pointed to the fact that stabilization of the feed factor as the tracer material was washed out of the system.

Similarly, Figure 45D shows the impact adding the tracer had on the flow rate and screw speed of the system. Once the tracer was added after the first refill, a flow rate deviation with a maximum value 5.98 g/s was observed. This deviation in the flow rate was attributed once again to the changes in feed factor between the tracer blend and the base material, as seen by the changes in screw speed in Figure 45D. In the same way as the results shown in Figure 45C, the screw speed was seen to decrease after the addition of the tracer and later increase as the tracer was washed with the two base material refills. Notably, the size of the flow rate deviation observed after the second refill was, once again, larger than the flow rate deviation due to the first refill. This result can be attributed to the rapidly changing feed factor inside of the feeder hopper due to back mixing and the inability of the controllers to rapidly adjust the flow rate to maintain the set point.

The results of Figure 45C and Figure 45D give rise to the possibility of using the feeder as a soft sensing unit to detect changes in material properties based on changes in the screw speed (and thus feed factor) during operation. Furthermore, the results also show that screw speed controllers ought to be properly tuned in order to quickly adjust the flow rate in the event of rapid

changing feed factors. In this work, the built-in controls provided a sufficiently accurate and rapid response, yet in future works it is suggested to revisit and tune these controls as a function of expected changes inside of the unit.

7.4.1.2. Silicified MCC with Acetaminophen tracer

Figure 46 shows the results for the silicified MCC RTD experiments. A total mass of 1,900 grams of material were dispensed, which resulted in experiment durations of 341.2 and 683.5 seconds for the higher and lower flow rate set points, respectively. Similarly to the case with anhydrous calcium di-diphosphate, the silicified MCC case showed there was back-mixing in the feeder given the results shown in Figure 46A and Figure 46B. The tracer concentration at the outlet of the unit began increasing immediately after the introduction of the tracer in the first refill, which indicated that the tracer blend profile did not follow the *no mixing scenario*. The increase in tracer concentration was followed by a washing out following the two subsequent base material refills.

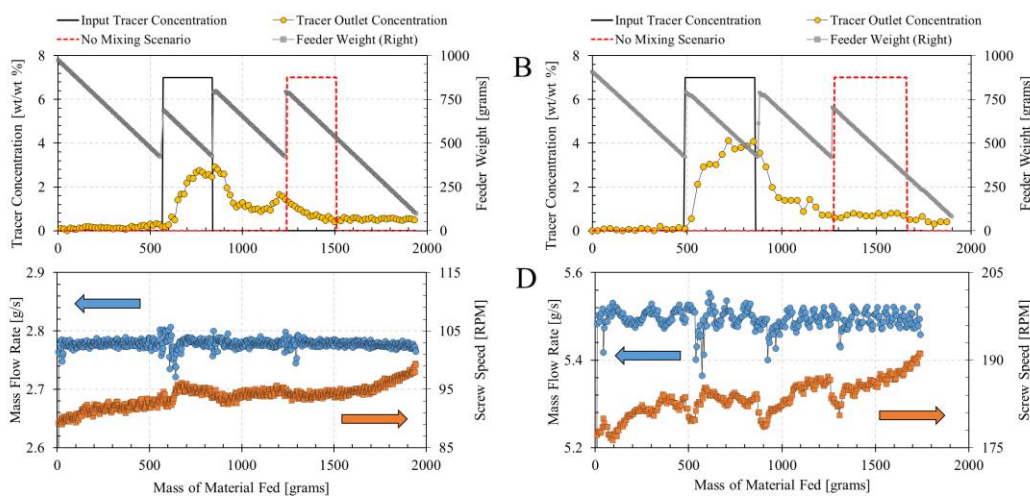


Figure 46. RTD experimental results using silicified MCC as the base and acetaminophen as the tracer material. Concentration and feeder weight profiles for the experiments with flow rate set point of (A) 2.78 g/s and (B) 5.5 g/s. Mass flow rate and screw speed profiles for the experiments with flow rate set points of (C) 2.78 g/s and (D) 5.5 g/s.

Figure 46C shows the impact of adding the tracer material on the flow rate and screw speed of the system. After the tracer blend was added in the first refill (mass of material fed = 539 grams), the mass flow rate profile showed notable disturbances, which involved a decrease in the flow rate of material with an increase in screw speed. As previously discussed this deviation can be attributed to the varying feed factor due to the difference in material properties between the tracer blend and the base material. Since the acetaminophen tracer had a lower feed factor than the base silicified MCC, a decrease in the feed factor was expected. Thus, an increase in the screw speed was expected to maintain the constant flow rate. After the second refill was performed with just base silicified MCC, the screw speed began to steadily increase as the tracer concentration was washed out of the system. Notably, the flow rate disturbance after the second refill was much lower than that for the first refill when compared to the anhydrous calcium di-phosphate case. This result can be attributed to the smaller difference between the feed factors of the base and the tracer.

Figure 45D, in line with the results for the smaller flow rate RTD experiment, shows the impact adding the tracer had on the flow rate and screw speed of the system. Once the tracer was added after the first refill, a flow rate decrease was observed followed by an adjustment of the screw speed to maintain the flow rate near the set point. Nevertheless, it is important to note that after the second and third refills, flow rate did decrease which indicated that silicified MCC refills had a transitory impact on the flow rate. This last observation was discussed by Engisch et al. [287, 293] and attributed to the intrinsic performance of feeders under gravimetric performance during refills.

7.4.1.3. *Acetaminophen with Caffeine tracer*

Lastly, Figure 47 shows the results for the acetaminophen RTD experiments using caffeine as a tracer. An averaged total mass of 1377 grams of material were dispensed, which resulted in experiment durations of 245.6 and 495.3 seconds for the higher and lower flow rate set points, respectively. Thus, this system was noted to have the shortest of all of the RTD experiments, a

result associated with the materials relatively low bulk density when compared with the aforementioned materials. Like the previous two cases, Figure 47A and Figure 47B show there was back-mixing in the feeder provided that the outlet concentration of caffeine tracer exiting the system did not follow the *no mixing scenario*. The results led to the conclusion that regardless of the material being used as a tracer, there was some level of back-mixing occurring in the system and that the feeders did not behave as plug flow (i.e., first in, first out) systems.

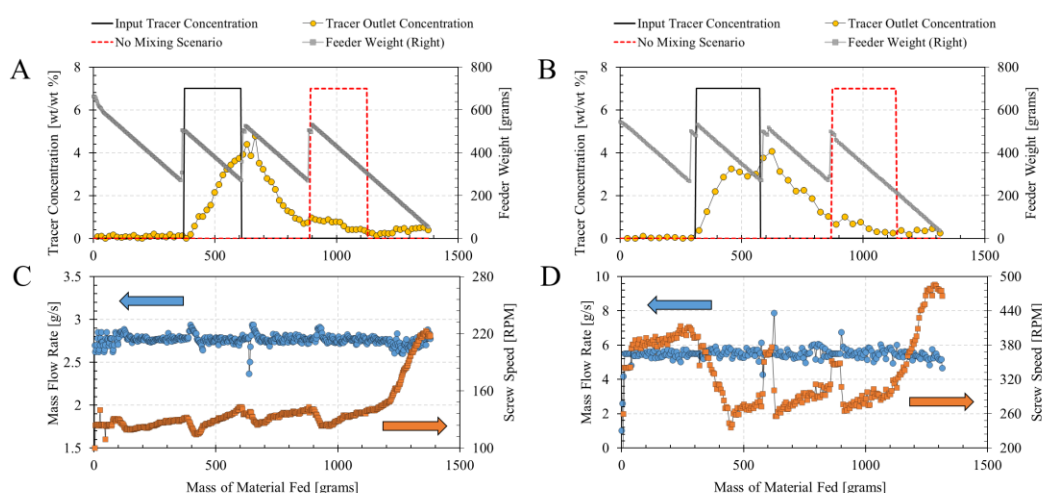


Figure 47. RTD experimental results using acetaminophen as the base and caffeine as the tracer material. Concentration and feeder weight profiles for the experiments with flow rate set point of (A) 2.78 g/s and (B) 5.5 g/s. Mass flow rate and screw speed profiles for the experiments with flow rate set points of (C) 2.78 g/s and (D) 5.5 g/s.

Outstandingly, it was noted from Figure 47 A and Figure 47B there was a slight delay in the decrease of the tracer material after the second refill (i.e., first wash out refill) was performed. This slight delay, although small, may indicate that the more cohesive acetaminophen did not mix as readily as the other two materials, which tended to have better flow properties. Figure 47 C and Figure 47D showed that the flow rate was relatively well controlled over the whole experimental, which the screw speed being regulated over a larger range of speeds when compared to the previous RTD experiments. The larger span of screw speeds was attributed to the high feed factor decay

constant of acetaminophen, which meant that the feed factor decreased much more significantly for this material as the feeder weight decreased.

7.4.2. RTD evaluation and metrics

Following the characterization of the concentration profiles, the RTD PDFs for each of the six experiments were calculated using the equations in Table 41. It is important to mention that only the outlet concentration profiles after the first refill (i.e., once the tracer blend was introduced) were used to calculate the RTD PDFs. The initial outlet concentration of tracer was then used as the starting point of the RTD PDF. Thus, the resulting $E(t)$ curves, shown in Figure 61A, B and C, begin at time equal to zero and proceed over the range of time following the first refill.

INSERT Figure 61 HERE

As expected, the $E(t)$ curves for the smaller flow rate experiments had a longer duration than those for the higher flow rate ones. Using the $E(t)$ results, the mean residence time (τ) was calculated using the equation listed in Table 43. The results for the τ are summarized in Table 35. Values of τ were halved when the flow rate was halved. This result indicates that the mixing inside of the feeder is proportionally related to the flow rate, an indication that bypassing and/or dead spots were not prominent in this system.

Table 35. Summary of RTD experimental results

Material	Flow Rate Set Point (kg/h)	Tracer Blend Step Duration (sec)	Tracer Blend Mean Residence Time (sec)	Ratio (τ_{20}/τ_{10})
Anhydrous calcium di-phosphate	10	182	278.4	–
	20	93	152.3	0.54
Silicified MCC	10	97	184.1	–
	20	68	84.0	0.46
Acetaminophen	10	85	124.2	–
	20	48	64.0	0.52

To visually compare the effect of flow rate on the RTD shape, which correlates with the level of mixing occurring in the system, the PDFs were standardized by multiplying the $E(t)$ by the mean residence time and the time axis was normalized over τ . Figure 61D, E, and F shows the

results of the standardized PDFs over the normalized time axis. The results indicate that for both anhydrous calcium di-phosphate and acetaminophen, the shape of the RTD did not vary significantly which in turn signified that the mixing was not affected greatly by the flow rate. Differences between the two standardized PDF profiles for silicified MCC were noted, particularly for the wash out sections of the RTD curves. The sharper decrease in the PDF values for $0.6 < \theta < 1$ for the 2.78 g/s case indicates that the tracer did not mix as effectively as in the 5.5 g/s case. The unmixed tracer blend for the smaller flow rate case appears to leave as a higher concentration pocket of material during $1.1 < \theta < 1.6$. Although these differences were noticeable, the authors suggest that the differences between the two flow rate RTD curves were relatively small. Thus, based on these findings, flow rate was shown to have little to no effect in the shape of the RTD curve.

Similarly to the comparison of the RTD shapes between flow rates, a comparison of the RTD profiles between materials at the given flow rates was performed. Figure 62 shows the comparison between the standardized RTD profiles for different materials at the two studied flow rates. Both figures show there are relatively small variations between the shapes in the curves. Thus, based on this result, the effect of base materials on the RTD inside of the hopper was found to be small.

INSERT Figure 62 HERE

The level of back mixing appeared to be high given that once the tracer was introduced in the feeder after first refill, the tracer concentration at the outlet began increasing immediately at an asymptotically rising rate. This result indicated that the tracer was added right above a well-mixing region which was preceded by a more plug flow (i.e., no mixing) region. This mixing behavior was observed by Escotet-Espinoza et al. [305] for K-Tron feeders, which showed that at higher levels of the hopper the material moved as a plug, until it reached the impeller region, characterized as a well-mix zone. For the GEA system, the conclusion that the tracer material was introduced right

above the well-mixed region was obtained from understanding that if the tracer would have entered in the well-mixed region, a sharp step like concentration increase would have been observed for the outlet concentration profile. In the following section, a model to predict the mixing and residence time distribution in the feeder is proposed.

7.5. FEEDER MODELING

7.5.1. Mixing and RTD model

The results from Figure 61 indicate there is a degree of backmixing occurring in the feeder hopper is preceded by a region of no mixing, also known as a plug flow region. The region of no mixing appears to occur at the upper levels of the hopper, wherein the material is not sheared (and thus mixed) by the bridge breaking impeller at the bottom of the feeder hopper. To predict the mixing behavior, herein we introduce an RTD model which is later calibrated for the GEA feeder system characterized in this study.

The proposed model to simulate the mixing behavior of this unit was chosen as a plug flow system followed by a perfectly mixed stirred tank (PMST). The plug flow model intends to describe the behavior of material in the upper sections of the feeder hopper, while the PMST aims at depicting the behavior near the bridge breaking system, where the mixing is most intense. Figure 48 depicts graphically the application of the model for the feeder hopper based on the RTD observations from Figure 61

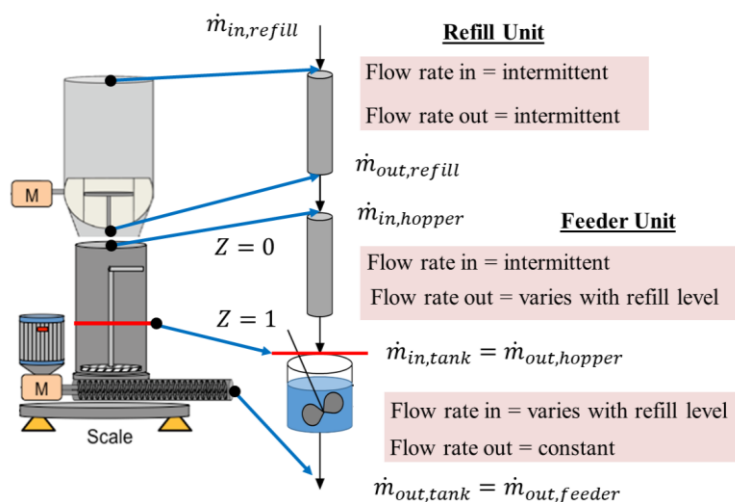


Figure 48. Schematic of proposed mixing model in the feeder unit to simulate the RTD

One of the major challenges of this model is that equations typically available in the literature or academic textbooks to model the behavior of plug flow-PMST system assume that the material holdup in the unit does not change as a function of time. This assumption does not apply for the feeding unit, given that the level of material in the hopper is constantly changing due to the effect of feeding and refilling. Therefore, a more complex model accounting for the moving boundary (i.e., level in the hopper) had to be proposed in order to evaluate the RTD of the unit.

The model for the moving boundary plug flow reactor was proposed by Garcia-Munoz et al. [51], who implemented it to established the delays in transfer pipes between powder blending and feed frame units. Garcia-Munoz et al. [51] implemented the model with a dispersion term given their system configuration and experimental evaluations. For this work, the feeder system is assumed to not have any dispersion in the upper levels of the hopper, which in turn leads to a value of dispersion equal to zero for the moving boundary equation proposed by Garcia-Munoz et al. [51]. The resulting equation used to predict the movement of tracer along the length of the upper hopper section is shown in Equation 35.

$$\frac{\partial (p_{i,hopper}(Z, t))}{\partial t} + \frac{v(t)}{L(t)} \frac{\partial (p_{i,hopper}(Z, t))}{\partial Z} = Z \frac{\partial L(t)}{\partial t} \frac{\partial (p_{i,hopper}(Z, t))}{\partial Z} \quad 35$$

$z \forall [0, L(t)] \quad Z = \frac{z}{L(t)} \quad Z \forall [0,1]$

where, $p_{i,hopper}$ is a given material property (e.g., bulk density, compressibility, flow function) for material i in the hopper, L is the height of material in the hopper's plug flow region, v the speed of the material as it traverses the height of material in the hopper's plug flow region, and Z is the normalized length of the feeder. The material properties being modeled include, but are not limited to, lot number (i.e., concentration), bulk density, true density (i.e., skeletal density), compressibility, permeability, cohesion, angle of internal friction, flow function coefficient, and particle size.

The height of material in the hopper (L) is calculated as a function of time by setting a volumetric balance around the feeder hopper's plug flow region. Equation 36 shows the relationship between the volumetric flow rates and the height of material in the unit.

$$A_F \frac{dL(t)}{dt} = \dot{V}_{in,hopper}(t) - \dot{V}_{out,hopper}(t) \quad 36$$

where, A_F is the cross sectional area of the feeder hopper, $\dot{V}_{in,hopper}$ is the inlet volumetric flow rate, and $\dot{V}_{out,hopper}$ is the output volumetric flow rate around the hoppers plug flow region. The volumetric flow rates are both a function of time and depend on whether or not there is material in the hopper or, in the case of $\dot{V}_{in,hopper}$ is a refill is being performed.

As noted in Figure 48, $Z = 0$ represents the upper edge of the powder bed, which moves downwards during feeding and upwards as the feeder fills. Only a single boundary conditions is needed for the boundary PDE shown in Equation 35. Given that the $P_{i,hopper}$ at $Z = 0$ depends on whether or not there is material entering the unit from a refill, the boundary condition for $P_{i,hopper}$ at the upper edge is given by the conditional statement provided in Equation 37.

$$\text{When, } \dot{V}_{in,hopper}(t) > 0 \quad 37$$

$$p_{i,hopper}(Z = 0, t) = p_{i,refill}(t)$$

Otherwise,

$$p_{i,hopper}(Z = 0, t) = p_{i,hopper}(Z = 0|+, t)$$

where, $p_{i,refill}(t)$ is the incoming property value from the refill unit and $p_{i,hopper}(Z = 0|+, t)$ is the property of the material just below the upper boundary. The second boundary condition effectively ensures that the property from the refill is only set as a condition once the refill has delivered the material into the feeder hopper.

Powder velocity over the hopper's plug flow region is calculated by the outlet volumetric flow rate and the cross-sectional area of the feeder, as shown in Equation 38.

$$v(t)A_F = \dot{V}_{out,hopper}(t) \quad 38$$

The mass of powder in the feeder hopper's plug flow region (W_{hopper}) is calculated based on the integral of the bulk density of material in the hopper ($\rho_{i,hopper}$) multiplied by the volume of material in the unit as shown in Equation 39. The volume of material is calculate using the level of material in the unit and the cross-sectional area, as $V_{powder,hopper}(t) = A_FL(t)$.

$$W_{hopper}(t) = A_FL(t) \int_0^1 \rho_{i,hopper}(Z, t) dZ \quad 39$$

The outlet volumetric flow rate from the plug flow region enters the PSMT so that,

$$\dot{V}_{out,hopper}(t) = \dot{V}_{in,tank}(t) \quad 40$$

where $\dot{V}_{in,tank}$ is the volumetric flow rate entering the PMST. Properties entering the PMST are assumed to mix well with the properties of the material already in the PMST. This “perfectly mixed” conditions is assumed for all properties entering the PMST and are described by Equation 41.

$$\frac{d(V_{powder,tank}(t) p_{i,tank}(t))}{dt} = \dot{V}_{in,tank} p_{i,hopper}(1,t) - \dot{V}_{out,tank} p_{i,tank}(t) \quad 41$$

where $V_{powder,tank}$ is the volume of powder material, $p_{i,hopper}(1,t)$ is a material property exiting the hopper's plug flow region, $p_{i,tank}$ is a material property of component i (herein assumed to be well mixed), and $\dot{V}_{out,tank}$ is the volumetric flow rate coming out of the PMST. Note that Equation 41 does not assume that $V_{powder,tank}$ is constant and maintains the variable inside of the time derivative. This approach then accounts for the changes in fill level in the PMST as the material is depleted.

The volume of powder material in the PMST is calculated similarly to the plug flow region. Equation 42 shows the volumetric balance around the system. The mass of material in the tank (W_{tank}) is calculated as $W_{tank}(t) = V_{powder,tank}(t) \rho_{tank}(t)$.

$$\frac{dV_{powder,tank}(t)}{dt} = \dot{V}_{in,tank}(t) - \dot{V}_{out,tank}(t) \quad 42$$

It is important to note there is a constraint in the maximum volume of the PSMT, given that the tank volume (V_{tank}) is a fraction of the whole feeder volume V_{feeder} so that $V_{feeder} = V_{tank} + V_{hopper}$. The volume of V_{tank} must be regressed from RTD data, which is performed in the subsequent section of the work.

The volumetric flow rate out of the tank is calculated using the mass flow rate out of the unit and the density of the material in the tank (ρ_{tank}).

$$\dot{m}_{out,feeder}(t) = \dot{V}_{out,tank}(t) \rho_{tank}(t) \quad 43$$

The mass flow rate out of the PSMT ties in the feed factor model shown in Equation 28 by calculating the mass flow rate as a function of the screw speed and feed factor, as shown in Equation 44.

$$\dot{m}_{out,feeder}(t) = \omega_{screw}(t) ff(t) \quad 44$$

Material property values used as inputs to the RSMs are those properties calculated for the material in the PSMT. The feeder weight used to calculate the feed factor (W_{feeder}) is provided by summing the masses of material in the feeder hopper's plug and PSMT regions such that $W_{feeder}(t) = W_{hopper}(t) + W_{tank}$.

7.5.2. Mixing and RTD model calibration

Using the results from the experimental RTD collected for the six experiments, the volume of the PMST (V_{tank}) in the characterized GEA feeder was estimated each experiment. Since the mass flow rate of the system was controlled and experimental data was collected for this process response, only Equations 35 through 43 were used to determine the value of V_{tank} . Performing the RTD under gravimetric conditions allows for variable such as the flow rate to be assumed as constants, easing the evaluation of the proposed mixing model.

Markedly, for these evaluations, the density inside of the feeder was assumed to remain unchanged by the addition of the tracer blend, meaning that the density of the material in the PSMT did not change throughout the RTD experiment. This was a reasonable assumption particularly for the cases where the screw speed remain relatively unchanged after adding the tracer (e.g., case study evaluating the RTD of caffeine in acetaminophen).

Based on these assumptions, the predictions of the proposed mixing model along with experimentally obtained concentration profiles from the RTD studies are shown in Figure 63. The results show there is relatively good agreement between the model predictions and the experimental concentration profiles.

INSERT Figure 63 HERE

The results from the calibration of the RTD model are shown in Table 38. All RTD model regressions had a high coefficient of determination ($R^2 > 80\%$) and low MAPE values (MAPE < 15%) indicating the model was able to predict accurately the tracer mixing. The average volume for V_{tank} was 939.4 ± 61.5 mL.

INSERT Table 38 HERE

The results in Table 38 are in agreement with the observation that the material was delivered tracer refills were performed right above the mixing region. Since the feeder was being refilled at a fill level of 60%, the effective fill volume for the unit would have been around 1,200 to 1,100 mL. Thus, the results corroborate the physical observations and present a plausible model to predict the mixing of material inside of the feeder hopper.

7.6. INTEGRATED MODEL IMPLEMENTATION

7.6.1. Integrated feeder model in gPROMS Model Builder™

The feeder model equations introduced over the course of this work were all implemented in in gPROMS Model Builder™ v4.2. Equations 28 through 44 were implemented along with some other equipment-related equations to simulate the behavior of the feeding unit. The integrated feeder model was composed of: (1) screw feeder model, (2) refill unit model, and (3) a PID control model. This latter model is provided standard within the Process Modeling Library (PML) within gPROMS Model Builder and the goal of the model was to control the screw speed as a function of flow rate based on a desired set point. This arrangement allows for users of the model to enter their chosen PID control parameters and even tune the feeder controls for particular products. Figure 49 shows the components for each of the models integrated in gPROMS.

controlled refill unit that performs automatic refills when provided a particular refill set point. This mode of operation mimics exactly the same operation than the real unit, and it intends to provide the user with the ability to test the impact of refill frequency on the feed factor profiles and the flow rate performance.

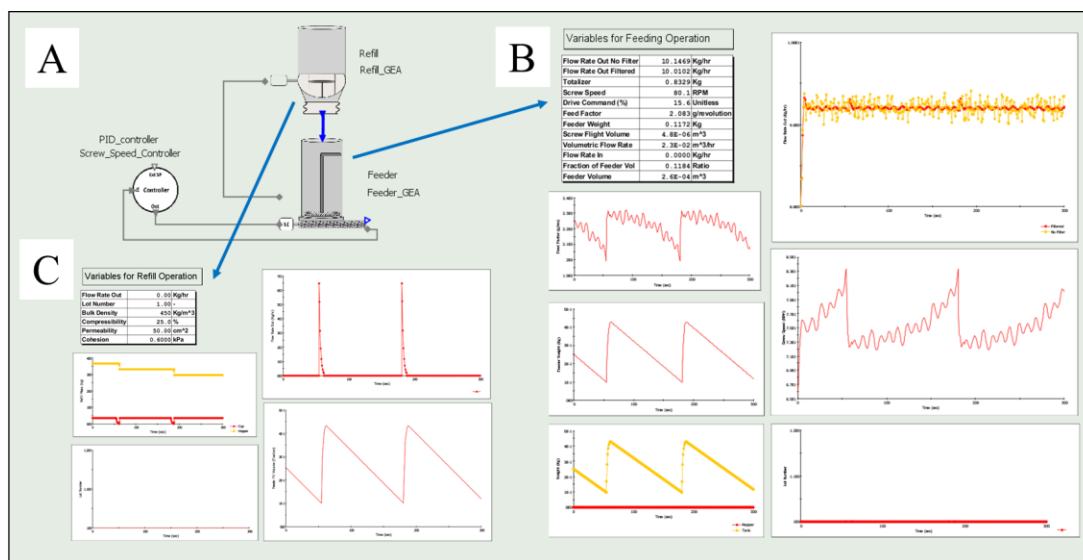


Figure 51. Results from the integrated feeder model programmed into gPROMS Model Builder™. (A) Flowsheet of the screw feeder, refill, PID control models. (B) Output results from the screw feeder model. (C) Output results for the refill unit model.

This model has been implemented by Wang et al. [62] to evaluate the effect of refill level on the disturbances provided to a continuous system. The findings showed the model was able to predict the effect of refill size on process disturbances.

7.6.2. Case studies evaluating the model

An evaluation of the integrated feeder model was performed to determine if the model was able to predict the effect of varying material properties while the unit was in operation. The evaluation involved studying the effect of abruptly changing the bulk density of a material being fed by performing a refill with a material whose bulk density was less than that of the starting material.

For this validation run, an experiment was performed wherein the GEA feeder unit began filled to capacity with MCC 4 and then was refilled with MCC 1. The change in grade of MCC provides a 25% decrease in bulk density, which was expected to cause an effect on the feeder flow rate and feed factor. The experiment was performed under gravimetric control using a 63:1 gearbox ratio and a screw pitch length of 20mm. The flow rate set point for the experiment was 10 kg/h. A total of two MCC 1 refills, each of 0.8 L in volume would be performed in order to observe the effects in feeder critical process parameters.

A feeder simulation using the integrated model was provided with the exact same specifications as those used for the feeder experiment. Figure 52 shows the results of the feeder experiment and the simulation using the integrated feeder model. Figure 52A shows the feed factor profile over time. Both the experimental data and the simulation results show good agreement between the feed factor values. As expected, the addition of MCC 1 cause a decrease in the feed factor perceived by the feeder unit. Notably, the sudden change in bulk density did not abruptly change the feed factor. The feed factor appears to exponentially decrease following the mixing behavior previously noted for the RTD experiments. Remarkably, the integrated feeder model predictions also updated the feed factor as a function of time and MCC 1 addition. The MAPE value between the feeder factor from the experiment and the simulated results was 4.7%. This result indicates that the model, as developed and implemented, provides an accurate representation of the feeding system, such as accounting for changes in material properties.

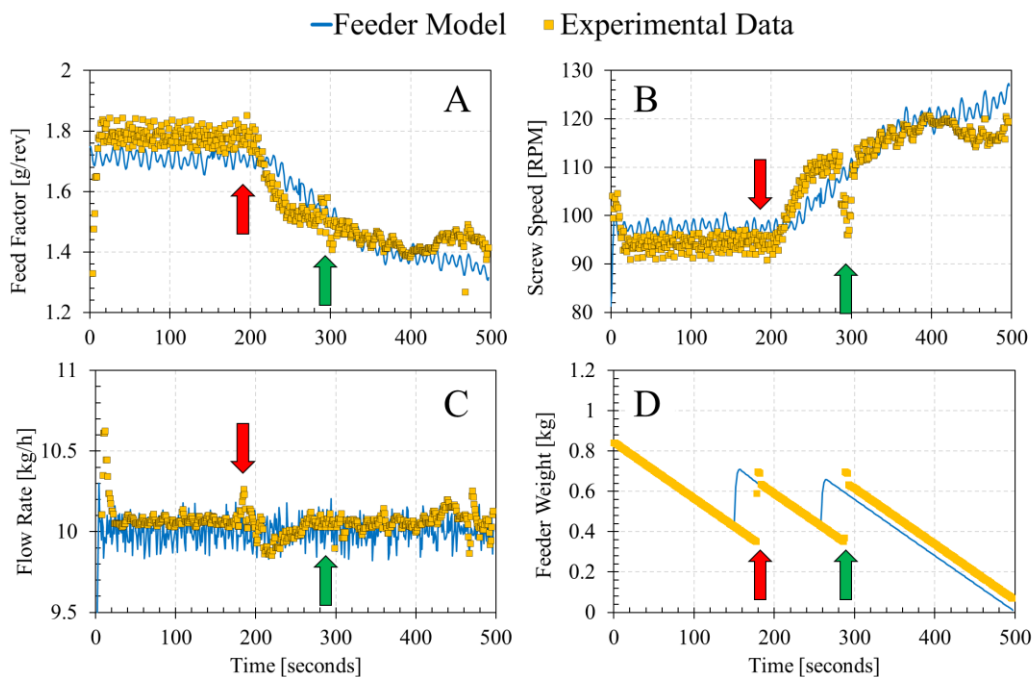


Figure 52. Comparison between experimental and simulated results for material properties change experiment. (A) feed factor profile, (B) screw speed profile, (C) flow rate profile, and (D) feeder weight profile. Arrows indicate the instances when MCC 1 was introduced in the system.

Figure 52B shows the variation in the screw speed as a function of time. The results between the feeder experiment and the model appear to agree well, shown by a MAPE value of 4.3%. During the second MCC 1 refill, shown by the second arrow on the time profile, it was seen that the screw speed decreased drastically for a few short seconds. This result was attributed to the fact that the feeder system did not update in time the feed factor values stored within the control logic and during the second refill the feed factor deviated from the corrected values.

The flow rate predictions, shown in Figure 52C appear to agree well with the predicted results by the integrated model. Notably, during the second and third refills, the feeder controls showed signs of adjustment while the integrated model did not show as large of deviation from the disturbance. This result was due to the exceedingly fast control parameters that were selected for the PID controller. Thus, the model was able to more quickly correct for the error from the changes

in bulk density and minimize the effect of the disturbance. Nevertheless a MAPE of 3.7% was obtained from comparing the two flow rate profiles.

7.7. CONCLUSIONS

In this chapter, the methodology for developing a unit operation model for a powder based unit operation was applied to a GEA compact feeder. The experimental design entailed evaluating the system using a series of materials relevant to the pharmaceutical industry and characterizing the behavior of the unit irrespective of formulation requirements. The experimental plan involved flow rate characterization and Residence Time Distribution (RTD) characterization. Feeder flow rate characterization was performed by measuring the accuracy and variability of material dispensing as a function of volumetric throughput and feeder hopper fill level. The characterization procedure, which included testing the feeder using eight feeder configurations based on the screw size and gear box configuration, was performed for nineteen different materials spanning a broad range of material properties

The feeder flow rate characterization showed there was a clear impact of material properties on the behavior of the unit. Further, the results indicated there was a consistent trend between the amount dispensed per screw revolution and the level of fill in the hopper. The consistent nature of the observed behavior led to the development of a phenomenological model which described the relationship between feed factor and feeder weight. This level 1 model, known as the feed factor model, was then implemented to evaluate the effect of material properties on the unit. Using the feed factor model, a level 2 and level 3 set of models were developed. The material properties collected for the materials in Chapter V were used to develop the material models for the feeder model.

Following the recommendations of Chapter VI, the RTD of the feeder was characterized for a variety of materials. Feeder RTD was considered to be an important point for characterization

because it can help with : (1) traceability of raw materials and (2) characterization of the dynamic response time to changes in incoming material properties. In both cases, the goal is to understand how long it takes for a new material (e.g., lot added due to refill or lots with new material properties) introduced into the feeder to “wash out” the material that was already in the feeder. The RTD for the GEA feeder was characterized using three different materials (i.e., tracer-base combinations) and two different flow rates. The results from the RTD profile indicate there was a degree of backmixing occurring in the system, which could be modeled using ideal models available in the RTD literature. The RTD model in conjunction with the flow rate model previously developed were validated with a special case study. The validation case study indicated that model predictions were in good agreement with the results, which corroborated both the findings of the experimental evaluation of the feeder, the formulated models for the unit, and the methodology proposed here for developing models to represent unit behavior.

7.8. LARGE TABLES AND FIGURES

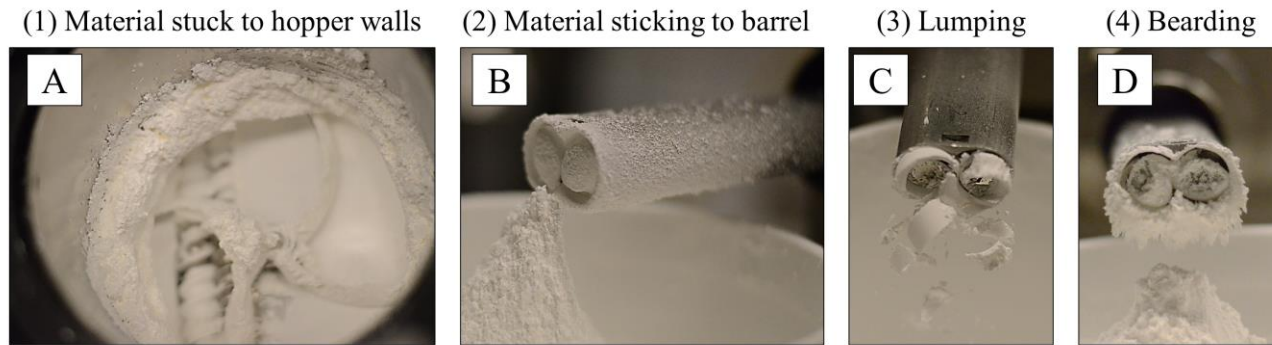


Figure 53. Visually observed challenges during experimentation: (A) material sticking to sides feeder hopper walls, (B) material sticking to barrel, (C) lumping of material, and (D) bearding at the barrel's outlet

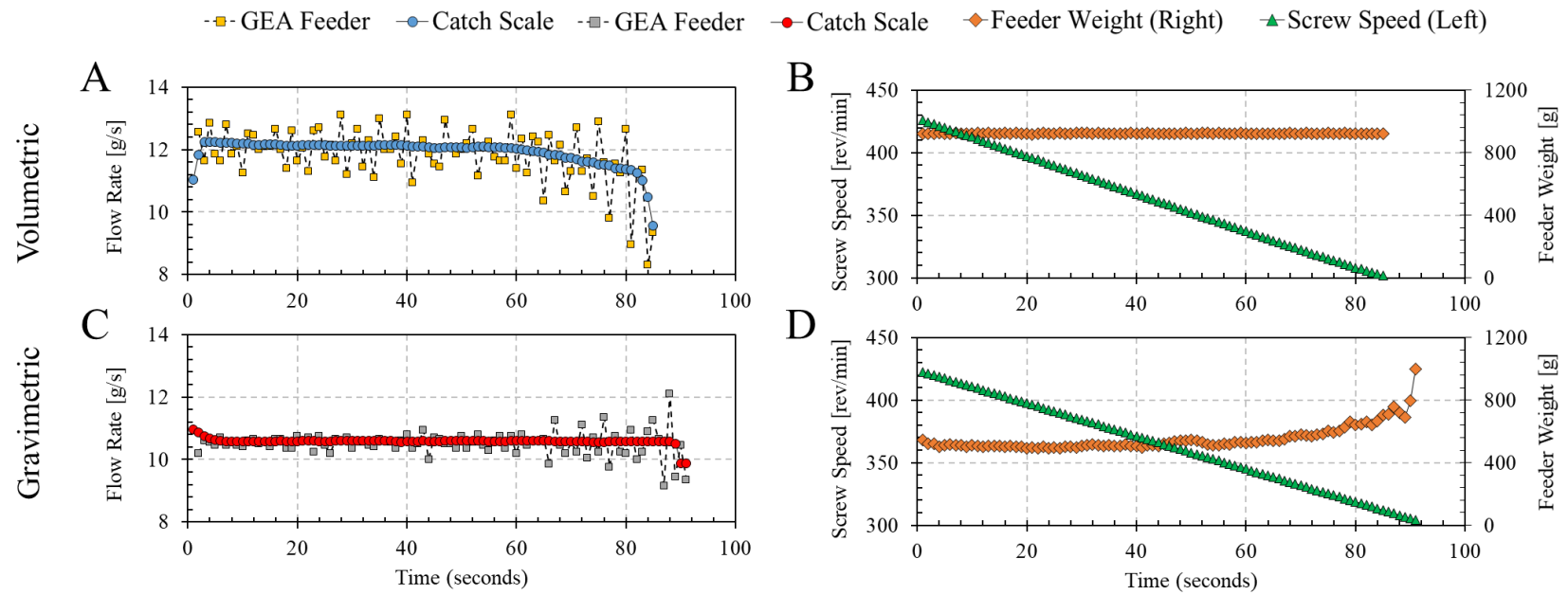


Figure 54. Results for volumetric and gravimetric feeding of MCC 4 using a 20mm pitch screw and a 63:1 gearbox ratio. (A) volumetric flow rate profiles, (B) screw speed and feeder weight for volumetric feeding, (C) gravimetric flow rate profile, and (D) screw speed and feeder weight for gravimetric feeding.

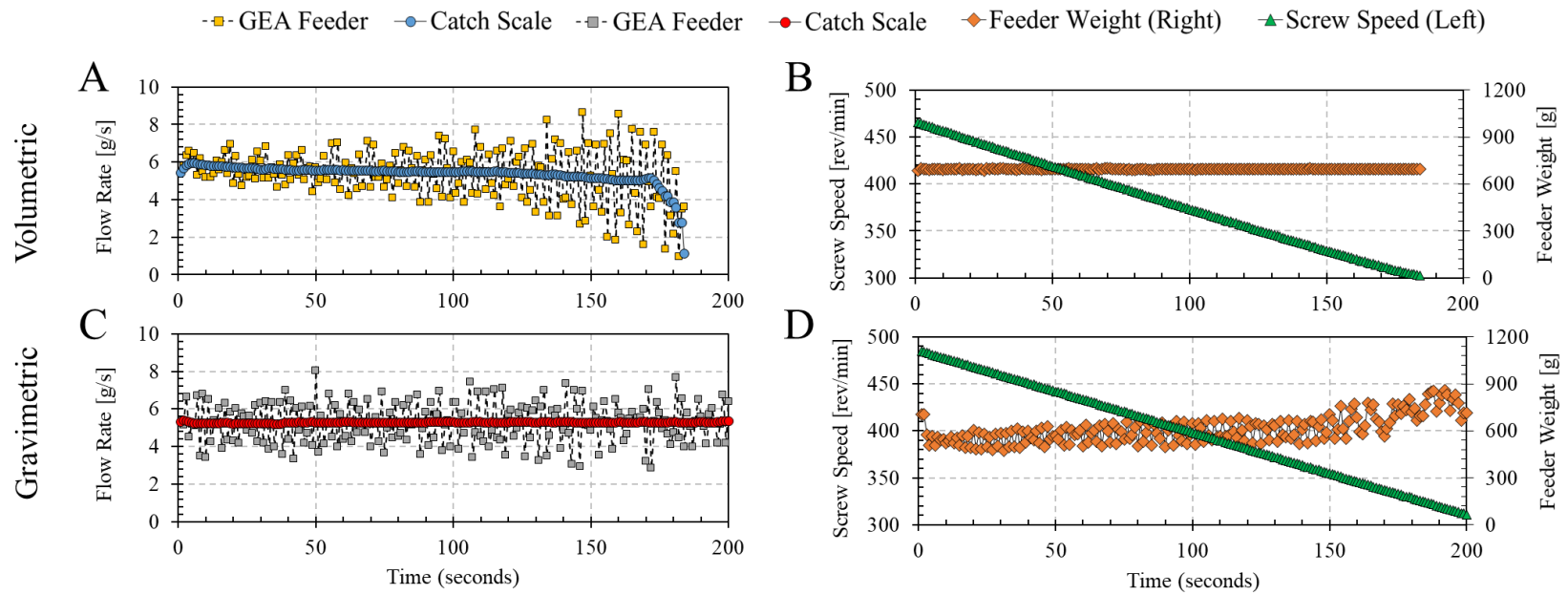


Figure 55. Results for volumetric and gravimetric feeding of MCC 4 using a 10mm pitch screw and a 63:1 gearbox ratio. (A) volumetric flow rate profiles, (B) screw speed and feeder weight for volumetric feeding, (C) gravimetric flow rate profile, and (D) screw speed and feeder weight for gravimetric feeding.

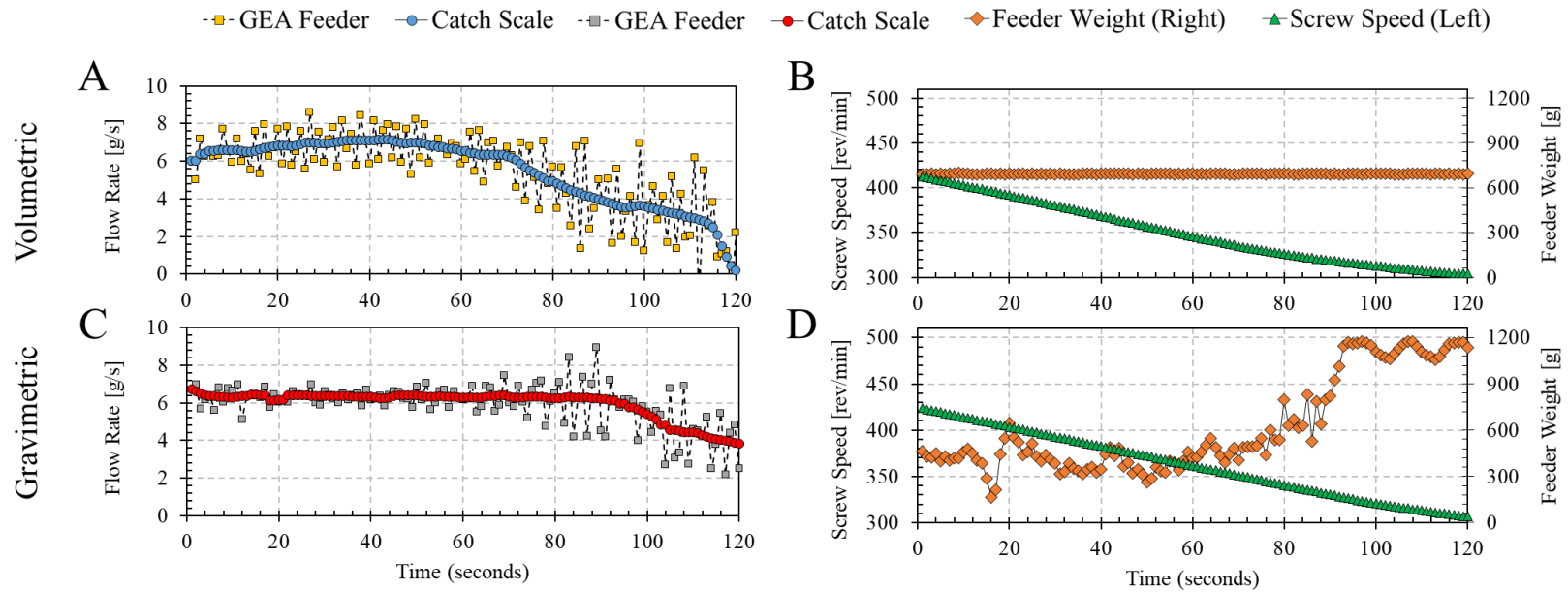


Figure 56. Results for volumetric and gravimetric feeding of Acetaminophen using a 20mm pitch screw and a 63:1 gearbox ratio. (A) volumetric flow rate profiles, (B) screw speed and feeder weight for volumetric feeding, (C) gravimetric flow rate profile, and (D) screw speed and feeder weight for gravimetric feeding.

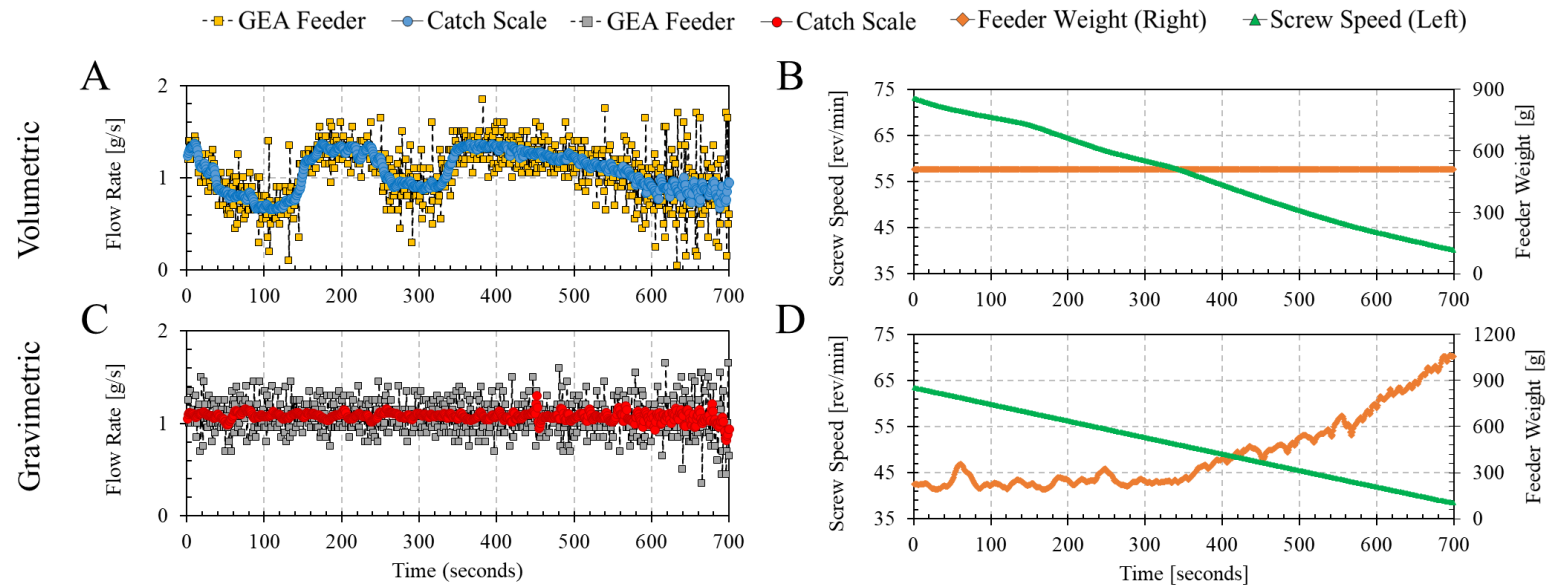


Figure 57. Results for volumetric and gravimetric feeding of Acetaminophen using a 20mm pitch screw and a 445:1 gearbox ratio. (A) volumetric flow rate profiles, (B) screw speed and feeder weight for volumetric feeding, (C) gravimetric flow rate profile, and (D) screw speed and feeder weight for gravimetric feeding.

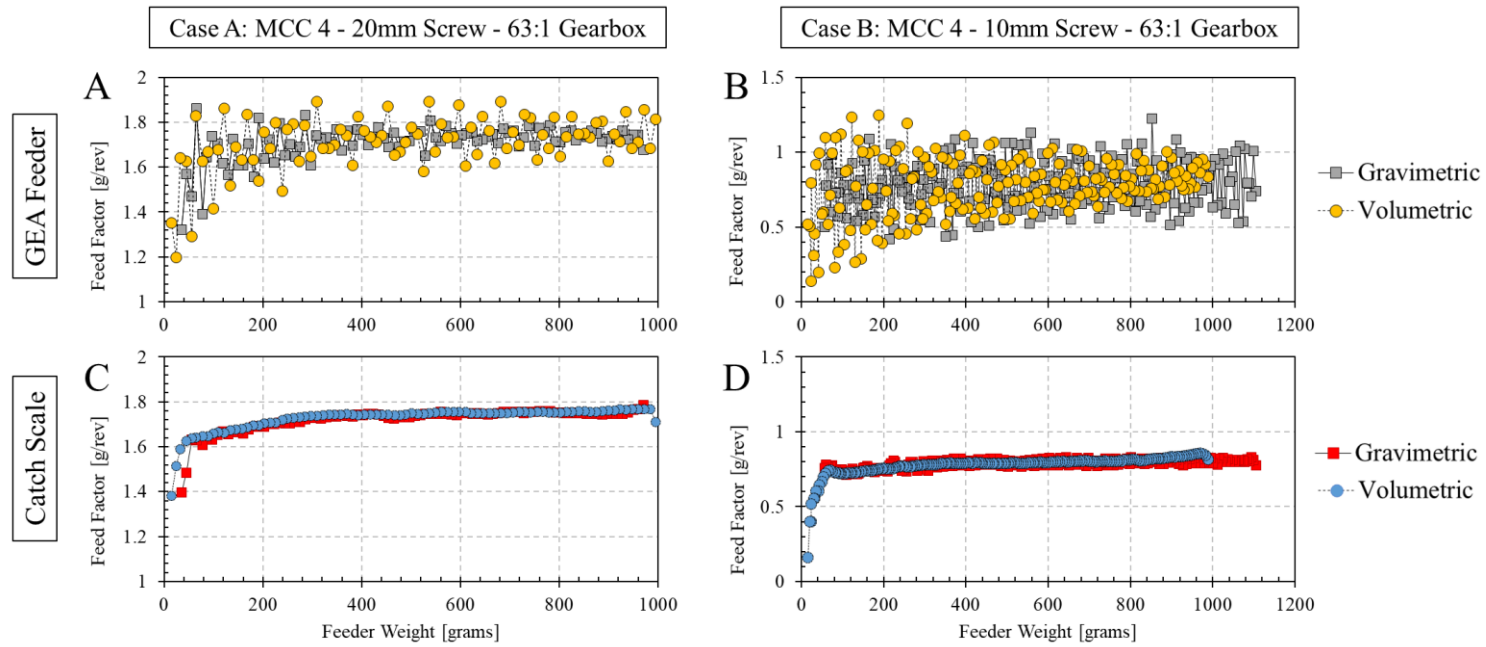


Figure 58. Feed factor profiles for Cases A and B for volumetric and gravimetric feeding. Feed factors calculated from (A) GEA feeder for Case A, (B) GEA feeder for Case B, (C) catch scale for Case A, and (D) catch scale for Case B.

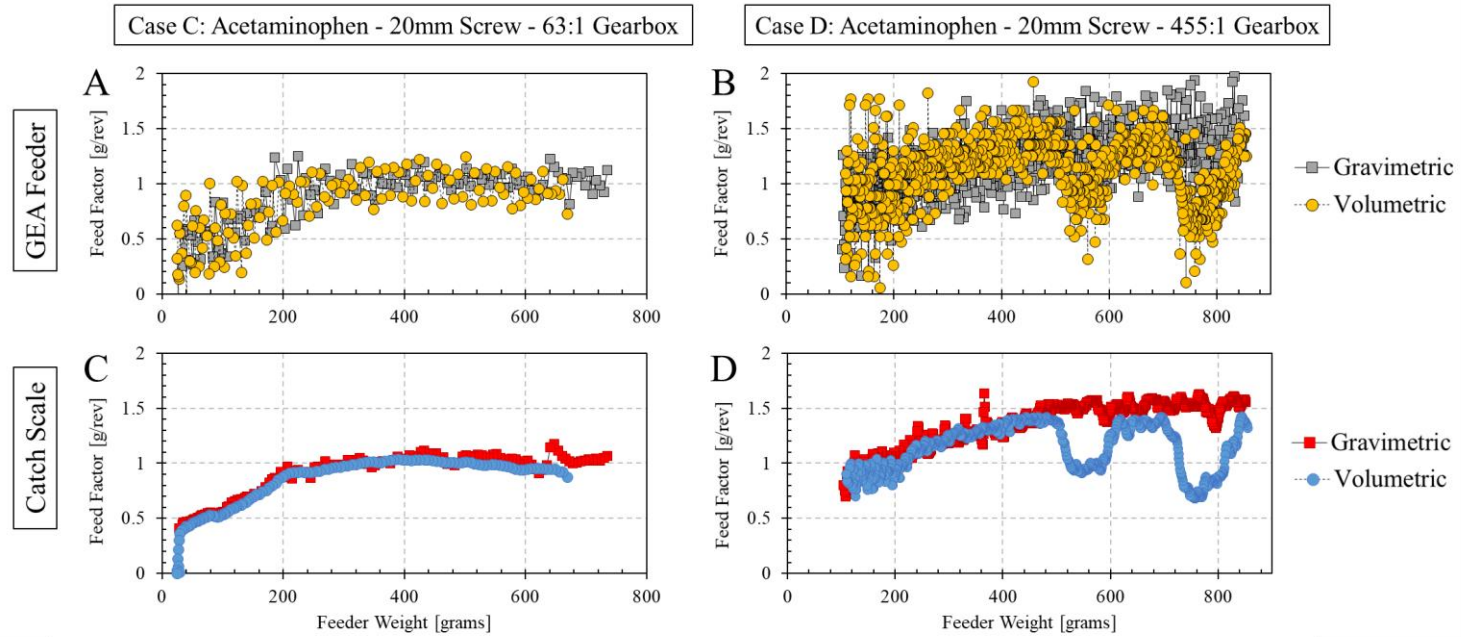


Figure 59. Feed factor profiles for Cases C and D for volumetric and gravimetric feeding. Feed factors calculated from (A) GEA feeder for Case C, (B) GEA feeder for Case D, (C) catch scale for Case C, and (D) catch scale for Case D.

Table 36. Results of regressing Equation 26 to feed factor shown in Case C

	Control	Volumetric		Gravimetric	
	Data Source	GEA Feeder	Catch Scale	GEA Feeder	Catch Scale
Model Parameter	ff_{max} (g/rev)	1.003	1.009	1.061	1.067
	ff_{min} (g/rev)	0.031	0.039	0.192	0.193
	β (1/kg)	8.544	8.545	7.040	7.174
Regression Statistics	R2	73%	97%	84%	97%
	p-value	< 0.01	< 0.01	< 0.01	< 0.01
Residual Statistics	Average (g/rev)	0.00	0.00	0.00	0.00
	St. Dev (g/rev)	0.178	0.049	0.131	0.048

St. Dev = Standard Deviation

Table 37. ANOVA table for the RSM models shown in Equations 29-33

ANOVA Table	ff_{max} Model			ff_{min} Model			$Ln \left[\frac{\beta}{x_2} \right]$ Model			$Ln \left[\frac{A_1}{x_2} \right]$ Model		
	Model	Error	Total	Model	Error	Total	Model	Error	Total	Model	Error	Total
DoF	16	220	236	10	226	236	11	208	219	4	232	236
Sum of Squares	116.8	8.0	124.8	82.7	23.3	106.0	138.4	58.5	196.8	42.8	102.1	144.9
Mean Square	7.3	0.04	–	8.3	0.1	–	12.6	0.3	–	10.7	0.4	–
F-Ratio	202.7	–	–	80.7	–	–	44.8	–	–	24.4	–	–
p-Value	<0.001	–	–	<0.001	–	–	<0.001	–	–	<0.001	–	–

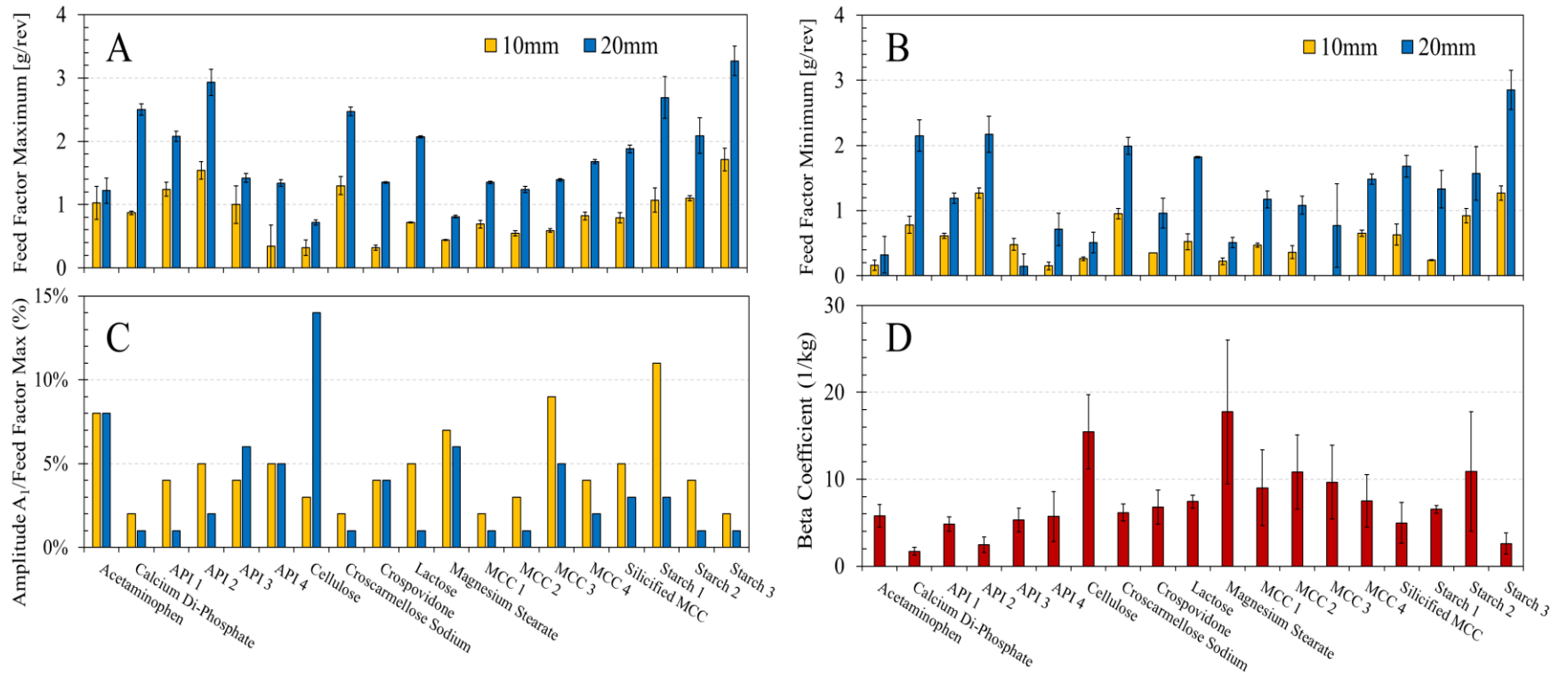


Figure 60. Feed factor coefficient results from

. (A) Maximum feed factor (ff_{max}), (B) minimum feed factor (ff_{min}), (C) ratio of the maximum amplitude obtained for the Fourier coefficients and the ff_{max} , and (D) rate of feed factor decay (β). Error bars represented one standard deviation.

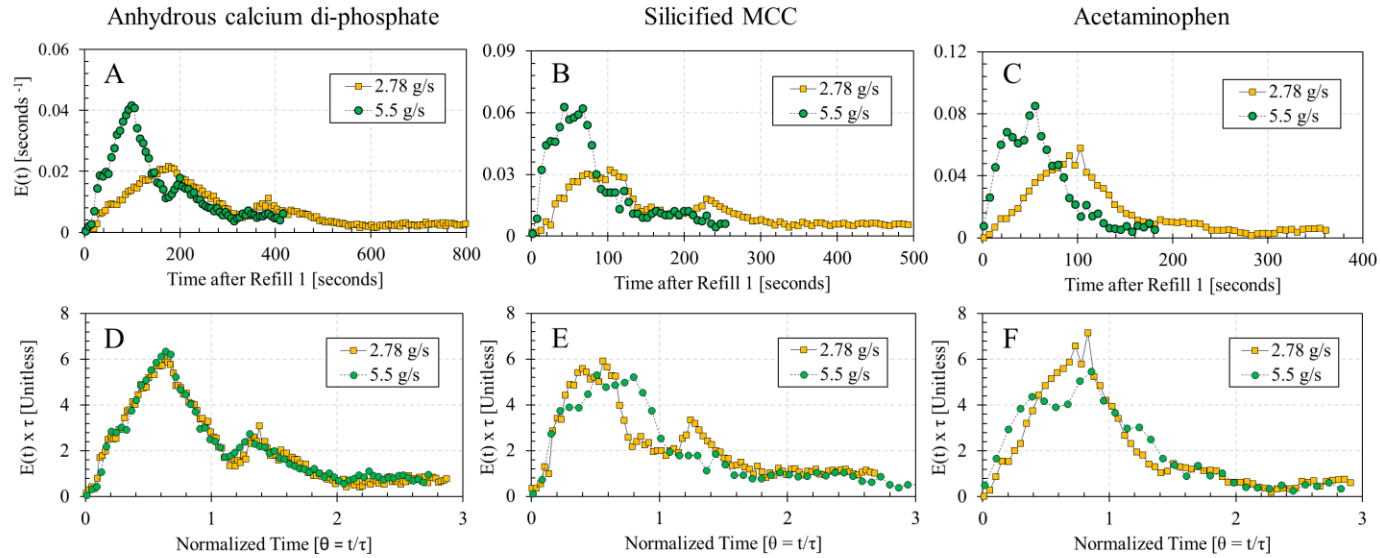


Figure 61. RTD PDF curve results for the RTD experiments comparing mixing based on mass flow rate: (A) anhydrous calcium di-phosphate, (B) silicified MCC, and (C) acetaminophen. Standardized RTD PDF curves comparing mixing based on mass flow rate: (D) anhydrous calcium di-phosphate, (E) silicified MCC, and (F) acetaminophen.

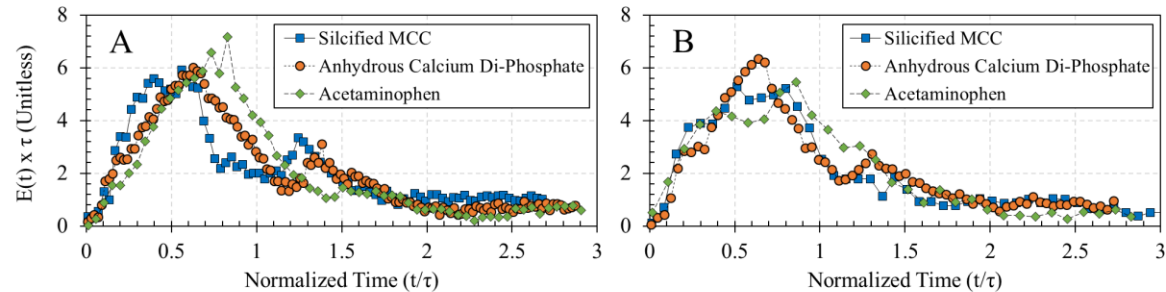


Figure 62. Standardized RTD PDF curve results comparing in hopper mixing between base materials. Flow rate set points of (A) 2.78 g/s and (B) 5.5 g/s.

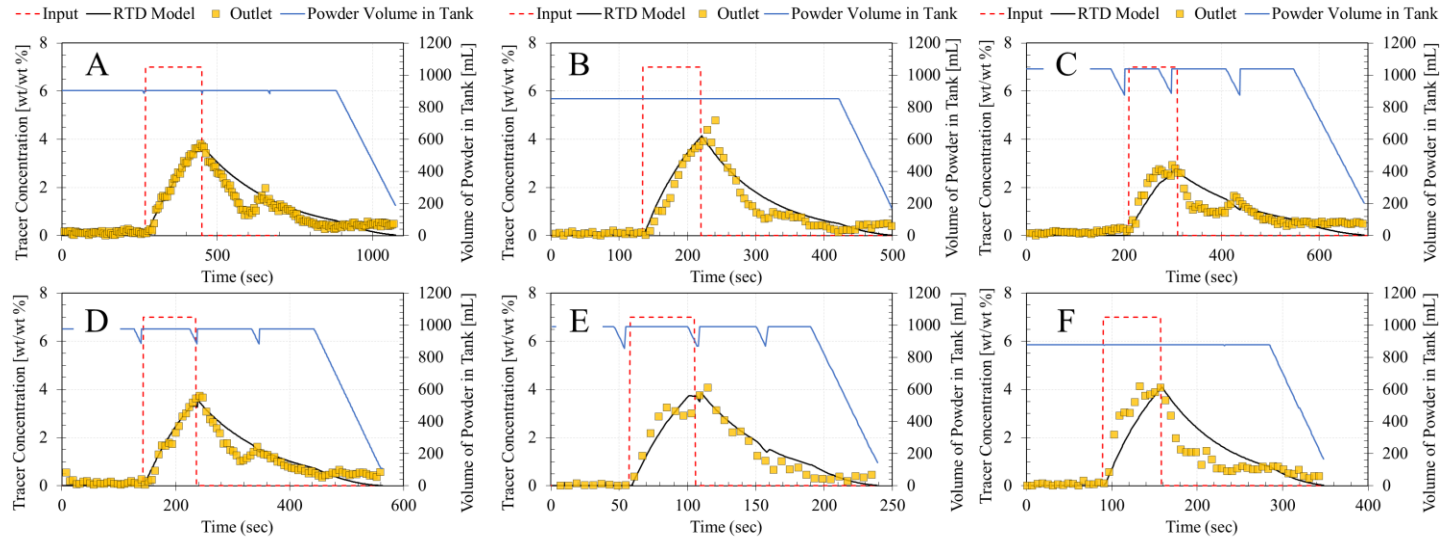


Figure 63. Results of the calibration of the RTD model using the experimental data collected in part 1 of this study. The concentration profiles are separated in based on mass flow rate. For the 10 kg/h: (A) anhydrous calcium di-phosphate, (B) acetaminophen, and (C) silicified MCC. For the 20 kg/h: (D) anhydrous calcium di-phosphate, (E) acetaminophen, and (F) silicified MCC.

Table 38. Results for the RTD model regression

Base Material	Flow Rate [kg/h]	V_{tank} [mL]	W_{tank} [g]	R^2	Space Time [sec]	Calculated MRT [sec]
Anhydrous Calcium Di-phosphate	10	902.5	667.8	94%	240.2	278.4
	20	975.1	721.6	94%	129.8	152.3
Acetaminophen	10	852.2	264.2	95%	95.0	124.2
	20	991.9	307.5	94%	55.3	64.0
Silicified MCC	10	1037.6	498.0	82%	179.2	184.1
	20	877.1	421.0	80%	75.7	84.0

CHAPTER VIII

8. CONCLUDING REMARKS

8.1. CONCLUSIONS

The current pharmaceutical process development and manufacturing paradigm is relatively inefficient and poorly understood when compared to other industries. Whereas most chemical industries (e.g., petrochemical, food, specialty chemicals) tend to be continuous in nature, sequential batch process scale-up remains the prime process development strategy in most of the pharmaceutical industry. Batch manufacturing in pharmaceuticals does not necessarily correspond to the most efficient manufacturing process given the number of steps and the need to scale up in order to meet demand. Typical pharmaceutical processes are composed of ten or more interacting processing steps, each one affected by several process parameters. This level of interaction makes process development a difficult and daunting task whose solutions are addressed using heuristic methods. Moreover, the constant demand of products for clinical trials, in most cases occurring in parallel with process development, force scientist to study the manufacturing process in an expedited manner. Scale up requires the purchase of larger equipment in order to increase productivity, leading to extended research efforts to maintain performance across equipment and scale. Thus, batch manufacturing processes are often poorly understood, rarely optimized, lack robustness, and are prone to unexpected failure. Lastly, risk assessment and failure mode analysis of batch processes is a substantial challenge.

Delays in technological advancement have been attributed to the current regulatory framework, high profit margins that do not push for innovation, time constraints during the drug approval process, and the varying physical and chemical properties of drug molecules that affect formulation and process design. However, as both the pharmaceutical industry and the regulatory environment change, it is expected that some of these challenges evolve to push for manufacturing innovation. In order to overcome some of the technological challenges associated with current pharmaceutical manufacturing paradigms, the industry has been investing in continuous drug product manufacturing technologies and better understanding of process operations.

Continuous drug product manufacturing technologies have the potential to address the issues associated with batch processing by reducing the gap between development and manufacturing. Since continuous process scale up is done through increasing production time and parallelization of the same continuous train of equipment, process knowledge acquired during development can be directly applied to manufacturing processes. Furthermore, continuous manufacturing practices allow for more efficient implementation of available process systems engineering (PSE) tools. PSE tools can provide insight to pharmaceutical development as means of evaluating and controlling manufacturing processes *in silico*. The use of PSE tools such as unit and process simulation, sensitivity, flexibility and feasibility analysis and optimization, as well as design of the optimal control strategy have the potential to improve process understanding and reduce product variability.

The pharmaceutical industry has recognized the value of implementing a systematic approach to drug product development where quality is *built* into the product and process. The US Food and Drug Administration (FDA) initiative on Quality-by-Design (QbD) promotes the design of the product and manufacturing process using principles of chemistry, engineering, material science, and quality assurance to ensure acceptable and reproducible product quality and performance throughout a product's lifecycle. Product quality is achieved through design of robust

processes that are control and optimized utilizing product and process knowledge. In the QbD paradigm, PSE models fit perfectly and can potentially be utilized at every stage of drug product development and manufacturing.

Efforts by industry, academia, and regulatory agencies over the past decade have made continuous manufacturing of solid oral dosages a reality. Major pharmaceutical and equipment manufacturing companies around the world are quickly embracing this novel manufacturing method by adding it to their technology portfolios for both legacy and new drug products. As the pharmaceutical industry modernizes its manufacturing practices and incorporates more efficient processing approaches, it needs to reevaluate which process design elements affect product quality and the means to study these systems. Several new unit operations (i.e., equipment) have been added to the paradigm. The behavior of these unit operations is not well known in pharmaceutical manufacturing cases and needs to be characterized before being implemented in the plants.

The work presented here aimed at studying, understanding, and characterizing the behavior of unit operations used in continuous manufacturing of pharmaceutical products. The main focus of the work was placed on three critical unit operations: feeders, blenders, and tablet presses. These three units are key for the CPM processes, as they are required in every single rout of solids pharmaceutical manufacturing. A methodology for developing phenomenological and residence time distribution models for these continuous powder-handling unit operations was presented for this work. The major challenges to address from the perspective of the methodology included: (1) establishing a mean to relate process inputs and outputs using process models, (2) integrate the effect of material properties into process models, and (3) provide cases that can serve as examples for implementing the methodology. Each of the studied unit operations served as a case study on which the methodology was tested and evaluated. The results from this study indicate that correlations between material properties and semi-empirical equation regression constants are sufficiently accurate. This proof of concept for developing correlations between raw material

properties and unit operation models can aid in process development, especially in the area of design space characterization and robustness analysis. Overall, this work has shown with this approach that it is possible to develop these correlations and have predictive capabilities of process performance based on material property values.

In conclusion, the 21st century pharmaceutical industry is experiencing economic and regulatory challenges that are driving efforts to reduce overall cost and improve pharmaceutical product quality. Industry challenges include: longer drug development time due to disease and treatment complexity, rising regulatory scrutiny during development, drug accessibility to patients, and growing expectations for medical compounds (e.g., fewer side effects, effectiveness). One critical setback for pharmaceutical companies that hinders the industry from addressing some its challenges is the reliance on outdated production facilities, equipment, and methods sharing the same technology as those in the beginning of the 20th century. Nevertheless, over the past decade pharmaceutical companies and universities have partnered to spearhead technology upgrades for the industry. Among these upgrades are continuous manufacturing methods, new equipment, and process engineering tools. My research focuses on experimentally understanding and characterizing the behavior of new equipment used in pharmaceutical continuous manufacturing processes in order to develop computer simulation tools (e.g., equations, software) that ease their application into current pharmaceutical manufacturing practices. These computer simulation tools can used to along with process engineering tools to design, improve, control, and assess the risk in pharmaceutical manufacturing processes. If and when fully implemented in the pharmaceutical industry, the continuous manufacturing equipment and process engineering tools will have the potential to cut manufacturing research cost, speed drug releases to market, reduce drug costs to patients, improve pharmaceutical product quality, and minimize harmful process waste. All this work is part of the great effort to make the pharmaceutical industry a safer and more effective industry for everyone.

8.2. SUGGESTIONS FOR FUTURE WORK

8.2.1. Application of the methodology to other unit operations

Within this work, focus was placed on applying the methodology introduced to develop a model for a feeding unit operation. The successful application of this modeling methodology leads to the suggestion that other unit operations within the CPM process can be evaluated, such as blenders and granulation equipment. Suggested in this work, is the application of the methodology for blending system.

Since blending systems have been extensively studied [137, 221, 306], model development would primarily focus on the residence time distribution and mass hold up modeling based on material properties (i.e., level 2 and level 3 modeling). Suggestions for the modeling include:

- Dynamically characterize mass hold up and mixing in a blender blending unit as a function of process conditions and material properties: this work may be provided as an extension of the previously performed experimental characterizations [137, 221], which primarily focused on the effects of blade speed and mass flow rate on the modeling of steady state mass hold blenders. Dynamic models would allow for better understanding of how the system reacts under non-steady state condition, some of which include: start up, shutdown, and changes in process conditions (i.e., blade speed). Dynamic hold up models have been developed using Markov Chains for non-pharmaceutical powder materials [254, 256, 257]. However, this model should include material properties of pharmaceutically relevant powder in order to expand the benefits of the models.
- Develop models correlating the raw ingredient material property to blend material properties: current models for mixing raw ingredients predict material properties as a weighted average of raw material properties [78, 307]. Efforts have been made to characterize the material properties of blends. However, these efforts have not been implemented nor validated for

continuous blending. This suggested avenue of research would allow researchers to incorporate material characterization models and integrate them to the mixing and phenomenological model.

8.2.2. Generalization of the feeder model

Throughout this work, the focus for developing the feeder model was placed on a particular equipment configuration (i.e., the GEA feeder was the only unit characterized). Although the feed factor model has been shown to hold for other units, several modifications may need to be applied to the model in order to generalize its use for other types of feeders. Thus, a suggestion for future work is to perform further experimentation of other feeder units, following the protocols established in this work to characterize the equipment under similar conditions.

The results of the characterization performed for different feeders may lead to the need to introduce equipment specific constants, some of which may be associated with a particular equipment configuration/design. These constants can ultimately be correlated to the dimensions or physical configurations of the unit, leading to the development of a model that not only takes into account process conditions, but also equipment configuration. Figure 64 shows the sequence of developing general models from the characterization of different types of units.

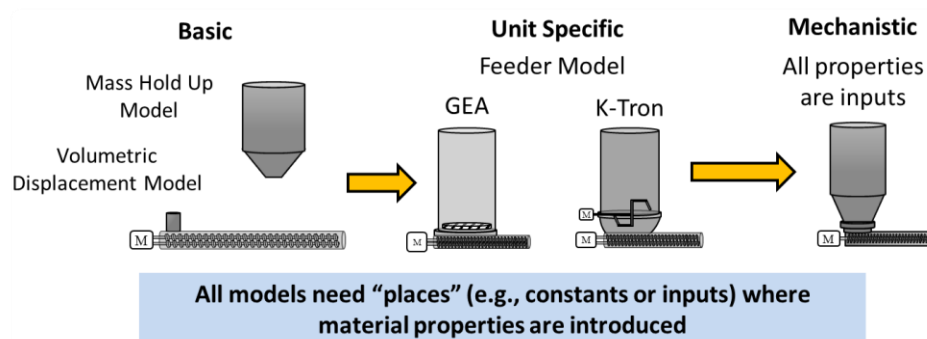


Figure 64. Development sequence of models from basic to general or “mechanistic” models

The resulting general feeder model would need to incorporate not only feeder dimensions, but also tooling selection and other major inputs for the unit.

CHAPTER IX

9. APPENDICES

9.1. APPENDIX A: MATERIAL PROPERTY MEASUREMENTS

The section contains the material property measurements as performed for the 20 materials listed in Table 8. They are described in this appendix as a mean to determine the relationship of the measurement to the describe variables.

9.1.1. Bulk and tapped density

Bulk and tapped density of the blends was estimated by following the standard procedure outlined in the United States Pharmacopeia Chapter <616> [308]. 50-100 g of powder were poured in a 250-mL graduated cylinder. The volume occupied by powder was noted ($n = 3$). The powder mass was divided by the observed volume (V_0) to obtain the bulk density. In order to estimate the tapped density of the powder formulation, the graduated cylinder was then tapped 1250 times using an AutotapTM Tapped Density Analyzer (Quantachrome Instruments, Florida, USA). The volume of powder after the 1250 tappings (V_{1250}) was recorded to compute the tapped density.

The bulk and tapped density calculations were used to further calculate the Hausner's Ratio (HR). This metric can be used to qualitatively designate the blends with their flow character. Hausner's Ratio is widely used to characterize powder flowability and can be defined quantitatively as the ratio of tapped (ρ_{tapped}) and bulk density (ρ_{bulk}), shown in Equation 45.

$$HR = \frac{\rho_{tapped}}{\rho_{bulk}} \quad 45$$

9.1.2. Particle size analysis

Particle size distribution analysis was conducted on a Beckman Coulter LS 13 320 Multi-Wavelength Laser Diffraction Particle Size Analyzer (Beckman Coulter, Indiana, USA). The instrument's Polarization Intensity Differential Scattering (PIDS) methodology along with a Tornado® dry powder dispersing system were used to measure the particle size distribution for a range of 0.017 to 2000 μm . The number of counts for each particle size was recorded and the d_{10} , d_{50} , and d_{90} and $D(3,2)$ were reported in units of micrometers (μm).

9.1.3. Powder flow measurements

The flow properties of all raw materials were characterized using an FT4 Powder tester (Freeman Technology Inc., Worcestershire, UK). Four different tests were performed for the materials: shear cell test, compressibility test, permeability test, and dynamic flow test. Each of the tests provided information that can be used to describe the flow behavior properties of the materials.

9.1.4. Shear cell test

The shear cell, originally developed by Jenike in the 1960s specifically for the design of hoppers and silos, has become an industry standard for characterizing powder flow in a broad range of applications. The result of a shear cell test is a yield locus, a plot of normal versus shear stress experienced in the powder bed during testing. The extrapolation of the best fit line through the yield locus to the y-axis (i.e., the shear stress at zero normal stress) gives the cohesion, a measure of the stress required to move particles against each other. Other important flow parameters that can be extracted from the yield locus diagram include the angle of internal friction, angle of wall friction, unconfined yield stress.

In this study, a Freeman Technology FT4 system's rotational shear cell was used. The testing procedure, described in detail in the works by Koynov et al. [217] and Wang et al. [218] consisted of four steps, which included: conditioning, consolidation, pre-shearing, and shearing. Initially, the powder is poured into a glass cylinder of 10 mm x 25 mm (D x H) dimensions. During conditioning, a helical blade was introduced into the powder and allowed to rotate while oscillating upwards and downwards. This step was performed to "condition" the sample and remove powder voids formed during pouring. Following conditioning, the consolidation test was performed using a vented piston, which applied a 3 kPa normal stress to the powder bed. The powder was then sheared to achieve a steady-state. Both the shear and normal stresses were recorded and labeled as a pre-shear point. After pre-shearing, the normal stress was slightly lowered, and the sample was further sheared to obtain a yield point. The consolidation–pre-shear–shear procedure was repeated for four equally spaced normal stresses, until a 15 kPa consolidation stress was achieved. The shear stress was plotted against the normal stress, yielding a τ - σ diagram. While many models to take into account the shape of the yield locus have been developed, a commonly used approach is the Mohr-Coulomb model to generate a linearized yield locus [309]. A linear regression is fitted through the yield points to obtain a mathematical expression for the linearized yield locus. The intercept of the yield locus on the shear stress τ -axis is defined as the cohesion (τ_1), which can be interpreted as the shear stress required to deform the powder when no normal stress is applied. The slope of the linearized yield locus is $\text{Tan}(\varphi)$, where φ is called the angle of internal friction (AIF), which is a measure of ease with which the powder particles will slide past one another in degrees [310]. To extract other flow indices, a Mohr circle was then plotted passing through the origin and tangent to the yield locus. The intercept of this Mohr circle with the normal stress σ -axis is defined as the unconfined yield strength (UYS or σ_c). A second Mohr circle was drawn tangent to yield locus and passing through the pre-shear point (σ_p, τ_p), with its intercept on the σ -normal stress axis called the major principal stress (MPS or σ_1). The flow function coefficient (FF), which

is often correlated to the arching phenomenon in hoppers, is defined as the ratio between the major principal stress (σ_1) and the unconfined yield strength (σ_c) [311]:

$$FF = \frac{\sigma_1}{\sigma_c} \quad 46$$

While these parameters are typically calculated, and reported as independent measurements, they can, in fact, be calculated from the mathematical expression in the Mohr circle analysis. The Mohr-Coulomb model in the τ - σ diagram can be described as:

$$\tau = \sigma \tan(\varphi) + \tau_1 \quad 47$$

For a straight line with slope equal to $\tan(\varphi)$ and intercept (cohesion) τ_1 , the unconfined yield strength can be expressed as a function of the cohesion and the angle of internal friction:

$$\sigma_c = 2\tau_1 \tan\left(45 + \frac{\varphi}{2}\right) \quad 48$$

For a circle tangent to the yield locus and passing through the pre-shear point (σ_p, τ_p), with its intercept on the σ -axis equal to the major principal stress (σ_1), one can show that the major principal stress can be related to the cohesion, the angle of internal friction, and the coordinate of the pre-shear point (σ_p, τ_p) [218]:

$$\sigma_1 = (1 + \sin(\varphi)) \left(\frac{A - \sqrt{A^2 \sin^2(\varphi) - \tau_p^2 \cos^2(\varphi)}}{\cos^2(\varphi)} \right) - \frac{\tau_1}{\tan(\varphi)} \quad 49$$

$$\text{where, } A = \sigma_p + \frac{\tau_1}{\tan(\varphi)}$$

9.1.5. Compressibility test

The compressibility of a material provides a way of testing the cohesion of a powder at a consolidation state different than that of the shear cell. Here, the powder bed is initially in an unconsolidated state. The compressibility test measures how much the volume of the powder bed changes with an applied normal stress. Since this test is done at relatively low normal stresses, it is a measure of the space between particles. In general, in a cohesive powder, particles are less densely

packed than in a free-flowing powder. Therefore, a higher compressibility is correlated with higher cohesion and a poorly flowing powder.

The compressibility test used in this study was also performed using the Freeman Technology FT4 system. The raw data was in the form of a compressibility profile, which describes the volume change versus applied normal stress. The test began by conditioning the powder, passing the aforementioned helical blade through the powder bed. A normal force is then slowly applied using a vented piston. The normal force began at 0.5 kPa and was increased to 15 kPa in 10 intervals while holding each load for 60 seconds. The change in volume due to the compression is measured at each load step. The compressibility index was calculated as a ratio of the initial and final densities.

While this test is closely related to the measurement of bulk and tapped density and the calculation of a Hausner index, and also to the more recently developed flow index/dilation test [312, 313], for cohesive powders the FT4 system provides much more accurate and reproducible results while requiring a much smaller amount of material.

9.1.6. Permeability test

Permeability is a measure of how easily a material can allow passage of a fluid (in our case air) through its bulk. For powders, it is influenced by many physical properties such as particle size distribution, cohesion, particle stiffness, particle shape, surface texture, and bulk density. External factors such as consolidation stress are also likely to influence permeability by changing the porosity and particle contact surface areas, making it more difficult for the air to pass through the bulk. Permeability is of interest when trying to understand the effects of many process situations such as flow in and out of hoppers, pneumatic transfer, vacuum transfer and specific processes such as vial filling, die filling, or dry dosage inhalation.

The permeability test used in this study is part of the Freeman Technology FT4 system. The raw data was in the form of a pressure drop required to maintain a constant air velocity through the powder bed versus applied normal stress. The test begins by conditioning the powder as previously described. A normal force was then slowly applied using a vented piston. The normal force began at 0.5 kPa and was increased to 15 kPa in 10 intervals while air flows through the powder bed. The pressure drop was measured at each load step. Pressure drop (ΔP), air flow rate (q), air viscosity (γ) and height of the powder bed (L) are measured and in conjunction with 50 were used to calculate the powder bed's permeability (κ).

$$\kappa = \frac{q\gamma L}{\Delta P} \quad 50$$

For the work described here, all measurements were performed close to room temperature (i.e., within the temperature range of 23.7 – 27.6°C), so the average air viscosity was taken as 184.82 Pa-second (i.e., viscosity of air at 26.67°C) for the calculations. The depth of the powder bed was held constant at 0.5 cm and the air cross-sectional velocity was regulated to 0.2 mm/second using the FT4 featured compressor.

9.1.7. Dynamic flow test

The shear rate that powders experience as they are handled and moved thorough any given process will vary from point to point. All manufacturing systems apply different shear rates at different locations or at different points in time. The sensitivity of a powder property to the shear rate is usually an important parameter when describing its flow properties. It is common that cohesive powders are more sensitive to changes in shear rate than non-cohesive or granular materials, mainly due to the high air content in the cohesive materials, and also to their tendency to form brittle meso-structures (e.g., agglomerates). Flow energy E is defined as the energy required to move a helical blade through a powder bed. The Freeman Technology FT4 dynamic test measures this energy as a function of time and shear rate.

To this end, the powder sample was loaded into the vessel and then conditioned using a helical blade in the same way as described previously. The blade, moving on the downward and upward direction, was then used for a testing cycle and the energy consumed to induce the powder to flow was measured. The energy can be different during this stage depending on material properties. The conditioning step followed by a testing cycle was repeated seven times with measured flow energy $E_1 - E_7$. The flow energy required on the seventh downward blade pass is known as the basic flow energy (BFE). The energy consumed during the seventh upward traverse is called the specific energy (SE).

The stability index, SI, reflects the change in flow energy over time,

$$SI = \frac{E_7}{E_1} \quad 51$$

where E_1 is the flow energy required on the first downward blade pass, and E_7 is the flow energy required on the seventh downward blade pass. A SI value of 1 suggests that the material is stable and non-friable. If SI is larger than 1, it indicates that a material requires more energy to flow over time, possibly due to de-aeration, agglomeration, moisture uptake, or electrostatic charges. If SI is smaller than 1, it may be caused by material attrition or de-agglomeration.

Four additional repetitions were performed with different shear rates (i.e., different blade tip speeds) after the measuring the BFE and SI. The four repetitions were performed with a tip speed ranging from 10 to 100 mm/s. The flow rate index (FRI) is the ratio between the required flow energy at 100 mm/s and 10 mm/s,

$$FRI = \frac{E_{11}}{E_8} \quad 52$$

where E_{11} is the basic flow energy at a blade tip speed of 100 mm/s, and E_8 is the basic flow energy at 10 mm/s. If materials are more sensitive to changes in flow rate, for example cohesive materials due to higher air content, the FRI values are typically higher.

9.2. APPENDIX B: STATISTICAL ANALYSIS METHODS

9.2.1. Principal Component Analysis (PCA)

PCA is a simple multivariate analysis technique that models dataset variation in terms of a smaller number of independent linear combinations of its data variables [314]. The linearly combined new variables, also known as principal components (PC), are orthogonal to each other and contain all of the variance (i.e., information) of the original dataset expressed in a new rotated axis [20, 21, 44, 222, 315-317]. Mathematically, PCA's transformation of a data set to PCs is equivalent to defining new orthogonal coordinates by linear rotation of a matrix (i.e., a change in coordinate system in a linear space).

One of PCA's main objectives is to select a subset of variables such that the original variables have the highest correlation with a set of PCs that can best reconstruct the original data matrix [40, 222]. The PCs, which initially match the number of dimensions, are obtained as the correlation matrix's eigenvectors of the original measurements. However, not all eigenvectors are retained, given that they contain decreasing amounts of information, and that the goal is to minimize the dataset's dimensionality. An important question is how to select the optimum number of eigenvectors, such that each one captures a statistically significant fraction of the observed variability. Several approaches are proposed, including a cumulative variance criteria and a statistical significance method. The cumulative variance criterion selects a threshold to determine the number PCs that will be retained after analysis. This method is one of the most widely used, as it can be adjusted based on the researchers target number of PCs needed. The more rigorous statistical method determines which principal components are statistically significant by means of the Bartlett test, which examines the fractional variance of each eigenvalue/eigenvector pair and calculates the corresponding p-value using the Chi-square distribution and degrees of freedom in the matrix [318].

By retaining only a small number of eigenvectors, the original set of measurements is effectively mapped into a smaller (sometimes much smaller) set of new variables. The reduction of data dimensionality by projecting the data onto orthogonal coordinates is an effective approach to efficiently generating process models for development, as well as minimizing the number of variables (i.e., number of material properties being measured) [44, 319-325]. Some of the major disadvantages of PCA include (1) that physical interpretation of the new variables is often ambiguous, (2) that model creating requires large amounts of experimental data and (3) that the method in some instances lacks robustness (i.e., principal components can be miscalculated and yield different results). These disadvantages are often addressed by performing sequential PCA analysis, which in turn allow researchers to examine the model limitations.

The application of PCA is often described by a set of square matrix equations, which is illustrated by the formula

$$X = TP' + U \quad 53$$

where X is the original data set with n observations of j variables, T is the score vector matrix (i.e., the transformed measurements), P' is the loading matrix (i.e., the coordinates of the old variables onto the new coordinate system) and U is a matrix containing residuals (i.e., the leftover value of each measurement not captured by the new coordinates). When the number of transformed data variables equals the number of original variables (i.e., the number of dimensions has not been reduced) the value of the residuals matrix is equal to zero. As the number of components being excluded increases, the magnitude of the U matrix increases. It is critically important to mention that when X is normalized (always a recommended practice), either matrix T or P' yields a matrix possessing orthonormal vectors (i.e., vectors with values from -1 to 1) to ensure that measurement units are not altering the results for each PCA. Typically, the presented orthonormal vector matrix is the loadings matrix.

9.2.2. Clustering Analysis

Clustering analysis is an unsupervised machine learning method used to classify any set of data into groups (i.e, clusters) with similar attributes without requiring a previously developed learning set (i.e., training set) [326, 327]. Data elements groups representing proximate collections of data elements based on a distance or dissimilarity function measured using different distance methods (e.g., Euclidean, Manhattan), wherein identical data pairs have zero distance or zero dissimilarity. This methodology proves to be very helpful when studying library sets, as it provides a means to establish relationships and partitions between the different data points [328]. Thus, this methodology becomes of interest when considering materials in a property library, particularly when attempting to classify these materials based on their properties.

In general, clustering analysis can be divided into hierarchical clustering and non-hierarchical clustering techniques. Examples of hierarchical techniques include ward, single linkage, and median, etc. Non-hierarchical techniques include K-means, K-medoids, and fuzzy clustering, etc. Selection of algorithms depends on data available, and can be validated by the stability of the clusters using simulation studies [329]. Among available algorithms, hierarchical categorical clustering and non-hierarchical K-means clustering are among the most commonly used methods [330, 331]. The reasons for their popularity include ease of implementation, speed of convergence, and adaptability to sparse data [332, 333]. Mathematically, categorical clustering determines the distance between points and, given a predefined number of groups, allocates the components in each group based on the maximum distances between groups. K-means clustering partitions all data points into predefined number of sets to minimize the within-cluster variance and, since the total variance of the data is constant, it also maximizes the between-cluster variance. Several statistical analysis packages (e.g., SAS®, JMP®, R) have programmed clustering methods, making them easier to be implemented in every field. Other mathematical modeling software (e.g., MatLab®, Mathematica®) have also programmed clustering methods. In the pharmaceutical field, clustering

was used to detect and predict adverse pharmaceutical drug effects, develop new marketing strategies, and analyze clinical trial data [334, 335].

9.3. APPENDIX C: METHODOLOGY TO PERFORM RTD EXPERIMENTS IN SOLIDS UNIT OPERATIONS

9.3.1. Tracer Properties

Selecting tracer materials to characterize a system is a not a trivial problem, as it pertains to a fundamental question: *which material's RTD is the experiment characterizing?* This question undertakes the objective of pushing process developers to understand what are: (1) the reasons for measuring the RTD and (2) the future applications of the RTD. Answering further, why is the RTD being measured, has profound implications regarding the selection of materials to be used in the study, and requires careful consideration in order to achieve the desired goals. Based on previous experience two major scenarios are often observed with regards to acquiring RTD results: (1) diagnose phenomenological equipment behavior and characterize mixing and (2) understand the dynamic behavior of upstream disturbances as they travel through the process. Although these two scenarios are closely tied, the latter is more closely related to a specific process rather than the equipment's intrinsic behavior.

The selection of tracer materials depends heavily on these two scenarios, especially with regards to future applications of results for model development. For example, if the goal is to establish the fate of a given amount of ingredients entering the system (e.g., lump of API or tracer entering the system) at fixed steady state conditions (e.g., inlet flow rate, blade speed), then it is best to use that specific ingredient to establish its RTD at the desired conditions. However, if the goal is to examine the general mixing behavior of a piece of equipment for a range of materials and conditions and to characterize the mean residence time of the system's components, then it is critical to understand how tracer material properties can affect RTD characterization.

From a tracer selection criteria standpoint, it is important to establish fundamental characteristics listed by Danckwerts for a good liquid tracer [104]. A tracer must:

1. Be detectable from other materials in the system, otherwise it will not be possible to establish the tracer's exit times and compute a RTD.
2. Be non-interactive with the system: a tracer ought not to be consumed, converted or transformed inside the equipment being studied nor should it affect the flow patterns inside of the system. This latter point is particularly important. If the tracer causes a change in the system, such a change would be misconstrued as part of the flow pattern being studied.
3. Have similar physical properties to those of the system: since the intent is to determine the RTD of materials in the system, the tracer should possess similar flow properties to those in the system.
4. Not adhere to equipment surfaces or walls: adherence to walls and other surfaces will distort RTD results by preventing the material from exiting the system. These artificially made *dead* or stagnant zones may lead to the erroneous conclusion regarding flow patterns in the system.
5. Be able to mix with other system components: similarly to the previous point, the material should be able to traverse the equipment interacting in a similar fashion as the other components in the system and exit as a homogenous stream to minimize observer error and minimize the probability of result misinterpretation.

Similar assertions have are made by other researchers [103, 229-231, 336] and, currently, these guidelines for selecting liquid tracers are standard in chemical engineering curricula.

Although the abovementioned guidelines were drafted for liquid systems, it is important to note they are also applicable to powder-based processes because the mathematics used for

describing the system remains the same. In addition to being distinguishable from the bulk material, solid tracers must have similar properties to the bulk powder, must not react with the bulk powder, must easily mix with the system (i.e., no segregation or agglomeration), and its movement must be representative of the flow of powder within the system. However, in the case of powder systems and given the cases presented before, accomplishing all of these requirements may prove to be a challenging task, particularly for the broader scenario requiring characterization of mixing behavior. For instance, attempting to determine the mixing behavior inside a processing unit by determining the dissipation of a specific ingredient pulse (or disturbance) may violate requirements 4 and 5 of Danckwert's tracer properties. Excess of tracer material in the system may change the behavior of the entire blend (e.g., densification, resistance to flow), effectively changing the system altogether and potentially misleading the system characterization.

It appears that proper selection of tracers has not received sufficient attention in recent efforts to characterize the RTD of continuous pharmaceutical powder processes. Tracers are often selected *ad hoc* or based on the availability of materials with easy means of detection. Tracer materials in several published works include pure active pharmaceutical ingredients (APIs), which tend to have poor flowing characteristics, often dissimilar to the bulk powder, and adhere to the walls and surfaces of vessels [101, 137, 260, 337, 338]. Although ease of detection is a key requirement for tracer materials (i.e., APIs often have distinct spectral peaks), it is equally important to also review other requirements of tracer properties to avoid misinterpretations of mixing behavior inside of the unit.

A poor tracer, whose physical properties: (1) are largely different from the properties of the bulk material, (2) alter the behavior of the bulk upon its addition, and (3) are not representative of materials in the system, may provide an inaccurate measure of the system's RTD of the system. This could have important consequences, particularly if these RTD models are being used to make control decisions for conforming/non-conforming intermediate material and final product. They

will also lead to the erroneous development of traceability models. An accurate measure of RTDs, a large part of which is the proper selection of tracers, is thus of paramount importance.

9.3.2. Tracer Addition

Two major methods are used for introducing a tracer into the system: pulse (or impulse) and step change [231, 232]. The methodology selection is paramount for both the evaluation and characterization of mixing behavior as well as the accurate mathematical representation of the system. Pulse experiments represent the *even, precise* and *instantaneous* introduction of a tracer in the system through an opening in the process. The process opening is often a port or valve, which researchers can open or close for sampling purposes. Pulse tracer addition is effective at keeping the tracer material requirements low as well as ensuring the system is not overwhelmed by a perpetual change in material concentration [336]. The resulting response out of a pulsed system is typically a distributed curve that begins and ends at the zero tracer concentration value. These curves allow for an interpretation of the system's mixing behavior; especially in terms of how a lump of material is dispersed over the unit's length by "backmixing" processes.

Step changes, on the other hand, require the *even, consistent, immediate, and continued* introduction (positive step) or depletion (negative step) of a tracer over the whole time window. This second method of tracer addition often requires large amounts of material to effectively produce the noticeable change in concentration at the system's outlet. It is important to note that the consistent and continued addition or removal of tracer material may lead to changes in the system's physical properties (e.g., flowability, density). Step changes provide a safer and convenient means of performing RTDs since the removal or addition of tracer can be performed on the closed system by means of varying the rate of feeding material from the sources (i.e., feeder), without having the researcher open the process to insert the tracer. The resulting response out of a system with a step input is a distribution curve that begins at the initial value and ends at the tracer

concentration set point. This latter point provides an advantage for detection methods (e.g., PAT tools) whose calibration and detectability are dependent on the original calibration method.

Figure 65 shows schematically both the inputs and outputs of pulsed and step change inputs, where t_0 represents the time of tracer addition or depletion. The pulse system shows how the tracer must be added exactly at time t_0 in one large lump, while the other two tracer addition methods show how the change in concentration is maintained over time after t_0 . The responses (i.e., output) of the system show how the tracer is dissipated over the unit and how the tracer is affected by the system.

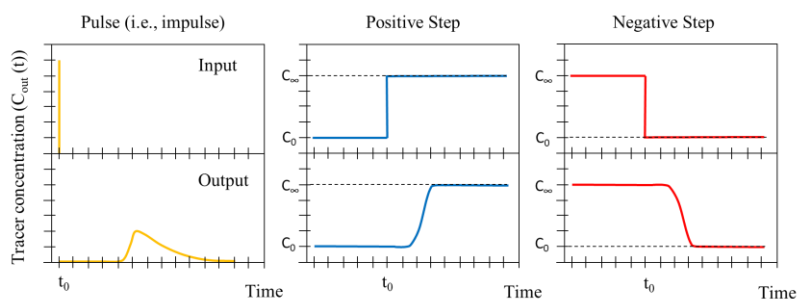


Figure 65. Schematic comparing input and outputs for several methods of introducing tracers for RTD experiments.

Both systems provide their advantages and challenges, which need to be considered when selecting a tracer and determining the characterization strategy for the system. Table 40 summarizes the tracer definitions as well as provide both the advantages and challenges for each.

INSERT Table 40 HERE

Historically, pulse systems have been used given their easy implementation and relatively low material requirement. However, pulse experiments are more difficult to perform due because of the need to ensure the tracer addition assumptions [339]. To avoid this problem, it is often recommended to perform a short step up and step down sequence to capture the system's behavior and more easily control the tracer addition. This latter form of tracer addition is known as a *variable step change*.

Based on tracer introduction characteristics, pulse tracer additions are mathematically represented using a Dirac Delta function while step inputs, whether continued or variable, are expressed using the Heaviside Theta function (i.e., a unit step function). Both mathematical representations of the tracer addition methods assume the materials are added at the *time instant* provided, meaning that accounting for the tracer introduction is critical for modeling purposes. Variations in the addition or recording of tracer inputs will dramatically affect the experimental and modeling results. If the timing is not correctly determined, imperfect pulse RTD methods may need to be used to account for the variation in the tracer addition method. Several authors have developed the mathematics for imperfect tracer addition [24, 231, 336, 340], yet they are not discussed in this work for the sake of brevity. Table 39 describes the different tracer addition methods with respect to their mathematical descriptions for a known and controlled introduction time (i.e., perfect tracer addition).

Table 39. Mathematical descriptors for different tracer addition methods.

Method	Function	Description	Equation
Pulse	Dirac Delta	Instantaneous and precise tracer addition over a very short (i.e., approaching zero) time period. At time a value approaches infinity, but the integral over the entire time period approaches 1.	$\delta(t - a) = \begin{cases} \infty & \text{if } t = a \\ 0 & \text{otherwise} \end{cases}$ $\int_0^{\infty} \delta(t - a) dt = 1$
Step change	Heaviside Theta	Sudden and continued tracer addition after time a has passed. The concentration is sustained until the end of experiment.	$u(t - a) = \begin{cases} 0 & \text{if } t < a \\ 1 & \text{if } t > a \end{cases}$
Variable step	Heaviside Theta	Sudden addition of tracer after time a sustained for a time period b , after which it is brought down back to the initial state.	$u(t - a) - u(t - a + b)$

Using these mathematical input descriptions, RTD models can be derived and used to analyze mixing systems given any tracer input.

Table 40. Summary of tracer addition methods along with the advantages and challenges of each method.

Tracer Addition Method	Description	Advantages	Challenges
Pulse (or Impulse)	Instantaneous, precise, and even addition of tracer	Tracer material requirement is relatively low System material properties are not largely affected Curve shape provides detailed information on the systems mixing dynamics	Determine the appropriate amount of tracer to be detectable Instantaneous addition of the entire tracer amount Large lumps of tracer may not be representative of system disturbances System needs to be opened to introduce the tracer material
Step Change	Continued, immediate, consistent, and even addition or depletion or tracer	Provide a known end point for pulse concentration, aiding detection methods System exposure is limited (i.e., system does not require operator interference) Representative of a change in concentration in the system or a long deviation	Immediate step changes are difficult to obtain from source systems (e.g., feeders) Tracer material requirements are relatively large System material properties may be broadly affected Higher potential of the tracer interacting with the system (e.g., sticking)

9.4. APPENDIX D: RTD MODELING

9.4.1. Calculation of RTD

After introducing the tracer and collecting the mixed results at the unit's outlet, researchers can derive two critical pieces of information about the system: the tracer's mean and distributed residence time. To determine those values, several calculations must be performed taking into account the tracer addition method and the outlet concentration results. These calculations intent to standardize the concentration values and transform them into distribution functions that can then be used to calculate subsequent residence time metrics. For cases when tracers are added using a pulse method, a *probability distribution function* (PDF) – also known as *probability density function* and *differential distribution function* – is calculated using the concentration of tracer at the system's outlet and the sum of that concentration over the whole time period. When tracers are added using step changes, a cumulative distribution function (CDF) is computed to perform the RTD calculations. Table 41 presents a summary of these equations. The integrals are further described as discrete sum to provide a mean to treat experimental data and convert it to distribution values. The time intervals for the integral are often suggested to be equally spaced, to minimize error between the numerical and analytical integral.

Table 41. Descriptions of distribution functions used to calculate RTD metrics. $C_{out}(t)$ represents the instantaneous concentration of tracer at the system's outlet as a function of time.

Name	Symbol	Input Signal	Equation
Probability distribution function (PDF)	$E(t)$	Pulse or impulse of tracer	$E(t) = \frac{C_{out}(t)}{\int_0^{\infty} C_{out}(t)dt} \cong \frac{C_{out}(t)}{\sum_0^{\infty} C_{out}(t)\Delta t}$
Cumulative distribution function (CDF)	$F(t)$	Positive ($X = \infty$) or negative ($X = 0$) step change of tracer	$F(t) = \frac{C_{out}(t)}{C_x}$

Both the cumulative and probability distribution functions can be computed from each other by taking the time derivate of the first in order to obtain the second distribution.

$$E(t) = \frac{dF(t)}{dt} \cong \frac{\Delta F(t)}{\Delta t} \quad 54$$

After normalizing the tracer measurement by computing the distribution functions, the results can be used to calculate distribution moments, which then can be interpreted as subsequent RTD metrics. Two major moment families can be derived with respect to the distribution's properties: moments relative to the origin (μ) and about the mean (γ). Using the probability distribution function $E(t)$, Equation 55 can be used to calculate any N-order moment (μ_N) about the distribution's origin.

$$\mu_N = \int_0^{\infty} t^N E(t) dt \cong \sum_0^{\infty} t^N E(t) \Delta t \quad 55$$

The first moment of the distribution about its origin (i.e., $N = 1$ in Equation 55) represents the distribution's mean value, which in RTD terms is known as the *mean residence time* or MRT. This value represents the average time tracer particles spend in the system. The MRT is often described using the Greek letter τ (i.e., $\tau = \mu_1$).

The MRT is related with the system's space-time ($\tau_{space\ time}$), shown in Equation 56, described as the ratio between the mass held up in the system ($M(t)$) over the incoming flow rate into the system ($\dot{m}_{in}(t)$); however, these two variables may not be the same depending on the system's flow behavior. For systems where the flow is close to ideal, the MRT will coincide with the space-time results since there are no major locations for the material in the system to *hide*. Yet, if the system exhibits a significant amount of non-ideality (e.g., bypassing, dead zones, preferential sticking, different transport rates, changes in flux) then the space-time results will not coincide with the MRT. Furthermore, the space-time results often refer to the bulk material's MRT in the system, not a specific tracer, making the results often not representative of tracer behavior.

$$\tau_{space\ time} = \frac{M(t)}{\dot{m}_in(t)} \quad 56$$

Following the description of the distribution about its origin, researchers can use the τ to describe the distribution's shape using the moments equation about its mean for any moment P (γ_P) using Equation 57.

$$\gamma_P = \int_0^{\infty} (t - \tau)^P E(t) dt \cong \sum_0^{\infty} (t - \tau)^P E(t) \Delta t \quad 57$$

Noting that the first moment about the mean yields a zero value (i.e., $\gamma_1 = 0$), the moments about the mean must be computed past the second moment (i.e., $P \geq 2$). The PDF's variance (σ^2) can be computed as the second moment of the distribution about its mean (i.e., $P = 2$ in 57). From the variance the distribution's standard deviation (σ) can be computed as $\gamma_2 = \sigma^2$. The distribution's standard deviation divided by the square mean residence time is denoted as the mean centered variance of the MRT or simply the MCV ($\sigma_t^2 = \sigma^2 / \tau^2$).

Another important distribution characteristic, skewness, can be described using the third distribution moments about the mean. The skewness can help detect bypassing or high degree of back-mixing in systems, based on the degree of positive or negative skewness. A negative value of skewness, for example, would indicate tracer material is heavily held back in the system (i.e., large majority moves slower than the mean), perhaps by segregation or by sticking to boundaries, whereas a positive skewness value would indicate that most tracer material is bypassing the mixing zones (i.e., traveling faster than the bulk flow).

Overall, the major metrics needed to describe the most significant RTD metrics are listed in Table 43, below.

INSERT Table 43 HERE

Within the RTD literature, MRT and MCV are presented as the two major metrics of study given that both of these metrics can be subsequently used for modeling and other analysis. On the other hand, skewness remains less utilized in the literature as it is a quantitative tool aimed at merely assessing the distribution's asymmetry. Nevertheless, in this work the authors find it important to include the skewness when trying to delve deeper into understanding mixing inside of systems, particularly in novel unit operations.

9.4.2. Phenomenological models

Several models have been developed to represent the RTD in equipment and vessels that often do not present ideal mixing scenarios such as plug flow or perfectly mixed. The vast majority of these models represent a mixing that is somewhere in between those of plug or perfectly mixed systems and are often derived on a case-by-case basis. A large number of these mixing models have been summarized by Levenspiel and Bischoff as well as other chemical engineering textbooks [103, 230, 231, 336]. Two of the most commonly used models for RTD in powder systems, particularly convective tubular blenders, are: (1) the axial dispersion (AD) equation, also known as the Fokker-Planck equation [51, 101, 250, 341] and (2) the tank-in-series model [34, 198, 266]. Both models are analogous to each other as they represent a signal filter that is characterized by two (2) regressed variables: a variance constant and the residence time constant. In this section, both models are described in detail for the particular case where a tracer is added at the inlet of the unit. Cases where the tracer is added along the unit's length are not covered in this discussion.

9.4.2.1. Axial dispersion (AD) model

The AD equation represents a system wherein components are transported by convective and dispersive methods along the length of the unit. For simplicity, the equation is derived assuming both a constant speed and transport area (i.e., flux) along the unit's length. These two assumptions are not valid while the unit is undergoing a transient change (e.g., start up, shut down, increases in

flow rate or change in blade speed), yet it serves as a satisfactory solution at steady state. The equation for the AD equation is shown in Equation 58.

$$\frac{\partial C}{\partial t} = D_z \frac{\partial^2 C}{\partial z^2} - v_z \frac{\partial C}{\partial z} \quad 58$$

where C is the concentration of a component along the unit's length, z the axial position, v_z velocity in the axial direction, D_z the dispersion coefficient in the axial direction, and t represents time. 58 can be normalized as shown in Equation 59 using $\theta = t/\tau_{dispersion}$, $\varepsilon = z/L$, and $Pe = (v_z L)/D_z$.

$$\frac{\partial C}{\partial \theta} = \frac{1}{Pe} \frac{\partial^2 C}{\partial \varepsilon^2} - \frac{\partial C}{\partial \varepsilon} \quad 59$$

where $\tau_{dispersion}$ is the residence time caused by dispersion of material, L is the unit's length, and Pe is the Peclet or Bodenstein dimensionless number. The Peclet dimensionless number represents the ratio between convective and dispersive transport and thus represents the level of dispersion in the system caused by mixing. This number can only be a positive real number, ranging from zero to infinity (i.e., $Pe \in \{\mathbb{R} \geq 0\}$). Large Pe values represent small amounts of dispersion (i.e., poor mixing), whereas smaller values represent greater amount of dispersion (i.e., better mixing). When $Pe = 0$ the system is said to be perfectly mixed, and when $Pe \rightarrow \infty$ the system approximates plug flow behavior.

The axial dispersion equation requires one initial condition and two boundary conditions to be solved. The initial condition in the system is often chosen as the steady state solution, wherein the concentration of tracer along the unit's length is zero (i.e., $C(\varepsilon, \theta = 0) = 0$). The boundary conditions to this partial differential equation vary depending on the system being represented. Four boundary condition forms can be considered: open-open, close-close, and mixed boundary conditions. The first two are the most commonly analyzed, as they represent the majority of dispersed systems. In the open-open boundary system, also known as the open vessel, dispersion (i.e., mixing) occurs before, within and after the unit boundaries, meaning mixing occurs

uninterrupted before and after the unit. For the close-close boundary system, also known as the closed vessel, dispersion only occurs within a set distance within the unit, typically specified as the unit's length. Figure 66 shows a schematic of the two systems based on their boundary conditions.

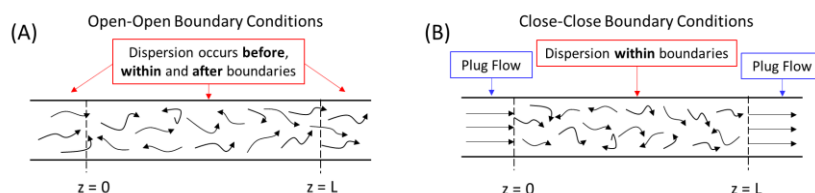


Figure 66. Schematic representations of the boundary conditions for the axial dispersion model. (A) Open-open boundary condition. (B) Close-close boundary condition.

The boundary conditions for each of these vessel types are listed in Table 42. The open vessel boundary conditions are recommended for systems with small dispersion ($Pe > 10$). Examples of these systems include those that resemble more closely plug flow. The close vessel boundary conditions are recommended for cases when dispersion is larger ($Pe < 10$), particularly when $Pe < 1$. The lower boundary of $Pe < 1$ is important to point since a system with such small Pe values is poorly represented by the equations derived for the open-open system. For very small Pe values the open vessel conditions effectively would predict that material disperses faster than it can convectively travel along the unit's length; a scenario that is not plausible given that convection is the major form of fluid transport in this system.

Table 42. Boundary conditions for two axial dispersion systems.

Vessel	Boundaries	Description	Equations	Recommended for
Open	Open-Open	Dispersion occurring before, within, and after the boundaries. The flow patterns remain undisturbed at the boundaries and the dispersion coefficient is non-zero over the entire system.	$\left. \frac{1}{Pe} \frac{\partial C}{\partial \varepsilon} \right]_{\varepsilon=0^-} = \left. \frac{1}{Pe} \frac{\partial C}{\partial \varepsilon} \right]_{\varepsilon=0^+}$ $\left. \frac{1}{Pe} \frac{\partial C}{\partial \varepsilon} \right]_{\varepsilon=1^-} = \left. \frac{1}{Pe} \frac{\partial C}{\partial \varepsilon} \right]_{\varepsilon=1^+}$	Small dispersion: $Pe > 10$

Close	Close-Close	Dispersion occurring only within the boundaries. The flow patterns change at the boundaries and the dispersion coefficient is zero before and after the system boundaries (i.e., plug flow).	$\frac{1}{Pe} \frac{\partial C}{\partial \varepsilon} \Big _{\varepsilon=0^-} = 0$ $\frac{1}{Pe} \frac{\partial C}{\partial \varepsilon} \Big _{\varepsilon=1^+} = 0$	Large dispersion: $Pe < 10$
-------	-------------	--	---	------------------------------------

Historically, most researchers have used the open vessel boundary conditions although powder blending system do not exactly resemble an open-open system [102]. This may be attributed to the fact that the open vessel boundary conditions provide a close form (i.e., analytical) solution to the dispersion equation. The close vessel boundary condition would require instead the use of numerical methods to solve the partial differential equation. However, even though the open-open boundary conditions may not exactly represent a powder blending system, it provides a sufficiently accurate approximation for our working range of dispersions values within powder blending system ($10 > Pe > 1$). Thus for this work, since there is interest in having an analytical solution for future analysis, open-open boundary conditions are assumed to solve 59. Readers interested in furthering the discussion of the differences with other boundary conditions for the axial dispersion equation are suggested to read the reviews previously referenced [103, 336]. The solution for the open vessel system using a pulse input was first derived by Levenspiel and Smith in 1957 and is shown in Equation 60.

$$C(\varepsilon, \theta) = C_{0,pulse} \sqrt{\frac{Pe}{4\pi\theta}} \text{Exp} \left[-\frac{Pe(\varepsilon - \theta)^2}{4\theta} \right] \quad 60$$

Since for a pulse input $E(\theta) = C(1, \theta)/C_{0,pulse}$, the PDF for the axial dispersion equation can be derived in both its normalized $E_{AD}(\theta)$ and time-dependent forms $E(t)$.

$$E_{AD}(\theta) = \tau_{dispersion} E(t) = \sqrt{\frac{Pe}{4\pi\theta}} \text{Exp} \left[-\frac{Pe(1 - \theta)^2}{4\theta} \right] \quad 61$$

With Equation 61, the PDF of an axially dispersed open-open system can be computed, following the assumptions set out by the boundary conditions and equations. Importantly, there are

two variables that must be regressed: (1) $\tau_{dispersion}$ and (2) Pe . Figure 71 shows the effect of varying the Pe and $\tau_{dispersion}$ on the PDF of a pulse input.

INSERT Figure 71 HERE

Increasing the Pe value increases the sharpness of the peak, meaning that a pulse is less dispersed at the unit's outlet. The lack of dispersion at the outlet is due to a smaller value of axial dispersion (D_z), which indicates the material travels as a plug throughout the unit's length. Increasing the dispersion's residence time at a constant Pe value yields a wider distribution of the pulse at the outlet of the unit. Intuitively, if the amount of time provided for the system to disperse increases, the outlet distribution would be wider.

9.4.2.2. Tank-in-series model

A continuous stirred tank reactor (CSTR), also known as the perfectly mixed continuous stirred tank (PMCSST), is an ideal type of chemical reactor in which reactants and products are well mixed in a fixed volume. Mixed materials are constantly being removed as fresh (i.e., unmixed) materials are added at the same flow rate. In this system, since the tank is perfectly mixed, the exit composition is the same as the concentration inside the tank as described by Equation 62.

$$\frac{d(M_r C)}{dt} = \dot{m}_{in} C_{\infty, step} - \dot{m}_{out} C \quad 62$$

where M_r is the mass of material in the reactor volume, C the outlet concentration, $C_{\infty, step}$ the inlet concentration caused by a positive step change, \dot{m}_{in} the inlet mass flow rate, and \dot{m}_{out} the outlet mass flow rate. It should be noticed that a step input is considered for this system since it allows an easier solution in a subsequent step using a finite series approach. Moreover, the step change allows for easier integration given that the inlet concentration does not change over time. However, it

should be highlighted that the exact same solution may be obtained for a pulse input using Laplace transformations, as shown by Himmelblau [103] and the work by Lorences et al. [216].

Returning to Equation 62, since the inlet and outlet mass flow rates are equal and the mass inside of the reactor space is constant, the tank equation can be written as shown in Equation 63.

$$\frac{d(C)}{dt} = \frac{\dot{m}_{in}}{M_r} (C_{0,step} - C) = \frac{1}{\tau_{tank}} (C_{0,step} - C) \quad 63$$

where τ_{tank} is the residence time in the tank. To solve this system, an initial condition must be provided. Once again, the steady state initial condition is selected to solve this system (i.e., $C(t = 0) = 0$).

The tank-in-series model, as the name implies, is derived from the application of the ideal mixing perfect stirred tank model in series. Multiple continuous stirred tanks are simulated in series by placing the outlet of previous units as the inlet of the subsequent one. Several identical tanks (n_r) intend to simulate the different mixing zones along the length of the unit. Figure 67 describes the tank-in-series system for an n_r number of tanks.

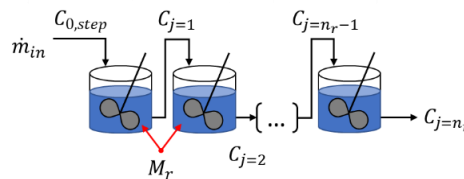


Figure 67. Schematic representation of a tank-in-series system

The differential equation resulting from the tank-in-series system is shown in Equation 64.

$$\frac{1}{n_r} \frac{d(C_j)}{dt} = \frac{1}{\tau_{tank}} (C_{j-1} - C_j) \quad 64$$

where C_j is the concentration at the outlet of reactor j on the series. The number of tank in the series has to be an integer number greater than one (i.e., $n_r \in \{\mathbb{Z} \geq 1\}$).

The result of setting up this system with more than one tank (i.e., $n_r > 2$) leads to a system of ordinary differential equations, which can be solved analytically using finite series or Laplace

transforms. For simplicity and similarly to the axial dispersion model, the system can be normalized with respect to time by introducing the variable $\vartheta = t/\tau_{tank}$. Using the method of finite series, the resulting concentration equation for the last tank in the series (C_{n_r}) assuming a constant step input concentration is given by the result of Equation 65.

$$C_{n_r}(\vartheta) = C_{0,step} \left(1 - \text{Exp}[-\vartheta] \sum_{k=0}^{n_r-1} \frac{\vartheta^k}{k} \right) \quad 65$$

From 65 and the definitions presented in Table 41, the CDF can be obtained for the tank-in series equation by dividing outlet concentration at reactor n_r by the incoming concentration (i.e., $\frac{C_{n_r}(\vartheta)}{C_{0,step}}$). Given the CDF described in Equation 9, the PDF of a step input system can be derived as shown in Equation 66.

$$E_{tank-in-Series}(\vartheta) = \tau_{tank-in-Series} E(t) = \frac{n_r \text{Exp}[-\vartheta] \vartheta^{n_r-1}}{(n_r - 1)!} \quad 66$$

where $\tau_{tank-in-Series}$ is the tank-in-series total mean residence time and its defined as the residence time in each tank times the number of tanks (i.e., $\tau_{tank-in-Series} = n_r \tau_{tank}$). Similar to 61, 66 can be used to compute the probability distribution function of a tank-in-series modeled system, following the conditions and assumptions set out by the equations system. Figure 72 shows the impact of varying n_r and τ_{tank} on both the PDF and CDF.

INSERT Figure 72 HERE

It should be noticed that in 66 the number of tanks can be any real number larger than 1 (i.e., $n_r \in \{\mathbb{R} \geq 1\}$). A reasonable explanation of a non-integer number of tanks (e.g., 2.1 or 3.8) is an integer series of tanks (e.g. 2 or 3 tanks) of equal size followed by a smaller tank equivalent to a fractional volume of the integer number of tanks such that $M_n = xM_r$, where x is the decimal value of the non-integer number (e.g., 0.1 or 0.8).

The results between the fractional n_r value and the “smaller tank at the end” scenario are not the same, yet they provide a close approximation of the system and an almost exact match when

$n_r > 3$. The difference between the two solutions is due in part to the implementation of the Gamma function, which does not have a zero-zero starting point in the distribution when the number of tanks is close to unity (i.e., $n_r \sim 1$). When the n_r is between 1 and 1.3, the Gamma function starts at a non-zero value (i.e., $E(t = 0) > 0$). This result is contrary to the solution set in Equation 65, wherein the initial condition forces the $E(t)$ to begin at a zero value.

9.4.2.3. Relationship between the AD and tank-in-series models

The axial dispersion and tank-in-series models provide analogous results with regards to the mixing occurring inside of a system. There is no mathematical (i.e., exact) way to compare or relate these models, given that their responses will not be identical. The models have been applied on a case-by-case basis, which considers both the system being characterized (i.e., geometry, size) and the process conditions. For example, if tracer material is added in the center of a blending system with both forwards and backwards mixing, the open vessel axial dispersion model would predict that dispersion occurs in both directions while the tank-in-series model would not yield any backwards mixing from the center of the system.

Although the two models do not have identical behavior, several authors have proposed correlations between these two models, by equating the second moments of the PDFs around the mean (i.e., the MCVs presented in Table 43). Notably, the residence times (i.e., the first moment of the PDF) must be equal. The MCV for the axial dispersion ($S_{\tau,AD}$) using the close vessel system and tank-in-series ($S_{\tau,tank-in-series}$) equations are shown below in Equations 67 and 68, respectively.

$$S_{\tau,AD} = \sigma_{\tau,AD}^2 = \frac{2}{Pe} \left[1 - \frac{(1 - \text{Exp}[-Pe])}{Pe} \right] \quad 67$$

$$S_{\tau,tank-in-series} = \sigma_{\tau,tank-in-series}^2 = \frac{1}{n_r} \quad 68$$

Equating these two MCVs leads to the correlation developed by Bischoff and others [103, 336, 340] of Pe and n_r , shown in Equation 69.

$$\frac{1}{n_r} = \frac{2}{Pe} \left[1 - \frac{1 - \text{Exp}[-Pe]}{Pe} \right] \quad 69$$

Simpler approximation of the relationship between the two variables leads to the following equation: $Pe \cong 2n_r + 1$ for systems with low dispersion. Other authors have approximated the results of Equation 69 for medium dispersion systems $Pe \cong n_r + \sqrt{8n_r + n_r^2}$. Using these last two relationships, the two models PDFs were compared, thus capturing the effects of changing one variable over time. The number of tanks can be changed in order to determine the impact to the PDF (Figure 68).

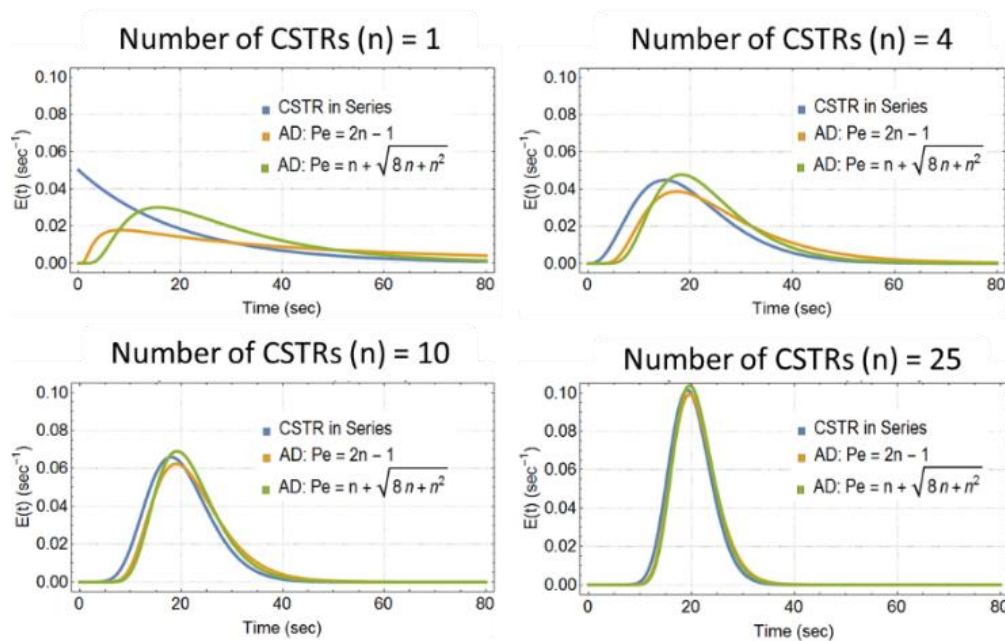


Figure 68. Comparison between tanks-in-series model and Axial Dispersion model over a broad range of mixing ($1 < n < 25$)

As observed, both the axial dispersion and tanks-in-series models are capable of simulating the PDFs under these conditions. A clear similarity can be observed when the number of tanks-in-series is very large, indicating low amounts of dispersions and back mixing. However, for low numbers of tanks ($n < 5$), which indicates a higher degree of mixing, the models have different

responses. The axial dispersion model is unable to predict a perfectly mixed scenario ($n=1$) using the relationship with the number of tanks. Thus, the degree of mixing is critical to evaluate in order to select the appropriate model for the case scenario. In order to evaluate in more detail the differences between the two models over at the large mixing, closer look at the differences between these models can be observed by using smaller numbers of tanks. Below, in Figure 69, we can observe the differences between the axial dispersion model and the tanks-in-series for low number of tanks (i.e., a high degree of mixing).

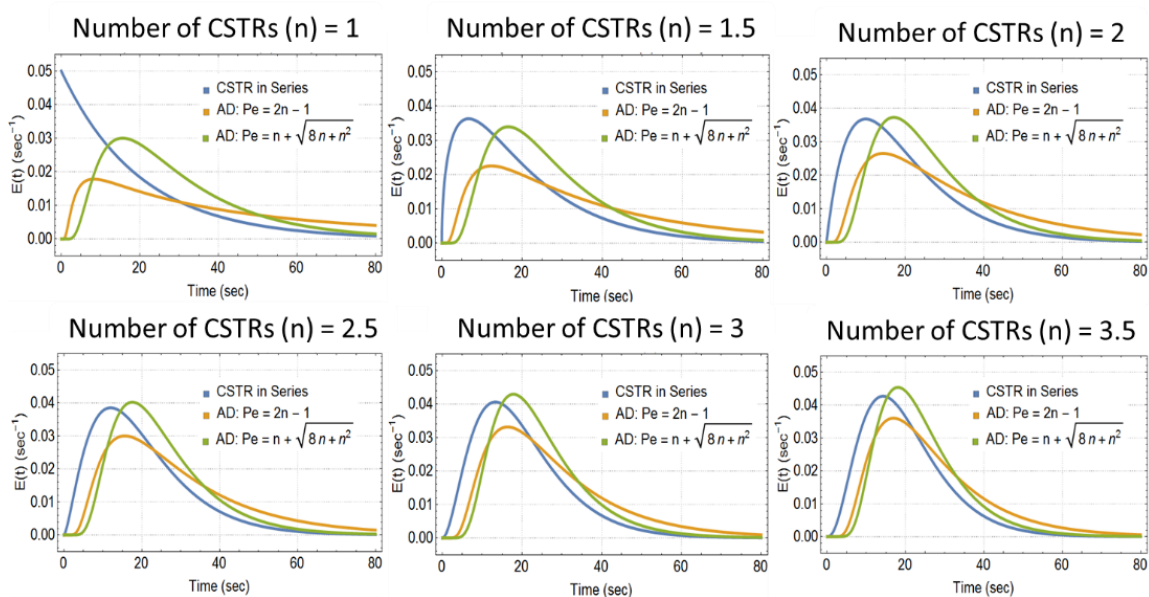


Figure 69. Comparison between tanks-in-series model and axial dispersion model for systems with vast mixing ($1 < n < 3.5$)

PDF curves show there are differences between these models at high levels of mixing. From the curves in Figure 69, we can observe that the tanks-in-series model PDF shows less degree of backmixing than CSTR compared to the axial dispersion model for n values less than 3.5. Further evaluation based on the maximum value of this distribution was assessed in order to capture the trend of this behavior. One of the major PDF results that can be used to compare is the maximum value of the distribution curve. This value can be obtained by maximizing the value of the curve and it represents the largest amount of material that leaves the unit during that specific residence

time. A set of PDF curves are evaluated for the two models at different numbers of tanks in order to obtain several maximum values. The values are plotted versus the number of tanks in Figure 70.

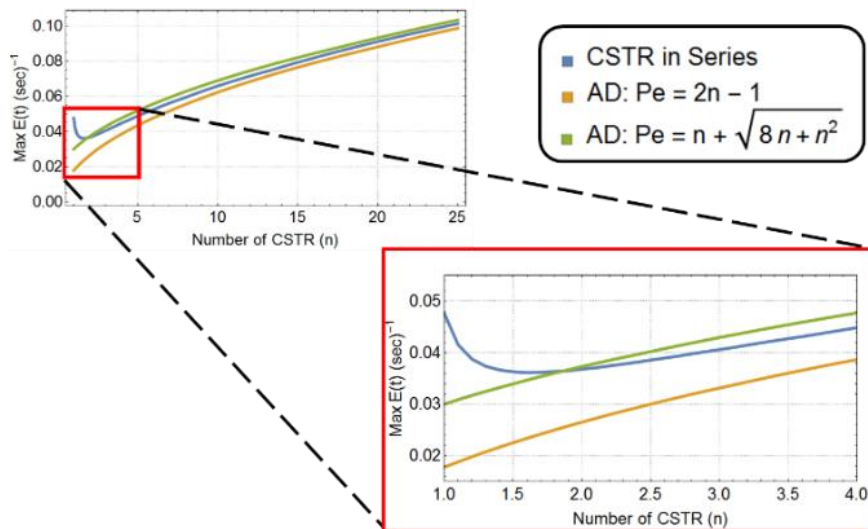


Figure 70. Comparison between the Axial Dispersion and CSTR in series for the maximum value of the Probability Distribution Function.

This difference therefore points to the fact that the axial dispersion model predicts a higher degree of mixing for low number of tank scenarios. From a risk management perspective higher mixing may not be viewed as a positive given that the model may predict better performance than observed. Given these results it is clear that the tank-in-series model is capable of capturing perfectly mixed scenarios, whereas the axial dispersion model is not able to do so. The axial dispersion shows a higher degree of dispersion (i.e., interaction between plug flow and mixing) over low ranges of number of tanks, which may not be ideal for characterizing the mixing of solid systems.

Table 44 summarizes the advantages and challenges associated with the implementation of these two models.

INSERT Table 44 HERE

Table 43. Summary of RTD metrics derived from probability distribution function values

Name	Symbol	Description	Equation
Mean residence time (MRT)	τ	Average time a tracer particle spends in the system from a distribution	$\tau = \mu_1 = \int_0^{\infty} t E(t) dt \cong \sum_0^{\infty} t E(t) \Delta t$
Mean centered variance of MRT (MCV)	σ_{τ}^2	Normalized range of time from which a particle spends inside of the system	$\sigma_{\tau}^2 = \frac{\gamma_2}{\tau^2} = \int_0^{\infty} \frac{(t - \tau)^2 E(t)}{\tau^2} dt \cong \sum_0^{\infty} \frac{(t - \tau)^2 E(t) \Delta t}{\tau^2}$
Mean centered skewness of MRT	ψ_{τ}	Degree of asymmetry in the PDF depicting non-ideality of mixing in the system	$\psi_{\tau} = \frac{\gamma_3}{\tau^3} = \int_0^{\infty} \frac{(t - \tau)^3 E(t)}{\tau^3} dt \cong \sum_0^{\infty} \frac{(t - \tau)^3 E(t) \Delta t}{\tau^3}$

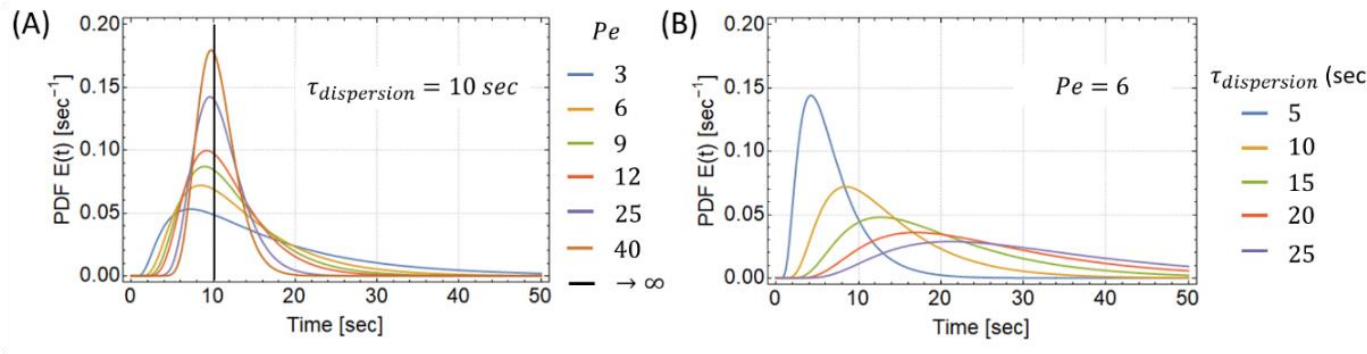


Figure 71. Effect of varying the regression parameters for the Axial Dispersion equation while keeping some constant. (A) Varying Pe while keeping $\tau_{dispersion}$ at 10 seconds. (B) Varying $\tau_{dispersion}$ while keeping Pe at 6.

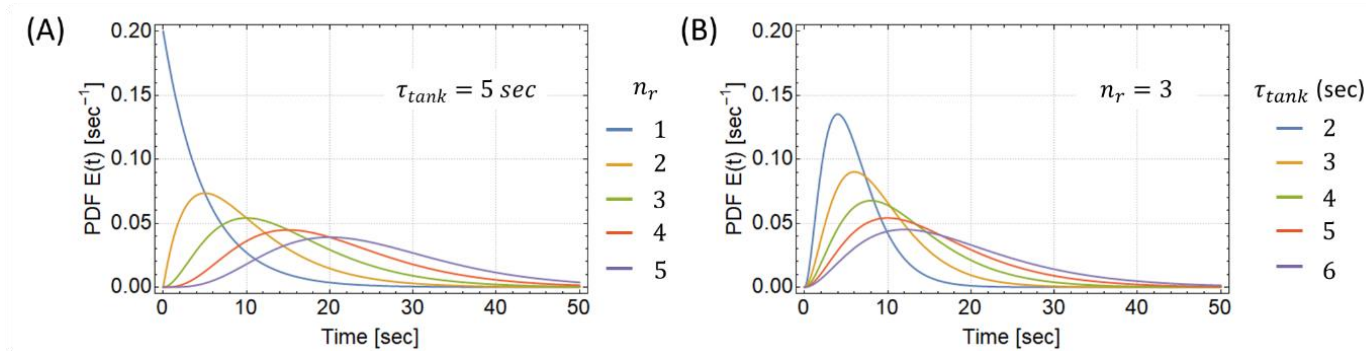


Figure 72. Effect of varying the regression parameters for the tank-in-series equation while keeping some constant. (A) Varying n_r while keeping τ_{tank} at 5 seconds. (B) Varying τ_{tank} while keeping n_r at 3.

Table 44. Advantages and challenges of RTD models

Model	Advantages	Challenges
Axial dispersion – Equation 61	<ul style="list-style-type: none"> • Axial dispersion coefficient (D_z) and fluid velocity (v_z) have theoretical and physical meanings • Model can be adapted based on the process conditions and equipment geometry • Equipment geometry affects the mixing model based on the model structure 	<ul style="list-style-type: none"> • Boundary conditions affect the results of the model for a given system • High dispersion (i.e, mixing) is poorly modeled in this system • Model does not have an analytical closed form for the closed vessel system • Parameters become meaningless if RTD of multiple equipment is being modeled
Tank-in-series – Equation 66	<ul style="list-style-type: none"> • Mathematical details for the models are comparatively simpler • Accounts for system changes and variations in process conditions given that no boundary conditions constraints the system • Used to simulate the behavior of equipment networks (i.e., multiple units) 	<ul style="list-style-type: none"> • Number of tanks (n_r) is a strictly empirical parameter, and thus has no physical meaning • Equipment geometry and process dimensions are not accounted for in the model • Black box approach to modeling the RTD • Fractional values of number of tanks do not have a theoretical basis

9.5. APPENDIX E: NIR METHOD DEVELOPMENT FOR REAL TIME MEASUREMENTS

As provided in Chapter VI, this section aims at providing the results collected by Dr. Roman-Ospino for the development and calibration of the real time NIR model that were used to collect the concentration of material exiting the blender for the RTD experiments.

After selecting the base and tracer materials, the online real-time measurement system was developed to quantify the tracer concentration during the RTD experiments. The use of online real-time measurements was chosen because it allowed two major advantages: (1) to generate information with enough frequency to obtain the fully resolved RTD, and (2) to enable making decisions about the start and endpoint of each experiment. The first advantage would prevent the loss of critical distribution information, which includes the distribution's start and maximum points. The second advantage ensured that no tracer was added before the previous pulse had completely exited the system. Furthermore, using online real time measurements minimizes material and time waste because the researchers are able to track the experimental progress using the real-time results coming from the sensors [342-346].

As discussed in section (2), near infrared (NIR) spectroscopy was used in this set of experiments due to its inherent versatility (i.e., no sample preparation required) and adaptation of different experimental setups. Fiber optic probes allow the sensor to be attached in the specific location required for the experiment. Projection of Latent Structures (PLS) is a suitable technique to analyze the multidimensional information from near infrared spectroscopy data leading to consistent composition measurements of particulate materials.

A total of seven calibration models were previously prepared for the binary mixture composed by MCC 2 and each tracer. Calibration blends were prepared for tracer concentrations of 3, 6 and 9% w/w with pure MCC 2 spectra included as 0% w/w. After optimization of each

model using independent samples, models were saved and uploaded into the option control process from OPUS for real time measurements. Importantly, only binary mixtures (base and tracer) were considered in this work, so randomization of multiple ingredients in the base blend was not necessary.

Figure 73 shows the spectral variation between the components of each model (i.e., MCC 2 and tracer). Standard normal variate (SNV) was applied to each spectrum to highlight the variation in vibrational information. Each data set was evaluated in multiple spectral ranges, data pretreatments and PLS factors to obtain the lowest root mean squared error of prediction (RMSEP) by using the test samples. The shaded area in Figure 73 corresponds to the spectral range that produced optimum results and the number of PLS factors was estimated calculating the RMSEP by test samples.

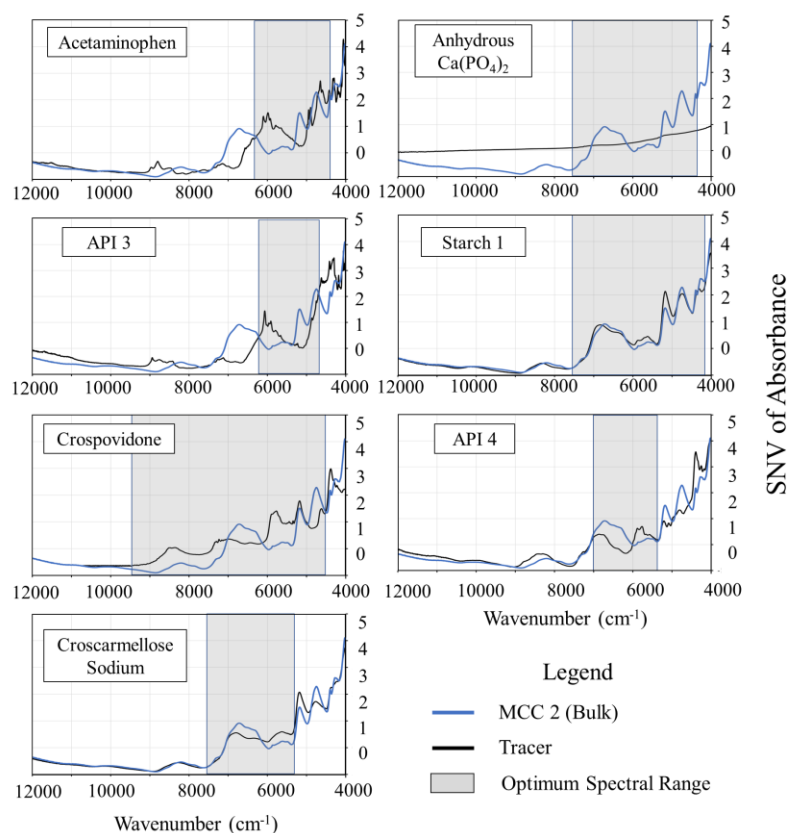


Figure 73. Spectral variation between the components of each tracer and the bulk MCC 2

Figure 74 shows the parity plot based on test samples for each calibration model. All of the tracers showed to have a highly linear ($R^2 > 95\%$) response between the predicted and reference values, indicating the models have good predictability.

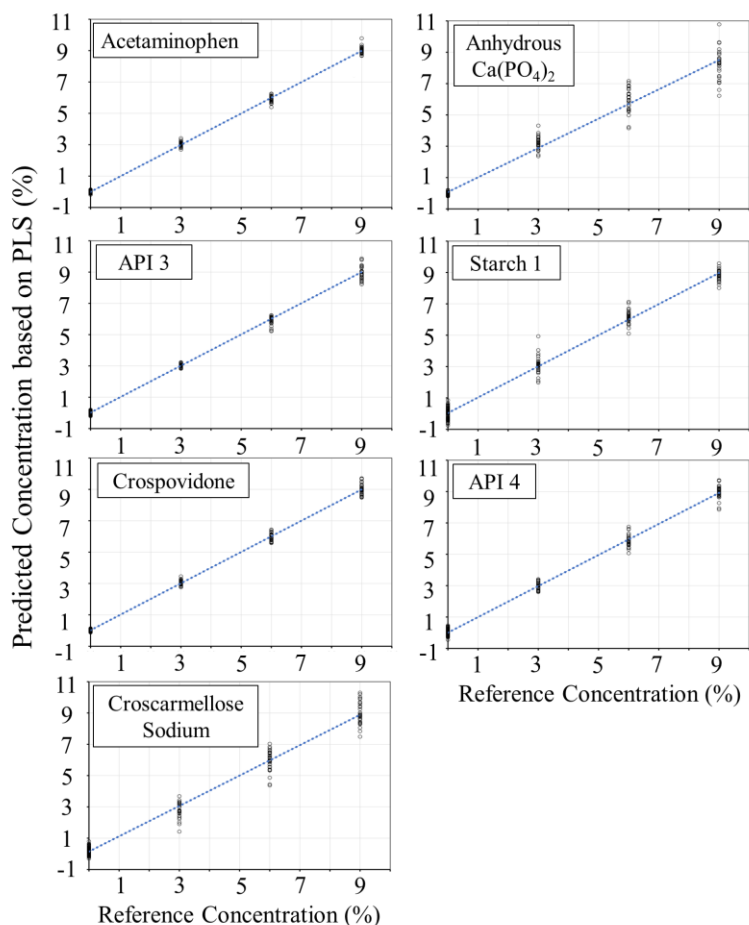


Figure 74. Parity plots for the concentration prediction of tracer in the bulk MCC 2 for all tracers

Table 46 shows the evaluation of calibration models with the lowest RMSEP values for each material. NIR method optimization was implemented by using several spectral ranges, data pretreatments and number of latent variables. Calibration models were selected for the RTD experiments based on the lowest RMSEP value predicting independent samples with known composition.

INSERT Table 46 HERE

In Table 45, the spectral correlation coefficient between MCC 2 and the tracers used for the RTD experiments are shown. The lowest correlation coefficient found for acetaminophen (0.8782) is also related to the low RMSEP value (0.15), the low numbers of latent variables (LV = 2) and the use of a single data preprocessing (SNV). The highest correlation coefficient was obtained for starch 1, representing an additional challenge in the construction of calibration models for chemically similar substances. For this case, optimized calibration model required a combination of data preprocessing (1st Derivative + Standard Normal Variate, SNV) and one additional latent variable to produce one of the highest RMSEP values in independent samples.

Table 45. Spectral correlation coefficient between bulk MCC and tracers

Tracer Material	Spectral Correlation Coefficient
Acetaminophen	87.8%
Anhydrous Calcium Di-Phosphate	91.8%
Croscarmellose Sodium	98.0%
Crospovidone	86.7%
Starch 1	98.9%
API 3	84.6%
API 4	93.4%

Table 46. Calibration models of in-line measurements of tracer concentration in RTD experiments.

Tracer	Spectral Range (cm ⁻¹)	Data pre-treatment	LV	RMSEP	Bias	R ²
Acetaminophen	6101-4246	SNV	2	0.15	0.01	99.8%
Anhydrous Calcium Di-Phosphate	7502-4246	MSC	3	0.61	0.1	96.9%
Croscarmellose Sodium	7502-5446 & 4601-4246	MSC	2	0.48	-0.1	98.1%
Crospovidone	9403-4597	MSC	3	0.18	-0.02	99.7%
Starch 1	7502-4138	1st Der (17 Pts)+SNV	3	0.44	-0.02	98.4%
API 3	6110-4697	MSC	2	0.28	-0.02	99.3%
API 4	5400-7000	MSC	3	0.28	0.02	99.3%

CHAPTER X

10. REFERENCES

1. WHO, *World Health Statistics 2015*. 2015, World Health Organization: Luxemburg.
2. Lindsley, C., *New 2016 Data and Statistics for Global Pharmaceutical Products and Projections through 2017*. ACS Chemical Neuroscience, 2017(8): p. 1635-1636.
3. PwC, *La R&D virtuelle*, in *Pharma 2020*, Industrie Pharmaceutique et des Sciences de la Vie, Editor. 2008, PricewaterhouseCoopers.
4. Kumar, V. and R.P. Sundarraj, *The Societal Value of Pharmaceutical Innovation*, in *Global Innovation and Economic Value*, V. Kumar and R.P. Sundarraj, Editors. 2018, Springer India: New Delhi. p. 147-187.
5. Khanna, I., *Drug discovery in pharmaceutical industry: productivity challenges and trends*. Drug Discov Today, 2012. **17**(19-20): p. 1088-102.
6. PwC, *From Vision to Decision*, in *Pharma 2020*, Global Pharmaceuticals and Life Sciences Industry Group, Editor. 2012, PricewaterhouseCoopers.
7. International, C., *2015 Pharmaceutical R&D Factbook*, in *R&D Factbooks*. 2015, Thomson Reuters.
8. Barton, J.H. and E.J. Emanuel, *The patents-based pharmaceutical development process: Rationale, problems, and potential reforms*. JAMA, 2005. **294**(16): p. 2075-2082.
9. Development, T.C.f.t.S.o.D., *Backgrounder: How New Drugs Move Through the Development and Approval Process*. 2001.
10. Garcia, T., G. Cook, and R. Nosal, *PQLI Key Topics - Criticality, Design Space, and Control Strategy*. Journal of Pharmaceutical Innovation, 2008. **3**(2): p. 60-68.
11. Lionberger, R.A., et al., *Quality by Design: Concepts for ANDAs*. The AAPS Journal, 2008. **10**(2): p. 268-276.
12. Nosal, R. and T. Schultz, *PQLI Definition of Criticality*. Journal of Pharmaceutical Innovation, 2008. **3**(2): p. 69-78.
13. Lawrence, X.Y., *Pharmaceutical quality by design: product and process development, understanding, and control*. Pharmaceutical research, 2008. **25**(4): p. 781-791.
14. FDA, U., *Guidance for Industry: PAT — A Framework for Innovative Pharmaceutical Development, Manufacturing, and Quality Assurance*, U.D.o.H.a.H. Services, Editor. 2004: Rockville, MD.
15. Challa, S. and R. Potumarthi, *Chemometrics-based process analytical technology (PAT) tools: applications and adaptation in pharmaceutical and biopharmaceutical industries*. Appl Biochem Biotechnol, 2013. **169**(1): p. 66-76.
16. Rantanen, J. and J. Khinast, *The Future of Pharmaceutical Manufacturing Sciences*. Journal of Pharmaceutical Sciences, 2015: p. n/a-n/a.

17. Aksu, B., et al., *Quality by Design Approach: Application of Artificial Intelligence Techniques of Tablets Manufactured by Direct Compression*. AAPS PharmSciTech, 2012. **13**(4): p. 1138-1146.
18. Yu, L.X., et al., *Understanding Pharmaceutical Quality by Design*. The AAPS Journal, 2014. **16**(4): p. 771-783.
19. Lepore, J. and J. Spavins, *PQLI Design Space*. Journal of Pharmaceutical Innovation, 2008. **3**(2): p. 79-87.
20. Kourti, T., *Pharmaceutical Manufacturing: The Role of Multivariate Analysis in Design Space, Control Strategy, Process Understanding, Troubleshooting, and Optimization*, in *Chemical Engineering in the Pharmaceutical Industry*. 2010, John Wiley & Sons, Inc. p. 853-878.
21. Ende, D., et al., *API Quality by Design Example from the Torcetrapib Manufacturing Process*. Journal of Pharmaceutical Innovation, 2007. **2**(3-4): p. 71-86.
22. Saraswat, M., et al., *Preparative purification of recombinant proteins: current status and future trends*. Biomed Res Int, 2013. **2013**: p. 312709.
23. Leuenberger, H., *New trends in the production of pharmaceutical granules: batch versus continuous processing*. European Journal of Pharmaceutics and Biopharmaceutics, 2001. **52**(3): p. 289-296.
24. Plumb, K., *Continuous processing in the pharmaceutical industry - Changing the mind set*. Chemical Engineering Research & Design, 2005. **83**(A6): p. 730-738.
25. Ting, N., *Dose Finding in Drug Development*. 2006, New York: Springer.
26. Makrydaki, F.G., C; Saranteas, K. *Dynamic Optimization of a Batch Pharmaceutical Reaction using the Design of Dynamic Experiments (DoDE): the Case of an Asymmetric Catalytic Hydrogenation Reaction*. in *Dynamics and Control of Process Systems*. 2010. Leuven, Belgium.
27. Toulouse, C.e.a., *Optimisation and scale-up of batch chemical reactors: impact of safety constraints*. Chemical Engineering Science, 1996. **51**(10).
28. Raaymakers, W.H., J, *Scheduling multipurpose batch process industries with no-wait restrictions by simulated annealing*. European Journal of Operational Research, 2000. **126**.
29. Ooi, S.M., et al., *Continuous processing and the applications of online tools in pharmaceutical product manufacture: developments and examples*. Therapeutic Delivery, 2013. **4**(4): p. 463-470.
30. Boukouvala, F., et al., *An integrated approach for dynamic flowsheet modeling and sensitivity analysis of a continuous tablet manufacturing process*. Computers & Chemical Engineering, 2012. **42**(0): p. 30-47.
31. Lee, S., et al., *Modernizing Pharmaceutical Manufacturing: from Batch to Continuous Production*. Journal of Pharmaceutical Innovation, 2015. **10**(3): p. 191-199.
32. Mascia, S., et al., *End-to-End Continuous Manufacturing of Pharmaceuticals: Integrated Synthesis, Purification, and Final Dosage Formation*. Angewandte Chemie International Edition, 2013. **52**(47): p. 12359-12363.
33. Singh, R., Ierapetritou, M., Ramachandran, R., *An engineering study on the enhanced control and operation of continuous manufacturing of pharmaceutical tablets via roller compaction*. International Journal of Pharmaceutics, 2012: p. Article in Press.
34. Engisch, W. and F. Muzzio, *Using Residence Time Distributions (RTDs) to Address the Traceability of Raw Materials in Continuous Pharmaceutical Manufacturing*. Journal of Pharmaceutical Innovation, 2016. **11**(1): p. 64-81.
35. Oka, S., *Effect of powder cohesion and segregation on pharmaceutical mixing and granulation*, in *Chemical Engineering*. 2016, Rutgers, The State University of New Jersey: New Brunswick, New Jersey.

36. Schaber, S.D., et al., *Economic Analysis of Integrated Continuous and Batch Pharmaceutical Manufacturing: A Case Study*. Industrial & Engineering Chemistry Research, 2011. **50**(17): p. 10083-10092.
37. Yu, L.X. and M. Kopcha, *The future of pharmaceutical quality and the path to get there*. International Journal of Pharmaceutics, 2017. **528**(1): p. 354-359.
38. Jarvinen, K., et al., *In-line monitoring of the drug content of powder mixtures and tablets by near-infrared spectroscopy during the continuous direct compression tableting process*. Eur J Pharm Sci, 2013. **48**(4-5): p. 680-8.
39. Fisher, A.C., et al., *Advancing pharmaceutical quality: An overview of science and research in the U.S. FDA's Office of Pharmaceutical Quality*. International Journal of Pharmaceutics, 2016. **515**(1): p. 390-402.
40. Rogers, A., A. Hashemi, and M. Ierapetritou, *Modeling of Particulate Processes for the Continuous Manufacture of Solid-Based Pharmaceutical Dosage Forms*. Processes, 2013. **1**(2): p. 67-127.
41. Gibson, M., *Pharmaceutical Preformulation and Formulation: A Practical Guide from Candidate Drug Selection to Commercial Dosage Form*. 2009, New York: Informa Healthcare.
42. Castle, B.C. and R.A. Forbes, *Impact of Quality by Design in Process Development on the Analytical Control Strategy for a Small-Molecule Drug Substance*. Journal of Pharmaceutical Innovation, 2013. **8**(4): p. 247-264.
43. Norioka, T., et al., *A Novel Approach to Establishing the Design Space for the Oral Formulation Manufacturing Process*. Chemical and Pharmaceutical Bulletin, 2013. **61**(1): p. 39-49.
44. Norioka, T., et al., *Optimization of the Manufacturing Process for Oral Formulations Using Multivariate Statistical Methods*. Journal of Pharmaceutical Innovation, 2011. **6**(3): p. 157-169.
45. Chatterjee, S. *FDA perspective on continuous manufacturing*. in *IFPAC Annual Meeting, Baltimore, MD*. 2012.
46. Moghtadernejad, S., et al., *A Training on: Continuous Manufacturing (Direct Compaction) of Solid Dose Pharmaceutical Products*. Journal of Pharmaceutical Innovation, 2018.
47. Ierapetritou, M., M.S. Escotet-Espinoza, and R. Singh, *Process Simulation and Control for Continuous Pharmaceutical Manufacturing of Solid Drug Products*. Continuous Manufacturing of Pharmaceuticals, 2017: p. 33-105.
48. Heider, P.L., et al., *Development of a Multi-Step Synthesis and Workup Sequence for an Integrated, Continuous Manufacturing Process of a Pharmaceutical*. Organic Process Research & Development, 2014. **18**(3): p. 402-409.
49. Rogers, A. and M. Ierapetritou, *Challenges and Opportunities in Pharmaceutical Manufacturing Modeling and Optimization*, in *Computer Aided Chemical Engineering*, J.D.S. Mario R. Eden and P.T. Gavin, Editors. 2014, Elsevier. p. 144-149.
50. Gernaey, K.V. and R. Gani, *A model-based systems approach to pharmaceutical product-process design and analysis*. Chemical Engineering Science, 2010. **65**(21): p. 5757-5769.
51. García-Muñoz, S., et al., *A flowsheet model for the development of a continuous process for pharmaceutical tablets: An industrial perspective*. AIChE Journal, 2018: p. n/a-n/a.
52. Braido, D., *Characterization and modeling the dissolution performance of tablets focusing on powder processing effects*. 2012.
53. Rogers, A., *Process systems engineering methods for the development of continuous pharmaceutical manufacturing processes*. 2015.
54. Wang, Y., *Using multivariate analysis for pharmaceutical drug product development*. 2016.

55. Rogers, A.J., C. Inamdar, and M.G. Ierapetritou, *An integrated approach to simulation of pharmaceutical processes for solid drug manufacture*. Industrial and Engineering Chemistry Research, 2014. **53**(13): p. 5128-5147.
56. Sen, M., et al., *Flowsheet optimization of an integrated continuous purification-processing pharmaceutical manufacturing operation*. Chemical Engineering Science, 2013. **102**: p. 56-66.
57. Singh, R., K.V. Gernaey, and R. Gani, *Model-based computer-aided framework for design of process monitoring and analysis systems*. Computers & Chemical Engineering, 2009. **33**(1): p. 22-42.
58. Gernaey, K.V., A.E. Cervera-Padrell, and J.M. Woodley, *A perspective on PSE in pharmaceutical process development and innovation*. Computers & Chemical Engineering, 2012. **42**: p. 15-29.
59. Tolsma, J.E., J.A. Clabaugh, and P.I. Barton, *Symbolic Incorporation of External Procedures into Process Modeling Environments*. Ind. Eng. Chem. Res., 2002. **41**: p. 3687 - 3876.
60. Morari, M., *Flexibility and resiliency of process systems*. Computers & Chemical Engineering, 1983. **7**(4): p. 423-437.
61. Swaney, R.E., Grossmann, I.E., *An Index for Operational Flexibility in Chemical Process Design Part I: Formulation and Theory*. AIChE Journal, 1985. **36**.
62. Wang, Z., M.S. Escotet-Espinoza, and M. Ierapetritou, *Process analysis and optimization of continuous pharmaceutical manufacturing using flowsheet models*. Computers & Chemical Engineering, 2017.
63. Mesbah, A., et al., *Model Predictive Control of an Integrated Continuous Pharmaceutical Manufacturing Pilot Plant*. Organic Process Research & Development, 2017. **21**(6): p. 844-854.
64. Haas, N.T., M. Ierapetritou, and R. Singh, *Advanced Model Predictive Feedforward/Feedback Control of a Tablet Press*. Journal of Pharmaceutical Innovation, 2017. **12**(2): p. 110-123.
65. Almaya, A., et al., *Control Strategies for Drug Product Continuous Direct Compression-State of Control, Product Collection Strategies, and Startup/Shutdown Operations for the Production of Clinical Trial Materials and Commercial Products*. J Pharm Sci, 2017. **106**(4): p. 930-943.
66. Lakio, S., et al., *Provoking an end-to-end continuous direct compression line with raw materials prone to segregation*. European Journal of Pharmaceutical Sciences, 2017. **109**(Supplement C): p. 514-524.
67. Singh, R., et al., *Advanced control of continuous pharmaceutical tablet manufacturing processes*, in *Methods in Pharmacology and Toxicology*. 2016. p. 191-224.
68. Singh, R., et al., *A systematic framework for onsite design and implementation of a control system in a continuous tablet manufacturing process*. Computers & Chemical Engineering, 2014. **66**: p. 186-200.
69. Gerogiorgis, D.I. and P.I. Barton, *Steady-state optimization of a continuous pharmaceutical process*. Computer Aided Chemical Engineering, 2009. **27**: p. 927-932.
70. Singh, R., et al., *Integrated moving horizon-based dynamic real-time optimization and hybrid MPC-PID control of a direct compaction continuous tablet manufacturing process*. Journal of Pharmaceutical Innovation, 2015. **10**(3): p. 233-253.
71. Escotet-Espinoza, M., *Flowsheet Models Modernize Pharmaceutical Manufacturing Design and Risk Assessment*. Pharmaceutical Technology, 2015. **39**(4).
72. García Muñoz, S., V. Padovani, and J. Mercado, *A computer aided optimal inventory selection system for continuous quality improvement in drug product manufacture*. Computers & Chemical Engineering, 2014. **60**: p. 396-402.

73. Tomba, E., M. Barolo, and S. García-Muñoz, *In-silico product formulation design through latent variable model inversion*. Chemical Engineering Research and Design, 2014. **92**(3): p. 534-544.
74. Singh, R., et al., *Closed-Loop Feedback Control of a Continuous Pharmaceutical Tablet Manufacturing Process via Wet Granulation*. Journal of Pharmaceutical Innovation, 2014. **9**(1): p. 16-37.
75. Singh, R., et al., *Implementation of an advanced hybrid MPC–PID control system using PAT tools into a direct compaction continuous pharmaceutical tablet manufacturing pilot plant*. International Journal of Pharmaceutics, 2014. **473**(1–2): p. 38-54.
76. Singh, R., M. Ierapetritou, and R. Ramachandran, *System-wide hybrid MPC–PID control of a continuous pharmaceutical tablet manufacturing process via direct compaction*. European Journal of Pharmaceutics and Biopharmaceutics, 2013. **85**(3, Part B): p. 1164-1182.
77. Singh, R., M. Ierapetritou, and R. Ramachandran, *Hybrid advanced control of flexible multipurpose continuous tablet manufacturing process via direct compaction*, in *Computer Aided Chemical Engineering*, K. Andrzej and T. Ilkka, Editors. 2013, Elsevier. p. 757-762.
78. Boukouvala, F., *Integrated Simulation and Optimization of Continuous Pharmaceutical Manufacturing*, in *Chemical and Biochemical Engineering*. 2013, Rutgers, The State University of New Jersey: New Brunswick, NJ.
79. Montgomery, D., *Design and Analysis of Experiments*. 9th ed. 2017, USA: Wiley.
80. Jacques, J., *Design of Experiments*. The Franklin Institute, 1996. **335B**(2): p. 259-279.
81. Browne, M.W., *Cross-Validation Methods*. J Math Psychol, 2000. **44**(1): p. 108-132.
82. Gong, G., *Cross-validation, the jackknife, and the bootstrap: Excess error estimation in forward logistic regression*. J. Am. Stat. Assoc., 1986. **81**: p. 108-113.
83. Steyerberg, E.W., et al., *Internal validation of predictive models: efficiency of some procedures for logistic regression analysis*. J Clin Epidemiol, 2001. **54**(8): p. 774-81.
84. Sargent, R. *Verification and Validation of Simulation Models*. in *Proceedings of the 2010 Winter Simulation Conference*. 2010.
85. Zhu, H.P., et al., *Discrete particle simulation of particulate systems: A review of major applications and findings*. Chemical Engineering Science, 2008. **63**(23): p. 5728-5770.
86. Wu, C.Y., et al., *Modelling the mechanical behaviour of pharmaceutical powders during compaction*. Powder Technology, 2005. **152**(1-3): p. 107-117.
87. Guoming, H., et al. *Modeling and simulation of transportation system of screw conveyors by the Discrete Element Method*. in *Mechanic Automation and Control Engineering (MACE), 2010 International Conference on*. 2010.
88. Ketterhagen, W.R., M.T.A. Ende, and B.C. Hancock, *Process Modeling in the Pharmaceutical Industry using the Discrete Element Method*. Journal of Pharmaceutical Sciences, 2009. **98**(2): p. 442-470.
89. Verkoeijen, D., et al., *Population balances for particulate processes—a volume approach*. Chemical Engineering Science, 2002. **57**(12): p. 2287-2303.
90. Barrasso, D. and R. Ramachandran, *A comparison of model order reduction techniques for a four-dimensional population balance model describing multi-component wet granulation processes*. Chemical Engineering Science, 2012. **80**(0): p. 380-392.
91. Sen, M., et al., *Multi-dimensional population balance modeling and experimental validation of continuous powder mixing processes*. Chemical Engineering Science, 2012. **80**(0): p. 349-360.
92. Kumar, A., et al., *Model-based analysis of high shear wet granulation from batch to continuous processes in pharmaceutical production – A critical review*. European Journal of Pharmaceutics and Biopharmaceutics, 2013. **85**(3, Part B): p. 814-832.

93. Sen, M., Ramachandran, R., *A multi-dimensional population balance model approach to continuous powder mixing processes*. *Advanced Powder Technology*, 2013. **24**(1): p. 51-59.
94. Barrasso, D., A. Tamrakar, and R. Ramachandran, *A reduced order PBM-ANN model of a multi-scale PBM-DEM description of a wet granulation process*. *Chemical Engineering Science*, 2014. **119**: p. 319-329.
95. Kremer, D.M. and B.C. Hancock, *Process simulation in the pharmaceutical industry: a review of some basic physical models*. *J Pharm Sci*, 2006. **95**(3): p. 517-29.
96. Hsu, S.H., Reklaitis, G.V., Venkatasubramanian, V., *Modeling and Control of Roller Compaction for Pharmaceutical Manufacturing. Part I: Process Dynamics and Control Framework*. *J Pharm Innov*, 2010. **5**: p. 14-23.
97. Bindhumadhavan, G., Seville, J.P.K., Adams, M.J., Greenwood, R.W., Fitzpatrick, S., *Roll compaction of a pharmaceutical excipient: Experimental validation of rolling theory for granular solids*. *Chemical Engineering Science*, 2005. **60**: p. 3891 – 3897.
98. Johanson, J.R., *A rolling theory for granular solids*. *AMSE Journal of Applied Mechanics*, 1965. **E32**(4): p. 842-848.
99. Reynolds, G., Ingale, R., Roberts, R., Kothari, S., Gururagan, B., *Practical application of roller compaction process modeling*. *Computers and Chemical Engineering*, 2010. **34**: p. 1049-1057.
100. Martin Kuentz, H.L., *A new model for the hardness of a compacted particle system, applied to tablets of pharmaceutical polymers*. *Powder Technology*, 2000. **111**: p. 145-153.
101. Gao, Y., et al., *Characterizing continuous powder mixing using residence time distribution*. *Chemical Engineering Science*, 2011. **66**(3): p. 417-425.
102. Gao, Y., Muzzio, F.J., Ierapetritou, M.G., *A review of the Residence Time Distribution (RTD) applications in solid unit operations*. *Powder Technology*, 2012. **228**: p. 416-423.
103. Himmelblau, D. and K. Bischoff, *Process Analysis and Simulation: Deterministic Systems*. 1968, New York, NY: Wiley.
104. Danckwerts, P.V., *Continuous flow systems: Distribution of residence times*. *Chemical Engineering Science*, 1953. **2**(1): p. 1-13.
105. Shvartsman, S.Y., et al., *Order reduction for nonlinear dynamic models of distributed reacting systems*. *Journal of Process Control*, 2000. **10**(2-3): p. 177-184.
106. Boukouvala, F. and M. Ierapetritou, *Surrogate-Based Optimization of Expensive Flowsheet Modeling for Continuous Pharmaceutical Manufacturing*. *Journal of Pharmaceutical Innovation*, 2013. **8**(2): p. 131-145.
107. Boukouvala, F. and M.G. Ierapetritou, *Feasibility analysis of black-box processes using an adaptive sampling Kriging-based method*. *Computers & Chemical Engineering*, 2012. **36**: p. 358-368.
108. Lang, Y.D., et al., *Reduced Order Model Based on Principal Component Analysis for Process Simulation and Optimization*. *Energy & Fuels*, 2009. **23**(3): p. 1695-1706.
109. Foss, B.A., Lohmann, B., Marquardt, W., *A field study of the industrial modeling process*. *Journal of Process Control*, 1998. **8**(5-6): p. 325-338.
110. Cameron, I.T. and G.D. Ingram, *A survey of industrial process modelling across the product and process lifecycle*. *Computers & Chemical Engineering*, 2008. **32**(3): p. 420-438.
111. Papadopoulos, A.I., Seferlis, P., *Generic modelling, design and optimization of industrial phosphoric acid production processes*. *Chemical Engineering and Processing: Process Intensification*, 2009. **48**(1): p. 493-506.
112. Othman, M.R., et al., *A Modular Approach to Sustainability Assessment and Decision Support in Chemical Process Design*. *Industrial & Engineering Chemistry Research*, 2010. **49**(17): p. 7870-7881.

113. Toebermann, J., -C., Rosenkranz, J., Werther, J., Gruhn, G., *Block-oriented process simulation of solids processes*. Computers & Chemical Engineering, 2000. **23**: p. 1773-1782.
114. Hartage, E.U., Pogodda, M., Reimers, C., Schwier, D., Gruhn, G., Werther J., *Flowsheet simulation of solids processes*. KONA, 2006. **24**: p. 146-156.
115. Boukouvala, F., Niotis, V., Ramachandran, R. Muzzio, F.J., Ierapetritou, M.G., *An integrated approach for dynamic flowsheet modeling and sensitivity analysis of a continuous tablet manufacturing process*. Computers and Chemical Engineering, 2012. **42**: p. 30-47.
116. McKenzie, P.K., S. Tom, J. Rubin, E., Futran, M., *Can Pharmaceutical Process Development Become High Tech?* AIChE Journal, 2006. **52**(12).
117. Florian-Algarin, M. and R. Méndez, *Blend uniformity and powder phenomena inside the continuous tumble mixer using DEM simulations*. AIChE Journal, 2015. **61**(3): p. 792-801.
118. Boonkanokwong, V., et al., *The effect of the number of impeller blades on granular flow in a bladed mixer*. Powder Technology, 2016. **302**: p. 333-349.
119. Liu, X., et al., *DEM study on the surface mixing and whole mixing of granular materials in rotary drums*. Powder Technology, 2017. **315**: p. 438-444.
120. Xiao, X., et al., *Experimental and DEM studies on the particle mixing performance in rotating drums: Effect of area ratio*. Powder Technology, 2017. **314**: p. 182-194.
121. O'Connor, T. and S. Lee, *Chapter 37 - Emerging Technology for Modernizing Pharmaceutical Production: Continuous Manufacturing A2 - Qiu, Yihong*, in *Developing Solid Oral Dosage Forms (Second Edition)*, Y. Chen, et al., Editors. 2017, Academic Press: Boston. p. 1031-1046.
122. Barasso, D. and R. Ramachandran, *A comparison of model order reduction techniques for a four-dimensional population balance model describing multi-component wet granulation process*. Chemical Engineering Science, 2012. **80**: p. 380-392.
123. Immanuel, C.D. and F.J. Doyle III, *Solution technique for a multi-dimensional population balance model describing granulation processes*. Powder Technology, 2005. **156**(2-3): p. 213-225.
124. Immanuel, C.D. and F.J. Doyle, *Computationally efficient solution of population balance models incorporating nucleation, growth and coagulation: application to emulsion polymerization*. Chemical Engineering Science, 2003. **58**(16): p. 3681-3698.
125. Boukouvala, F., Dubey, A., Vanarase, A., Ramachandran, R., Muzzio, F.J., Ierapetritou, M., *Computational Approaches for Studying the Granular Dynamics of Continuous Blending Processes, 2 – Population Balance and Data-Based Methods*. Macromolecular Materials and Engineering, 2012. **297**: p. 9-19.
126. Wassgren, C.R., et al., *Incorporation particle flow information from discrete element simulations in population balance models of mixer-coaters*. Chemical Engineering Science, 2011. **66**(16): p. 3592-3604.
127. Hlinak, A.J., et al., *Understanding critical material properties for solid dosage form design*. Journal of Pharmaceutical Innovation, 2006. **September/October**: p. 12-17.
128. Ng, K.M., *Design and development of solids processes – A process systems engineering perspective*. Powder Technology, 2002. **126**(3): p. 205-210.
129. Sin, G., Gernaey, K.V., Eliasson Lantz, A., *Good modelling practice (GMP) for PAT applications: Propagation of input uncertainty and sensitivity analysis*. Biotechnology Progress, 2009. **25**: p. 1043-1053.
130. Ramachandran, R., Immanuel, C.D., Stepanek, F., Lister, J.D., Doyle, F.J. III, *A mechanistic model for breakage in population balances of granulation: Theoretical kernel development and experimental validation*. Chemical Engineering Research and Design, 2009. **87**: p. 598-614.

131. Saltelli, A., Chan, K., Scott, E.M., *Sensitivity Analysis*. 2000, Chichester: John Wiley & Sons Ltd.
132. Saltelli, A., S. Tarantola, and F. Campolongo, *Sensitivity analysis as an ingredient of modeling*. *Statistical Science*, 2000. **15**(4): p. 377-395.
133. Balci, O., *Golden Rules of Verification, Validation, Testing, and Certification of Modeling and Simulation Applications*. *SCS M&S Magazine*, 2010. **4**.
134. Min, F.Y.Y., M.; Wang, Z.C. , *Knowledge-based method for the validation of complex simulation models*. *Simul. Model. Pract*, 2010. **19**: p. 500-515.
135. Stephanopoulos, G. and G.V. Reklaitis, *Process systems engineering: From Solvay to modern bio- and nanotechnology.: A history of development, successes and prospects for the future*. *Chemical Engineering Science*, 2011. **66**(19): p. 4272-4306.
136. Ierapetritou, M.G. and R. Ramachandran, *Process simulation and data modeling in solid oral drug development and manufacture*. 2016: Springer.
137. Vanarase, A.U., J.G. Osorio, and F.J. Muzzio, *Effects of powder flow properties and shear environment on the performance of continuous mixing of pharmaceutical powders*. *Powder Technology*, 2013. **246**: p. 63-72.
138. Qiu, D.Z.a.Y., *Understanding Material Properties in Pharmaceutical Product Development and Manufacturing: Powder Flow and Mechanical Properties*. *Journal of Validation Technology*, 2010: p. 65-77.
139. Jeong, S.H., et al., *Material properties for making fast dissolving tablets by a compression method*. *Journal of Materials Chemistry*, 2008. **18**(30): p. 3527-3535.
140. Ferrari, F., et al., *Investigation on bonding and disintegration properties of pharmaceutical materials*. *International Journal of Pharmaceutics*, 1996. **136**(1): p. 71-79.
141. Shah, A.C. and A.R. Mlodozieniec, *Mechanism of surface lubrication: Influence of duration of lubricant-excipient mixing on processing characteristics of powders and properties of compressed tablets*. *Journal of Pharmaceutical Sciences*, 1977. **66**(10): p. 1377-1382.
142. Hernandez, E., et al., *Prediction of dissolution profiles by non-destructive near infrared spectroscopy in tablets subjected to different levels of strain*. *Journal of Pharmaceutical and Biomedical Analysis*, 2016. **117**: p. 568-576.
143. Fell, J.T. and J.M. Newton, *The tensile strength of lactose tablets*. *Journal of Pharmacy and Pharmacology*, 1968. **20**(8): p. 657-659.
144. Pawar, P., et al., *The effect of mechanical strain on properties of lubricated tablets compacted at different pressures*. *Powder Technology*, 2016. **301**: p. 657-664.
145. Jennifer Wang, H.W., Divyakant Desai, *Lubrication in tablet formulations*. *European Journal of Pharmaceutics and Biopharmaceutics*, 2010. **75**: p. 1-15.
146. H. Vromans, A.H.D.B., G. K. Bolhuis, C. F. Lerk, K. D. Kussendrager, H. Bosch, *Studies on tableting properties of lactose Part 2. Consolidation and compaction of different types of crystalline lactose*. *Pharmaceutisch Weekblad*, 1985. **7**: p. 186-193.
147. P. J. Sheskey, R.T.R.e.a., *Effects of lubricant level. method of mixing, and duration of mixing on a controlled-release matrix tablet containing hydroxyl methyl cellulose*. *Drug Development and Industrial Pharmacy*, 1995. **21**(19): p. 2151-2165.
148. Bolhuis, G.K., et al., *Film formation by magnesium stearate during mixing and its effect on tableting*. *Pharmaceutisch Weekblad*, 1975. **110**(16): p. 317-325.
149. Vromans, H. and C.F. Lerk, *Densification properties and compactibility of mixtures of pharmaceutical excipients with and without magnesium stearate*. *International Journal of Pharmaceutics*, 1988. **46**(3): p. 183-192.
150. Zuurman, K., K. Van der Voort Maarschalk, and G.K. Bolhuis, *Effect of magnesium stearate on bonding and porosity expansion of tablets produced from materials with*

- different consolidation properties*. International Journal of Pharmaceutics, 1999. **179**(1): p. 107-115.
151. Duberg, M. and C. Nyström, *Studies on direct compression of tablets. VI. Evaluation of methods for the estimation of particle fragmentation during compaction*. Acta Pharmaceutica Suecica, 1982. **19**(6): p. 421-436.
152. Jackson, S., I.C. Sinka, and A.C.F. Cocks, *The effect of suction during die fill on a rotary tablet press*. European Journal of Pharmaceutics and Biopharmaceutics, 2007. **65**(2): p. 253-256.
153. Sinka, I.C., L.C.R. Schneider, and A.C.F. Cocks, *Measurement of the flow properties of powders with special reference to die fill*. International Journal of Pharmaceutics, 2004. **280**(1): p. 27-38.
154. Vadodaria, S., *Correlation of compression models to material properties*, in *Chemical and Biochemical Engineering*. 2016, Rutgers University: Piscataway, NJ.
155. Razavi, S.M., et al., *Toward predicting tensile strength of pharmaceutical tablets by ultrasound measurement in continuous manufacturing*. International Journal of Pharmaceutics, 2016. **507**(1-2): p. 83-89.
156. Fell, J.T. and J.M. Newton, *Determination of Tablet Strength by the Diametral-Compression Test*. Journal of Pharmaceutical Sciences, 1970. **59**(5): p. 688-691.
157. Mallick, S., *Rearrangement of particle and compactibility, tabletability and compressibility of pharmaceutical powder: A rational approach*. Journal of Scientific and Industrial Research, 2014. **73**(1): p. 51-56.
158. Martínez, L., et al., *Correlation between compactibility values and excipient cluster size using an in silico approach*. Drug Development and Industrial Pharmacy, 2013. **39**(2): p. 374-381.
159. Demšar, U., et al., *Principal Component Analysis on Spatial Data: An Overview*. Annals of the Association of American Geographers, 2013. **103**(1): p. 106-128.
160. Race, A.M., et al., *Memory Efficient Principal Component Analysis for the Dimensionality Reduction of Large Mass Spectrometry Imaging Data Sets*. Analytical Chemistry, 2013. **85**(6): p. 3071-3078.
161. Fan, J., F. Han, and H. Liu, *Challenges of Big Data analysis*. National Science Review, 2014. **1**(2): p. 293-314.
162. Koynov, A., I. Akseli, and A.M. Cuitiño, *Modeling and simulation of compact strength due to particle bonding using a hybrid discrete-continuum approach*. International Journal of Pharmaceutics, 2011. **418**(2): p. 273-285.
163. Patel, S., A.M. Kaushal, and A.K. Bansal, *Effect of particle size and compression force on compaction behavior and derived mathematical parameters of compressibility*. Pharm Res, 2007. **24**(1): p. 111-24.
164. Shang, C., et al., *Break force and tensile strength relationships for curved faced tablets subject to diametrical compression*. International Journal of Pharmaceutics, 2013. **442**(1-2): p. 57-64.
165. Capece, M., et al., *On the relationship of inter-particle cohesiveness and bulk powder behavior: Flowability of pharmaceutical powders*. International Journal of Pharmaceutics, 2016. **511**(1): p. 178-189.
166. Sun, C.C., *True Density of Microcrystalline Cellulose*. Journal of Pharmaceutical Sciences, 2005. **94**(10): p. 2132-2134.
167. U. I. Leinonen, H.U.J., P. A. Vihervaara, E. S. U. Laine, *Physical and Lubrication Properties of Magnesium Stearate*. Journal of Pharmaceutical Sciences, 1992. **81**(12): p. 1194-1198.
168. Becher, P.F., *Microstructural Design of Toughened Ceramics*. Journal of the American Ceramic Society, 1991. **74**(2): p. 255-269.

169. Meyers, M.A., A. Mishra, and D.J. Benson, *Mechanical properties of nanocrystalline materials*. Progress in Materials Science, 2006. **51**(4): p. 427-556.
170. Sigmund, W.M., N.S. Bell, and L. Bergström, *Novel Powder-Processing Methods for Advanced Ceramics*. Journal of the American Ceramic Society, 2000. **83**(7): p. 1557-1574.
171. Zhilyaev, A.P., et al., *Mechanical behavior and microstructure properties of titanium powder consolidated by high-pressure torsion*. Materials Science and Engineering: A, 2017. **688**(Supplement C): p. 498-504.
172. Amherd Hidalgo, A., et al., *Powder Metallurgy Strategies to Improve Properties and Processing of Titanium Alloys: A Review*. Advanced Engineering Materials, 2017. **19**(6): p. 1600743-n/a.
173. Kallip, K., et al., *Microstructure and mechanical properties of near net shaped aluminium/alumina nanocomposites fabricated by powder metallurgy*. Journal of Alloys and Compounds, 2017. **714**(Supplement C): p. 133-143.
174. Khodabakhshi, F. and A. Simchi, *The role of microstructural features on the electrical resistivity and mechanical properties of powder metallurgy Al-SiC-Al₂O₃ nanocomposites*. Materials & Design, 2017. **130**(Supplement C): p. 26-36.
175. Shen, J., et al., *The formation of bimodal multilayered grain structure and its effect on the mechanical properties of powder metallurgy pure titanium*. Materials & Design, 2017. **116**(Supplement C): p. 99-108.
176. Bezemer, G.L., et al., *Cobalt Particle Size Effects in the Fischer–Tropsch Reaction Studied with Carbon Nanofiber Supported Catalysts*. Journal of the American Chemical Society, 2006. **128**(12): p. 3956-3964.
177. Min, M.-k., et al., *Particle size and alloying effects of Pt-based alloy catalysts for fuel cell applications*. Electrochimica Acta, 2000. **45**(25): p. 4211-4217.
178. Xie, H.Y. and D. Geldart, *Fluidization of FCC powders in the bubble-free regime: effect of types of gases and temperature*. Powder Technology, 1995. **82**(3): p. 269-277.
179. Chegini, G.R. and B. Ghobadian, *Effect of Spray-Drying Conditions on Physical Properties of Orange Juice Powder*. Drying Technology, 2005. **23**(3): p. 657-668.
180. Moreyra, R. and M. Peleg, *Effect of Equilibrium Water Activity on the Bulk Properties of Selected Food Powders*. Journal of Food Science, 1981. **46**(6): p. 1918-1922.
181. Agudelo, C., et al., *Effect of process technology on the nutritional, functional, and physical quality of grapefruit powder*. Food Science and Technology International, 2016. **23**(1): p. 61-74.
182. Fitzpatrick, J.J., S.A. Barringer, and T. Iqbal, *Flow property measurement of food powders and sensitivity of Jenike's hopper design methodology to the measured values*. Journal of Food Engineering, 2004. **61**(3): p. 399-405.
183. Kondor, A. and S.A. Hogan, *Relationships between surface energy analysis and functional characteristics of dairy powders*. Food Chemistry, 2017. **237**(Supplement C): p. 1155-1162.
184. Mani, S., L.G. Tabil, and S. Sokhansanj, *Effects of compressive force, particle size and moisture content on mechanical properties of biomass pellets from grasses*. Biomass and Bioenergy, 2006. **30**(7): p. 648-654.
185. Hasa, D. and W. Jones, *Screening for new pharmaceutical solid forms using mechanochemistry: A practical guide*. Advanced Drug Delivery Reviews, 2017. **117**(Supplement C): p. 147-161.
186. Sun, C.C., *Microstructure of Tablet—Pharmaceutical Significance, Assessment, and Engineering*. Pharmaceutical Research, 2017. **34**(5): p. 918-928.
187. Aksu, B., De Beer, T., Folestad, S., Ketolainen, J., Linden, H., Lopes, J.A., de Matas, M., Oostra, W., Rantanen, J., Weimer, M., *Strategic funding priorities in the pharmaceutical*

- sciences allied to Quality by Design (QbD) and Process Analytical Technology (PAT)*. European Journal of Pharmaceutical Sciences, 2012. **47**: p. 402-405.
188. ECA. "Why Did FDA Change Their Guideline on Process Validation?". GMP News 2011 [cited 2013; Available from: http://www.gmp-compliance.org/eca_news_2600.html].
189. Llusà, M., et al., *Shear-induced APAP de-agglomeration*. Drug Development and Industrial Pharmacy, 2009. **35**(12): p. 1487-1495.
190. Muzzio, F.J., T. Shinbrot, and B.J. Glasser, *Powder technology in the pharmaceutical industry: the need to catch up fast*. Powder Technology, 2002. **124**(1): p. 1-7.
191. Chaudhuri, B., et al., *Cohesive effects in powder mixing in a tumbling blender*. Powder Technology, 2006. **165**(2): p. 105-114.
192. Harmonisation, I.C.o., *Harmonised Tripartite Guideline: Pharmaceutical Development Q8(R2)*. 2009, International Conference on Harmonisation of Technical Requirements for Registration of pharmaceuticals for human use.
193. Ma, L., L. Deng, and J. Chen, *Applications of poly(ethylene oxide) in controlled release tablet systems: a review*. Drug Development and Industrial Pharmacy, 2014. **40**(7): p. 845-851.
194. Williams, R.O., et al., *Investigation of Excipient Type and Level on Drug Release from Controlled Release Tablets Containing HPMC*. Pharmaceutical Development and Technology, 2002. **7**(2): p. 181-193.
195. Li, H., R.J. Hardy, and X. Gu, *Effect of drug solubility on polymer hydration and drug dissolution from polyethylene oxide (PEO) matrix tablets*. AAPS PharmSciTech, 2008. **9**(2): p. 437-43.
196. Portillo, P.M., Vanarase, A.U., Ingram, A., Seville, J.K., *Investigation of the effect of impeller rotation rate, powder flowrate, and cohesion on powder flow behavior in a continuous blender using PEPT*. Chemical Engineering Science, 2010. **65**: p. 5685-5668.
197. Portillo, P.M., Ierapetritou, M.G., Muzzio, F.J., *Effects of rotation rate, mixing angle, and cohesion in two continuous mixers—A statistical approach*. Powder Technology, 2009. **194**: p. 217-227.
198. Van Snick, B., et al., *Development of a continuous direct compression platform for low-dose drug products*. Int J Pharm, 2017. **529**(1-2): p. 329-346.
199. Osorio, J.G., et al., *Characterization of resonant acoustic mixing using near-infrared chemical imaging*. Powder Technology, 2016. **297**(Supplement C): p. 349-356.
200. Sudah, O.S., et al., *Simulation and experiments of mixing and segregation in a tote blender*. AIChE Journal, 2005. **51**(3): p. 836-844.
201. Muzzio, F.J., et al., *Evaluating the mixing performance of a ribbon blender*. Powder Technology, 2008. **186**(3): p. 247-254.
202. Jackson, S., I.C. Sinka, and A.C. Cocks, *The effect of suction during die fill on a rotary tablet press*. Eur J Pharm Biopharm, 2007. **65**(2): p. 253-6.
203. Mehrotra, A., et al., *A modeling approach for understanding effects of powder flow properties on tablet weight variability*. Powder Technology, 2009. **188**(3): p. 295-300.
204. Emady, H.N., et al., *Granule formation mechanisms and morphology from single drop impact on powder beds*. Powder Technology, 2011. **212**(1): p. 69-79.
205. Oka, S., et al., *The effects of improper mixing and preferential wetting of active and excipient ingredients on content uniformity in high shear wet granulation*. Powder Technology, 2015. **278**: p. 266-277.
206. Aulton, M.E., M. Banks, and D.K. Smith, *The wettability of powders during fluidized bed granulation*. Journal of Pharmacy and Pharmacology, 1977. **29**(S1): p. 59P-59P.
207. Faqih, A.M.N., et al., *Effect of moisture and magnesium stearate concentration on flow properties of cohesive granular materials*. International Journal of Pharmaceutics, 2007. **336**(2): p. 338-345.

208. Pingali, K., et al., *Mixing order of glidant and lubricant – Influence on powder and tablet properties*. International Journal of Pharmaceutics, 2011. **409**(1): p. 269-277.
209. Mehrotra, A., et al., *Influence of shear intensity and total shear on properties of blends and tablets of lactose and cellulose lubricated with magnesium stearate*. International Journal of Pharmaceutics, 2007. **336**(2): p. 284-291.
210. Llusa, M., et al., *Measuring the hydrophobicity of lubricated blends of pharmaceutical excipients*. Powder Technology, 2010. **198**(1): p. 101-107.
211. Arratia, P.E., et al., *Characterizing mixing and lubrication in the Bohle Bin blender*. Powder Technology, 2006. **161**(3): p. 202-208.
212. Nomura, T., T. Satoh, and H. Masuda, *The environment humidity effect on the tribo-charge of powder*. Powder Technology, 2003. **135-136**: p. 43-49.
213. Matsusaka, S., et al., *Triboelectric charging of powders: A review*. Chemical Engineering Science, 2010. **65**(22): p. 5781-5807.
214. Naik, S., R. Mukherjee, and B. Chaudhuri, *Triboelectrification: A review of experimental and mechanistic modeling approaches with a special focus on pharmaceutical powders*. International Journal of Pharmaceutics, 2016. **510**(1): p. 375-385.
215. Siraj, M.S., et al., *Effect of blade angle and particle size on powder mixing performance in a rectangular box*. Powder Technology, 2011. **211**(1): p. 100-113.
216. Lorences, M.J., et al., *Fluid bed gas RTD: Effect of fines and internals*. Powder Technology, 2006. **168**(1): p. 1-9.
217. Koynov, S., B. Glasser, and F. Muzzio, *Comparison of three rotational shear cell testers: Powder flowability and bulk density*. Powder Technology, 2015. **283**(Supplement C): p. 103-112.
218. Wang, Y., et al., *A method to analyze shear cell data of powders measured under different initial consolidation stresses*. Powder Technology, 2016. **294**(Supplement C): p. 105-112.
219. Allen, T., *Particle Size Measurement*. Vol. 4. 1990, USA: Springer, Dordrecht.
220. Govedarica, B., et al., *The use of single particle mechanical properties for predicting the compressibility of pharmaceutical materials*. Powder Technology, 2012. **225**: p. 43-51.
221. Vanarase, A.U. and F.J. Muzzio, *Effect of operating conditions and design parameters in a continuous powder mixer*. Powder Technology, 2011. **208**(1): p. 26-36.
222. Rajalahti, T. and O.M. Kvalheim, *Multivariate data analysis in pharmaceuticals: a tutorial review*. Int J Pharm, 2011. **417**(1-2): p. 280-90.
223. Koynov, S., *Using statistical methods to optimize powder flow measurements and to predict powder processing performance*, in *Chemical and Biochemical Engineering*. 2015, Rutgers University: New Brunswick, NJ.
224. Abdullah, E.C. and D. Geldart, *The use of bulk density measurements as flowability indicators*. Powder Technology, 1999. **102**(2): p. 151-165.
225. Fu, X., et al., *Effect of particle shape and size on flow properties of lactose powders*. Particuology, 2012. **10**(2): p. 203-208.
226. Wang, Y., et al., *Controlled shear system and resonant acoustic mixing: Effects on lubrication and flow properties of pharmaceutical blends*. Powder Technology, 2017. **322**: p. 332-339.
227. Koynov, S., et al., *Measurement of the axial dispersion coefficient of powders in a rotating cylinder: dependence on bulk flow properties*. Powder Technology, 2016. **292**: p. 298-306.
228. Nauman, E.B., *Residence Time Distributions*. 3rd ed. Advances in Industrial Mixing, ed. S.E.I. Kresta, AW; Dickey, DS; Atieno-Obeng, V. 2016, USA: Wiley.
229. Kresta, S.M., et al., *Handbook of Industrial Mixing : Science and Practice*. 2004, Hoboken, UNITED STATES: John Wiley & Sons, Incorporated.
230. Biegler, L., *Perry's Chemical Engineering Handbook*, ed. D.W. Green. 2008, New York, NY: McGraw-Hill Companies.

231. Levenspiel, O., *Chemical Reaction Engineering*. 3rd ed. ed. 1999, Hoboken: Wiley.
232. Fogler, H., *Essential of Chemical Reaction Engineering*. 2016, USA: Prentice Hall.
233. Bošković, D. and S. Loebbecke, *Modelling of the residence time distribution in micromixers*. *Chemical Engineering Journal*, 2008. **135**(Supplement 1): p. S138-S146.
234. Georget, E., et al., *Residence time distributions in a modular micro reaction system*. *Journal of Food Engineering*, 2013. **116**(4): p. 910-919.
235. Leray, S., et al., *Residence time distributions for hydrologic systems: Mechanistic foundations and steady-state analytical solutions*. *Journal of Hydrology*, 2016. **543**(Part A): p. 67-87.
236. Berezhkovskiy, L.M., *Determination of Mean Residence Time of Drug in Plasma and the Influence of the Initial Drug Elimination and Distribution on the Calculation of Pharmacokinetic Parameters*. *Journal of Pharmaceutical Sciences*, 2009. **98**(2): p. 748-762.
237. Pernenkil, L. and C.L. Cooney, *A review on the continuous blending of powders*. *Chemical Engineering Science*, 2006. **61**(2): p. 720-742.
238. Ambler, P.A., et al., *Residence time distribution of solids in a circulating fluidized bed: Experimental and modelling studies*. *Chemical Engineering Science*, 1990. **45**(8): p. 2179-2186.
239. Zhu, J.X., et al., *Cocurrent downflow circulating fluidized bed (downer) reactors — A state of the art review*. *The Canadian Journal of Chemical Engineering*, 1995. **73**(5): p. 662-677.
240. Weinekötter, R. and H. Gericke, *Mixing of Solids*. 2013: Springer Netherlands.
241. Paredes, I.J., et al., *The effect of operating conditions on the residence time distribution and axial dispersion coefficient of a cohesive powder in a rotary kiln*. *Chemical Engineering Science*, 2017. **158**(Supplement C): p. 50-57.
242. Thomas, R., et al., *Residence time investigation of a multiple hearth kiln using mineral tracers*. *Chemical Engineering and Processing: Process Intensification*, 2009. **48**(4): p. 950-954.
243. Ngako, S., et al., *Numerical investigation of bed depth height, axial velocity and mean residence time of inert particles in steady state industrial cement rotary kiln: Case of Figuil Plant in Cameroon*. *Powder Technology*, 2015. **271**(Supplement C): p. 221-227.
244. Geng, S., et al., *Prediction of solids residence time distribution in cross-flow bubbling fluidized bed*. *Powder Technology*, 2017. **320**(Supplement C): p. 555-564.
245. Yoo, H., et al., *Effect of the jet direction of gas nozzle on the residence time distribution of solids in circulating fluidized bed risers*. *Journal of the Taiwan Institute of Chemical Engineers*, 2017. **71**(Supplement C): p. 235-243.
246. Zou, Z., et al., *CFD simulation of solids residence time distribution in a multi-compartment fluidized bed*. *Chinese Journal of Chemical Engineering*, 2017.
247. Zhang, B., et al., *Modeling study of residence time of molten slag on the wall in an entrained flow gasifier*. *Fuel*, 2018. **212**(Supplement C): p. 437-447.
248. Zhang, Y., et al., *CFD simulation and experiment of residence time distribution in short-contact cyclone reactors*. *Advanced Powder Technology*, 2015. **26**(4): p. 1134-1142.
249. Youssef, Z., et al., *Residence time distribution in a biomass pretreatment reactor: Experimentation and modeling*. *Chemical Engineering Research and Design*, 2017. **125**(Supplement C): p. 233-244.
250. Gao, Y.J., M. Ierapetritou, and F. Muzzio, *Periodic Section Modeling of Convective Continuous Powder Mixing Processes*. *Aiche Journal*, 2012. **58**(1): p. 69-78.
251. Gao, Y., M. Ierapetritou, and F. Muzzio, *Determination of the Confidence Interval of the Relative Standard Deviation Using Convolution*. *Journal of Pharmaceutical Innovation*, 2013. **8**(2): p. 72-82.

252. Portillo, P.M., Muzzio, F.J., Ierapetritou, M.G., *Using Compartment Modeling to Investigate Mixing Behavior of a Continuous Mixer*. Journal of Pharmaceutical Innovation, 2008. **3**: p. 161-174.
253. Portillo, P.M., M.G. Ierapetritou, and F.J. Muzzio, *Characterization of continuous convective powder mixing processes*. Powder Technology, 2008. **182**(3): p. 368-378.
254. Marikh, K., et al., *Flow Analysis and Markov Chain Modelling to Quantify the Agitation Effect in a Continuous Powder Mixer*. Chemical Engineering Research and Design, 2006. **84**(11): p. 1059-1074.
255. Berthiaux, H., K. Marikh, and C. Gatumel, *Continuous mixing of powder mixtures with pharmaceutical process constraints*. Chemical Engineering and Processing, 2008. **47**(12): p. 2315-2322.
256. Ammarcha, C., et al., *Predicting bulk powder flow dynamics in a continuous mixer operating in transitory regimes*. Advanced Powder Technology, 2012. **23**(6): p. 787-800.
257. Ammarcha, C., et al., *Transitory powder flow dynamics during emptying of a continuous mixer*. Chemical Engineering and Processing: Process Intensification, 2013. **65**: p. 68-75.
258. Ammarcha, C., et al., *Continuous powder mixing of segregating mixtures under steady and unsteady state regimes: Homogeneity assessment by real-time on-line image analysis*. Powder Technology, 2017. **315**(Supplement C): p. 39-52.
259. Galbraith, S.C., et al., *Modeling and simulation of continuous powder blending applied to a continuous direct compression process*. Pharmaceutical Development and Technology, 2018: p. 1-11.
260. Mateo-Ortiz, D. and R. Méndez, *Relationship between residence time distribution and forces applied by paddles on powder attrition during the die filling process*. Powder Technology, 2015. **278**: p. 111-117.
261. Šašić, S., et al., *Detailed analysis of the online near-infrared spectra of pharmaceutical blend in a rotary tablet press feed frame*. Journal of Pharmaceutical and Biomedical Analysis, 2015. **103**: p. 73-79.
262. Mateo-Ortiz, D., F.J. Muzzio, and R. Méndez, *Particle size segregation promoted by powder flow in confined space: The die filling process case*. Powder Technology, 2014. **262**: p. 215-222.
263. Ward, H.W., et al., *Monitoring blend potency in a tablet press feed frame using near infrared spectroscopy*. Journal of Pharmaceutical and Biomedical Analysis, 2013. **80**: p. 18-23.
264. Mendez, R., F. Muzzio, and C. Velazquez, *Study of the effects of feed frames on powder blend properties during the filling of tablet press dies*. Powder Technology, 2010. **200**(3): p. 105-116.
265. De Leersnyder, F., et al., *Development and validation of an in-line NIR spectroscopic method for continuous blend potency determination in the feed frame of a tablet press*. Journal of Pharmaceutical and Biomedical Analysis, 2018. **151**: p. 274-283.
266. Van Snick, B., et al., *Continuous direct compression as manufacturing platform for sustained release tablets*. Int J Pharm, 2017. **519**(1-2): p. 390-407.
267. Byrn, S., et al., *Achieving Continuous Manufacturing for Final Dosage Formation: Challenges and How to Meet Them May 20–21 2014 Continuous Manufacturing Symposium*. Journal of Pharmaceutical Sciences, 2015. **104**(3): p. 792-802.
268. Kruisz, J., et al., *RTD modeling of a continuous dry granulation process for process control and materials diversion*. International Journal of Pharmaceutics, 2017. **528**(1): p. 334-344.
269. Mangal, H. and P. Kleinebudde, *Experimental determination of residence time distribution in continuous dry granulation*. International Journal of Pharmaceutics, 2017. **524**(1): p. 91-100.

270. Kumar, A., et al., *Mixing and transport during pharmaceutical twin-screw wet granulation: Experimental analysis via chemical imaging*. European Journal of Pharmaceutics and Biopharmaceutics, 2014. **87**(2): p. 279-289.
271. Lee, K.T., A. Ingram, and N.A. Rowson, *Twin screw wet granulation: The study of a continuous twin screw granulator using Positron Emission Particle Tracking (PEPT) technique*. European Journal of Pharmaceutics and Biopharmaceutics, 2012. **81**(3): p. 666-673.
272. Kumar, A., et al., *Linking granulation performance with residence time and granulation liquid distributions in twin-screw granulation: An experimental investigation*. European Journal of Pharmaceutical Sciences, 2016. **90**(Supplement C): p. 25-37.
273. Vanarase, A.U., et al., *Real-time monitoring of drug concentration in a continuous powder mixing process using NIR spectroscopy*. Chemical Engineering Science, 2010. **65**(21): p. 5728-5733.
274. Esbensen, K.H. and P. Paasch-Mortensen, *Process Sampling: Theory of Sampling – the Missing Link in Process Analytical Technologies (PAT)*, in *Process Analytical Technology*. 2010, John Wiley & Sons, Ltd. p. 37-80.
275. Esbensen, K.H., et al., *Adequacy and verifiability of pharmaceutical mixtures and dose units by variographic analysis (Theory of Sampling) – A call for a regulatory paradigm shift*. International Journal of Pharmaceutics, 2016. **499**(1): p. 156-174.
276. Osorio, J.G. and F.J. Muzzio, *Evaluation of resonant acoustic mixing performance*. Powder Technology, 2015. **278**(Supplement C): p. 46-56.
277. Hirschberg, C., C.C. Sun, and J. Rantanen, *Analytical method development for powder characterization: Visualization of the critical drug loading affecting the processability of a formulation for direct compression*. Journal of Pharmaceutical and Biomedical Analysis, 2016. **128**: p. 462-468.
278. Müllertz, A., Y. Perrie, and T. Rades, *Analytical Techniques in the Pharmaceutical Sciences*. 2016: Springer New York.
279. Gao, Y.J., et al., *Characterizing continuous powder mixing using residence time distribution*. Chemical Engineering Science, 2011. **66**(3): p. 417-425.
280. Kreyszig, E., *Advanced Engineering Mathematics*. 2011, USA: Wiley.
281. Jones, J.G., *On the Numerical Solution of Convolution Integral Equations and Systems of Such Equations*. Mathematics of Computation, 1961. **15**(74): p. 131-142.
282. Bassingthwaighe, J.B., *Physiology and Theory of Tracer Washout Techniques for the Estimation of Myocardial Blood Flow: Flow Estimation From Tracer Washout*. Progress in cardiovascular diseases, 1977. **20**(3): p. 165-189.
283. Bassingthwaighe, J.B. and G.A. Holloway, Jr., *Estimation of blood flow with radioactive tracers*. Semin Nucl Med, 1976. **6**(2): p. 141-61.
284. Bassingthwaighe, J.B. and T. Yipintsoi, *Organ blood flow, wash-in, washout, and clearance of nutrients and metabolites*. Mayo Clin Proc, 1974. **49**(4): p. 248-55.
285. Bassingthwaighe, J.B., *Circulatory Transport and the Convolution Integral*. Mayo Clinic proceedings. Mayo Clinic, 1967. **42**(3): p. 137-154.
286. Tian, G., et al., *A dimensionless analysis of residence time distributions for continuous powder mixing*. Powder Technology, 2017. **315**(Supplement C): p. 332-338.
287. Engisch, W.E. and F.J. Muzzio, *Method for characterization of loss-in-weight feeder equipment*. Powder Technology, 2012. **228**: p. 395-403.
288. Yang, S., Evans, J.R.G., *Metering and dispensing of powder; the quest for new solid freeforming techniques*. Powder Technology, 2007. **178**: p. 56-72.
289. Yu, Y., *Theoretical Modelling and Experimental Investigation of the Performance of Screw Feeders*, in *Mechanical Engineering*. 1997, University of Wollongong.

290. Bortolamasi, M. and J. Fottner, *Design and sizing of screw feeders*, in *International Congress for Particle Technology*. 2001: Nuremberg, Germany.
291. Pan, H., R.G. Landers, and F. Liou, *Dynamic Modeling of Powder Delivery Systems in Gravity-Fed Powder Feeders*. *Journal of Manufacturing Science and Engineering*, 2005. **128**(1): p. 337-345.
292. Cleary, P.W., *DEM modelling of particulate flow in a screw feeder Model description*. *Progress in Computational Fluid Dynamics, an International Journal*, 2007. **7**(2): p. 128-138.
293. Engisch, W.E. and F.J. Muzzio, *Loss-in-Weight Feeding Trials Case Study: Pharmaceutical Formulation*. *Journal of Pharmaceutical Innovation*, 2014. **10**(1): p. 56-75.
294. Engisch, W.E., *Loss-in-weight feeding in continuous powder manufacturing*. 2014.
295. Gao, Y.J., F. Muzzio, and M. Ierapetritou, *Characterization of Feeder Effects on Continuous Solid Mixing Using Fourier Series Analysis*. *Aiche Journal*, 2011. **57**(5): p. 1144-1153.
296. Capece, M., Z. Huang, and R. Davé, *Insight Into a Novel Strategy for the Design of Tablet Formulations Intended for Direct Compression*. *Journal of Pharmaceutical Sciences*, 2017. **106**(6): p. 1608-1617.
297. Jallo, L.J., et al., *Improvement of flow and bulk density of pharmaceutical powders using surface modification*. *International Journal of Pharmaceutics*, 2012. **423**(2): p. 213-225.
298. Ghoroi, C., et al., *Multi-faceted characterization of pharmaceutical powders to discern the influence of surface modification*. *Powder Technology*, 2013. **236**: p. 63-74.
299. Han, X., C. Ghoroi, and R. Davé, *Dry coating of micronized API powders for improved dissolution of directly compacted tablets with high drug loading*. *International Journal of Pharmaceutics*, 2013. **442**(1): p. 74-85.
300. Blackshields, C.A. and A.M. Crean, *Continuous powder feeding for pharmaceutical solid dosage form manufacture: a short review*. *Pharmaceutical Development and Technology*, 2017: p. 1-7.
301. Van Snick, B., et al., *Continuous direct compression as manufacturing platform for sustained release tablets*. *International Journal of Pharmaceutics*, 2017. **519**(1): p. 390-407.
302. Schulze, D., *Powder and Bulk Solids*. 2008, Springer: New York, NY. p. 339-342.
303. Falk, J., et al., *Mass flow and variability in screw feeding of biomass powders — Relations to particle and bulk properties*. *Powder Technology*, 2015. **276**(0): p. 80-88.
304. Vanel, L., et al., *Stresses in Silos: Comparison Between Theoretical Models and New Experiments*. *Physical Review Letters*, 2000. **84**(7): p. 1439-1442.
305. Oka, S.S., et al., *Design of an integrated continuous manufacturing system*. *Continuous Manufacturing of Pharmaceuticals*, 2017: p. 405-446.
306. Portillo, P., et al., *Quality by Design Methodology for Development and Scale-up of Batch Mixing Processes*. *Journal of Pharmaceutical Innovation*, 2008. **3**(4): p. 258-270.
307. Boukouvala, F., F.J. Muzzio, and M.G. Ierapetritou, *Design Space of Pharmaceutical Processes Using Data-Driven-Based Methods*. *Journal of Pharmaceutical Innovation*, 2010. **5**(3): p. 119-137.
308. Pharmacopeia, T.U.S., <616> *Bulk Density and Tapped Density of Powders*, in *Stage 6 Harmonization*. 2012, The United States Pharmacopeia: The United States Pharmacopeial Convention.
309. Vegter, H. and A. Van den Boogaard, *A plane stress yield function for anisotropic sheet material by interpolation of biaxial stress states*. *International Journal of Plasticity*, 2006. **22**(3): p. 557-580.
310. Falticeanu, C., et al., *New methods for assessing the frictional properties in a mass of consolidated powder*. In *Proceeding of Balkantrib*, 2005. **5**: p. 132.

311. Schulze, D., *Powders and bulk solids: behavior, characterization, storage and flow*. 2007: Springer.
312. Alexander, A.W., et al., *Avalanching flow of cohesive powders*. Powder Technology, 2006. **164**(1): p. 13-21.
313. Vasilenko, A., et al., *Role of consolidation state in the measurement of bulk density and cohesion*. Powder Technology, 2013. **239**: p. 366-373.
314. Kroonenberg, P.M., *Applied Multiway Data Analysis*. Wiley Series in Probability and Statistics. 2008, Hoboken, NJ: John Wiley & Sons, Inc.
315. Cui, Y., et al., *Variable selection in multivariate modeling of drug product formula and manufacturing process*. Journal of Pharmaceutical Sciences, 2012. **101**(12): p. 4597-4607.
316. Hayashi, Y., et al., *Reliability evaluation of nonlinear design space in pharmaceutical product development*. Journal of Pharmaceutical Sciences, 2012. **101**(1): p. 333-341.
317. Kikuchi, S., et al., *Latent structure analysis in pharmaceutical formulations using Kohonen's self-organizing map and a Bayesian network*. Journal of Pharmaceutical Sciences, 2011. **100**(3): p. 964-975.
318. Snedecor, G.W.a.C., William G. , *Statistical Methods*. 1989, USA: Iowa State University Press.
319. Onuki, Y., M. Morishita, and K. Takayama, *Formulation optimization of water-in-oil-water multiple emulsion for intestinal insulin delivery*. J Control Release, 2004. **97**(1): p. 91-9.
320. Palabiyik, M.e.a., *Multivariate Optimization Model in a Partial Least Squares-1 Method for Simultaneous Determination of Dorzolamide Hydrochloride and Timolol Maleate in Eye Drops*. Current Pharmaceutical Analysis, 2013. **9**(4): p. 404-412.
321. Takayama, K., et al., *Multivariate spline interpolation as a novel method to optimize pharmaceutical formulations*. Pharmazie, 2004. **59**(5): p. 392-5.
322. ten Berge, J., *Least Squares Optimization in Multivariate Analysis*. 1993, Leiden: DSWO Press.
323. Varshosaz, J., S. Eskandari, and M. Tabakhian, *Production and optimization of valproic acid nanostructured lipid carriers by the Taguchi design*. Pharm Dev Technol, 2010. **15**(1): p. 89-96.
324. Vignaduzzo, S., et al., *Multivariate Optimization and Validation of a CZE Method for the Analysis of Pridinol Mesylate and Meloxicam in Tablets*. Chromatographia, 2011. **74**(7-8): p. 609-617.
325. Yasuda, A., et al., *Self-organizing map analysis using multivariate data from theophylline powders predicted by a thin-plate spline interpolation*. Journal of Pharmaceutical Sciences, 2010. **99**(11): p. 4535-4542.
326. Gan, G., C. Ma, and J. Wu, *Data clustering: theory, algorithms, and applications*. Vol. 20. 2007: Siam.
327. Aggarwal, C.C. and C.K. Reddy, *Data clustering: algorithms and applications*. 2013: CRC press.
328. Berkhin, P., *A survey of clustering data mining techniques*, in *Grouping multidimensional data*. 2006, Springer. p. 25-71.
329. Hennig, C., *Cluster-wise assessment of cluster stability*. Computational Statistics & Data Analysis, 2007. **52**(1): p. 258-271.
330. Murtagh, F. and P. Contreras, *Algorithms for hierarchical clustering: an overview*. Wiley Interdisciplinary Reviews: Data Mining and Knowledge Discovery, 2012. **2**(1): p. 86-97.
331. Murtagh, F. and P. Contreras, *Algorithms for hierarchical clustering: an overview, II*. Wiley Interdisciplinary Reviews: Data Mining and Knowledge Discovery, 2017. **7**(6): p. e1219-n/a.

332. Oyelade, O., O. Oladipupo, and I. Obagbuwa, *Application of k Means Clustering algorithm for prediction of Students Academic Performance*. arXiv preprint arXiv:1002.2425, 2010.
333. Detroyer, A., et al., *Exploratory chemometric analysis of the classification of pharmaceutical substances based on chromatographic data*. Journal of Chromatography A, 2000. **897**(1): p. 23-36.
334. Hand, D.J., *Principles of Data Mining*. Drug Safety, 2007. **30**(7): p. 621-622.
335. Balakin, K., *Pharmaceutical Data Mining: Approaches and Applications for Drug Discovery*. Vol. 6. 2009: John Wiley & Sons.
336. Froment, G., K. Bischoff, and J. Wilde, *Chemical Reactor Analysis and Design*. 2011, Hoboken, NJ: Wiley.
337. Gao, Y., et al., *Improving Continuous Powder Blending Performance Using Projection to Latent Structures Regression*. Journal of Pharmaceutical Innovation, 2013. **8**(2): p. 99-110.
338. Gao, Y., F.J. Muzzio, and M.G. Ierapetritou, *A review of the Residence Time Distribution (RTD) applications in solid unit operations*. Powder Technology, 2012. **228**(0): p. 416-423.
339. Perry, R.H.G., Don W, *Perry's Chemical Engineering Handbook*. 5th ed. 2005, New York: McGraw-Hill.
340. Hill, C., *An Introduction to Chemical Engineering Kinetics & Reactor Design*. 1977, USA: Wiley.
341. Pernenkil, L., Cooney, C.L., *A review on the continuous blending of powders*. Chemical Engineering Science, 2006. **61**: p. 720-742.
342. Vanarase, A.U., et al., *Real-time monitoring of drug concentration in a continuous powder mixing process using NIR spectroscopy*. Chemical Engineering Science, 2010. **65**(21): p. 5728-5733.
343. Shi, Z., et al., *Process characterization of powder blending by near-infrared spectroscopy: Blend end-points and beyond*. Journal of Pharmaceutical and Biomedical Analysis, 2008. **47**(4): p. 738-745.
344. Sekulic, S.S., et al., *On-Line Monitoring of Powder Blend Homogeneity by Near-Infrared Spectroscopy*. Analytical Chemistry, 1996. **68**(3): p. 509-513.
345. Rantanen, J., et al., *Use of In-Line Near-Infrared Spectroscopy in Combination with Chemometrics for Improved Understanding of Pharmaceutical Processes*. Analytical Chemistry, 2005. **77**(2): p. 556-563.
346. Popo, M., et al., *Blend uniformity analysis using stream sampling and near infrared spectroscopy*. AAPS PharmSciTech, 2002. **3**(3): p. 61-71.